

---

Electronic Thesis and Dissertation Repository

---

2-9-2017 12:00 AM

## First-order statistical speckle models improve robustness and reproducibility of contrast-enhanced ultrasound perfusion estimates

Matthew R. Lowerison, *The University of Western Ontario*

Supervisor: Dr. James C. Lacefield, *The University of Western Ontario*

Joint Supervisor: Dr. Ann F. Chambers, *The University of Western Ontario*

A thesis submitted in partial fulfillment of the requirements for the Doctor of Philosophy degree in Medical Biophysics

© Matthew R. Lowerison 2017

Follow this and additional works at: <https://ir.lib.uwo.ca/etd>



Part of the [Biophysics Commons](#)

---

### Recommended Citation

Lowerison, Matthew R., "First-order statistical speckle models improve robustness and reproducibility of contrast-enhanced ultrasound perfusion estimates" (2017). *Electronic Thesis and Dissertation Repository*. 4399.

<https://ir.lib.uwo.ca/etd/4399>

This Dissertation/Thesis is brought to you for free and open access by Scholarship@Western. It has been accepted for inclusion in Electronic Thesis and Dissertation Repository by an authorized administrator of Scholarship@Western. For more information, please contact [wlsadmin@uwo.ca](mailto:wlsadmin@uwo.ca).

## Abstract

Contrast-enhanced ultrasound (CEUS) permits the quantification and monitoring of adaptive tumor responses in the face of anti-angiogenic treatment, with the goal of informing targeted therapy. However, conventional CEUS image analysis relies on mean signal intensity as an estimate of tracer concentration in indicator-dilution modeling. This discounts additional information that may be available from the first-order speckle statistics in a CEUS image. Heterogeneous vascular networks, typical of tumor-induced angiogenesis, lead to heterogeneous contrast enhancement of the imaged tumor cross-section.

To address this, a linear (B-mode) processing approach was developed to quantify the change in the first-order speckle statistics of B-mode cine loops due to the incursion of microbubbles. The technique, named the EDoF (effective degrees of freedom) method, was developed on tumor bearing mice (MDA-MB-231LN mammary fat pad inoculation) and evaluated using nonlinear (two-pulse amplitude-modulated) contrast microbubble-specific images. To improve the potential clinical applicability of the technique a second-generation compound probability density function for the statistics of two-pulse amplitude modulated contrast-enhanced ultrasound images was developed. The compound technique was tested in an antiangiogenic drug trial (bevacizumab) on tumor bearing mice (MDA-MB-231LN), and evaluated with gold-standard histology and contrast-enhanced X-ray computed tomography. The compound statistical model could more accurately discriminate anti-VEGF treated tumors from untreated tumors than conventional CEUS image. The technique was then applied to a rapid patient-derived xenograft (PDX) model of renal cell carcinoma (RCC) in the chorioallantoic membrane (CAM) of chicken embryos. The ultimate goal of the PDX model is to screen RCC patients for *de novo* sunitinib resistance.

The analysis of the first-order speckle statistics of contrast-enhanced ultrasound cine loops provides more robust and reproducible estimates of tumor blood perfusion than conventional image analysis. Theoretically this form of analysis could quantify perfusion heterogeneity and provide estimates of vascular fractal dimension, but further work is required to determine what physiological features influence these measures. Treatment sensitivity matrices, which combine vascular measures from CEUS and power Doppler, may be suitable for screening of *de novo* sunitinib resistance in patients diagnosed with renal cell carcinoma. Further studies

are required to assess whether this protocol can be predictive of patient outcome.

**Keywords:** high-frequency ultrasound, contrast-enhanced ultrasound, speckle statistics, patient-derived xenograft, breast cancer, renal cell carcinoma, image analysis, tumor heterogeneity, anti-angiogenesis, chorioallantoic membrane

## Co-Authorship Statement

Chapter 2 was published in *IEEE Transactions on Ultrasonics, Ferroelectrics and Frequency Control* as: **M. R. Lowerison**, M. N. Hague, A. F. Chambers, and J. C. Lacefield, “Improved Linear Contrast-Enhanced Ultrasound Imaging via Analysis of First-Order Speckle Statistics,” *IEEE Trans. Ultrason., Ferroelect., Freq. Control.*, vol. 63, no. 9 p. 1409-1421, 2016. All authors contributed to editing the paper. Nicole Hague, at the time a laboratory technician in Dr. Chambers’ lab, was responsible for the animal model, including animal handling, animal care, cell injections, and coordinating the necessary surgeries for the mouse tumor model. I acquired the contrast-enhanced ultrasound cine loops, with the help of Carl Postenka assisting with some of the tail vein injections during the study. I developed the mathematical model presented in this chapter and applied it to the acquired images. I tested the new method by manually segmenting tumor cross-sections and comparing the results with conventional techniques. I conducted all analysis and statistical comparisons on the produced data. I worked on this project under the supervision of Dr. James Lacefield and Dr. Ann Chambers.

Chapter 3 was published in *Medical Physics* as: **M. R. Lowerison**, J. J. Tse, M. N. Hague, A. F. Chambers, D. W. Holdsworth, and J. C. Lacefield, “Compound Speckle Model Detects Anti-Angiogenic Tumor Response in Preclinical Nonlinear Contrast-Enhanced Ultrasonography,” *Med. Phys.*, vol. 44, no. 1, p. 99-111, 2017. All authors contributed to editing the paper. Nicole Hague, at the time a laboratory technician in Dr. Chambers’ lab, was responsible for developing the mouse model of human breast cancer used in this study. Her contributions included animal handling, animal care, tumor inoculation, and the dosing and injection of bevacizumab. Justin Tse, a Ph.D. candidate under the supervision of Dr. Holdsworth, developed and implemented the protocols specific to the contrast-enhanced CT portion of this study. Justin developed the novel erbium-based CT contrast agent, produced batches of CT contrast-agent for this study, aided in the animal surgeries to perfuse the CT contrast-agent, and imaged the mice on a small-animal X-ray CT. I performed the endpoint surgeries to perfuse the mice with the erbium-based CT contrast agent. I acquired the contrast-enhanced ultrasound cine loops used in this study. I developed the compound statistical model presented in this chapter

and applied it to the acquired CEUS images. I manually segmented the tumor cross-sections on CEUS images, the tumor and kidney boundaries on contrast-enhanced CT volumes, and counted the microvascular density of histology sections gathered during this study. I conducted all analysis and statistical comparisons on the produced data. I worked on this project under the supervision of Dr. James Lacefield and Dr. Ann Chambers.

Chapter 4 is in preparation for submission to *Nature* with authors: **M. R. Lowerison**, H. S. Leong, Y. Fedyshyn, S. Prokopec, K. C. Williams, C. T. Gavin, C. Willie, C. Mazzola, Q. Zhang, J. Gomez-Lemus, J. Brugarolas, A. F. Chambers, P. C. Boutros, J. C. Lacefield, and N. E. Power. Dr. Hon Leong and I are co-first authors of this manuscript. He organized the project and provided the lab space for embryo cultivation, tumor engraftment, drug dosing, cell culture, and immunohistochemistry. Yaroslav Fedyshyn was responsible for preparing patient tumor tissues for direct fragment engraftment, and for culturing the patient-derived cell lines used in this study. Stephenie Prokopec performed next generation sequencing and genomics analysis on patient derived tissues. Dr. Karla Williams and Carson Gavin aided in tumor fragment engraftment into chicken embryos, and in drug-dosing of tumor-bearing embryos. Chantalle Willie and Dr. Clarisse Mazzola were responsible for the targeted therapy drug panel evaluations conducted using tumor take rate as the main outcome measure. Dr. Qi Zhang provided the images and Fuhrman grades for Supplementary Figure 1. Dr. Jose Gomez-Lemus was the primary pathologist in this study. Dr. James Brugarolas generously supplied patient-derived cell lines used during this study, and provided expert advice in the development of the PDX model. Dr. Paul Boutros was responsible for supervising the genomics analysis. Dr. Nicolas Power conducted the nephrectomies described in this study and supplied the patient tumor tissues. I aided in the engraftment of patient-derived tissues into the CAM assay, and in the dosing of tumor specimens. I acquired the ultrasound images, including 2D CEUS cine loops and 3D power Doppler volumes, analyzed in this study. I manually segmented tumor cross-sections on CEUS images, tumor boundaries on Doppler volumes, and conducted all analysis and statistical comparisons on the produced data. I worked on this project under the supervision of Dr. James Lacefield and Dr. Ann Chambers.

Chapter 5 is in preparation for submission to *Ultrasound in Medicine & Biology* with authors: **M. R. Lowerison**, A. F. Chambers, H. S. Leong, N. E. Power, and J. C. Lacefield.

The imaging data used in this chapter came from the work presented in Chapter 4. I was responsible for developing the mathematical model presented in this chapter, applying it to the acquired images, and conducting all of the analysis and statistical comparisons on presented in this chapter. I worked on this project under the supervision of Dr. James Lacefield and Dr. Ann Chambers.

# Acknowledgements

I would like to acknowledge everyone who has helped me throughout my time at the Robarts Research Institute and at the University of Western Ontario.

First of all, I want to acknowledge my supervisors, Dr. James Lacefield and Dr. Ann Chambers. Together, they provided the perfect environment for me to flourish as a student and as a scientist. They gave me the freedom to pursue my own ideas, along with the guidance, expertise, and encouragement to complete my project. Thank you for providing me with this opportunity!

Thank you to my advisory committee, Dr. Dan Goldman and Dr. Rob Bartha, for their helpful advice and suggestions throughout the course of my graduate degree. In particular, I would like to thank Dr. Goldman for his guidance on mathematical modeling of microvascular blood flow.

I will take a moment here to acknowledge the past and current members of the Lacefield and Chambers labs: Christopher Waring, Dr. Mai Elfarnawany, Adem Hadj Boussaad, Omar Mansour, Szymon Kowal, Milica Krstic, and Sean Leith. It was great to have you as my peers during this journey, and to see you grow along side with me. Your ideas were always helpful, and your progress served as inspiration for me to continue with my work. Carl Postenka deserves my gratitude for helping me perform mouse tail-vein injections - a tedious and often frustrating task. And a huge thank you to Nicole Hague for developing and implementing the animal cancer models presented in Chapters 2 & 3. Nicole is an absolutely amazing animal tech who does the work of three people!

The work presented in this thesis would not have been possible without collaboration. I would like to acknowledge Ashley Makela, a licensed sonographer from Dr. Paula Fosters lab, for helping us set the gold standard settings for our power Doppler imaging. Dr. Amanda Hamilton, also from Paulas group, for helping me with the logistics of CAM studies as well as lending me some insight into the biological aspects of my experiments. Several members of Dr. David Holdsworths lab helped me with the CT data presented in Chapter 3. In particular, Justin Tse lent his expertise and provided considerable effort to allow us to acquire exquisite contrast-

enhanced CT images of mouse vasculature. Justin, I promise that any future collaborations will not require getting up to work at 4am! Chris Norley and Steven Pollmann helped us set up the scan and reconstruction protocols for those images, and Hristo Nikolov helped us construct a specimen holder for imaging small tissue samples.

The collaboration with Dr. Hon Sing Leong and Dr. Nicholas Power was transformative for my research, aspirations, and even life goals. Over the years Hon has become a mentor to me, and together we've been able to do absolutely astonishing projects. He deserves my thanks, albeit begrudgingly at the time, for pushing me well outside of my comfort zone. I also want to acknowledge some of the members in his group: Yaroslav Fedyshyn, Dr. Mario Cepeda, Dr. Karla Williams, Yohan Kim, Rich Berish, and Johanna Garzon.

I would also like to acknowledge my funding sources over the years. I was funded by Ontario Graduate Scholarships for 2012-2013 and 2015-2016. I also acknowledge funding and support from the Pamela Greenaway Kohlmeier Translational Breast Cancer Research Unit, the Kidney Cancer Research Network of Canada, the Canadian Urological Oncology Group, and the Western Graduate Research Scholarship.

Last, but not least, a huge thank you to my family for their love and support throughout my life.

The pursuit of my doctoral studies has been nothing short of life changing, and I owe much to the wonderful people who have helped me on this journey. It has been a privilege to work with all of you!



# Table of Contents

<b>Abstract</b>	<b>ii</b>
<b>Co-Authorship Statement</b>	<b>iv</b>
<b>Acknowledgements</b>	<b>vii</b>
<b>List of Figures</b>	<b>xv</b>
<b>List of Symbols</b>	<b>xxii</b>
<b>List of Acronyms and Abbreviations</b>	<b>xxv</b>
<b>1 Introduction</b>	<b>1</b>
1.1 Overview . . . . .	1
1.2 The Utility of Perfusion Imaging in Oncology . . . . .	2
1.2.1 Characteristics of Tumor Blood Vessels . . . . .	4
1.2.2 Motivation for Targeted Angiogenic Therapy . . . . .	6
Metastatic Setting . . . . .	7
Adjuvant Setting . . . . .	8
Neoadjuvant Setting . . . . .	9
1.2.3 Combination of Anti-Angiogenic Drugs with other Therapies . . . . .	9
Chemotherapy . . . . .	10
Radiotherapy . . . . .	10
Immunotherapy . . . . .	10
Vascular Normalization to Relieve Hypoxic Stress . . . . .	11
1.2.4 Surrogate Measures of Treatment Efficacy . . . . .	11
1.3 Perfusion Imaging Techniques . . . . .	12
1.3.1 Dynamic Contrast Enhanced X-ray Computed Tomography (DCE-CT) .	13
1.3.2 Single-photon emission computed tomography (SPECT) . . . . .	13
1.3.3 Positron emission tomography (PET) . . . . .	14
1.3.4 Dynamic Contrast Enhanced Magnetic Resonance Imaging (DCE-MRI)	14
1.3.5 Doppler Ultrasound . . . . .	15
1.3.6 Contrast Enhanced Ultrasound (CEUS) . . . . .	15
1.4 Overview of Contrast-Enhanced Ultrasound . . . . .	16
1.4.1 Contrast-Enhanced Ultrasound Applications . . . . .	16
General Radiology . . . . .	16

	Echocardiography . . . . .	17
	Imaging the Liver . . . . .	17
	Therapeutic Applications . . . . .	17
	Detection, Diagnosis, and Characterization of Solid Tumors . . . . .	18
1.4.2	Composition of Microbubble Contrast Agents . . . . .	18
1.4.3	Microbubble Response to Acoustic Radiation . . . . .	19
	Low Incident Pressure . . . . .	22
	Moderate Incident Pressure . . . . .	22
	High Incident Pressure . . . . .	22
1.4.4	Microbubble Specific Imaging . . . . .	25
	Digital Image Subtraction . . . . .	25
	Second Harmonic Imaging . . . . .	25
	Multi-pulse Processing . . . . .	26
	Pulse Inversion . . . . .	27
	Amplitude Modulation . . . . .	27
	Pulse Inverted Amplitude Modulation . . . . .	29
	Burst Imaging . . . . .	31
1.4.5	Indicator Dilution Theory . . . . .	31
1.4.6	Common Kinematic Models for Bolus Enhancement . . . . .	32
	Lognormal Function . . . . .	33
	Gamma Variate Function . . . . .	34
	Diffusion with Drift Model . . . . .	35
	The Lagged Normal Function . . . . .	35
	Comparison of Indicator-dilution Models for Bolus CEUS Imaging . . . . .	36
1.4.7	Common Kinematic Models for Destruction Reperfusion . . . . .	36
	Mono-exponential Kinematic Model . . . . .	39
	Krix's Multivessel Model . . . . .	39
	Arditi's Perfusion Model . . . . .	40
	Hudson's Lognormal Perfusion Model . . . . .	41
	Comparison of Models for Destruction-Reperfusion CEUS Imaging . . . . .	41
1.5	Overview of Speckle Statistics . . . . .	42
1.5.1	Fully Developed Speckle . . . . .	43
	No Coherent Component (Rayleigh) . . . . .	43
1.5.2	Non-Rayleigh Speckle . . . . .	44
	No Coherent Component (K-Distribution) . . . . .	44
	Coherent Component (Homodyned K-Distribution) . . . . .	45
	Approximation to the Homodyned K-distribution (Nakagami) . . . . .	46
1.6	Challenges in Contrast Enhanced Ultrasound . . . . .	47
1.6.1	Frame-to-frame Variability due to Subject Motion can mask Contrast Perfusion . . . . .	47
1.6.2	Preclinical CEUS Processing Techniques can be Highly Susceptible to Motion Artifacts . . . . .	47
1.6.3	CEUS uses 2-D Sampling to Measure Perfusion in a 3-D Vascular Network . . . . .	48

1.6.4	The Relationship between Microbubble Concentration and Contrast Signal is Complex and Multifactorial . . . . .	48
1.6.5	Contrast Perfusion in Heterogeneous Vascular Networks ( <i>e.g.</i> tumors) may be Poorly Represented by Point Estimates of Mean Contrast Intensity . . . . .	49
1.6.6	Signal Processing can Alter Indicator-Dilution Curve Shape and Interpretation . . . . .	49
1.7	Hypothesis and Objectives . . . . .	49
1.8	Thesis Outline . . . . .	50
1.8.1	Chapter 2 . . . . .	51
1.8.2	Chapter 3 . . . . .	51
1.8.3	Chapter 4 . . . . .	52
1.8.4	Chapter 5 . . . . .	52
1.8.5	Chapter 6 . . . . .	53
	References . . . . .	53
<b>2</b>	<b>Improved Linear CEUS Imaging via Analysis of First-Order Speckle Statistics</b>	<b>65</b>
2.1	Introduction . . . . .	66
2.2	Statistical Model . . . . .	68
2.2.1	Contrast-Enhanced Speckle Statistics . . . . .	68
2.2.2	Parameter Estimation . . . . .	72
2.3	Materials and Methods . . . . .	72
2.3.1	Animal Model . . . . .	72
2.3.2	Image Acquisition . . . . .	73
2.3.3	Image Analysis . . . . .	74
2.3.4	Wash-In Curve Analysis . . . . .	74
2.4	Results . . . . .	76
2.4.1	Contrast-Enhanced Speckle Histograms . . . . .	76
2.4.2	Wash-In Curves . . . . .	76
2.4.3	Comparison of EDoF and TNC Wash-In Curves . . . . .	78
2.4.4	Wash-In Curve Parameter Estimation . . . . .	80
2.5	Discussion . . . . .	85
2.6	Conclusions . . . . .	88
	References . . . . .	88
<b>3</b>	<b>Compound Speckle Model Detects Anti-Angiogenic Tumor Response in Preclinical Nonlinear CEUS</b>	<b>92</b>
3.1	Introduction . . . . .	93
3.2	Statistical Model . . . . .	95
3.2.1	Nonlinear Contrast Speckle Statistics . . . . .	95
3.2.2	Parameter Estimation . . . . .	97
3.3	Materials and Methods . . . . .	99
3.3.1	Cell Line and Animal Model . . . . .	99
3.3.2	CEUS Image Acquisition . . . . .	99
3.3.3	CEUS Image Analysis . . . . .	100
3.3.4	Wash-In Curve Analysis . . . . .	101

3.3.5	Whole Mouse CT Contrast Agent Perfusion . . . . .	102
3.3.6	CT Imaging . . . . .	103
3.3.7	CT Analysis . . . . .	103
3.3.8	Histology and Staining . . . . .	104
3.3.9	Statistical Analysis . . . . .	105
3.4	Results . . . . .	105
3.4.1	Weighting Function Analysis . . . . .	105
3.4.2	Contrast-Enhanced MicroCT . . . . .	107
3.4.3	Surrogate Measures of Vascular Complexity . . . . .	107
3.4.4	Histological Validation . . . . .	109
3.4.5	Bolus Time-Intensity Kinematics . . . . .	109
	Area Under Curve ( <i>AUC</i> ): . . . . .	109
	Blood Velocity Metrics ( <i>MTT</i> and <i>t<sub>p</sub></i> ): . . . . .	113
	Wash-in Rate ( <i>WiR</i> ): . . . . .	113
3.5	Discussion . . . . .	113
3.6	Conclusions . . . . .	116
	References . . . . .	116

**4 PDXovo: Ultrafast Prediction of Drug Sensitivities via Intratumoral Multiregional Analysis 121**

4.1	Introduction . . . . .	122
4.2	Material and Methods . . . . .	124
4.2.1	Regulatory Ethics Board Approvals . . . . .	124
4.2.2	Preparation of Reagents . . . . .	124
4.2.3	Cell Culture Techniques . . . . .	124
4.2.4	Primary RCC cell line generation and culture . . . . .	124
4.2.5	Cancer Cell Preparation for chick embryo CAM engraftment . . . . .	125
4.2.6	Engraftment of Cell lines and/or Patient derived xenografts into the CAM	125
4.2.7	Engraftment of Patient Tumor Fragments into the CAM . . . . .	126
4.2.8	Volumetric Ultrasound Imaging Protocol . . . . .	126
4.2.9	Contrast-Enhanced Ultrasound Protocol . . . . .	127
4.2.10	Volumetric Ultrasound Quantification . . . . .	128
4.2.11	Contrast-Enhanced Ultrasound Perfusion Analysis . . . . .	128
4.2.12	Biopsy Classification Matrix . . . . .	129
4.3	Results . . . . .	129
4.3.1	Engrafted Renal Cell Carcinoma Tumors on the Chorioallantoic Membrane of Chick Embryos . . . . .	129
4.3.2	Ultrasound Evaluation of Intratumoral Hemodynamics in RCC PDXs in the CAM . . . . .	130
4.3.3	Functional Heterogeneity of Intratumoral Biopsies on RCC PDXs Ex Ovo . . . . .	132
4.3.4	Targeted Therapy Drug Panel Evaluation on RCC PDXs with the PDX-ovo Platform . . . . .	135
4.3.5	Engrafted Patient Tumors Maintain Viability in the CAM through Co-Option of Pre-Existing Tumor Vasculature . . . . .	137

4.3.6	Multi-region Exome and Gene Copy Number Variation Analysis of PDX Samples . . . . .	139
4.4	Discussion . . . . .	141
4.5	Conclusions . . . . .	145
	References . . . . .	145
<b>5</b>	<b>Compound Speckle Model Reduces CEUS Variability in a PDX Model of RCC</b>	<b>150</b>
5.1	Introduction . . . . .	151
5.2	Materials and Methods . . . . .	154
5.2.1	Patient Characteristics . . . . .	154
5.2.2	Preparation of Reagents . . . . .	154
5.2.3	Engraftment of Patient Tumor Fragments into the CAM . . . . .	155
5.2.4	Volumetric Ultrasound Imaging Acquisition Protocol . . . . .	155
5.2.5	Contrast-Enhanced Ultrasound Image Acquisition Protocol . . . . .	156
5.2.6	Volumetric Ultrasound Image Analysis . . . . .	156
5.2.7	Contrast-Enhanced Ultrasound Image Analysis . . . . .	156
5.2.8	Wash-in Curve Analysis . . . . .	157
5.2.9	Biopsy Classification as Drug Resistant or Sensitive . . . . .	157
5.3	Results . . . . .	158
5.3.1	Engraftment Efficiency of Renal Cell Carcinoma Tumors . . . . .	158
5.3.2	Application of the Compound Speckle Model to RCC PDX CEUS Data	160
5.3.3	Compound Model Reduces Coefficient of Variation of CEUS Blood Volume Estimates . . . . .	161
5.3.4	Correlations Among Ultrasound Vascular Metrics . . . . .	161
5.3.5	Quantification of Ultrasound Images to Classify Tumor Biopsies . . . . .	163
5.3.6	Dual Modality Patient Classification . . . . .	163
5.4	Discussion . . . . .	167
5.5	Conclusion . . . . .	170
	References . . . . .	171
<b>6</b>	<b>Summary and Future Work</b>	<b>175</b>
6.1	Summary . . . . .	175
6.1.1	Chapter 2: Improved Linear Contrast-Enhanced Ultrasound Imaging via Analysis of First-Order Speckle Statistics . . . . .	175
6.1.2	Chapter 3: Compound Speckle Model Detects Anti-Angiogenic Tumor Response in Preclinical Nonlinear Contrast-Enhanced Ultrasonography	176
6.1.3	Chapter 4: PDX <sub>ovo</sub> : Ultrafast Prediction of Drug Sensitivities via Intratumoral Multiregional Analysis . . . . .	176
6.1.4	Chapter 5: Compound Speckle Model Reduces Contrast Ultrasound Variability in a Patient-Derived Xenograft Model of Renal Cell Carcinoma . . . . .	177
6.2	Future Work . . . . .	177
6.2.1	Technical improvements . . . . .	177
6.2.2	Next steps for preclinical validation . . . . .	180
6.2.3	Plans for clinical translation . . . . .	181

6.3 Final Remarks . . . . .	183
References . . . . .	183
<b>A Copyright Agreements</b>	<b>186</b>
<b>B Ethics Approval for Animal Subjects</b>	<b>188</b>
<b>C Ethics Approval for Surgical Specimens from Human Patients</b>	<b>189</b>
<b>Curriculum Vitae</b>	<b>190</b>

# List of Figures

1.1	Diagrammatic example of tumor-induced angiogenesis. Angiogenesis is induced by hypoxic tumors (left panel), supports primary tumor growth (middle panel), and facilitates metastatic spread (right panel). . . . .	3
1.2	Contrast-enhanced micro-CT image of a mouse kidney, showing an orderly branching network. More details concerning the experiment this image came from can be found in Chapter 3 of this thesis. Image courtesy of Justin Tse. . .	4
1.3	Diagram depicting a cut away view of a tumor with visible vasculature. The tumor vasculature is structurally chaotic and disorganized. . . . .	5
1.4	Schematic demonstrating the therapy targets for clear cell RCC. Anti-angiogenic drugs are to the bottom and left of this network. *Not FDA approved for use in RCC. . . . .	8
1.5	Microbubbles have the largest scattering cross-section at their resonant frequency.	20
1.6	The backscatter intensity, and microbubble response, depend on the mechanical index of imaging. . . . .	21
1.7	Simulated microbubble response to low incident pressure. The microbubble's radius oscillates in a linear manner, yielding a scattered pulse with few harmonic components. This simulation was performed using Hoff's BubbleSim package for a single 3 $\mu\text{m}$ shelled microbubble (shell thickness 4 nm) excited with a 2.5 cycle, 0.07 MPa pulse with a center frequency of 2.25 MHz [97]. . .	23
1.8	Simulated microbubble response to moderate incident pressure. The microbubble's radius responds asymmetrically, resulting in a wide range of harmonic and subharmonic components in the scattered echo. In this simulation, a single 3 $\mu\text{m}$ shelled microbubble (shell thickness 4 nm) is excited with a 2.5 cycle, 0.7 MPa pulse with a center frequency of 2.25 MHz. The scattered pressure was calculated using Hoff's Bubblesim package [97]. . . . .	24
1.9	An example of a harmonic imaging bandwidth. The overlap of transmit and receive bandwidths leads to reduced specificity in microbubble imaging. . . . .	26
1.10	Diagrammatic example of wave form responses to pulse inversion processing. . .	28
1.11	Diagrammatic example of wave form responses to amplitude modulation processing. . . . .	30
1.12	Diagrammatic example of bolus injection. The initial delta function becomes spread out by transit through the circulatory system prior to entering the imaging plane. . . . .	33
1.13	Example of the four indicator dilution models fitted to the same raw dataset. The raw data points were synthetically produced by adding random noise to a lognormal wash-in curve. . . . .	37

1.14	Illustrative representation of destruction-reperfusion imaging. Microbubbles are administered via a constant infusion, yielding a steady-state of indicator transit (panel A). In (B) a high-energy ultrasound pulse bursts all of the microbubbles in the imaging plane. The contrast agent is then allowed to reperfuse into the vasculature in (C). . . . .	38
1.15	Example of the four destruction-reperfusion models fitted to the same raw dataset. The raw data points were synthetically produced by adding random noise to a monoexponential wash-in curve. . . . .	42
1.16	Graph of the Rayleigh probability density function, which is fully defined by single scaling parameter. The signal-to-noise ratio (SNR) of Rayleigh-distributed speckle will be approximately 1.91. SNR is calculated from the ratio of $\bar{a}/\sigma_R$ , which is constant in the Rayleigh distribution. . . . .	45
2.1	Representative tumor images with manual ROIs taken (a) prior to contrast enhancement and (b) immediately following a microbubble bolus and the probability density function fit to image histogram data taken (c) at baseline and (d) after enhancement. The histograms show signal magnitude in arbitrary units (a.u.). A Nakagami distribution with effective degrees of freedom (c) $n^* = 2.96$ and (d) $n^* = 4.15$ was the closest fit to the data. . . . .	77
2.2	Wash-in curves for the three methods of contrast analysis applied to a representative tumor. The dotted line is a nonlinear regression fit to a simplified gamma variate function, (2.9). The curves have signal-to-noise ratios of (a) 25.5 dB for nonlinear CEUS, (b) 18.1 dB for conventional linear CEUS, and (c) 28.7 dB for the EDoF method, respectively. Nonlinear and conventional linear CEUS data are reported in arbitrary unit (a.u.). . . . .	79
2.3	Wash-in curves for the three methods of contrast analysis applied to a tumor with high subject movement. The statistical EDoF method demonstrates improved robustness to motion artifacts. Signal-to-noise ratios for the fitted wash-in curves are (a) 23.2 dB for nonlinear CEUS, (b) 16.1 dB for conventional linear CEUS, and (c) 35.7 dB for the EDoF method. Nonlinear and conventional linear CEUS data are reported in arbitrary unit (a.u.). . . . .	79
2.4	An example comparison of the EDoF method to a sliding-window based TNC. On linearized envelope data, the (a) EDoF method produced interpretable wash-in curves, but the (c) results of TNC processing were difficult to analyze. The curve shape of the two methods was very similar on log-compressed image data (b) and (d), with the main difference being the peak signal amplitude. . . . .	80
2.5	Linear regression for area under curve (AUC) for the two linear contrast methods in comparison to gold-standard nonlinear CEUS. The (a) linear subtraction method did not demonstrate a strong correlation to the AUC for nonlinear CEUS ( $R^2 = 0.2420, p = 0.0005$ ) and was outperformed by the (b) EDoF method ( $R^2 = 0.4591, p < 0.0001$ ). The correlation of AUC between the linear techniques was weak ( $R^2 = 0.3448, p < 0.0001$ ). All areas are reported in arbitrary units (a.u.). . . . .	81



2.6	Linear regression of the maximum amplitude of the wash-in curve, $Y_{max}$ , for the two linear contrast methods in comparison to gold-standard nonlinear CEUS. (a) The linear subtraction estimate was statistically significantly correlated with the gold-standard $Y_{max}$ from nonlinear CEUS ( $R^2 = 0.3834, p < 0.0001$ ). (b) The EDoF estimate exhibited marginally higher correlation ( $R^2 = 0.5916, p < 0.0001$ ). (c) Comparing the linear methods yielded a coefficient of determination of $R^2 = 0.5142, p < 0.0001$ . Nonlinear and conventional linear CEUS data are reported in arbitrary units (a.u.). . . . .	82
2.7	Linear regression for time of maximum enhancement $T_{max}$ estimated using the two linear contrast methods in comparison to gold-standard nonlinear CEUS. The (a) linear subtraction method ( $R^2 = 0.3084, p < 0.0001$ ) was similar in performance to the (b) EDoF method ( $R^2 = 0.4746, p < 0.0001$ ). (c) The two linear methods were weakly correlated ( $R^2 = 0.1878, p = 0.0033$ ). . . . .	83
2.8	Linear regression for the wash-in curve shape parameter, $\alpha_v$ , estimated using the two linear contrast methods in comparison to gold-standard nonlinear CEUS. The (a) linear subtraction method ( $R^2 = 0.0422, p = 0.1710$ ) was outperformed by the (b) EDoF method ( $R^2 = 0.3156, p < 0.0001$ ). The correlation in $\alpha_v$ parameter estimates between the linear techniques was weak ( $R^2 = 0.1322, p = 0.0165$ ). All reported units are dimensionless. . . . .	84
3.1	Representative CEUS tumor images (anatomical transverse plane, 14 days post inoculation) taken at (a) baseline (unenhanced) and at (b) peak bolus enhancement, with (c) corresponding Pareto fits to intensity ROI histograms, and (d) weighting functions. The change in area of overlap (yellow region) over time in (d) was used to construct wash-in curves as demonstrated in (e). . . . .	106
3.2	Contrast-enhanced CT images of (a) a MIP projection through the whole mouse body, (b) a binarized kidney, (c) a control tumor, and (d) bevacizumab treated tumor. The box-plot in (e) demonstrates the mean HU of the segmented tumor volumes (whiskers are min to max, box extends from the 25th to 75th percentiles), along with the corresponding LDA analysis to the right. . . . .	108
3.3	The (a) compound model weighting functions for a representative tumor at both baseline and peak enhancement levels. (b) Box-plot of span of the estimated sigma value with corresponding (c) linear discriminant analysis. (d) Diagrammatic example of power spectrum analysis on a contrast-enhanced CT tumor volume. (e) Box-plot of fractal dimension of contrast-CT tumors and kidneys, along with (f) linear discriminant analysis. . . . .	110
3.4	Low magnification images of H&E stained histology sections taken from (a) vehicle treated tumor and (b) bevacizumab treated tumor. Higher magnification reveals evidence of vascular perfusion of silicone-based contrast agent (arrows), with the relatively higher microvascular density of (c) control tumors compared to (d) bevacizumab treated tumors. Quantified MVD is plotted in (e) with an LDA performed in (f). . . . .	111

3.5 The compound model detected a significant reduction of *AUC* in bevacizumab treated tumors compared to control. Conventional processing did not demonstrate a significant effect. (a) Box-plot of conventional CEUS analysis *AUC* with corresponding (c) linear discriminant analysis. (b) Box-plot of compound model's *AUC*, along with (d) linear discriminant analysis. . . . . 112

4.1 Patient derived xenograft (PDX) models for renal cell carcinoma (RCC) tumors using chick embryos. A) Primary RCC tumor resected for intratumor core extraction. Each core is divided into fragments and then implanted into the chorioallantoic membrane (CAM) of a chick embryo ex ovo. B) RCC tumor fragments are implanted on EDD-9 embryos and are viable on the CAM for another 10 days. C) Diagram demonstrating that tumor tissue extends below the surface of the CAM. D) Histological examination of tumor sections revealed viable xenograft tissue and a clear cell RCC subtype. E) At endpoint, contrast agent (microbubbles) is intravenously injected and then high-frequency ultrasound imaging performed to quantify tumor volume and the rate of tumor perfusion using a destruction-reperfusion protocol. This permits the investigator to definitively reveal functional tumor vasculature with various biophysical parameters (relative blood flow, relative blood volume). . . . . 131

4.2 Ultrasound evaluation of intratumoral hemodynamics in RCC PDXs in the CAM. A) Tumor volume and vasculature superficially estimated when tumor cells are fluorescently labeled. Tumors generated using sunitinib sensitive cell lines (786-O and XP185) demonstrated a reduction in tumor growth and vessel formation in response to topical application of the targeted therapy. In comparison, tumors grown from resistant cell lines (XP121 and T258) did not demonstrate a treatment effect. B) When ultrasound imaging is performed, the tumor volume can be delineated (left panel), and fine structures of the tumor can be imaged when using B-mode ultrasound imaging (middle panel). When power Doppler mode ultrasound imaging is performed, areas of red blood cell movement are identified throughout the tumor and overlaid onto the B-mode image (orange-red signal, right panel). Feeding arterioles have been labeled with cyan arrows. C) Contrast enhanced ultrasound imaging confirms the presence of internal tumor vasculature. Sunitinib treated XP185 tumors demonstrated a reduction in vessel specific enhancement in comparison to vehicle control (left panel). Peripheral enhancement pattern implies lack of capillary bed in tumor core. Therapy on resistant T258 tumors did not show a trend between signal intensity and treatment group. . . . . 133

- 4.3 Functional heterogeneity of intratumoral cores on RCC PDXs *ex ovo*. A representative patient had 6 tumor cores taken from their primary tumor (labeled C1-C6), and 3 tumor cores taken from a nearby metastatic site (labeled Met1-Met3), for CAM engraftment ( $n > 36$  embryos/core). One half of each tumor core cohort received topical application of sunitinib and the other half received vehicle control. Patient tumor fragments underwent both volumetric and perfusion ultrasound analysis (middle graphs, shown here only from this representative patient). This patient exhibited intratumoral functional heterogeneity both within untreated tumor cores, and in response to sunitinib therapy. The metastatic cores also exhibited heterogeneity within untreated samples, but was more consistently sensitive to sunitinib. . . . . 134
- 4.4 Core classification and genomic analysis of RCC PDXs *ex ovo*. A) Sunitinib sensitivity matrix for each core biopsies taken from all patients. Patient tumor cores were classified as being a responder (green), partial responder (yellow), or non-responder (red) on the basis of both the power Doppler vascularity metric and contrast-enhanced ultrasound blood volume. The number in each box represents the F-statistic for that particular core. B) Exome and copy number variation (CNV) analysis was performed on all biopsy samples, and representative PDX samples from each tumor core that was implanted into the PDX*ovo* model. . . . . 136
- 4.5 Targeted therapy drug panel evaluation on RCC PDXs. Five different targeted therapies used for the treatment of metastasis were evaluated on A) three commercially available RCC cell lines, B) three RCC PDX cell lines from patients sensitive to sunitinib and, C) three RCC PDX cell lines from patients resistant to sunitinib. The asterisk denotes lack of tumor take in that drug treatment group. The fraction of tumor take rates is presented above each bar for each drug treatment group. D-F) A patient derived cell line, harvested from a “partial responder” metastatic core, subjected to a drug panel of antiangiogenic and anti-proliferative drugs. Tumor volume and VI was quantified for each treatment group using reconstructed 3-D power Doppler ultrasound. D) A trend toward reduced tumor volume was noted for all tested antiangiogenic therapies (sunitinib, pazopanib, sorafenib), but this did not reach statistical significance. No consistent trend for tumor volume was noted for the anti-proliferative drugs (everlimus and sirolimus). E) A statistically significant reduction in tumor vascularity was observed only for sorafenib therapy ( $22.5 \pm 5.6\%$  vs.  $6.8 \pm 1.3\%$ ,  $p < 0.05$ ), with no trend observed in tumor vascularity for any of the other treatments. F) A scatter plot of tumor vascularity versus tumor volume demonstrated no clear correlation between the two measures. . . . . 138

4.6	Pre-existing vessel co-option leads to rapid vascularization of patient tissues. A) Histology of engrafted PDX show densely vascularized tumor tissue evident from a large amount of red blood cells present in the section. B) Parametric contrast-enhanced ultrasound imaging corroborates dense vascularization and highlights functional heterogeneity in this PDX tumor. Structural and temporal vessel heterogeneity are also apparent in the time kinetics of the contrast enhancement. C) Sections from RCC PDX bearing embryos that were injected with an endothelial cell specific lectin (lens culinaris agglutinin) and stained with anti-CD31-FITC antibody and Hoechst. Low magnification (10x) confocal imaging demonstrates extensive tumor vasculature throughout the PDX. D) High magnification (20x) reveals that the majority of human CD31+ve microvessels (green) were also positive for lectin (red), revealing a co-option of both host (chick) and tumor (human) vessels. This implies that the CAM reperuses pre-existing tumor vasculature to maintain PDX tissue viability. E) This pattern of vascular co-option was consistent among all examined patient tumors regardless of subtype (chromophobe RCC). . . . .	140
4.7	A) The total SNV count per fragment sample. B) The proportion of variants of the given base change and the functional consequence per fragment sample. C) The profile of the mutated genes for each sample demonstrating the functional consequence on that gene. RCC fragments that exhibited resistance to sunitinib (C1, C4, and C3) clustered on the basis of SNVs in the ZNF569 gene locus. D) The proportion of samples demonstrating a variant within each gene, the ZNF569 SNVs within the ZNF569 gene loci were the most abundant SNV type throughout the tumor regardless of region. . . . .	142
5.1	CEUS analysis of a sample tumor. A) Selected frames from a CEUS cine loop that represent different phases of contrast wash in. From left to right these frames represent baseline signal, arteriole enhancement, and complete perfusion. B) Weighting functions constructed using intensity samples taken from the CEUS frames shown in (A). The inset to the right demonstrates how the enhanced fraction at the third time point was calculated. C) The conventional CEUS wash-in curve of contrast signal intensity for this tumor. D) A wash-in curve constructed using the enhanced fraction estimated from the statistical method's weighting functions. The wash-in curve samples highlighted by the red and blue dots in (c) and (d) correspond to the "fast flow" and "slow flow" frames, respectively, in (a). . . . .	159
5.2	Example ultrasound images taken from a tumor-bearing embryo, showing evidence of A) feeding arterioles (2-D power Doppler image, yellow lines denote placement of Doppler color box) and B) dense capillary networks (nonlinear CEUS image). Bottom panels show 3-D reconstruction of C) tumor anatomy (B-mode) and D) arteriole network (power Doppler). . . . .	160

5.3	Comparisons of perfusion and vascularity parameters produced in this study. A-C) Linear regressions between the three modalities were significant in all cases. A) Conventional CEUS blood volume to Doppler vascularization index correlation ( $R^2 = 0.1955$ , $p = 0.0013$ ). B) Compound CEUS enhanced volume fraction to Doppler vascularization index correlation ( $R^2 = 0.4331$ , $p < 0.0001$ ). C) Correlation between the two CEUS analysis blood volume estimates ( $R^2 = 0.2707$ , $p = 0.0001$ ). D) The correlation between the log-normal $\sigma_{LN}$ and compound model's blood volume estimate ( $R^2 = 0.2302$ , $p = 0.0004$ ). . . . .	162
5.4	Sensitivity or resistance classification of tumor biopsies based on ultrasound image quantification. A) Doppler and CEUS vascular metrics from a representative patient diagnosed with clear cell RCC, taken from Patient 3. Note that most biopsies demonstrate a sunitinib-dependent decrease in vascularization index and/or blood volume or enhanced volume fraction. B) Doppler and CEUS vascular metrics from the patient diagnosed with chromophobe RCC (Patient 4). In each case a statistically significant decrease in a vascular metric would classify that biopsy as sunitinib sensitive (in green); otherwise, the biopsy was considered resistant (in red). C) Matrices demonstrating the sensitive/resistant classification using each ultrasound modality for every biopsy from all patients in this study. . . . .	164
5.5	A) Scatter plots of Doppler VI and CEUS blood volume or enhanced volume fraction from a suspected sunitinib-sensitive biopsy. A linear discriminant analysis demonstrates that a simple decision boundary is able to correctly classify the majority of treated and untreated tumor fragments in a drug sensitive biopsy. B) An equivalent scatter plot from a sunitinib-resistant biopsy taken from the patient with chromophobe RCC. The choice of decision boundary is less obvious, and does not perform well as a classifier. . . . .	165
5.6	Treatment sensitivity of tumor biopsies was classified using a combination of power Doppler VI with one of the CEUS techniques. A) Drug sensitivity matrix constructed using Doppler VI and conventional CEUS blood volume for all patient cores in this study. B) An equivalent sensitivity matrix generated using Doppler VI and the compound statistical CEUS enhanced volume fraction. The number in each box is the F-statistic comparing ultrasound vascular metrics for treated and control fragments from that particular core. . . . .	166
6.1	Example superposition of two monoexponential curve fits to the wash-in curves from Figure 5.1. This relatively simple analysis could extract the fast and slow-flow components of the compound model's wash-in curve. On the conventional CEUS data, both of the components are overlapping. . . . .	179
6.2	Sorafenib dose response curves of tumor volume and power Doppler VI, taken from a patient derived cell line engrafted into the CAM. The cell line originated from one of the metastatic biopsies taken from the patient diagnosed with chromophobe RCC. . . . .	181

# List of Symbols

$\alpha$	Gamma shape parameter
$\alpha_k$	Magnitude of signal component in random-walk model
$\alpha_v$	Gamma variate shape parameter
$\beta$	Gamma scale parameter
$\beta_v$	Gamma variate scale parameter
$\delta_{tot}(r, f)$	Total effect of microbubble damping
$\lambda$	Generic ‘rate constant’ used in multiple indicator-dilution models
$\phi$	Phase
$\phi_k$	Phase of signal component in random-walk model
$\rho$	Scaling parameter in EDoF derivation
$\sigma$	Standard deviation
$\sigma_e$	Diffuse signal energy
$\sigma_{LN}$	Lognormal shape parameter
$\sigma_R$	Scale parameter of Rayleigh distribution
$\sigma_s(r, f)$	Scattering cross-section
$\sigma_{sc}$	Effective cross-section of scatterers
$\theta$	Random variable to parameterize compound model
$\mu$	Mean value
$\omega$	Angular frequency
$\omega_i$	Relative weighting in mixture model
$\Omega$	Nakagami scaling parameter
$a$	Amplitude

$A_C$	Total vascular cross-section
$AUC$	Area under curve
$B$	Transducer bandwidth
$B(y, z)$	Ultrasound beam function in Hudson's perfusion model
$BW(y)$	Beam width in Hudson's perfusion model
$BS(y)$	Beam separation in Hudson's perfusion model
$C$	Amount of indicator
$d$	Width of the ultrasound beam in the elevation plane
$D$	Coefficient of effective longitudinal diffusion
$D_e$	Extent of microbubble destruction in elevation plane in Arditi's perfusion model
$f$	Frequency
$f_0$	Fundamental frequency
$f_r$	Undamped resonant microbubble frequency
$F$	Relative Blood Flow
$F_D$	Fractal dimension
$F(z, t)$	Blood flow function in Hudson's perfusion model
$I$	Backscatter signal intensity
$k$	Number of subregions in mixture model
$K$	Transmit-receive parameter in Arditi's perfusion model
$m$	Nakagami shape parameter
$m_{FD}$	Slope of log-log plot of power vs. frequency
$m_{krix}$	Initial slope in Krix's multivessel model
$M$	Effective density of scatterers
$MTT$	Mean transit time of indicator
$n$	Degrees of freedom
$n^*$	Reduced effective degrees of freedom

$N(0, \sigma_i^2)$	Zero-mean, circularly symmetric complex Gaussian distribution
$p(t)$	Arbitrary transmit waveform
$p(I)$	Exponential Probability Density Function
$PD$	Lognormal distribution of transit times in Arditi's perfusion model
$r$	Radius
$s$	Demodulated analytic signal
$s_c$	Coherent signal energy
$t$	Time
$t_p$	Time to peak
$T_{max}$	Time of the wash-in curve peak
$v$	Blood velocity
$V$	Relative Blood Volume
$w$	Weighting function
$WiR$	Wash-in rate
$Y_{max}$	Amplitude at curve peak
$Y(t)$	Time dependent contrast intensity



# List of Acronyms and Abbreviations

2-D	Two-dimensional
3-D	Three-dimensional
ANOVA	Analysis of variance
AUC	Area under curve
AVADO	Avastin And Docetaxel
BLES	Bovine lipid extract surfactant
CAM	Chorioallantoic membrane
ccRCC	Renal cell carcinoma (clear cell subtype)
CD31	Platelet endothelial cell adhesion molecule
CEUS	Contrast-enhanced ultrasound
CNV	Copy number variation
CoV	Coefficient of variation
CT	Computed tomography
DCE-MRI	Dynamic contrast enhanced magnetic resonance imaging
DCE-CT	Dynamic contrast enhanced x-ray computed tomography
DMSO	Dimethyl sulfoxide
DNA	Deoxyribonucleic acid
EDD	Embryonic development day
EDoF	Effective degrees of freedom
EDTA	Ethylenediaminetetraacetic acid
EGF	Epidermal growth factor
FBS	Fetal bovine serum

FDA	United States Food and Drug Administration
FDG	Fluorodeoxyglucose
FITC	Fluorescein isothiocyanate
HEPES	4-(2-hydroxyethyl)-1-piperazineethanesulfonic acid
HU	Hounsfield unit
LDA	Linear discriminant analysis
LDEV	Lactose dehydrogenase elevating virus
LDRW	Local density random walk
mBC	Metastatic breast cancer
MEM	Minimal essential medium
MI	Mechanical index
micro-CT	High-resolution x-ray computed tomography
MIP	Maximum-intensity projection
MLE	Maximum likelihood estimator
mRCC	Metastatic renal cell carcinoma
MRI	Magnetic resonance imaging
MVD	Micro-vascular density
NGS	Next generation sequencing
OS	Overall survival
PBS	Phosphate buffered saline
PD-1	Programmed cell death protein 1
PDF	Probability density function
PDX	Patient derived xenograft
PDX <sub>ovo</sub>	Ex ovo chicken embryo patient derived xenograft model
PET	Positron emission tomography
PFS	Progression-free survival
PRF	Pulse repetition frequency

RCC	Renal cell carcinoma
RECIST	Response Evaluation Criteria In Solid Tumours
RF	Radio-frequency
RIBBON	Regimens in Bevacizumab for Breast Oncology
RNA-Seq	Ribonucleic acid sequencing, or transcriptome profiling
ROI	Region of interest
RPMI	Roswell Park Memorial Institute medium
SNR	Signal-to-noise ratio
SNV	Single nucleotide variation
SPECT	Single-photon emission computed tomography
TGC	Time gain compensation
TKI	Tyrosine kinase inhibitor
TNC	Time-Nakagami curve
VEGF	Vascular endothelial growth factor
VHL	von Hippel-Lindau tumor suppressor gene
VI	Vascularization index

# Chapter 1

## Introduction

### 1.1 Overview

Blood perfusion, a functional parameter that describes blood flow at the capillary level, reflects the physiological and metabolic stresses experienced by tissue. It summarizes the adaptive responses of angiogenesis, the growth of new blood vessels, which occurs both in the normal tissue environment and under conditions of pathology. Such pathologies include tissue repair, disease, and the progression of cancer. A measurement of blood perfusion that falls outside of the normal range can be indicative of heart disease, stroke, tumor growth, or metastasis. Blood perfusion is of interest in the field of oncology, as tumor-induced angiogenesis perturbs the delicate balance of pro- and anti-angiogenic factors present in normal tissue. This leads to chaotic, tortuous, and inefficient vascular beds that are characterized by structural, functional, and temporal heterogeneity.

Contrast-enhanced ultrasound (CEUS) provides a means to monitor tumor perfusion and quantify adaptive tumor responses in the face of anti-angiogenic treatment, with the goal of informing targeted therapy. CEUS has several advantages over competing perfusion modalities: it lacks ionizing radiation, has a high frame rate, low cost, and only requires a small dose of contrast agent. However, conventional CEUS image analysis uses mean signal intensity as an estimate of tracer mass in indicator-dilution modeling. This discounts additional information that may be available from the first-order speckle statistics in a CEUS image. Heterogeneous vascular networks, typical of tumor-induced angiogenesis, should lead to heterogeneous

contrast enhancement of the imaged tumor cross-section. An image analysis technique that characterizes and quantifies these heterogeneities could prove to be useful for tumor vascular characterization, and in the evaluation of anti-cancer therapies that target tumor vasculature.

This thesis presents and evaluates novel image analysis techniques to expand the utility of contrast-enhanced ultrasound perfusion imaging. In this thesis, a B-mode processing approach that quantifies the change in first-order speckle statistics due to the incursion of microbubbles was developed in tumor-bearing mice and evaluated using nonlinear contrast enhancement. It eliminates the need for a cumbersome image subtraction step in preclinical contrast-enhanced imaging. To improve clinical applicability, a second-generation method for analyzing the first-order speckle statistics of two-pulse amplitude-modulated CEUS images was developed using an antiangiogenic drug trial on tumor bearing mice and evaluated with gold-standard histology and contrast-enhanced X-ray computed tomography. This technique was then applied to a clinically relevant drug trial on patient tumor fragments engrafted into the chorioallantoic membrane (CAM) of the chicken embryo. This study used a front-line small molecule tyrosine kinase inhibitor (sunitinib) on patient derived renal cell carcinoma xenografts as an antiangiogenic agent, to predict patient specific drug resistance. The goal of all studies was to quantify metrics of tumor blood perfusion and generate estimates of perfusion heterogeneity.

To provide some context for the ensuing chapters, this chapter first reviews the rationale for imaging perfusion in oncology and briefly describes the most common perfusion modalities used in the clinical and preclinical setting. As the focus of this thesis is on the development of contrast-enhanced ultrasound image analysis, an overview of CEUS is included. The overview will cover the composition of microbubble contrast agents, the acoustic response of microbubbles, microbubble specific imaging, and some common indicator dilution methods used in CEUS. It will then briefly review ultrasound speckle statistics, and the common applications of CEUS.

## **1.2 The Utility of Perfusion Imaging in Oncology**

Broadly speaking, the term ‘cancer’ describes a group of genetic diseases that are characterized by deregulated and uncontrolled cell division, unconstrained and invasive cell proliferation, and

metastatic spread throughout the body [1]. It is a diverse group of diseases that exhibits a high degree of genetic and phenotypic heterogeneity [2]. The causes of oncogenic transformation in normal cells are multi-factorial and can include, but are not limited to, genetic predisposition, environmental factors such as exposure to carcinogenic chemicals and/or ionizing radiation, bacterial or viral infections, and random errors in DNA replication. Furthermore, cancerous cells may be more susceptible to additional DNA damage due to a reduced ability to self-regulate and repair. This, in turn, implies that the cells within a tumor can become progressively more genetically diverse as the disease develops. This has wide reaching implications for understanding the progression of the disease and in designing effective anti-cancer therapies.

Prevailing research states that, without a supporting vascular network, the size of a tumor is limited to around  $2 \text{ mm}^3$  [3]. The metastatic spread of the disease will be restricted to immediately adjacent tissues in the absence of blood vessels and lymphatics to provide transit around the body [4]. Almost all known forms of cancer will release pro-angiogenic signaling molecules to prompt the formation of a supporting vascular network [5]. Tumor-induced angiogenesis, then, has gained interest as a therapeutic target owing to its importance in cancer development, its ubiquity in the tumorigenic environment, and the relative genetic homogeneity of endothelial cells relative to cancer cells.

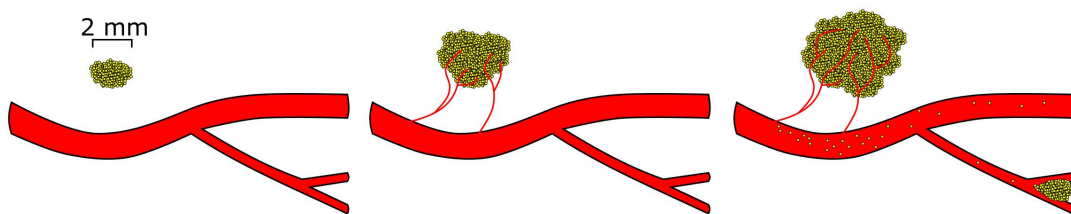


Figure 1.1: Diagrammatic example of tumor-induced angiogenesis. Angiogenesis is induced by hypoxic tumors (left panel), supports primary tumor growth (middle panel), and facilitates metastatic spread (right panel).

However, conventional treatment response criteria, such as RECIST (Response Evaluation Criteria In Solid Tumours - version 1.1 [6]), are insensitive to the early stage effects of a successful anti-angiogenic therapy. Inhibition of the formation of tumor vasculature can eventually lead to reductions in tumor size, but these effects can take several months to manifest themselves [7]. This poses a serious problem for clinical trials and preclinical models of anti-angiogenic therapies. There is, therefore, a need for vascular specific imaging to evaluate the

treatment efficacy of these types of therapy. Perfusion imaging is a functional imaging technique that provides biophysical estimates of the blood flow dynamics through tissues. These techniques provide the framework for evaluation of anti-angiogenic treatments. The following sections will discuss the unique characteristics of tumor blood vessels, the motivation for targeting angiogenesis in the treatment of cancer, and surrogate measures of treatment efficacy as measured by perfusion imaging.

### 1.2.1 Characteristics of Tumor Blood Vessels

Blood perfusion in normal tissues is supplied by an orderly, hierarchical, vascular network that is regulated by metabolic demand - a network maintained by a balance of pro- and anti-angiogenic molecular factors. Capillaries are consistently distributed to provide adequate oxygen and nutrients to surrounding cells, with any hypoxic stresses leading to adaptive remodeling of the network to meet demand [8].

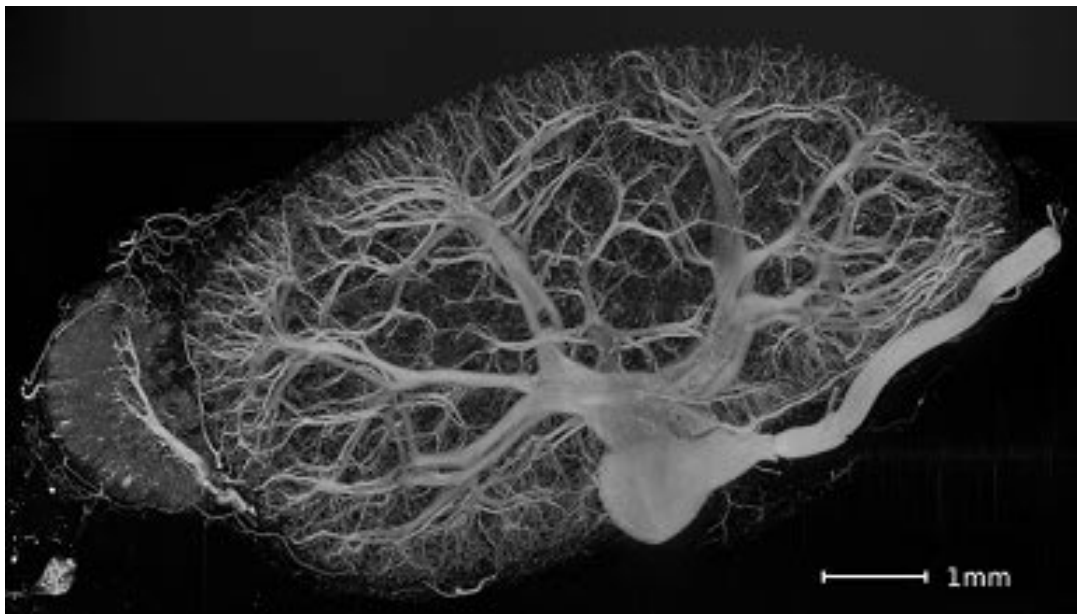


Figure 1.2: Contrast-enhanced micro-CT image of a mouse kidney, showing an orderly branching network. More details concerning the experiment this image came from can be found in Chapter 3 of this thesis. Image courtesy of Justin Tse.

Tumor vasculature, by contrast, is characterized by irregular structural topography and functional heterogeneity. The rapid division of cancer cells, along with the accompanying

metabolic stresses, results in a regional overexpression of pro-angiogenic factors that overpowers the adaptive quality of controlled vascular remodeling [9]. A cancerous blood supply is a disorganized mass of underdeveloped vessels, exhibiting flow pathways that are tortuous and circuitous. The boundary between capillary, arteriole, and venule is unclear in these networks [10], and the diameter and shape of blood vessels is inconsistent [11, 12]. Vessels exhibit hyper-permeability due to their discontinuous endothelial lining and a lack of supporting smooth muscle [13]. The accumulation of fluids leaking from blood vessels leads to an elevated interstitial fluid pressure [14, 15].

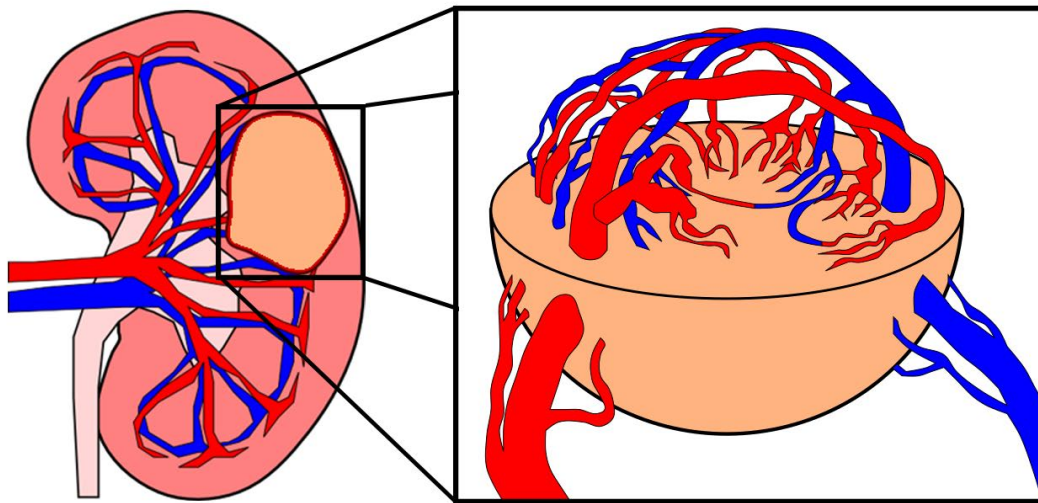


Figure 1.3: Diagram depicting a cut away view of a tumor with visible vasculature. The tumor vasculature is structurally chaotic and disorganized.

These factors, in addition to flow resistance from irregular network geometry, combine to greatly limit blood perfusion through tumor vasculature. These inefficient networks often exhibit regions of hypoxia and sluggish flow, and are inadequate at supplying the tissue demand of oxygen and nutrients. This functional heterogeneity has clinical consequences that may not be immediately intuitive; for example, the efficacy of both radiotherapy [16] and chemotherapy [17] is reduced in hypoxic regions. Anti-angiogenic therapy has undergone a paradigm shift recently, with the focus of treatment switching from complete vascular elimination to instead inducing vascular normalization. The next section highlights the rationale for the focus of anti-angiogenic therapy.



## 1.2.2 Motivation for Targeted Angiogenic Therapy

In 1971, Judah Folkman pioneered the concept of anti-angiogenic therapy for solid tumors. He observed that tumor tissues have abnormally high vascularization, that tumors can stimulate the proliferation of endothelial cells, and that tumors will not grow beyond 2 mm<sup>3</sup> in the absence of angiogenesis [18, 19]. Thus the original motivation for targeting angiogenesis in solid tumors was straightforward: vascular suppression through anti-angiogenic therapy could, in effect, ‘starve’ a tumor.

The development of anti-angiogenic drugs was spurred on by the discovery of vascular endothelial growth factor-A (VEGF-A), a glycoprotein that is critical for inducing angiogenesis, vasculogenesis, and endothelial cell growth. This protein also increases vascular permeability, promotes cell migration, and can inhibit apoptosis. The observations that most tumors will overexpress VEGF-A, and that selectively inhibiting VEGF-A will reduce tumor growth in animal models, led to numerous applications of VEGF-A therapy in the clinic.

More recently, the notion of ‘vascular normalization’ via VEGF-A therapy has shifted the motivation for anti-angiogenic therapy. Instead of ‘starving’ a tumor through excessive vascular inhibition, the goal is to ‘prune’ the inefficient and tortuous vessels in a tumor [20]. This works synergistically with other anti-cancer therapies by improving drug delivery and relieving tumor hypoxia. This is discussed in more detail in Section 1.2.3.

A final point when considering the clinical impact of anti-angiogenic therapy is that few biomarkers exist to select patients that are considered good recipients for the treatment [21]. Thus it is almost always dosed in an unselected manner. This has had the consequence that the use of anti-angiogenic agents has had little impact on patient survival and overall survival in the clinic. A developing area of research is the use of surrogate markers of treatment efficacy to select those patients that will respond at an early time point [22, 23]. One such candidate is perfusion imaging, serving as an ‘imaging biomarker’, a topic that will be covered in Section 1.2.4.

The motivation for the use of anti-angiogenic drugs in different therapy settings is discussed below.

## Metastatic Setting

The motivation for the use of anti-angiogenic therapy in the metastatic setting closely follows the initial idea that angiogenesis is a limiting step in the development of cancer. As tumors require a vascular supply to grow, inhibiting angiogenesis could induce cancer dormancy, and stop the spread of metastatic disease. So far, evaluating the clinical efficacy of anti-angiogenic therapy for metastatic disease has been anything but straightforward. It has been established that only certain types of cancer have metastases that respond to this therapy, and the mechanism causing this inconsistency is unknown [24].

Specifically, metastatic renal cell carcinoma (mRCC) epitomizes successful anti-angiogenic therapy. Four FDA-approved tyrosine kinase inhibitors that target VEGF-A (sunitinib, pazopanib, sorafenib, and axitinib) have shown an improved progression free and overall survival for patients with mRCC [25–28]. The most common subtype of RCC is clear cell RCC (ccRCC) [29], and 91% of clear cell RCC patients have a somatic inactivation of the von Hippel-Lindau (VHL) tumor suppressor gene [30]. VHL is involved in hypoxia signaling and cell metabolism homeostasis, making it a suitable target for anti-angiogenic therapy. Histology from this subtype has a characteristically ‘clear’ cytoplasm due to the accumulation of glycogen and fat deposits within ccRCC cells. Rarer subtypes, such as papillary RCC (named for its ‘finger-like’ or papillae structures) and chromophobe RCC (which exhibits eosinophilic cytoplasm) do not typically exhibit inactivation of VHL; thus, there is rarely a clinical benefit of anti-angiogenic therapies for these subtypes.

A diagram depicting common therapeutic agents targeting the VHL pathway, adapted from [31], is shown in Figure 1.4. There has also been clinical benefit in the application of anti-angiogenic agents for the treatment of metastatic colorectal cancer [32], hepatocellular carcinoma [33], pancreatic neuroendocrine tumors [34], ovarian cancer [35], and non-small-cell lung cancer [36].

In contrast, anti-angiogenic therapy has not been shown to improve patient survival for cancers of the breast [37], prostate [38], pancreas [39], or in melanoma [40]. The history of anti-angiogenic therapy for metastatic breast cancer (mBC) is particularly noteworthy. Bevacizumab, an anti-VEGF monoclonal antibody, was given accelerated approval for the treatment

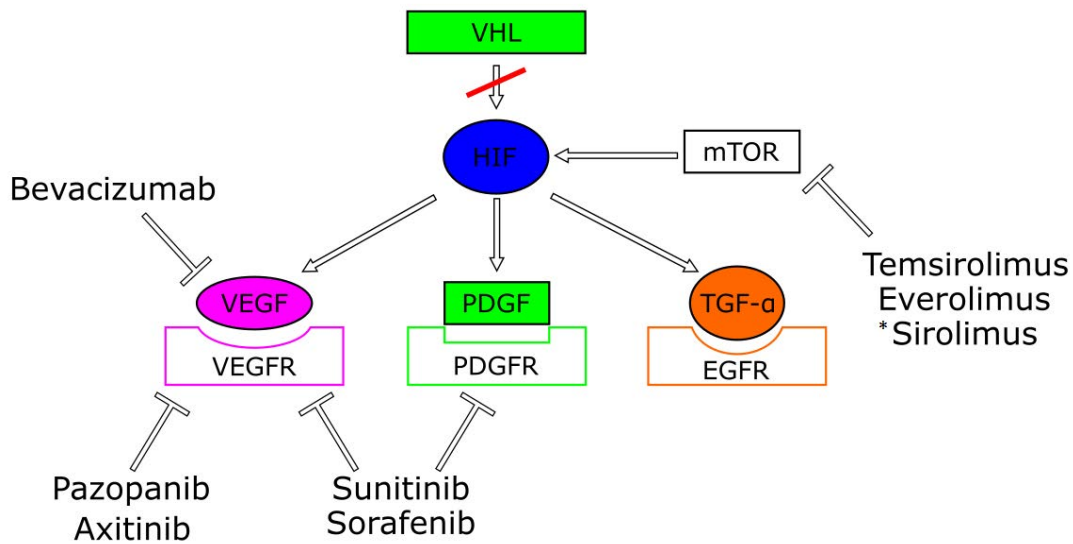


Figure 1.4: Schematic demonstrating the therapy targets for clear cell RCC. Anti-angiogenic drugs are to the bottom and left of this network. \*Not FDA approved for use in RCC.

of mBC by the FDA in 2008, based on the extremely promising results of the E2100 phase III trial [41]. The E2100 phase III trial found that paclitaxel (a chemotherapeutic agent) plus bevacizumab, versus paclitaxel alone, improved progression-free survival (PFS; 11.8 vs. 5.9 months) in patients with mBC but had no effect on overall survival (OS). Subsequent phase III trials of bevacizumab combined with chemotherapy (AVADO [42], RIBBON-1 [43], and RIBBON-2 [44]) found only very modest improvements in PFS, and no change in OS. This led to the FDA withdrawing its approval of bevacizumab for the treatment of mBC in 2010, due to the conclusion that these studies did not demonstrate that bevacizumab improved patient survival.

### Adjuvant Setting

Anti-angiogenic agents are administered after the surgical removal of a tumor (adjuvant therapy) to prevent the growth of micro-metastasis, and to avoid the possibility of a local relapse. Somewhat surprisingly, efficacy of anti-angiogenic agents for a specific cancer in the metastatic setting does not translate into efficacy for that cancer in the adjuvant setting. For example, a comparison between colorectal cancer patients that received chemotherapy plus bevacizumab versus chemotherapy alone showed no increase in overall survival in the adjuvant setting [45],

a finding that contrasts with the clear clinical benefit of anti-angiogenic therapy for metastatic colorectal cancer [32]. This disparity highlights the vast heterogeneity of cancerous disease: the genotype, phenotype, and response to therapy in established metastatic disease can be very different than those of micro-metastasis.

### **Neoadjuvant Setting**

There are two main motivations for anti-angiogenic therapy prior to surgical removal (neoadjuvant therapy): to cytoreduce a non-resectable lesion so that it can be safely excised, or to downstage the disease in the hope of reducing the risk of both local relapse and/or metastasis. The current recommended clinical practice for patients with initially unresectable colorectal liver metastasis is preoperative chemotherapy [46], with evidence showing that bevacizumab in combination with chemotherapy may provide a larger benefit [47, 48].

It is worth noting that the neoadjuvant setting most closely resembles what is being tested in the majority of animal models of anti-angiogenic therapy.

### **1.2.3 Combination of Anti-Angiogenic Drugs with other Therapies**

Tumor perfusion is inefficient, leading to regions of hypoxia and cellular acidosis. This microenvironment is known to accelerate tumor progression and confer resistance to chemotherapy, radiotherapy, and immunotherapy [20]. From this we would predict that patients with impaired and heterogeneous tumor perfusion will not respond well to conventional therapies. Furthermore, targeting VEGF-A signaling has been shown to modify the vasculature in mouse tumors, by pruning immature and leaky vessels, and by remodeling the remaining vasculature, so that it more closely resembles normal vasculature. Thus, the reasoning goes, anti-angiogenic therapy will be synergistic with other targeted therapies by inducing, at least transiently, a state of vascular normalization that improves local drug delivery and efficacy. In the following sections we will briefly overview the rationale for combining anti-angiogenic agents with chemotherapeutics, radiotherapy, immunotherapy, and finally the potential survival benefit of relieving hypoxic stress.

## **Chemotherapy**

The combination of anti-angiogenic agents with chemotherapy appears contradictory. In the classical view, targeting VEGF will reduce the amount of active vasculature in the tumor and lower the leakiness of blood vessels. Reduced vasculature should decrease the dosage of chemotherapeutic agent to the tumor, and the now non-leaky vessels will prevent the agent from leaving the interstitial space. Both of these factors should greatly reduce the dosage of drug to tumor tissues.

What has been found, surprisingly, is that the opposite occurs: the combination of chemotherapy with anti-angiogenic agents increases the dosage of chemotherapeutic agent to tumorous tissue, and leads to improved patient outcomes. The inefficient organization and aberrant morphology of tumor vasculature reduces drug delivery to the tumor mass [49]. Intra-tumoral drug delivery is further worsened by the high interstitial fluid pressure within the tumor. Following anti-angiogenic therapy tumor tissue undergoes a transient phase of vascular normalization, whereby blood perfusion and drug delivery are improved.

## **Radiotherapy**

Molecular oxygen has an extremely high electron affinity, making it a potent chemical radiosensitizer of tissue. The absorption of ionizing radiation by oxygen leads to the production of reactive oxygen species - a group of highly reactive DNA damaging molecules [50, 51]. Tumor hypoxia limits tissue oxygen supply, thus reducing production of reactive oxygen species, and decreases the therapeutic effectiveness of a given dose of radiation. The combination of anti-angiogenic agents with radiotherapy improves the therapeutic effectiveness of radiation, allowing for more healthy tissues to be spared, provided that the tumor becomes adequately oxygenated.

## **Immunotherapy**

The tumor microenvironment modulates immune response. Hypoxia, and cellular acidosis, can alter the phenotype of circulating macrophages to be protumorigenic and immunosuppressive. This microenvironment mitigates the efficiency of immune effector cells, and can suppress T

lymphocyte activity. Low blood perfusion induced hypoxia can inhibit the ability of dendritic cells to process tumor antigens, which prevents them from presenting tumor antigens to lymphocytes [52]. The judicious application of anti-angiogenic agents to alleviate hypoxia can turn an immunosuppressive microenvironment into an immunosupportive one. This can allow for a lower dose of immunotherapeutic drugs which would reduce clinical costs and the potential for patient toxicity [53].

### **Vascular Normalization to Relieve Hypoxic Stress**

RK Jain has put forward the hypothesis that increasing tumor blood flow, through the judicious use of anti-angiogenic agents to normalize vasculature, may in of itself confer a survival benefit to patients [54]. Hypoxia creates an abnormal microenvironment that is characterized by cellular acidosis and immunosuppression. This in turn creates a selective survival pressure on cancer cells that may increase their invasive and metastatic potential, can confer a resistance to apoptosis, and reduces the effectiveness of systemic therapies. Although this is a relatively new paradigm for cancer treatment, there is some evidence that increased tumor perfusion/vascular normalization can improve survival of patients diagnosed with glioblastoma [55, 56].

### **1.2.4 Surrogate Measures of Treatment Efficacy**

Ultimately, the goal of a therapy is to improve the overall survival (OS) and progression-free survival (PFS) in the patient population. However, assessing treatment efficacy in clinical trials via a significant increase in patient survival is both costly and time consuming. These trials require a large patient population, can take years to complete, and have a high risk of patient drop-out. Furthermore, patient survival does not consider pre-existing health conditions, nor the cause(s) of death.

An alternative approach instead relies on one or more ‘biomarkers’ of therapy response measured from a patient at an earlier stage of treatment. These biological markers are quantifiable metrics that are indicative of the current disease state. For example, one of the most widely used biomarkers of cancer treatment response is a decrease in the anatomical size of a tumor. An established set of rules governing the assessment of this biomarker was codified in

the RECIST criteria [6]. A substantial decrease in tumor burden, classified as partial and/or complete response by RECIST, has been shown to be a good predictor of improved survival for most forms of cancer [57].

However, conventional treatment response criteria, such as RECIST, are insensitive to the early stage effects of a successful anti-angiogenic therapy. Anti-angiogenic therapy can eventually lead to reductions in tumor size, but these effects can take several months to manifest [7]. Instead, many researchers posit that perfusion imaging provides a more appropriate readout for the evaluation of anti-angiogenic agents by offering biophysical estimates of the blood flow dynamics through tissues. This hypothesis was supported by a recent study by Bjarnason *et. al.* [23] which demonstrated that CEUS could inform the modification of sunitinib dosage scheduling for patients with mRCC, leading to improvements of OS and PFS. A brief overview of some commonly used perfusion imaging techniques is provided below, in Section 1.3.

### 1.3 Perfusion Imaging Techniques

There are several techniques available for perfusion imaging in both the clinical and preclinical setting. Generally, these modalities rely on a vascular tracer to provide additional signal from blood flow, and perfusion metrics are derived from indicator-dilution kinetics from a region of interest. Each competing modality represents a trade-off between spatial resolution, temporal resolution, cost, specificity, and patient exposure to ionizing radiation. The modalities discussed below are predominantly clinical imaging techniques that represent the most widely used and studied methods of perfusion imaging. The modalities with dynamic contrast enhancement are analyzed using kinematic indicator modeling that closely resembles the models used in CEUS. These techniques, therefore, represent the direct competitors for the potential clinical translation of the analysis methods being developed for CEUS in this thesis. Ultrasound was selected over the other modalities due to its low relative cost, high spatial and temporal resolution, and potential for high throughput. It was preferred over competing pre-clinical optical techniques as those modalities have lower potential for clinical translation.

### **1.3.1 Dynamic Contrast Enhanced X-ray Computed Tomography (DCE-CT)**

Computed tomography (CT) refers to a processing technique that combines projection information, taken from multiple angles along a common axis of rotation, into cross-sectional images. The most common form of tomography uses x-ray images, projections of the attenuation of high energy photons through a subject, to produce high resolution anatomical images. Photon absorption, the main mechanism of image contrast, depends on the atomic number and density of the tissue being imaged. Intravenous CT contrast agents, such as iodine, are high atomic number agents. Dynamic contrast enhanced CT (DCE-CT) applies indicator dilution techniques to the influx of iodine, and resulting radio-opacification, to yield perfusion metrics from an imaged tissue. The increase in signal intensity is linearly dependent on the contrast concentration; however, kinetic models must account for the freely diffusible nature of small molecule agents [58]. This modality also suffers from a moderate to high radiation dosage to the patient, and iodine contrast agents are potentially nephrotoxic [59].

### **1.3.2 Single-photon emission computed tomography (SPECT)**

Single-photon emission computed tomography (SPECT) is a nuclear medicine tomographic imaging technique that relies on the detection of intravenously injected radioisotopes to produce three-dimensional images of relative blood perfusion. SPECT tracers, for example Technetium-99m ( $^{99m}\text{Tc}$ ) or Thallium-201 ( $^{201}\text{Tl}$ ), continuously decay by releasing gamma-ray photons. These elements can be bound to a wide array of pharmaceuticals for different imaging applications. Volumes are reconstructed via computed tomography using projection images of gamma photon emission within the patient, giving a three-dimensional volume of the radio-tracer distribution. Although SPECT has a relatively poor resolution ( $\sim 1$  cm [60]), its low cost and the large number of SPECT tracer labeled pharmaceuticals make it a widely-used modality for myocardial perfusion imaging and functional brain imaging. In oncology, it is commonly combined with x-ray computed tomography to produce a hybrid imaging modality (SPECT/CT).



### 1.3.3 Positron emission tomography (PET)

Positron emission tomography (PET), much like SPECT, is a functional imaging modality that measures the spatial distribution of a radio-indicator. In this case positron-emitting radionuclides. The system indirectly measures the presence of PET tracers, such as  $^{15}\text{O}$ -water or  $^{18}\text{F}$ -FDG, by detecting the two gamma photons that result from positron-electron annihilation. To satisfy the requirement of conservation of momentum, this matter-antimatter interaction results in the two gamma-ray photons being emitted at a  $\sim 180$ -degree angle to each other. A cylindrical gamma camera that surrounds the patient detects these two photons within a narrow time window and plots them along a line of coincidence. The coincidence of detection reduces the ambiguity in three-dimensional reconstruction, leading to an improved resolution over SPECT (PET resolution 2-3 mm [61]).

### 1.3.4 Dynamic Contrast Enhanced Magnetic Resonance Imaging (DCE-MRI)

Magnetic resonance imaging (MRI) exploits the precessional frequency of tissues, typically targeting hydrogen atoms in water, which have been placed into a strong uniform magnetic field (1.5-9 Tesla). An isotope with an uneven number of protons and/or neutrons has an intrinsic magnetic moment and angular momentum. They will align their magnetic moments with the direction of an external magnetic field, and begin to precess to conserve angular momentum. The frequency of this precession, or Larmor frequency, depends on the strength of the external field and the gyromagnetic ratio of the isotope. Energy can be transferred efficiently into, and out of, the system with a radio-frequency (RF) pulse tuned to the Larmor frequency. Spatial information (*i.e.* imaging data) is acquired with the addition of selection gradients that modify the Larmor frequency in a predictable and locational manner. The sample is probed by exciting tissue protons with an RF pulse and recording the magnetization as it undergoes relaxation.

Contrast agents, such as Magnevist, provide perfusion data by modifying the relaxation rate of surrounding tissues. This manifests as a temporal change in the imaging intensity data which, when coupled with an arterial input function and an appropriate kinetic model, can produce estimates of blood perfusion and vascular leakiness in the region of interest.

### 1.3.5 Doppler Ultrasound

The term ultrasound refers to a frequency range of sound waves that is outside of the human audible range (*i.e.* greater than 20 kHz). Medical ultrasound evolved as an imaging modality from radar and sonar technology in the 1940s and 1950s - imaging data are produced from reflected echoes from deep within tissues. The ratio of reflected versus transmitted energy will depend on the degree of acoustic impedance mismatch at the tissue interface.

The Doppler effect describes a phenomenon of a predictable frequency shift in a reflected sound wave, relative to the transmitted wave, when there is absolute motion between the transducer and the scattering object. Doppler ultrasound takes advantage of this frequency shift to discriminate between echoes from moving red blood cells and echoes from solid tissues. The magnitude and direction of the frequency shift corresponds to the magnitude and direction of blood velocity, either toward or away from the transducer, and the power of the Doppler signal depends on the number of red blood cells in the sampling volume. These two measures are the basis for color- and power-Doppler ultrasound imaging, respectively. Both color Doppler and power Doppler images typically consist of a color overlay on top of a B-mode image for anatomical context. A color Doppler image maps the mean Doppler frequency to a red (away from transducer) to blue (toward transducer) map, whereas a power Doppler image maps the total power of the Doppler signal to a red-yellow map. Power Doppler is preferentially used over color Doppler for the purposes of perfusion imaging: the signal processing is more sensitive to small vessels, can detect slower velocity, and is not affected by aliasing of high velocities.

### 1.3.6 Contrast Enhanced Ultrasound (CEUS)

Contrast-enhanced ultrasound is a perfusion imaging modality that relies on an intravenous injection of a signal enhancing microbubble contrast agent. An in-depth description of this perfusion imaging technique can be found in the following section.

## 1.4 Overview of Contrast-Enhanced Ultrasound

Contrast-enhanced ultrasound detects signal from vasculature using micron diameter bubbles (microbubbles) to greatly increase the acoustic backscatter from blood. This section overviews some applications of CEUS, the nature and composition of microbubbles, a brief description of microbubble response to acoustic radiation, forms of microbubble specific imaging and functional imaging, and finally some common types of indicator-dilution models used in contrast-enhanced ultrasound imaging.

### 1.4.1 Contrast-Enhanced Ultrasound Applications

The high contrast-to-tissue ratio of CEUS imaging, along with the varied response of microbubbles to acoustic waves, has led to a diverse array of clinical applications for this modality. These applications are briefly discussed below, divided into the categories of echocardiography, potential therapeutic applications, and the detection, diagnosis, and characterization of solid tumors.

#### **General Radiology**

The use of microbubbles in general radiological examination can be divided into two broad groups: the enhancement of ultrasound signal intensity from blood vessels, and the injection of microbubbles into lumen to improve tissue delineation. Ambiguous Doppler examinations can be salvaged with microbubble enhancement to improve diagnostic accuracy, so called ‘Doppler-rescue’ [62]. For example, transcranial Doppler signal is heavily attenuated while traversing the skull and contrast enhancement improves the detection of flow in intracranial arteries [63]. Enhancement is not limited to vascular imaging, as microbubbles have been previously used in the diagnosis of vesicoureteric reflux by injection into the bladder [64], and to test the patency of fallopian tubes via intrauterine injection [65].

### **Echocardiography**

Historically, the first reported use of microbubble contrast agent in ultrasound imaging was by Gramiak and Shah for the enhancement of the aortic root in cardiology [66]. The addition of microbubbles to the heart is still commonly performed in the clinic to make the tissue-blood boundary clearer, thus improving the delineation of the endocardial border [67]. Properly evaluating myocardial function is critical in the management of many heart pathologies, with the addition of microbubble enhancement demonstrating tangible improvements in diagnostic accuracy [68]. Ultrasound contrast agents have also been used to evaluate myocardial perfusion [69, 70] and to directly measure cardiac output [71].

### **Imaging the Liver**

Liver contrast imaging greatly improves the visibility of focal liver lesions such as metastatic tumors and hepatocellular carcinoma [72–76]. Contrast-enhancement substantially increases ultrasound's sensitivity to metastatic disease in the liver, particularly for detecting lesions that are under 1 cm in diameter [76]. Furthermore, the enhancement pattern of liver lesions can lead to increased specificity in ultrasound liver imaging. Benign hemangiomas demonstrate a characteristic peripheral enhancement pattern [77]. Many benign lesions show a late uptake of microbubbles [78], with early enhancement being typical of the vascular shunting seen in malignancies and cirrhosis [79, 80].

### **Therapeutic Applications**

Microbubbles can aid in drug delivery through sonoporation and/or by acting as drug carrying containers [67]. The structure of the contrast agent permits surface-ligand targeting of specific regions of interest, an important factor when considering effective dose and systemic toxicity. Microbubbles will cavitate in response to strong acoustic pressures, creating temporary non-lethal perforations in cell membranes that permeabilize the endothelial lining in capillaries. These now leaky blood vessels permit the diffusion of therapeutic agents, particularly macromolecules which are usually too large to pass through the intact endothelial lining [81].

## Detection, Diagnosis, and Characterization of Solid Tumors

CEUS is routinely used outside of North America for the detection and diagnosis of abdominal lesions. The use of microbubbles has been shown to significantly improve the diagnostic accuracy of solid tumors in the liver [82–86], kidney [87], prostate [88], bladder [89], and many others [90]. The weight of evidence supporting the clinical benefit of CEUS in the diagnosis of liver lesions (see also Section 1.4.1) has led to the recent FDA approval of Lumason<sup>®</sup> (SonoVue) for liver imaging applications [91]. It has also seen off-label use in the evaluation of anti-angiogenic treatment response for patients with metastatic renal cell carcinoma [92–94].

In this thesis, CEUS is used to extract perfusion indices from solid tumors via an intravascular injection of microbubbles that enhances ultrasound backscatter from microvasculature. These perfusion indices, which reflect the underlying physiology of the tumor vasculature, are used to discriminate between treated and untreated cohorts in preclinical cancer models.

### 1.4.2 Composition of Microbubble Contrast Agents

Microbubble contrast agents are composed of a gas-filled core, typically a neutral heavy gas (*e.g.* perfluorocarbons), encapsulated by a stabilizing shell. Shell materials can include phospholipids, polysaccharides, or albumin and other proteins. The exact nature of the shell material and encapsulated gas will dictate the microbubbles' response to acoustic radiation. As such, microbubbles are often engineered for specific imaging applications and optimized for the frequency range and ultrasound system being used. Their development as an indicator went through several phases of evolution, each step improving upon a desirable characteristic of the shell-gas combination.

*Zeroth generation:* The earliest type of microbubbles used for clinical ultrasound image enhancement were formed spontaneously from the agitation of saline. This was first reported by Gramiak and Shah for the enhancement of the aortic root in cardiology [66]. The image contrast was attributed to the high compressibility of the trapped gas leading to a large impedance mismatch with the surrounding blood and tissues. The size distribution of these bubbles was poorly controlled, which increased the risk of embolism. Furthermore, the lifetime of this contrast agent was limited to a few seconds in circulation.

*First generation:* The first manufactured microbubbles added a stabilizing shell to encapsulate atmospheric gases. For example, the Alunex<sup>®</sup> (GE Healthcare Systems) contrast agent used a manufacturing process that led to an air-filled albumin shell. This increased the imaging lifetime of the agent. Alunex<sup>®</sup> was the first microbubble contrast agent approved by Food and Drug Administration (FDA) for clinical ultrasound imaging.

*Second generation:* The next step in microbubble engineering was to incorporate a heavy gas, typically a fluorocarbon, to reduce the rate of gas loss across the shell membrane. This further improved the lifetime of microbubbles in blood circulation. Examples of these agents include Optison<sup>™</sup> (GE Healthcare Systems), which is a protein-shelled microsphere containing a fluorinated gas, and Definity<sup>®</sup> (Lantheus Medical Imaging) which was the first agent to use a phospholipid shell to contain a fluorocarbon gas. The pliable lipid shell of Definity<sup>®</sup> produced pronounced resonance effects of the microbubble in the face of ultrasound waves, leading to new imaging schemes to improve the detection of the agent in tissues. The contrast agent used in all studies presented in this thesis, Vevo Micromarker<sup>™</sup>, is a second-generation agent.

### 1.4.3 Microbubble Response to Acoustic Radiation

Microbubbles behave as damped spring-mass systems in response to acoustic waves. As a consequence they exhibit oscillatory standing waves at their resonant frequencies. The size distribution of microbubbles that are most relevant for vascular perfusion (*i.e.* a diameter of less than 5  $\mu\text{m}$  to allow flow through capillaries) serendipitously exhibit strong resonances, and larger scattering cross-sections, at medical ultrasound frequencies (5 MHz).

When attempting to optimize the transmit frequency of microbubble imaging, it can be useful to investigate the scattering cross-section of the microbubble as a function of frequency and bubble size. The scattering cross-section describes the ratio of the scattering power relative to the incident ultrasound intensity; it is modeled as follows:

$$\sigma_s(r, f) = \frac{4\pi r^2}{\left(\left(\frac{f_r(r)}{f}\right)^2 - 1\right)^2 + \delta_{tot}(r, f)^2}, \quad (1.1)$$

where  $f$  is the frequency,  $r$  is the resting state radius,  $f_r(r)$  is the the undamped resonant fre-

quency of the microbubble [95], and  $\delta_{tot}(r, f)$  is the total effect of damping due to a stabilizing shell. This relationship is shown in Figure 1.5.

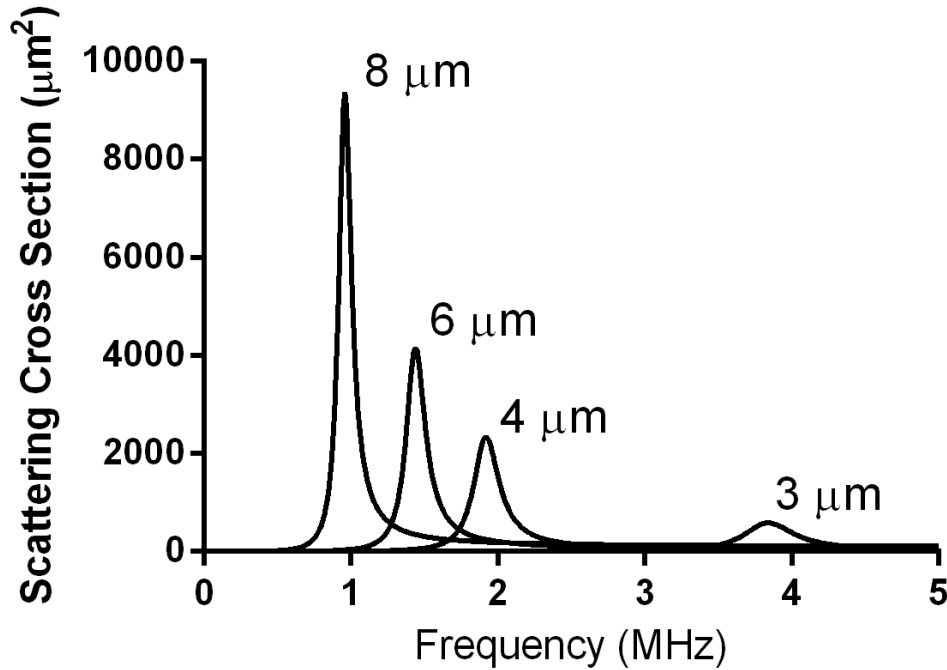


Figure 1.5: Microbubbles have the largest scattering cross-section at their resonant frequency.

Microbubbles have a variable response to acoustic energy that depends on the magnitude of the incident pressure. The outer shell of microbubbles can be compromised when exposed to a peak negative pressure that is beyond the Blake threshold. To explore a microbubble's response to incident pressure, it is useful to define a quantity referred to as the Mechanical Index (MI):

$$MI = \frac{\hat{P}_{neg}(MPa)}{\sqrt{freq(MHz)}}. \quad (1.2)$$

This index is based on an analytical model of a gas bubble in a liquid medium during the propagation of sound as the peak negative pressure approaches the Blake threshold [96]. It is not based on first principles, and thus is usually reported as a unit-less quantity.

The following section will describe in more detail the differences in the acoustic response that can be expected from microbubbles as they are exposed to variable intensities of acoustic radiation.

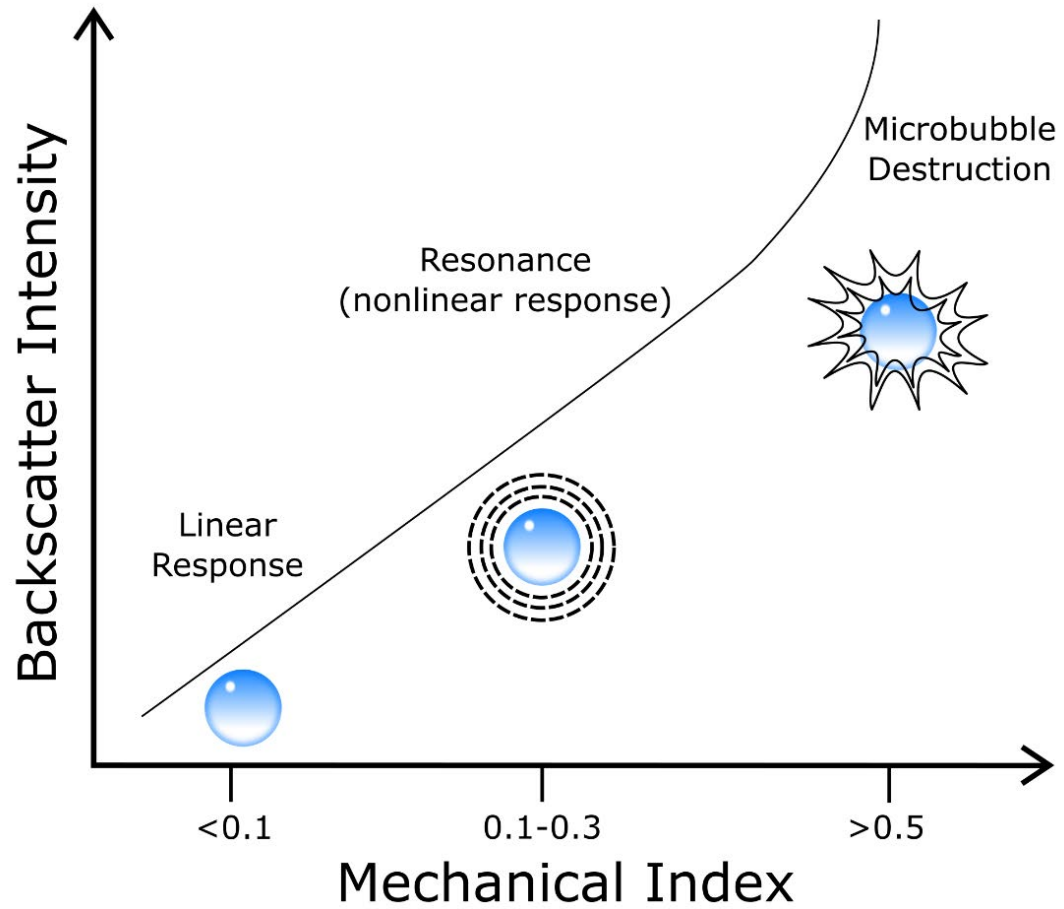


Figure 1.6: The backscatter intensity, and microbubble response, depend on the mechanical index of imaging.



### **Low Incident Pressure**

At low acoustic energies ( $MI < 0.1$ ), microbubbles behave as linear oscillators. The radial expansion and contraction of the microbubble is symmetric, leading to a scattering response with few harmonic components. An example of the oscillatory response of a microbubble to low acoustic pressure, and the corresponding scattered pulse from the microbubble, is shown below in Figure 1.7. This figure depicts the simulated microbubble response as predicted by the Hoff equation [97], and is meant for demonstrative purposes only. More sophisticated models, such as the Marmottant equation [98], take the physical properties of a lipid monolayer coating into account but are beyond the scope of this thesis.

### **Moderate Incident Pressure**

Microbubbles respond in a nonlinear manner when exposed to moderate acoustic pressures ( $0.1 < MI < 0.3$ ) that are around the resonant frequency of the contrast agent. The microbubble begins to vibrate with an uneven degree of radial expansion and contraction, leading to a characteristic nonlinear oscillatory response. Typically, the duration and degree of the expansion phase will outweigh the contraction phase. This nonlinear response generates a radiated energy spectrum with a wide range of harmonic and subharmonic components relative to the incident ultrasound frequency [99]. An example of this nonlinear behavior is shown in Figure 1.8.

### **High Incident Pressure**

At high pressure ( $MI > 0.5$ ) microbubbles will undergo extreme oscillations that compromise the outer shell and lead to the release of bubble contents. This response is referred to as inertial cavitation - a rapid collapse of the bubble structure that produces a shockwave of acoustic energy. The 'burst' or 'flash' of bubbles as they cavitate is readily detectible by an ultrasound transducer, an early technique to produce blood specific image contrast. The intentional cavitation of microbubbles is typically used in contrast-enhanced Doppler imaging (often referred to as Doppler rescue), and in destruction-reperfusion protocols.

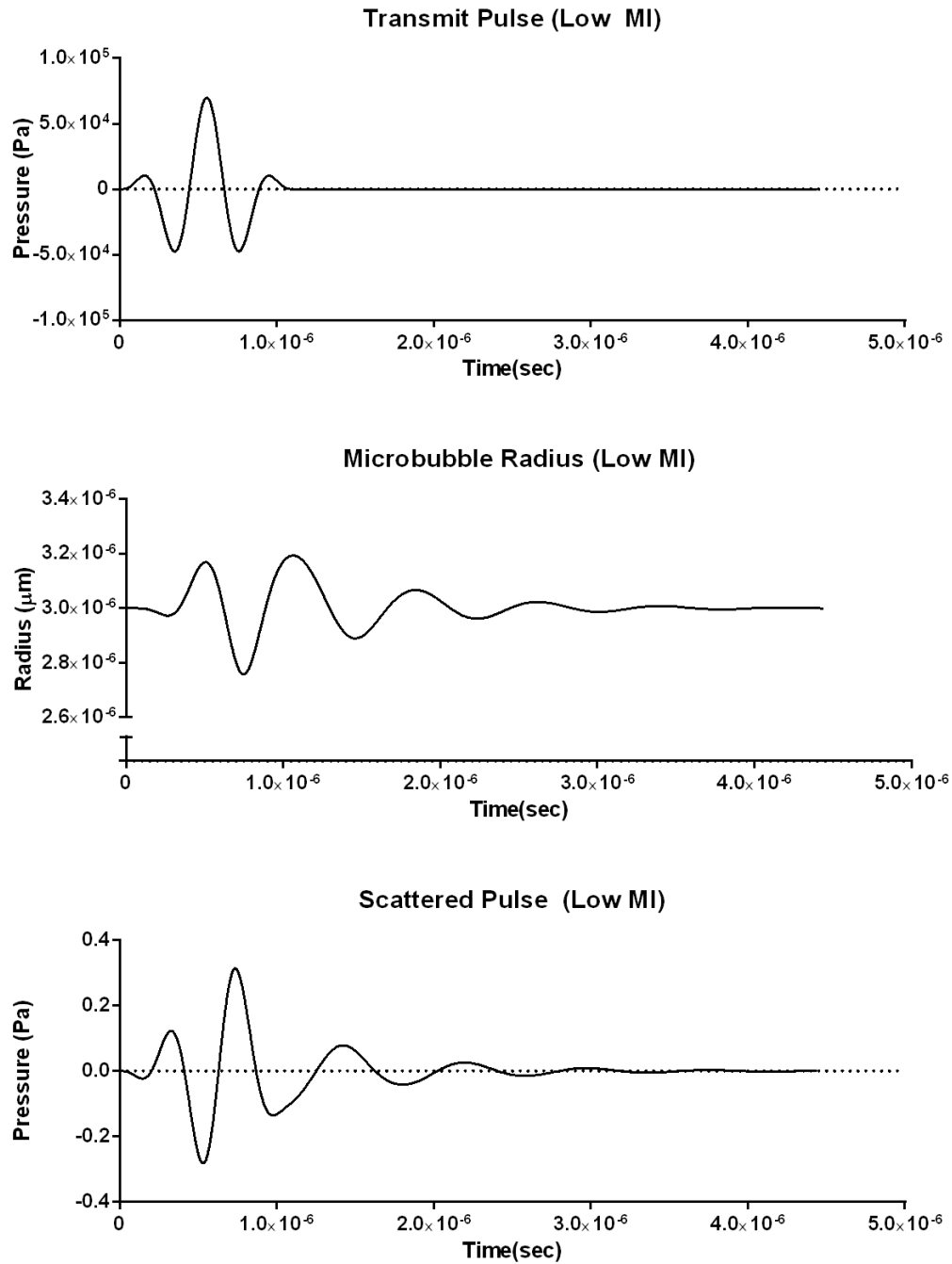


Figure 1.7: Simulated microbubble response to low incident pressure. The microbubble's radius oscillates in a linear manner, yielding a scattered pulse with few harmonic components. This simulation was performed using Hoff's BubbleSim package for a single  $3 \mu\text{m}$  shelled microbubble (shell thickness 4 nm) excited with a 2.5 cycle, 0.07 MPa pulse with a center frequency of 2.25 MHz [97].

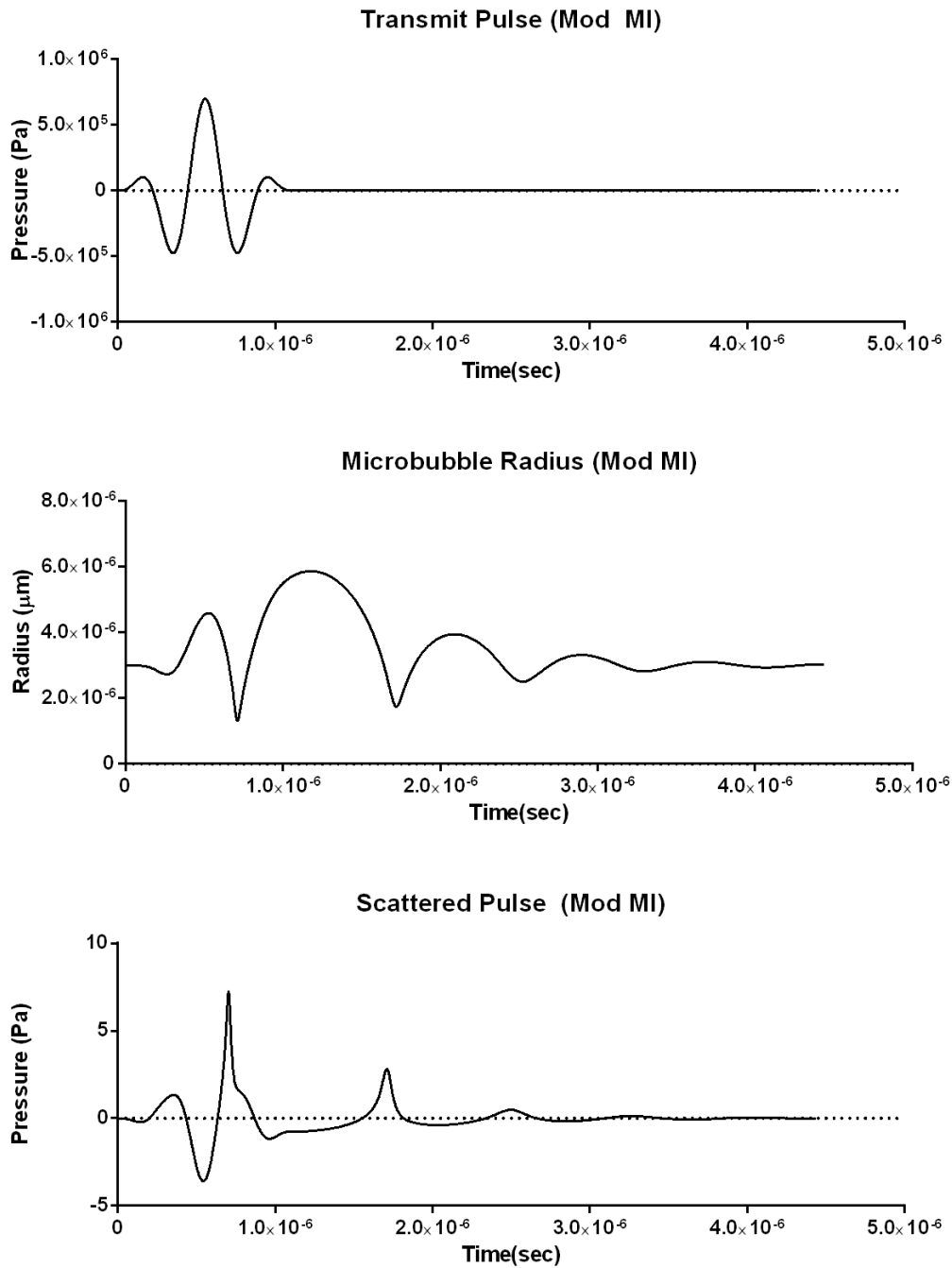


Figure 1.8: Simulated microbubble response to moderate incident pressure. The microbubble's radius responds asymmetrically, resulting in a wide range of harmonic and subharmonic components in the scattered echo. In this simulation, a single  $3 \mu\text{m}$  shelled microbubble (shell thickness  $4 \text{ nm}$ ) is excited with a 2.5 cycle,  $0.7 \text{ MPa}$  pulse with a center frequency of  $2.25 \text{ MHz}$ . The scattered pressure was calculated using Hoff's Bubblesim package [97].

### 1.4.4 Microbubble Specific Imaging

The unique acoustic properties of microbubbles lend themselves to contrast-specific forms of imaging. In the following section, these techniques have been organized based on the physical bubble response that each method is trying to exploit.

#### Digital Image Subtraction

The earliest form of microbubble imaging involved taking advantage of the high acoustic impedance mismatch between air and tissue. This leads to a time-dependent increase in the backscatter magnitude of B-mode ultrasound images as microbubbles gradually flow into the imaging plane. Quantification is performed with baseline image subtraction, where the enhanced B-mode frames taken from every time point of the cine loop are subtracted from an unenhanced reference image.

This technique is limited in its ability to produce meaningful vascular images [100]. There are inherent difficulties with frame-to-frame registration, and this processing is highly susceptible to tissue motion. As well, the nature of ultrasound image speckle lends variable texture to the image, meaning that an individual B-mode pixel may not enhance in a way that could be easily predicted. As such, other forms of microbubble signal processing are greatly preferred over this technique, however, they may not be available to some pre-clinical scanners (*e.g.* those with swept-scan transducers).

#### Second Harmonic Imaging

Harmonic imaging was one of the first techniques proposed to take advantage of the nonlinear scattering of microbubbles in response to sound waves. Acoustic waves are transmitted centered at a fundamental frequency,  $f_0$ , and the received signal is bandpass filtered at the second harmonic,  $2f_0$ . In principle, this should suppress all linear scattering from background tissues but retain the nonlinear response from microbubbles.

This form of processing must contend with a trade-off between contrast and imaging resolution. Any overlap in transmit and receive bandwidth leads to ambiguity as to the origin of the scattering. Reducing the transmit bandwidth, thereby limiting the overlap and increasing

the system specificity, will compromise the axial resolution of the contrast image.

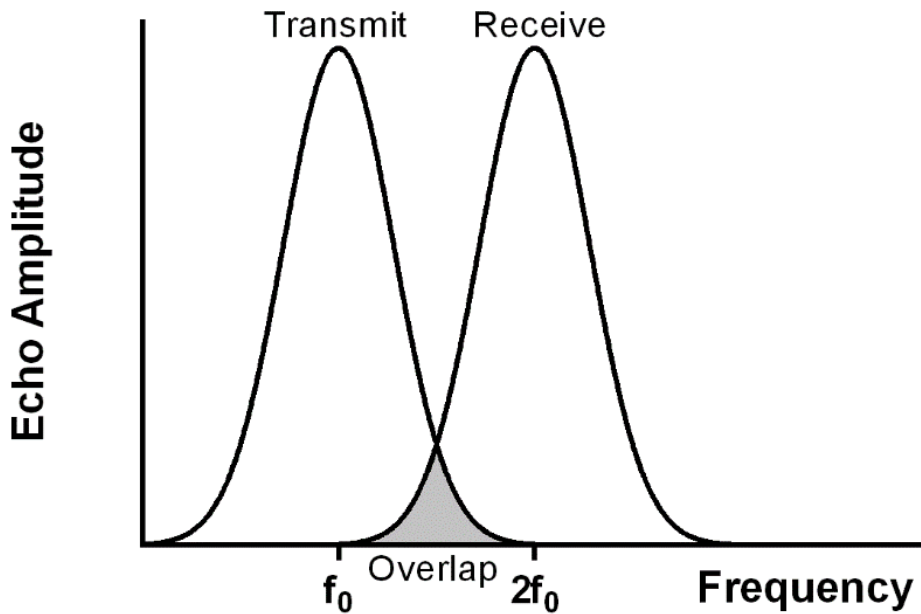


Figure 1.9: An example of a harmonic imaging bandwidth. The overlap of transmit and receive bandwidths leads to reduced specificity in microbubble imaging.

Other limitations of second harmonic imaging include large transducer bandwidth requirements. A transmit signal centered at  $f_0$  with a frequency range  $f_0 \pm B/2$  would require a receive frequency response that spans  $2f_0 \pm B$  to capture all reflected second harmonics. This leads to an exceptionally large passband of at least  $f_0 - B/2$  to  $2f_0 + B$ . Transmission efficiency is low when the transmit band is shifted close to the lower cutoff bound. Likewise, the shift of the receive filter to the upper cut off of the transducer's frequency response limits the sensitivity to nonlinear signals. This is further compounded with the unfavorable frequency dependent attenuation of the high-frequency (*i.e.* microbubble) components.

### Multi-pulse Processing

Multi-pulse processing was developed to alleviate many of the shortcomings of second harmonic imaging. Two or more pulses that differ in amplitude, phase, or both, are transmitted along the same line of sight. The assumption is that tissues will respond in a linear manner

to these modulations, allowing for a linear combination of the received echoes to suppress the non-contrast background. Any nonlinear scattering, ideally originating only from the microbubble contrast agent, will remain after the cancellation and thus yield a high contrast-to-tissue ratio.

### **Pulse Inversion**

Pulse inversion is a multi-pulse contrast-specific imaging technique that involves transmission of two pulses of equal amplitude but opposite phase in rapid succession [101]. The two scan lines are then shifted to align in time and summed together. This should result in the complete cancellation of tissue reflections, which are assumed to respond in a linear manner to the phase difference, but retain the even harmonics of nonlinear reflectors such as microbubbles. Nonlinear component separation [102], which assumes is that the received echo is a sum of nonlinear components, can be used to make an arithmetic prediction of a pulsing scheme with a  $180^\circ$  phase shift, yielding a contrast-specific image constructed from the summation of pulses:

$$f(p(t)) + f(-p(t)) = 2a_2p(t)^2 + 2a_4p(t)^4 + \dots \quad (1.3)$$

where  $p(t)$  is some arbitrary transmit waveform,  $f(p(t))$  is the pulse distortion on the received echo, and  $a_n$  are constants.

It should be noted that this retains all even harmonics of the transmitted pulse, with the suppression of all odd harmonics. This is shown diagrammatically below, in Figure 1.10. The limitations of this technique are similar to those found in second harmonic imaging, namely that a large transducer bandwidth is required to receive the reflected odd harmonics.

### **Amplitude Modulation**

Amplitude modulation is another pulsing scheme that is in some sense the complement of pulse inversion: the second pulse has the same phase as the first, but it differs in amplitude [103]. The received reflections from the lower amplitude pulse are linearly scaled to match the magnitude of the higher amplitude pulse. The two pulses are then subtracted from one another. Any tissue scattering should scale linearly with the amplitude change, so signals reflected from anatomical

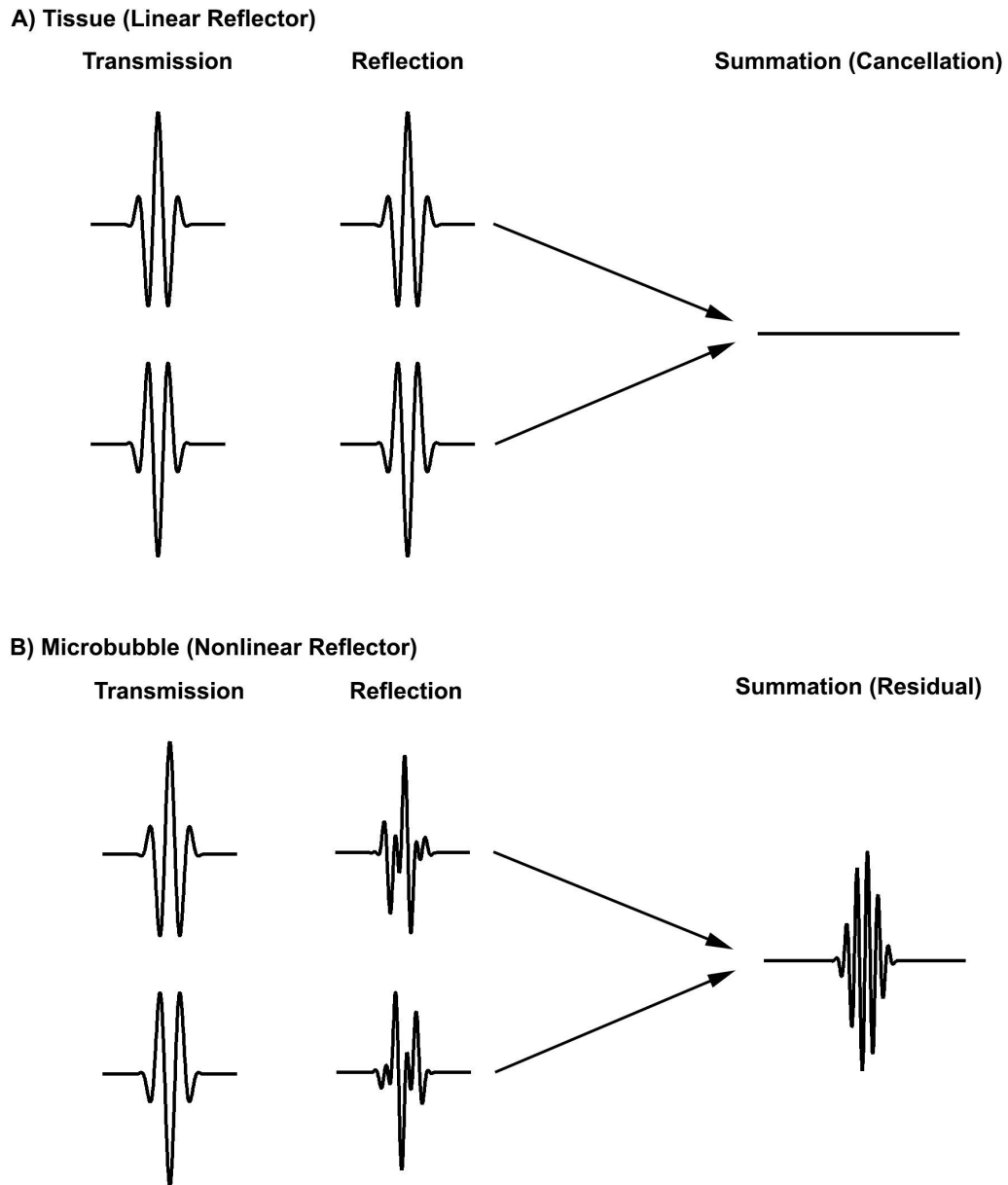


Figure 1.10: Diagrammatic example of wave form responses to pulse inversion processing.

structures will be suppressed in the subtraction. Microbubble contrast agents respond in a nonlinear fashion to the amplitude difference and thus are retained after the subtraction. A simple example of a  $\frac{1}{2}$  amplitude pulsing scheme with scaled subtraction of the two pulses:

$$f(2p(t)) - 2f(p(t)) = 2a_2p(t)^2 + 6a_3p(t)^3 + \dots \quad (1.4)$$

This example is further described below, in Figure 1.11, using a depiction of the wave form response to this processing.

It should be noted that Equation 1.4 demonstrates that amplitude modulation retains both the even and odd harmonics of the signal, and that the coefficients of the higher order components are of greater magnitude. Furthermore third order harmonic spectrum exhibits spectral foldback onto the transmit bandwidth (*i.e.* a peak centered at  $f_0$ ) [104]. It is expected then that amplitude modulated processing should outperform pulse inversion by circumventing the need for a broad transducer bandwidth, and by retaining more of the contrast-specific signal after processing.

### **Pulse Inverted Amplitude Modulation**

Pulse inverted amplitude modulation is a combination of the above two multi-pulse schemes [104]. Two pulses are fired in rapid succession along the same scan line that differ in both amplitude and phase. An example is shown below for a half phase shifted second pulse that is scaled by  $\frac{1}{2}$  amplitude, where the summation of these two pulses shows the most promising result out of the three multi-pulse methods:

$$f(2p(t)) - 2f(p(t)) = 2a_2p(t)^2 + 6a_3p(t)^3 + \dots \quad (1.5)$$

This form of processing should yield the most contrast signal by retaining the odd harmonics, as in amplitude modulation, with additional contribution from even harmonics. In practice pulse inverted amplitude modulation tends to have statistically similar performance to amplitude modulation [105].



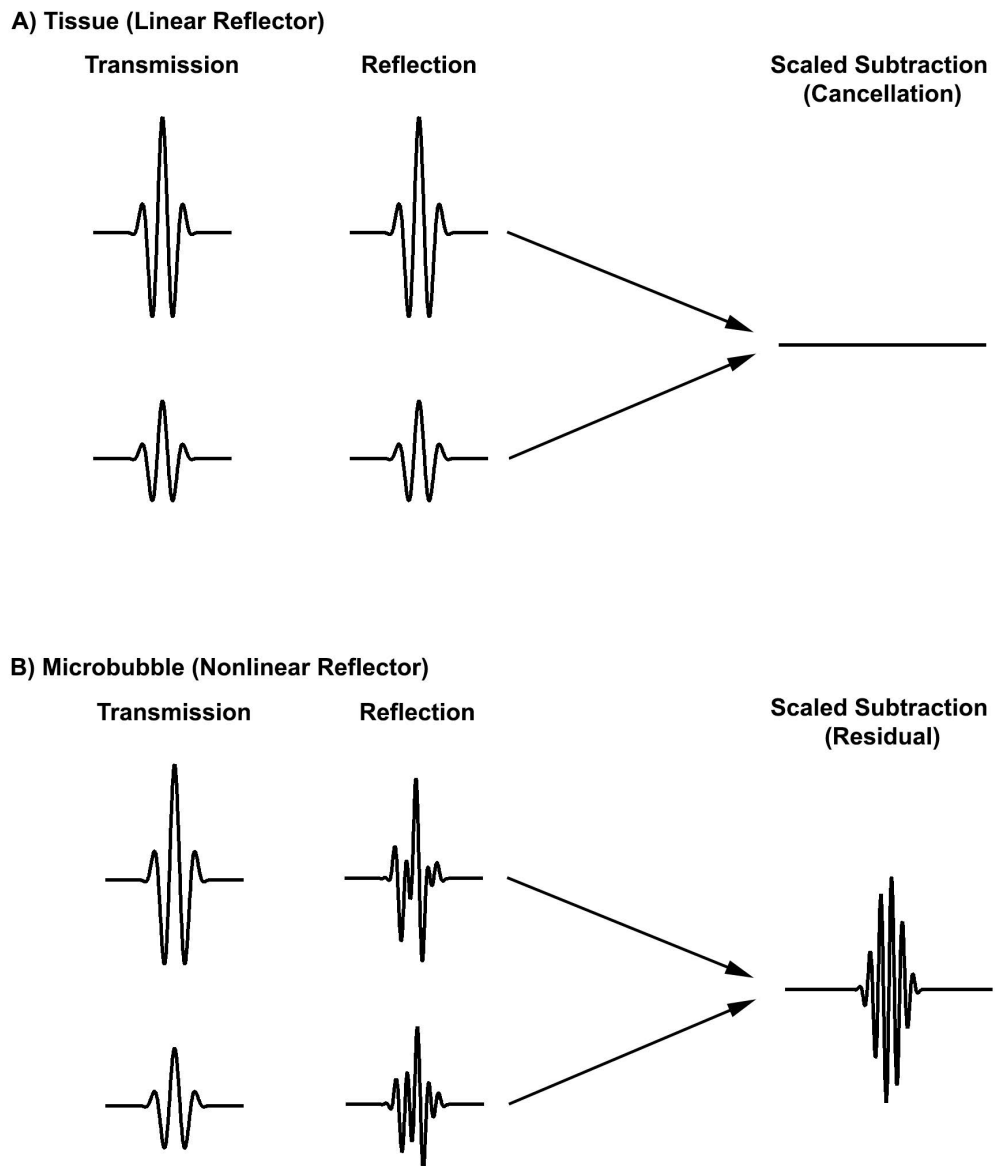


Figure 1.11: Diagrammatic example of wave form responses to amplitude modulation processing.

### **Burst Imaging**

As the name implies, burst imaging relies on the intentional cavitation of microbubbles within the imaging plane to enhance signal from vasculature. In current practice this is typically performed to salvage ambiguous Doppler examinations, a technique referred to as ‘Doppler Rescue’ [62]. The principle is straightforward, the shockwave released during the cavitation of microbubbles leads to high amplitude reflected echoes that are also temporally decorrelated. Some limitations of this technique include acoustic shadowing, flash artefacts, signal saturation, and the transient nature of the enhancement.

### **1.4.5 Indicator Dilution Theory**

Indicator dilution methods work on the assumption that the kinematics of an imaged intravascular tracer should reflect the physiology of local blood circulation. Dispersion of the indicator, through branching vascular architecture, Brownian motion, or turbulence, will lead to tracer particles traversing the imaging plane at different time points. As such, the indicator dilution curve is often interpreted as the probability density function of the indicator transit times of the microvasculature. Relating the dynamics of indicator dilution to physiological features relies on several assumptions for both model-free perfusion metrics, as well as model-based hemodynamic indices.

In CEUS imaging, the instantaneous microbubble concentration, or mass of indicator, is unknown. Instead, analysis is performed on the backscatter intensity  $I(t)$  of the contrast signal with the assumption that there is a linear relationship between the number of microbubbles in the imaging plane and the intensity [106]. This means that all perfusion indices are relative measures of blood kinematics. The Stewart-Hamilton relations [107] provide estimates of the volumetric blood flow rate ( $F$ ) and the blood volume ( $V$ ), with no assumption on the shape of the indicator-dilution curve:

$$F = C \cdot (AUC)^{-1} \quad (1.6)$$

$$V = F \cdot MTT \quad (1.7)$$

where  $C$  is the amount of indicator in the bolus injection,  $AUC$  is the area under the indicator-dilution curve, and  $MTT$  is the mean transit time through the imaging cross-section. To ensure that different curves can be directly compared, the amount and concentration of the injected microbubble solution (*i.e.*  $C$ ) must be kept constant.

There are two main techniques for supplying microbubbles (the tracer) in CEUS imaging. The first is an intravenous injection of a bolus of microbubbles, equivalent to the conventional dosing techniques of contrast-enhanced CT or contrast-enhanced MRI. The second technique, referred to as destruction reperfusion imaging [69], is unique to CEUS. Destruction-reperfusion involves the use of temporary high-energy acoustic waves to ‘burst’ all microbubbles within the imaging volume. This creates what is effectively a negative bolus of indicator. Each technique has its own advantages and disadvantages. These two methods require different kinematic models to capture and explain their time-intensity characteristics.

#### 1.4.6 Common Kinematic Models for Bolus Enhancement

Bolus enhancement describes the technique where a large amount of indicator is injected ‘instantaneously’ into the venous system, producing a delta function for the system input. It is much simpler to implement than destruction-reperfusion techniques as it avoids the complexities involved with constant infusion, such as the set-up of catheterization, surgical tubing, controlled constant flow rates, and agitation of the indicator to maintain a constant injection concentration. Also, a single bolus injection requires less total indicator and set-up time than constant infusion.

However, it has several limitations that reduce its applicability to quantitative imaging. A true bolus injection is not physiologically plausible, especially when considering the small time scale of contrast-ultrasound imaging. The path of indicator through the circulatory system prior to entering the imaging plane convolves the delta input with a more complicated function, representing cardio-pulmonary transit, that is unknown (see Figure 1.12). This greatly reduces the reproducibility of the technique, and limits the physiological interpretation of indicator dilution metrics. Furthermore, repeated bolus imaging of the same imaging ROI requires full clearance of the indicator, a process that can take hours.

Despite the above limitations bolus imaging is still useful for clinical and pre-clinical imag-

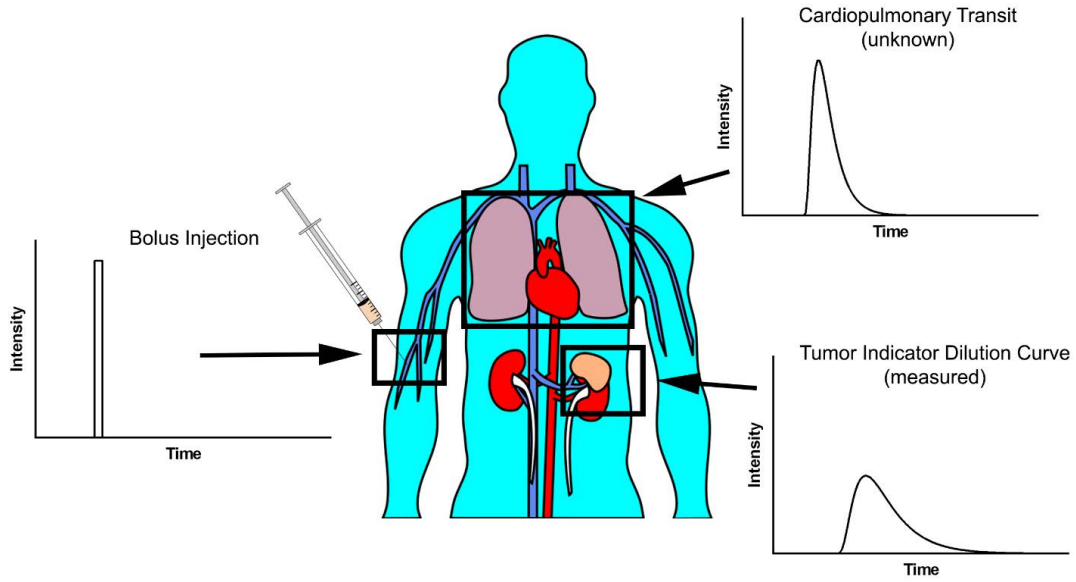


Figure 1.12: Diagrammatic example of bolus injection. The initial delta function becomes spread out by transit through the circulatory system prior to entering the imaging plane.

ing. It is also the more popular technique for clinical contrast agent administration. The rest of this section is a brief description of the indicator dilution models commonly used in bolus CEUS imaging, adapted from [108]. This thesis uses the Gamma Variate Function in Chapter 2, and the Diffusion with Drift Model in Chapter 3.

### Lognormal Function

The lognormal distribution is a widely used density function describing several phenomenon in biological sciences [109, 110]. The application of the lognormal function to biological phenomenon is usually an empirical fit with little physiological justification, but for vascular networks the lognormal distribution is drawn readily if it is assumed that an arbitrary vascular tree will exhibit a fractal branching geometry [111]. The lognormal indicator dilution model, first introduced to CEUS by [112], is as follows:

$$I(t) = \frac{AUC}{\sqrt{2\pi}\sigma(t-t_0)} e^{-((\ln(t-t_0)-\mu)^2)/(2\sigma^2)} + I_0 \quad (1.8)$$

where the parameters  $\mu$  and  $\sigma$  are the mean and standard deviation of the random variable's logarithm. The two constants  $t_0$  and  $I_0$  are time and intensity offsets, respectively, to fit ex-

perimental data to the assumptions of the theoretical model. The time offset represents the estimated bolus arrival time; this value can be set to zero by truncating the data. The signal intensity offset is the baseline signal intensity caused by acquisition noise and incomplete cancellation of the tissue signal.

### Gamma Variate Function

The gamma variate probability density function arises from an extension of the Erlang distribution. The assumption of the model is that blood flow is comprised of  $n$  homogeneous mixing chambers of equal volume that are connected in series [113]. Blood, or indicator, flow is unidirectional from one compartment to the next, with each compartment having only one input and one output. For a one compartment system, this model simplifies to a mono-exponential wash-out. If the constraint on an integer number of compartments is relaxed, then the gamma variate function can be extracted [114]:

$$I(t) = \frac{AUC}{\beta_v^{\alpha_v+1} \Gamma(\alpha_v + 1)} (t - t_0)^{\alpha_v} e^{-(t-t_0)/\beta_v} + I_0 \quad (1.9)$$

where  $\alpha_v \equiv n - 1$ ,  $\beta_v = \frac{V}{nF}$  is the time constant of a single compartment, and  $\Gamma(x) = (x - 1)!$ .

The gamma variate model is widely used in CEUS, and other perfusion modalities, owing to its simplicity relative to other indicator dilution models. However, a criticism of the standard gamma variate formulation is that the relationship between curve shape and the governing parameters is unintuitive. Thus, the simplified gamma variate function was introduced as a reformulation of the standard gamma variate function where there is no coupling between the parameters [115]:

$$I(t) = I_{max} t'^{\alpha_v} e^{\alpha_v(1-t')} + I_0. \quad (1.10)$$

where  $\alpha_v$  is a curve shape parameter,  $I_{max}$  is the peak signal intensity,  $T_{max}$  is the time point when  $I(t) = I_{max}$ , and  $t' = t/T_{max}$ .

### Diffusion with Drift Model

The diffusion with drift model considers the transit of indicator to be dependent on both diffusion and convection:

$$\frac{\partial C(x, t)}{\partial t} = D \frac{\partial^2 C(x, t)}{\partial x^2} - v \frac{\partial C(x, t)}{\partial x}, \quad (1.11)$$

where  $C(x, t)$  is the concentration of indicator at location  $x$  and time  $t$ ,  $D$  is a coefficient of effective longitudinal diffusion, and  $v$  is the blood velocity. The parameter  $D$  is an umbrella variable that represents the contributions of many unknown physical mechanisms (*e.g.* turbulent blood flow, vascular bed topography, etc.).

Equation 1.11 was solved [116] for an impulse bolus injection, with no special boundary conditions at the outlet, to obtain the local density random walk model (LDRW):

$$I(t) = AUC \left( \frac{e^\lambda}{\mu} \right) \sqrt{\frac{\mu}{t-t_0}} \frac{\lambda}{2\pi} \exp \left[ -\frac{\lambda}{2} \left( \frac{\mu}{t-t_0} + \frac{t-t_0}{\mu} \right) \right] + I_0 \quad (1.12)$$

where  $\mu$  is the mean transit time of indicator,  $\lambda$  is inversely proportional to the skewness of the curve,  $t_0$  is a time delay before wash-in occurs, and  $I_0$  is an intensity offset.

### The Lagged Normal Function

The first group to propose the lagged normal function as an indicator dilution model [117] considered the idealized case where a single large artery flows into a capillary bed. The large vessel was characterized by a Gaussian dispersion of tracer transit times, and the capillary bed was a homogenous mixing chamber characterized by an exponential function. Mathematically, the model is a convolution of a Gaussian density function,  $f(\tau)$ , with one or more exponential density functions,  $g(t - \tau)$ :

$$I(t) = \int_{-\infty}^t f(\tau) g(t - \tau) d\tau \quad (1.13)$$

where the density functions are defined below:

$$f(t) = \frac{1}{\sqrt{2\pi\sigma^2}} e^{-(t-\mu)^2/(2\sigma^2)}, \quad -\infty < t < \infty \quad (1.14)$$

$$g(t) = \lambda e^{-\lambda t}, \quad t \geq 0 \quad (1.15)$$

The compartment represented by the Gaussian distribution has a *MTT* of  $\mu$ , and a transit time variance of  $\sigma^2$ . The mixing compartment only has a rate constant parameter,  $\lambda$ . It has been demonstrated [118] that the lagged-normal indicator-dilution model can be represented by:

$$I(t) = \frac{AUC}{2} K [1 + \text{erf}(L)] + I_0 \quad (1.16)$$

where  $\text{erf}()$  is the error function, and

$$K = \lambda \exp[-\lambda t + \lambda\mu + \frac{1}{2}\lambda^2\sigma^2], \quad L = \frac{t - \mu - \lambda\sigma^2}{(2\sigma^2)^{1/2}} \quad (1.17)$$

### Comparison of Indicator-dilution Models for Bolus CEUS Imaging

The differences between the models can be roughly summarized by the characteristics of the initial wash-in phase and the shape of the curve tail during wash-out (see Figure 1.13). The general consensus is that the local density random walk model has superior fitting performance for bolus wash-in images [108].

#### 1.4.7 Common Kinematic Models for Destruction Reperfusion

The observation that microbubbles will cavitate under high acoustic pressures led to the development of a novel method to quantify blood perfusion, known as destruction-reperfusion, or disruption-replenishment. This technique, introduced by Wei *et al.* in 1998 [69], is unique to contrast-enhanced ultrasound. Instead of relying on an intravenous bolus injection of contrast agent washing into the imaging plane, destruction-reperfusion uses a constant infusion of microbubbles into systemic circulation and implements a high-energy ultrasound pulse to induce the complete destruction of all indicator within an acoustic window. This creates what is

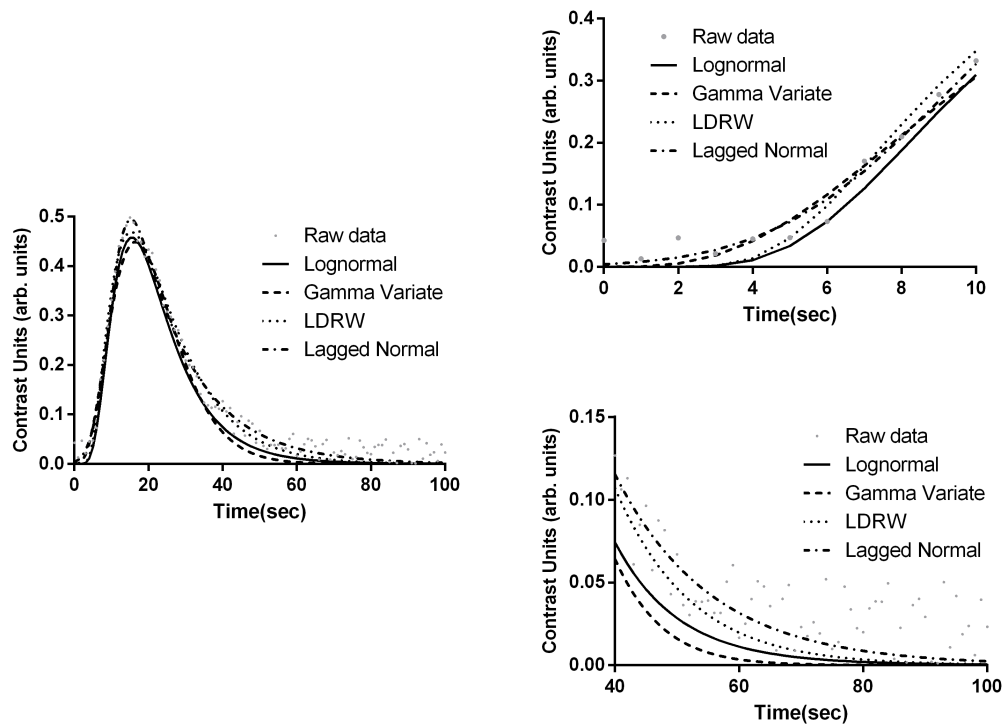


Figure 1.13: Example of the four indicator dilution models fitted to the same raw dataset. The raw data points were synthetically produced by adding random noise to a lognormal wash-in curve.



effectively a ‘negative’ bolus for indicator-dilution analysis. A diagram depicting destruction-reperfusion can be found in Figure 1.14.

This technique has several advantages over conventional tracer-based methods, particularly that the input kinetics into the indicator-dilution model are greatly simplified and that the technique is repeatable either within the same imaging plane (to gauge measurement error and reproducibility) or across multiple imaging planes in the organ of interest (to give a more global measurement of perfusion). In bolus imaging, the delta function of an instantaneous injection is first convolved by an unknown density function representing the vasculature of cardio-pulmonary passage before entering the imaging plane (Figure 1.12). Destruction-reperfusion imaging, however, only depends on the blood flow of vasculature that is adjacent to the imaging plane (Figure 1.14).

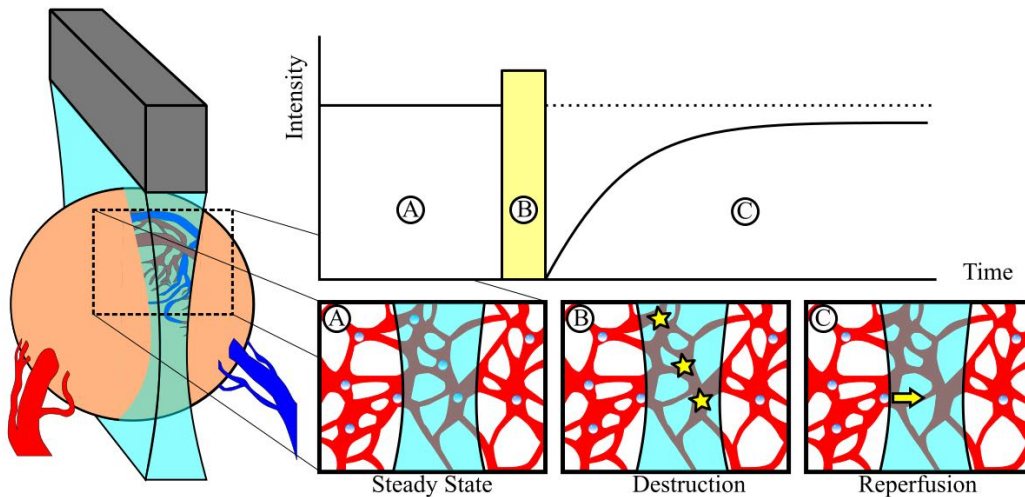


Figure 1.14: Illustrative representation of destruction-reperfusion imaging. Microbubbles are administered via a constant infusion, yielding a steady-state of indicator transit (panel A). In (B) a high-energy ultrasound pulse bursts all of the microbubbles in the imaging plane. The contrast agent is then allowed to reperfuse into the vasculature in (C).

The rest of this section introduces some of the common indicator-dilution models used to quantify perfusion data acquired with destruction-reperfusion techniques. The simplified input kinetics, relative to bolus imaging, has allowed for the inclusion of ultrasound acquisition parameters in the more complex destruction-reperfusion models. This, in turn, has led to improved perfusion quantification accuracy and repeatability over conventional bolus techniques.

This thesis uses the mono-exponential kinematic model to characterize destruction-reperfusion cine loops in Chapters 4 and 5. This model was selected because the kinematics of the statistical parameters are difficult to predict, and it's currently unclear how ultrasound beam geometry affects the time course of the speckle model.

### **Mono-exponential Kinematic Model**

The most commonly used destruction-reperfusion model is a mono-exponential fit, proposed by Wei *et al.* [69], that represents microbubble circulation as a perfect mixing chamber of blood in tissue.

$$I(t) = I_{max}(1 - e^{-\lambda t}) \quad (1.18)$$

where the maximum signal intensity,  $I_{max}$ , is interpreted as the relative blood volume and the parameter  $\lambda$  is the mean flow velocity in the imaging region of interest. The product  $I_{max} \times \lambda$ , equivalent to the slope at time zero, is an estimate of the flow rate.

This model's popularity is owed primarily to its simplicity and the ease and robustness of fitting the parameters to the model. However, its major criticisms are that it is not a realistic model of tissue perfusion and the reproducibility of the parameters is low.

### **Krix's Multivessel Model**

In 2003 Krix *et al.* proposed a multivessel model [119], based on a three-dimensional distribution of vessel velocities and blood flow angles, to address the concerns raised about the physiological interpretation of a mono-exponential fit. The multivessel model is a piecewise-defined function, comprised of two sub-functions applied with an interval boundary at the two-thirds maximum intensity time-point. The initial phase of reperfusion is modeled by a linear equation with a slope  $m_{krix}$ :

$$m_{krix} = \frac{I_{2/3max}}{t_{2/3}} \quad (1.19)$$

where  $t_{2/3}$  is the time at which  $I = (2/3)I_{max}$ . The mean velocity in the model is calculated as:

$$\bar{v} = d \cdot \frac{m_{krix}}{I_{2/3max}} \quad (1.20)$$

where  $d$  is the width of the ultrasound beam in the elevation plane. After the two-thirds intensity time-point, the intensity signal is modeled as:

$$I(t) = I_{max} \cdot \left(1 - \frac{d^2}{3(\bar{v} \cdot t)^2}\right) \quad (1.21)$$

### Arditi's Perfusion Model

In 2006 Arditi *et al.* [120] developed one of the first perfusion models that considers the influence of ultrasound acquisition in addition to a realistic microvascular model. The authors chose a Gaussian function as a transmit/receive sensitivity distribution and a lognormal distribution to model blood flow. The Arditi perfusion model is as follows:

$$I(t) = I_{max} \int_0^{\infty} PD(\tau) \cdot perf\left(1.94 \frac{KD_e}{2\tau}(t - \tau)\right) d\tau \quad (1.22)$$

where  $PD$  is a probability density function of flow transit times,  $K$  is a transmit-receive parameter,  $D_e$  is the extent of microbubble destruction in the elevational direction,  $\tau$  is flow transit time, and  $perf$  is a function defined as:

$$perf(q) = 0.5 \cdot (1 + erf(q)) \quad (1.23)$$

The distribution of transit times was assumed to follow a lognormal probability density function:

$$PD(\tau) = \frac{1}{\sqrt{2\pi}\sigma\tau} e^{-([\ln(\tau)-\mu]^2)/(2\sigma^2)} \quad (1.24)$$

where  $\mu$  and  $\sigma^2$  are the mean and variance of the distribution of the natural logarithm of transit times.

### Hudson's Lognormal Perfusion Model

Much like the above Arditi model, Hudson's perfusion model also accounts for ultrasound beam geometry in addition to a physiologically plausible model of blood perfusion [121]. It is a generalized model that is composed of two independent functions, an 'ultrasound beam' component  $B(y, z)$  and a 'blood flow' component  $F(z, t)$ . The model is outlined below:

$$I(t) = \int_V B(y, z) \cdot F(z, t) dV \quad (1.25)$$

where the  $z$ -coordinate is distance in the elevational direction and the  $y$ -coordinate is imaging depth. The main differences from the Arditi model are the ability to account for the non-uniformity of microbubble destruction and sensitivity in the ultrasound beam geometry, and the distinction between the boundaries of microbubble destruction and microbubble detection. Furthermore, the beam geometry is modeled as a  $\text{sinc}^2$  function, as opposed to a Gaussian distribution:

$$B(y, z) = \text{sinc}^2 \left( \frac{2z}{BW(y)} - \frac{2BS(y) + BW(y)}{BW(y)} \right) \cdot \Pi(y, z) \quad (1.26)$$

where  $BW(y)$  is a 'beam width' function representing the elevational sampling size at some imaging depth ' $y$ ',  $BS(y)$  is a 'beam separation' function to account for the difference between the boundaries of microbubble destruction and detection, and  $\Pi(y, z)$  is a rectangular window. The 'blood flow' component is modeled as a lognormal distribution of flow velocities:

$$F(z, t) = \frac{A_C}{2} \cdot \text{erfc} \left( \frac{\ln(v) - \mu_f}{\sigma_f \sqrt{2}} \right) \quad (1.27)$$

where  $A_C$  is the total vascular cross-section,  $v$  is velocity,  $\text{erfc}$  is the complementary error function, and  $\mu_f$  and  $\sigma_f$  are the mean and standard deviation of the natural logarithms of velocity, respectively.

### Comparison of Models for Destruction-Reperfusion CEUS Imaging

Each of the above destruction-reperfusion models represent a trade-off between ease of implementation and power of physiological interpretation. The mono-exponential fit is the simplest

model, one that will fit practically any dataset, but has the worst reproducibility and poorly represents vessel physiology. The models that account for ultrasound beam geometry more precisely capture the sigmoidal wash-in shape of indicator, and exhibit superior reproducibility and physiological interpretation, but are often prohibitively complicated to implement in most clinical settings. The differences between wash-in shape captured by the model can be seen in Figure 1.15.

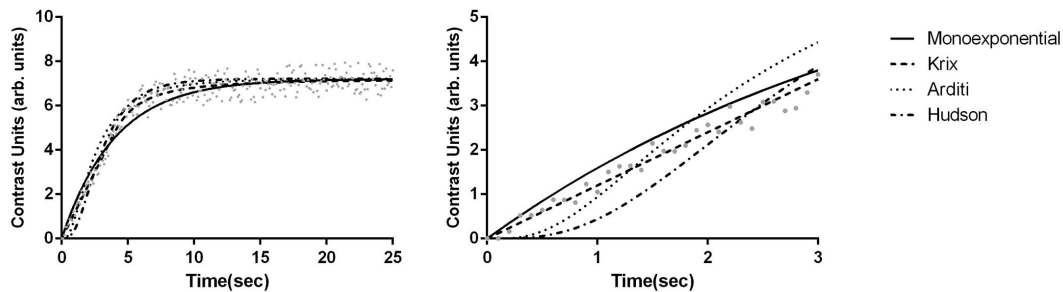


Figure 1.15: Example of the four destruction-reperfusion models fitted to the same raw dataset. The raw data points were synthetically produced by adding random noise to a monoexponential wash-in curve.

## 1.5 Overview of Speckle Statistics

Speckle is a signal intensity pattern that manifests in all coherent imaging techniques including, but not limited to, confocal laser scanning microscopy, radar, optical coherence tomography, and medical ultrasound. This section concerns specifically the statistical nature and physical interpretations of speckle in acoustic imaging for medical ultrasound, but can be generalized to most forms of speckle phenomena.

The substructure of almost all acoustically scattering materials consists of a collection of randomly distributed sub-resolution scatterers. Ultrasound signals received from these scattering materials will consist of many coherent wave components, each reflected off a different sub-resolution scatterer. The result is a granular or mottled intensity pattern to the image due to the interference of the randomly phased coherent wave components. The position and magnitude of an individual speckle cell is unpredictable *a priori*, however the speckle texture follows a well-defined probability density function.

To define these distributions, and the situations in which they arise, we must first introduce phasors (Equation 1.28) a complex number representing the amplitude and phase of a sinusoidal wave.

$$ae^{\pm j(\omega t + \phi)} = a \cos(\omega t + \phi) \pm j a \sin(\omega t + \phi) \quad (1.28)$$

We can simplify this notation by considering only the scattering of a single frequency, removing the need for the inclusion of the  $\omega$  component, so that the phasor notation becomes  $ae^{j\phi}$ . A monotone wave disturbance, for example the scattering of an incident sound wave by an individual sub-resolution scatterer, can be represented using this phasor notation. Thus, the result of ultrasound scattering from many small independent scatterers is the complex addition of many small independent phasors - a random phasor sum. This random phasor sum can be conceptualized as a random walk on the complex plane.

In the following sections, we will consider some commonly encountered distributions of scatterers, along with their corresponding speckle probability density functions. This thesis builds upon the models presented here, which describe the statistics of B-mode images, and applies them to scattering from CEUS cine loops. In the context of this thesis, the backscatter signal intensity of microbubbles flowing through vasculature is seen as roughly analogous to that arising from randomly distributed sub-resolution scatterers at a high concentration. We will first consider the case of fully developed speckle.

### 1.5.1 Fully Developed Speckle

#### No Coherent Component (Rayleigh)

The derivation in this section is taken from [122], which first considered the case involving many scatterers with no periodicity in their location (coherent signal). We assume that there are a large number of scatterers per resolution cell, that the medium is homogeneous, the scatterers are randomly distributed, and that the region being imaged is distant from the transducer of the ultrasound system. From this we can state that the amplitude and phase of each elementary phasor (those reflected from a sub-resolution scatterer) are statistically independent from one another. The signal from this homogenous material is then a sum of  $N$  complex phasors [123,

124], with the  $k$ th phasor having a random length  $\alpha_k / \sqrt{N}$  and random phase  $\phi_k$ .

$$ae^{j\phi} = \frac{1}{\sqrt{N}} \sum_{k=1}^N \alpha_k e^{j\phi_k} \quad (1.29)$$

This random phasor sum can be conceptualized as a random walk on the imaginary plane, originating from the origin. We further assume that the lengths  $\alpha_k$  are identically distributed for all  $k$ , and that the phases  $\phi_k$  are uniformly distributed on  $(-\pi, \pi)$ .

By the central limit theorem, as  $N \rightarrow \infty$  the probability density functions of the real,  $r$ , and imaginary,  $i$ , components are Gaussian. We've also assumed that the real and imaginary components are uncorrelated and statistically independent. Therefore, the joint probability density function of the random phasor sum is the two-dimensional Gaussian:

$$P(r, i | \sigma^2) = \frac{1}{2\pi\sigma^2} e^{-\left(\frac{r^2+i^2}{2\sigma^2}\right)} \quad (1.30)$$

The probability density function of the length of the random phasor sum  $a = \sqrt{r^2 + i^2}$ , which is equivalent to the signal magnitude measured by an ultrasound transducer, is the Rayleigh distribution:

$$P(a | \sigma_R) = \frac{a}{\sigma_R^2} e^{-\frac{a^2}{2\sigma_R^2}}, a \geq 0 \quad (1.31)$$

where  $a$  is the echo amplitude and  $\sigma_R$  is the scale parameter of the distribution.

## 1.5.2 Non-Rayleigh Speckle

### No Coherent Component (K-Distribution)

We will now consider the case where either the number of scatterers per resolution cell is low, or the scattering cross-sections of the scatterers are different from one another, or both. This invalidates the assumption of a large number of independent identically distributed scatterers in the medium. The echo envelope from a variable density of random scatterers, with no coherent component to the signal, has been shown to follow a K-distribution [125, 126]:

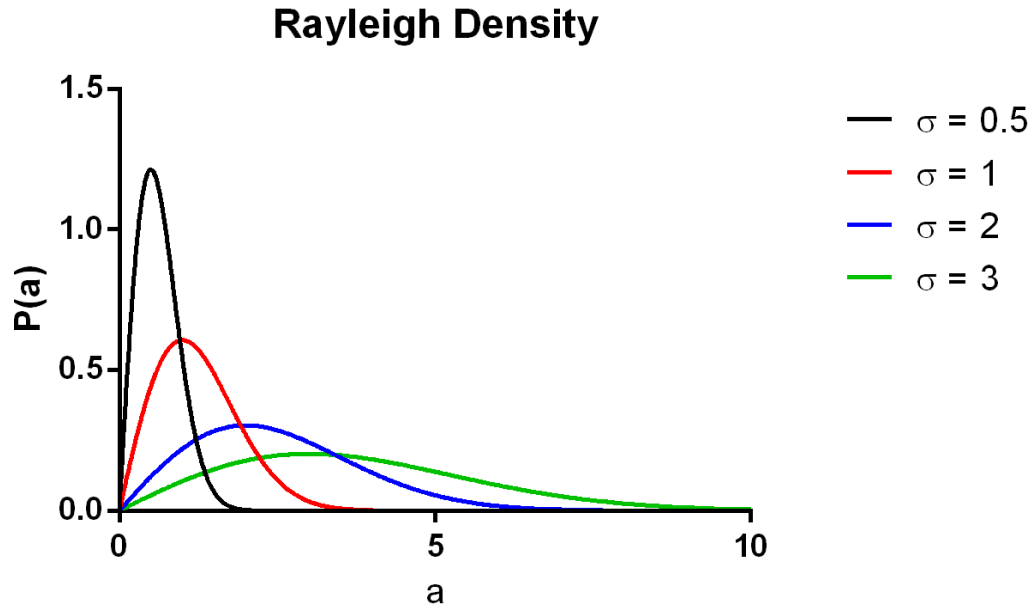


Figure 1.16: Graph of the Rayleigh probability density function, which is fully defined by single scaling parameter. The signal-to-noise ratio (SNR) of Rayleigh-distributed speckle will be approximately 1.91. SNR is calculated from the ratio of  $\bar{a}/\sigma_R$ , which is constant in the Rayleigh distribution.

$$P(a|M, \sigma_{sc}^2) = \frac{4a^M}{(2\sigma_{sc}^2)^{\frac{M+1}{2}} \Gamma(M)} K_{M-1} \left( \sqrt{\frac{2}{\sigma_{sc}^2}} a \right), M > 0, \sigma_{sc} > 0 \quad (1.32)$$

where  $K_z$  is the modified Bessel function of the second kind with order  $z$ ,  $\Gamma(z)$  is the gamma function,  $a$  is echo amplitude,  $M$  is a parameter representing the effective density of the scatterers, and  $\sigma_{sc}$  represents the effective cross section of the scatterers. When the scatterer density  $M \rightarrow \infty$  the K-distribution becomes the Rayleigh distribution.

This model was first applied to ultrasound imaging by Shankar *et al.* [127] where the parameter  $M$  was viewed as the density of scatterers (*i.e.* the number of scatterers per resolution cell) multiplied by a coefficient that depends on the scanning parameters, geometry, and the backscatter coefficient statistics.

### Coherent Component (Homodyned K-Distribution)

The case of a variable effective density of scatterers with a coherent signal component (*i.e.* periodically located scatterers) can be accounted for using the homodyned K-distribution [126,



128]. This probability density function does not have a closed form expression, so it is represented in terms of the improper integral:

$$P(a|M, s_c, \sigma_e) = a \int_0^{\infty} x I_0(s_c x) I_0(ax) \left(1 + \frac{x^2 \sigma_e^2}{2M}\right)^{-M} dx \quad (1.33)$$

where  $I_0(z)$  is the modified Bessel function of the first kind with order zero,  $a$  is echo amplitude,  $s_c^2$  is the coherent signal energy,  $\sigma_e^2$  is the diffuse signal energy, and  $M$  is the effective density of the scatterers.

The K-distribution is a special case of the homodyned K-distribution (when  $s_c = 0$ ). When the effective density of scatterers  $M$  approaches infinity the homodyned K-distribution becomes the Rician distribution [123, 124]. Equivalently, if there is no coherent component and a very high number of effective scatterers per resolution cell, then the homodyned K-distribution approaches the Rayleigh distribution.

The homodyned K-distribution is a three-parameter compound representation of a Rician distribution (2 parameters) modulated by a gamma distribution (1 parameter). Despite representing a wide range of scattering conditions, the use of this distribution to describe speckle is limited, owing to its complex analytic formulation and the computational difficulty in generating estimates of the governing parameters. This limitation led to the introduction of the Nakagami distribution as a simplified approximation to the homodyned K-distribution for ultrasound speckle [129].

### **Approximation to the Homodyned K-distribution (Nakagami)**

The Nakagami distribution is a relatively new distribution, being formulated in 1960 as a model for fading in long-distance high-frequency radio wave propagation [130]. The Nakagami distribution has been applied to many wave related phenomena including medical ultrasound, wireless communication, and meteorology. It was introduced as an empirical model of ultrasound speckle by Shankar [129] with the justification that it approximates the homodyned K-distribution. It is currently the most commonly used model for ultrasonic tissue characterization [131]. The Nakagami distribution has the following probability density function:

$$f(|s|; m, \Omega) = \frac{2m^m}{\Gamma(m)\Omega^m} |s|^{2m-1} e^{-\frac{m}{\Omega}|s|^2}, \quad (1.34)$$

where the shape parameter,  $m$ , and the scale parameter,  $\Omega$ , can be estimated from the moments of the envelope:

$$m = \frac{E^2[a^2]}{Var[a^2]}, \quad \Omega = E[a^2] \quad (1.35)$$

The shape parameter  $m$  was found to be able to separate different scattering conditions, with an  $m < 0.5$  representing a low scatterer density, the density function is pre-Rayleigh for  $0.5 < m < 1$ , Rayleigh for  $m = 1$ , and Rician for  $m > 1$ . In the absence of regularly spaced scatterers,  $m$  can be thought of as a clustering parameter that increases with increasing scatterer density. The scale parameter  $\Omega$  is a measure of the average power.

## 1.6 Challenges in Contrast Enhanced Ultrasound

### 1.6.1 Frame-to-frame Variability due to Subject Motion can mask Contrast Perfusion

Motion artifacts (respiratory motion, subject movement, tissue deformation) lead to erratic microbubble sampling that alters the shape of the wash-in curve and interferes with the ability to extract perfusion parameters and quantify blood flow [132]. There are a number of motion correction algorithms that have been successfully applied to CEUS cine loops to account for in-plane tissue rotation and translation [132, 133]. However, out-of-plane motion produces unpredictable tissue sampling that is often impossible to correct for with two-dimensional imaging.

### 1.6.2 Preclinical CEUS Processing Techniques can be Highly Susceptible to Motion Artifacts

A frequently used form of CEUS processing in the preclinical setting is digital image subtraction, where a baseline image is formed by averaging a short cine loop of unenhanced frames.

This baseline image is then subtracted from all subsequent enhanced frames to reveal regions of contrast infiltration. Unfortunately, this processing is highly susceptible to registration errors and motion artifacts [134], which lead to reduced contrast-to-tissue ratios [135] in small animal imaging. Chapter 2 of this thesis is focused on developing a new technique for preclinical B-mode CEUS quantification that does not rely on an image subtraction step, as many preclinical scanners do not have access to the multi-pulse ‘contrast-specific’ techniques outlined in Section 1.4.4.

### **1.6.3 CEUS uses 2-D Sampling to Measure Perfusion in a 3-D Vascular Network**

The most common current CEUS practice involves the measurement of an indicator-dilution curve through a 2-D cross-section of the organ or tumor of interest. Two-dimensional sampling of a 3-D vascular network may not reflect the overall physiology within the organ, particularly in heterogeneous vasculature, and is susceptible to bias in the selection of the imaging plane [136, 137]. This may negatively impact both the accuracy and reproducibility of perfusion indices drawn using CEUS as the perfusion indices will depend on the variable transducer placement and tissue movement. This challenge is most pronounced in longitudinal studies.

### **1.6.4 The Relationship between Microbubble Concentration and Contrast Signal is Complex and Multifactorial**

The received echo intensity from a CEUS acquisition depends on an interplay of microbubble specific components (microbubble concentration, size distribution, shell composition, and gas contents), ultrasound acquisition and transmission settings (transmit/receive frequency, transmit pressure, receiver gain, and frame rate), and underlying physiology (nonlinear propagation, tissue attenuation, blood flow, volume, and perfusion). All of these factors undermine the method’s reproducibility and ability to measure the physiology of interest [134, 138].

### **1.6.5 Contrast Perfusion in Heterogeneous Vascular Networks (*e.g.* tumors) may be Poorly Represented by Point Estimates of Mean Contrast Intensity**

The conventional technique for CEUS perfusion quantification involves fitting an indicator-dilution model to point estimates of the mean contrast signal intensity over time. These estimates are taken from an ROI that surrounds the cross-section of the organ/tumor of interest. This discounts additional perfusion information that may be available from the temporal, and spatial, enhancement heterogeneity that occurs during indicator wash-in. Several groups have applied additional image processing and analysis to CEUS cine loops to assess tumor perfusion heterogeneity, as discussed in Chapter 3 of this thesis.

### **1.6.6 Signal Processing can Alter Indicator-Dilution Curve Shape and Interpretation**

The indicator-dilution curve shape, and corresponding perfusion indices, depend on the signal processing that occurs to convert microbubble acoustic intensity into image pixel values. In conventional CEUS processing, this is done under the assumption that there is a linear relationship between the number of microbubbles in the imaging plane and the backscatter intensity [106]. Even when this assumption holds true, intensity scaled perfusion indices, such as peak intensity and area-under-curve, will depend on the dynamic range and gain of scan conversion [139]. This issue is exacerbated if images undergo log-compression.

This challenge is of particular interest for this thesis as we are attempting to develop new variables, extracted via CEUS image analysis, to plot onto indicator dilution curves.

## **1.7 Hypothesis and Objectives**

The overall hypotheses of this thesis are that analyzing the first-order speckle statistics of CEUS images can provide more robust perfusion indices over conventional techniques, and allows for the quantification of the perfusion heterogeneity in tumor cross-sections. We posit that

the first-order statistics of speckle in contrast-enhanced ultrasound images can be understood and analyzed using the same models and tools used in literature for B-mode scattering. The long-term goal of this work is to improve the microvascular quantification of pre-clinical anti-angiogenic agent trials. To achieve this research goal, this thesis has been divided into the following four specific technical objectives:

1. Develop and evaluate, by comparison with nonlinear CEUS acquisition, a linear processing approach that uses the first-order speckle statistics of B-mode cine loops to quantify tumor vascular perfusion in a pre-clinical mouse model.
2. Develop a second-generation model, that expands on the one outlined above, that can be applied to nonlinear (two-pulse amplitude-modulated) CEUS images. This objective is necessary to improve the potential clinical applicability of the technique.
3. Improve the clinical translation of pre-clinical anti-angiogenic trials by developing a CEUS imaging protocol for an ultrafast patient-derived xenograft (PDX) model of RCC in chicken embryos to screen for patient-specific drug resistance(s). Assess intratumoral functional heterogeneity by producing drug sensitivity matrices from multiple core biopsies within the same tumor.
4. Apply the statistical CEUS analysis technique developed in objective 2 to the data set acquired in objective 3 to quantify RCC PDX perfusion heterogeneity and improve the confidence in patient core classification as resistant/sensitive to sunitinib therapy.

## 1.8 Thesis Outline

This thesis presents and evaluates novel image analysis techniques to expand the utility of contrast-enhanced ultrasound perfusion imaging, with a specific focus on quantifying perfusion heterogeneity. Each of the four objectives outlined above is addressed in one of the chapters summarized in this section. Chapters 2 through 5 represent work that is either published or in preparation for submission to a peer-reviewed journal. Chapter 6 is a discussion of future directions for this research and includes concluding remarks for the work so far.

### 1.8.1 Chapter 2

Chapter 2 presents a linear (B-mode) processing approach, named the EDoF (effective degrees of freedom) method, to quantify the change in the first-order speckle statistics of B-mode cine loops due to the incursion of microbubbles. The technique was developed on tumor bearing mice (MDA-MB-231LN mammary fat pad inoculation) and evaluated using nonlinear (two-pulse amplitude modulated) contrast microbubble specific images. In the proposed method, the speckle signal is approximated as a mixture of temporally varying random processes, representing the microbubble signal, superimposed onto spatially heterogeneous tissue backscatter in multiple subvolumes within the region of interest. It eliminates the need for a cumbersome image subtraction step in preclinical contrast enhanced imaging. The EDoF method shows promise for improving the robustness of linear CEUS based on reduced frame-to-frame variability compared with the conventional linear subtraction time-intensity curves. Wash-in curve parameters estimated using the EDoF method also demonstrate higher correlation to nonlinear CEUS than the conventional linear method.

### 1.8.2 Chapter 3

Chapter 3 aims to improve the potential clinical applicability of the technique presented in Chapter 2 by developing a second-generation model for the analysis of the first-order speckle statistics of two-pulse amplitude modulated contrast-enhanced ultrasound images. The compound technique was tested on an antiangiogenic drug trial (bevacizumab) on tumor bearing mice (MDA-MB-231LN), and evaluated with gold-standard histology and contrast-enhanced X-ray computed tomography. The area under curve produced using the compound statistical model could more accurately discriminate anti-VEGF treated tumors from untreated tumors than conventional contrast-enhanced ultrasound image processing. Vascular complexity, estimated using the ultrasound compound statistical model, performed similarly to micro-CT fractal dimension with respect to discrimination between treated and control tumors.

### 1.8.3 Chapter 4

Chapter 4 introduces an ultrafast PDX model of RCC in chicken embryos that permits quantification of tumor volume, tumor vascularity, and tumor perfusion via ultrasound in a high-throughput manner. For this proof of concept study, we relied on conventional ultrasound indices of vascularity (power Doppler vascularization index) and perfusion (CEUS). The vascularization index (VI) of the tumor was estimated by calculating the percentage of voxels in the segmented tumor volume that contained detected blood flow (*i.e.* Doppler color pixels). Tumor perfusion was quantified using CEUS estimates of relative blood volume. Implantation of tumor specimens into the chorioallantoic membrane (CAM) of the chicken embryo resulted in high engraftment efficiencies, permitting large scale “tumor avatar” studies that demonstrated intratumoral functional heterogeneity in the context of sunitinib treatment. These findings suggest that genetic tumor heterogeneity exists, but evidence for a direct relationship to the drug resistant phenotype did not manifest in DNA mutations, as determined by exome sequencing and gene copy number variation analysis. Therefore, these results support a phenotype based readout to predict drug resistance as opposed to a genotype signature, and that drug resistance to targeted therapy is heterogeneous across the tumor.

### 1.8.4 Chapter 5

Chapter 5 combines the compound speckle model (Chapter 3) with the data set acquired from the CAM PDX model (Chapter 4) to quantify PDX perfusion heterogeneity and to improve the confidence in patient core classification as resistant/sensitive to sunitinib therapy. First-order speckle analysis reduced the coefficient of variation of CEUS estimates of blood volume compared to conventional CEUS methods. With all three of the vascular quantification techniques presented in this study we observed intratumoral functional heterogeneity, both within untreated core biopsies and in the response to sunitinib therapy. Treatment sensitivity matrices constructed with compound speckle model could discriminate clear cell from chromophobe RCC samples, suggesting that the assay can detect sunitinib resistance at the biopsy level, and may be suitable for screening of *de novo* drug resistance in patients with mRCC.

### **1.8.5 Chapter 6**

Chapter 6 is a discussion of the potential future directions for this research, including technical improvements, the next steps for preclinical validation, and plans for clinical translation. It concludes with some final remarks concerning the significance of the research presented in this thesis.



# References

- [1] D. Hanahan and R. A. Weinberg, “Hallmarks of Cancer: The Next Generation,” *Cell*, vol. 144, no. 5, pp. 646–674, Mar. 2011.
- [2] A. Marusyk and K. Polyak, “Tumor heterogeneity: causes and consequences,” *Biochim. Biophys. Acta*, vol. 1805, no. 1, p. 105, Jan. 2010.
- [3] A. Jones and A. L. Harris, “New developments in angiogenesis: a major mechanism for tumor growth and target for therapy,” *Cancer J. Sci. Am.*, vol. 4, no. 4, pp. 209–217, Aug. 1998.
- [4] J. Folkman, “Role of angiogenesis in tumor growth and metastasis,” *Semin. Oncol.*, vol. 29, no. 6 Suppl 16, pp. 15–18, Dec. 2002.
- [5] D. A. McNamara, J. H. Harmey *et al.*, “Significance of angiogenesis in cancer therapy,” *Br. J. Surg.*, vol. 85, no. 8, pp. 1044–1055, Aug. 1998.
- [6] E. A. Eisenhauer, P. Therasse *et al.*, “New response evaluation criteria in solid tumours: revised RECIST guideline (version 1.1),” *Eur. J. Cancer*, vol. 45, no. 2, pp. 228–247, Jan. 2009.
- [7] M. A. Hayat, *Cancer Imaging: Lung and Breast Carcinomas*. Academic Press, Oct. 2007.
- [8] G.-H. Fong, “Mechanisms of adaptive angiogenesis to tissue hypoxia,” *Angiogenesis*, vol. 11, no. 2, pp. 121–140, 2008.
- [9] G. Bergers and L. E. Benjamin, “Tumorigenesis and the angiogenic switch,” *Nat. Rev. Cancer*, vol. 3, no. 6, pp. 401–410, Jun. 2003.
- [10] M. A. Konerding, E. Fait, and A. Gaumann, “3d microvascular architecture of pre-cancerous lesions and invasive carcinomas of the colon,” *Br. J. Cancer*, vol. 84, no. 10, pp. 1354–1362, May 2001.
- [11] M. W. Dewhirst, H. Kimura *et al.*, “Microvascular studies on the origins of perfusion-limited hypoxia,” *Br. J. Cancer. Suppl.*, vol. 27, pp. S247–251, Jul. 1996.
- [12] D. M. McDonald and P. L. Choyke, “Imaging of angiogenesis: from microscope to clinic,” *Nature Med.*, vol. 9, no. 6, pp. 713–725, Jun. 2003.

- [13] P. Carmeliet and R. K. Jain, "Angiogenesis in cancer and other diseases," *Nature*, vol. 407, no. 6801, pp. 249–257, Sep. 2000.
- [14] R. T. Tong, Y. Boucher *et al.*, "Vascular normalization by vascular endothelial growth factor receptor 2 blockade induces a pressure gradient across the vasculature and improves drug penetration in tumors," *Cancer Res.*, vol. 64, no. 11, pp. 3731–3736, Jun. 2004.
- [15] P. Vaupel, H. P. Fortmeyer *et al.*, "Blood flow, oxygen consumption, and tissue oxygenation of human breast cancer xenografts in nude rats," *Cancer Res.*, vol. 47, no. 13, pp. 3496–3503, Jul. 1987.
- [16] J. K. Mohindra and A. M. Rauth, "Increased cell killing by metronidazole and nitrofurazone of hypoxic compared to aerobic mammalian cells," *Cancer Res.*, vol. 36, no. 3, pp. 930–936, Mar. 1976.
- [17] S. Koch, F. Mayer *et al.*, "Efficacy of cytotoxic agents used in the treatment of testicular germ cell tumours under normoxic and hypoxic conditions in vitro," *Br. J. Cancer*, vol. 89, no. 11, pp. 2133–2139, Dec. 2003.
- [18] J. Folkman, E. Merler *et al.*, "Isolation of a tumor factor responsible for angiogenesis," *J. Exp. Med.*, vol. 133, no. 2, pp. 275–288, Feb. 1971.
- [19] J. Folkman, "Tumor angiogenesis: therapeutic implications," *N. Engl. J. Med.*, vol. 285, no. 21, pp. 1182–1186, 1971.
- [20] S. Goel, D. G. Duda *et al.*, "Normalization of the vasculature for treatment of cancer and other diseases," *Physiol. Rev.*, vol. 91, no. 3, pp. 1071–1121, Jul. 2011.
- [21] R. K. Jain, D. G. Duda *et al.*, "Biomarkers of response and resistance to antiangiogenic therapy," *Nat. Rev. Clin. Oncol.*, vol. 6, no. 6, pp. 327–338, Jun. 2009.
- [22] A. Jahangiri and M. K. Aghi, "Biomarkers predicting tumor response and evasion to anti-angiogenic therapy," *Biochim. Biophys. Acta*, vol. 1825, no. 1, pp. 86–100, Jan. 2012.
- [23] G. A. Bjarnason, B. Khalil *et al.*, "Outcomes in patients with metastatic renal cell cancer treated with individualized sunitinib therapy: correlation with dynamic microbubble ultrasound data and review of the literature," *Urol. Oncol.*, vol. 32, no. 4, pp. 480–487, May 2014.
- [24] J. M. L. Ebos and R. S. Kerbel, "Antiangiogenic therapy: impact on invasion, disease progression, and metastasis," *Nat. Rev. Clin. Oncol.*, vol. 8, no. 4, pp. 210–221, Apr. 2011.
- [25] R. J. Motzer, T. E. Hutson *et al.*, "Sunitinib versus interferon alfa in metastatic renal-cell carcinoma," *N. Engl. J. Med.*, vol. 356, no. 2, pp. 115–124, Jan. 2007.

- [26] C. N. Sternberg, I. D. Davis *et al.*, “Pazopanib in locally advanced or metastatic renal cell carcinoma: results of a randomized phase III trial,” *J. Clin. Oncol.*, vol. 28, no. 6, pp. 1061–1068, Feb. 2010.
- [27] B. Escudier, T. Eisen *et al.*, “Sorafenib in advanced clear-cell renal-cell carcinoma,” *N. Engl. J. Med.*, vol. 356, no. 2, pp. 125–134, Jan. 2007.
- [28] B. I. Rini, B. Escudier *et al.*, “Comparative effectiveness of axitinib versus sorafenib in advanced renal cell carcinoma (AXIS): a randomised phase 3 trial,” *Lancet*, vol. 378, no. 9807, pp. 1931–1939, Dec. 2011.
- [29] P. Cairns, “Renal Cell Carcinoma,” *Cancer Biomarkers*, vol. 9, no. 1-6, pp. 461–473, 2011.
- [30] W. M. Linehan, R. Srinivasan, and L. S. Schmidt, “The genetic basis of kidney cancer: a metabolic disease,” *Nat. Rev. Urol.*, vol. 7, no. 5, pp. 277–285, May 2010.
- [31] W. M. Linehan and R. Srinivasan, “Targeted therapies: Treating advanced kidney cancer—miles to go before we sleep,” *Nat. Rev. Clin. Oncol.*, vol. 10, no. 11, pp. 614–615, Nov. 2013.
- [32] H. Hurwitz, L. Fehrenbacher *et al.*, “Bevacizumab plus irinotecan, fluorouracil, and leucovorin for metastatic colorectal cancer,” *N. Engl. J. Med.*, vol. 350, no. 23, pp. 2335–2342, Jun. 2004.
- [33] J. M. Llovet, S. Ricci *et al.*, “Sorafenib in Advanced Hepatocellular Carcinoma,” *N. Engl. J. Med.*, vol. 359, no. 4, pp. 378–390, Jul. 2008.
- [34] E. Raymond, L. Dahan *et al.*, “Sunitinib Malate for the Treatment of Pancreatic Neuroendocrine Tumors,” *N. Engl. J. Med.*, vol. 364, no. 6, pp. 501–513, Feb. 2011.
- [35] T. J. Perren, A. M. Swart *et al.*, “A phase 3 trial of bevacizumab in ovarian cancer,” *N. Engl. J. Med.*, vol. 365, no. 26, pp. 2484–2496, Dec. 2011.
- [36] A. Sandler, R. Gray *et al.*, “Paclitaxel-carboplatin alone or with bevacizumab for non-small-cell lung cancer,” *N. Engl. J. Med.*, vol. 355, no. 24, pp. 2542–2550, Dec. 2006.
- [37] J. P. Crown, V. Diras *et al.*, “Phase III trial of sunitinib in combination with capecitabine versus capecitabine monotherapy for the treatment of patients with pretreated metastatic breast cancer,” *J. Clin. Oncol.*, vol. 31, no. 23, pp. 2870–2878, Aug. 2013.
- [38] W. K. Kelly, S. Halabi *et al.*, “Randomized, double-blind, placebo-controlled phase III trial comparing docetaxel and prednisone with or without bevacizumab in men with metastatic castration-resistant prostate cancer: CALGB 90401,” *J. Clin. Oncol.*, vol. 30, no. 13, pp. 1534–1540, May 2012.
- [39] H. L. Kindler, D. Niedzwiecki *et al.*, “Gemcitabine plus bevacizumab compared with gemcitabine plus placebo in patients with advanced pancreatic cancer: phase III trial of the Cancer and Leukemia Group B (CALGB 80303),” *J. Clin. Oncol.*, vol. 28, no. 22, pp. 3617–3622, Aug. 2010.

- [40] K. T. Flaherty, S. J. Lee *et al.*, “Phase III trial of carboplatin and paclitaxel with or without sorafenib in metastatic melanoma,” *J. Clin. Oncol.*, vol. 31, no. 3, pp. 373–379, Jan. 2013.
- [41] K. Miller, M. Wang *et al.*, “Paclitaxel plus bevacizumab versus paclitaxel alone for metastatic breast cancer,” *N. Engl. J. Med.*, vol. 357, no. 26, pp. 2666–2676, Dec. 2007.
- [42] D. W. Miles, A. Chan *et al.*, “Phase III study of bevacizumab plus docetaxel compared with placebo plus docetaxel for the first-line treatment of human epidermal growth factor receptor 2-negative metastatic breast cancer,” *J. Clin. Oncol.*, vol. 28, no. 20, pp. 3239–3247, Jul. 2010.
- [43] N. J. Robert, V. Diras *et al.*, “RIBBON-1: randomized, double-blind, placebo-controlled, phase III trial of chemotherapy with or without bevacizumab for first-line treatment of human epidermal growth factor receptor 2-negative, locally recurrent or metastatic breast cancer,” *J. Clin. Oncol.*, vol. 29, no. 10, pp. 1252–1260, Apr. 2011.
- [44] A. M. Brufsky, S. Hurvitz *et al.*, “RIBBON-2: a randomized, double-blind, placebo-controlled, phase III trial evaluating the efficacy and safety of bevacizumab in combination with chemotherapy for second-line treatment of human epidermal growth factor receptor 2-negative metastatic breast cancer,” *J. Clin. Oncol.*, vol. 29, no. 32, pp. 4286–4293, Nov. 2011.
- [45] C. J. Allegra, G. Yothers *et al.*, “Bevacizumab in stage II-III colon cancer: 5-year update of the National Surgical Adjuvant Breast and Bowel Project C-08 trial,” *J. Clin. Oncol.*, vol. 31, no. 3, pp. 359–364, Jan. 2013.
- [46] B. Nordlinger, E. V. Cutsem *et al.*, “Combination of surgery and chemotherapy and the role of targeted agents in the treatment of patients with colorectal liver metastases: recommendations from an expert panel,” *Ann. Oncol.*, p. mdn735, Jan. 2009.
- [47] T. Gruenberger, D. Arnold, and L. Rubbia-Brandt, “Pathologic response to bevacizumab-containing chemotherapy in patients with colorectal liver metastases and its correlation with survival,” *Surg. Oncol.*, vol. 21, no. 4, pp. 309–315, Dec. 2012.
- [48] R. Wong, D. Cunningham *et al.*, “A multicentre study of capecitabine, oxaliplatin plus bevacizumab as perioperative treatment of patients with poor-risk colorectal liver-only metastases not selected for upfront resection,” *Ann. Oncol.*, vol. 22, no. 9, pp. 2042–2048, Sep. 2011.
- [49] R. K. Jain, “Delivery of molecular and cellular medicine to solid tumors,” *Adv. Drug Deliv. Rev.*, vol. 46, no. 1-3, pp. 149–168, Mar. 2001.
- [50] R. Baskar, K. A. Lee *et al.*, “Cancer and radiation therapy: current advances and future directions,” *Int. J. Med. Sci.*, vol. 9, no. 3, pp. 193–199, 2012.
- [51] H. E. Barker, J. T. E. Paget *et al.*, “The tumour microenvironment after radiotherapy: mechanisms of resistance and recurrence,” *Nature Reviews Cancer*, vol. 15, no. 7, pp. 409–425, Jul. 2015.

- [52] G. T. Motz and G. Coukos, “Deciphering and reversing tumor immune suppression,” *Immunity*, vol. 39, no. 1, pp. 61–73, Jul. 2013.
- [53] Y. Huang, S. Goel *et al.*, “Vascular normalization as an emerging strategy to enhance cancer immunotherapy,” *Cancer Res.*, vol. 73, no. 10, pp. 2943–2948, May 2013.
- [54] R. Jain, “Antiangiogenesis Strategies Revisited: From Starving Tumors to Alleviating Hypoxia,” *Cancer Cell*, vol. 26, no. 5, pp. 605–622, Nov. 2014.
- [55] A. G. Sorensen, T. T. Batchelor *et al.*, “A “vascular normalization index” as potential mechanistic biomarker to predict survival after a single dose of cediranib in recurrent glioblastoma patients,” *Cancer Res.*, vol. 69, no. 13, pp. 5296–5300, Jul. 2009.
- [56] A. G. Sorensen, K. E. Emblem *et al.*, “Increased survival of glioblastoma patients who respond to antiangiogenic therapy with elevated blood perfusion,” *Cancer Res.*, vol. 72, no. 2, pp. 402–407, Jan. 2012.
- [57] P. Therasse, E. A. Eisenhauer, and J. Verweij, “RECIST revisited: a review of validation studies on tumour assessment,” *Eur. J. Cancer*, vol. 42, no. 8, pp. 1031–1039, May 2006.
- [58] H. Lusic and M. W. Grinstaff, “X-Ray Computed Tomography Contrast Agents,” *Chem. Rev.*, vol. 113, no. 3, Mar. 2013.
- [59] T. G. Gleeson and S. Bulugahapitiya, “Contrast-Induced Nephropathy,” *Am. J. Roentgenol.*, vol. 183, no. 6, pp. 1673–1689, Dec. 2004.
- [60] M. M. Khalil, J. L. Tremoleda *et al.*, “Molecular SPECT Imaging: An Overview,” *Int. J. Mol. Imaging.*, vol. 2011, p. e796025, Apr. 2011.
- [61] W. W. Moses, “Fundamental Limits of Spatial Resolution in PET,” *Nucl. Instr. Meth. Phys. Res. A*, vol. 648 Supplement 1, pp. S236–S240, Aug. 2011.
- [62] K. Satchithananda, M. E. K. Sellars *et al.*, “Microbubble Ultrasound Contrast Agents in the Visualization of Peripheral Vasculature in ‘Doppler Rescue’: A Review,” *Ultrasound*, vol. 12, no. 4, pp. 176–184, Nov. 2004.
- [63] F. Ries, C. Honisch *et al.*, “A transpulmonary contrast medium enhances the transcranial Doppler signal in humans,” *Stroke*, vol. 24, no. 12, pp. 1903–1909, Dec. 1993.
- [64] K. Darge, J. Troeger *et al.*, “Reflux in young patients: comparison of voiding US of the bladder and retrovesical space with echo enhancement versus voiding cystourethrography for diagnosis,” *Radiology*, vol. 210, no. 1, pp. 201–207, Jan. 1999.
- [65] A. Strandell, T. Bourne *et al.*, “The assessment of endometrial pathology and tubal patency: a comparison between the use of ultrasonography and X-ray hysterosalpingography for the investigation of infertility patients,” *Ultrasound Obstet. Gynecol.*, vol. 14, no. 3, pp. 200–204, Sep. 1999.
- [66] R. Gramiak and P. M. Shah, “Echocardiography of the aortic root,” *Invest. Radiol*, vol. 3, no. 5, pp. 356–366, Oct. 1968.

- [67] M. J. K. Blomley, J. C. Cooke *et al.*, “Microbubble contrast agents: a new era in ultrasound,” *The BMJ*, vol. 322, no. 7296, pp. 1222–1225, May 2001.
- [68] J. L. Cohen, J. Cheirif *et al.*, “Improved left ventricular endocardial border delineation and opacification with OPTISON (FS069), a new echocardiographic contrast agent. Results of a phase III Multicenter Trial,” *J. Am. Coll. Cardiol.*, vol. 32, no. 3, pp. 746–752, Sep. 1998.
- [69] K. Wei, A. R. Jayaweera *et al.*, “Quantification of Myocardial Blood Flow With Ultrasound-Induced Destruction of Microbubbles Administered as a Constant Venous Infusion,” *Circulation*, vol. 97, no. 5, pp. 473–483, Feb. 1998.
- [70] D. M. Skyba, A. R. Jayaweera *et al.*, “Quantification of myocardial perfusion with myocardial contrast echocardiography during left atrial injection of contrast. Implications for venous injection,” *Circulation*, vol. 90, no. 3, pp. 1513–1521, Sep. 1994.
- [71] M. Mischi, T. Kalker, and E. Korsten, “Videodensitometric Methods for Cardiac Output Measurements,” *EURASIP J. Adv. Signal Process*, vol. 2003, no. 5, pp. 479–489, 2003.
- [72] J. Hohmann, T. Albrecht *et al.*, “Ultrasonographic detection of focal liver lesions: increased sensitivity and specificity with microbubble contrast agents,” *Eur. J. Radiol.*, vol. 46, no. 2, pp. 147–159, May 2003.
- [73] C. J. Harvey, M. J. Blomley *et al.*, “Pulse-inversion mode imaging of liver specific microbubbles: improved detection of subcentimetre metastases,” *Lancet*, vol. 355, no. 9206, pp. 807–808, Mar. 2000.
- [74] T. Albrecht, C. W. Hoffmann *et al.*, “Phase-inversion sonography during the liver-specific late phase of contrast enhancement: improved detection of liver metastases,” *AJR Am. J. Roentgenol.*, vol. 176, no. 5, pp. 1191–1198, May 2001.
- [75] M. J. Blomley, T. Albrecht *et al.*, “Improved imaging of liver metastases with stimulated acoustic emission in the late phase of enhancement with the US contrast agent SH U 508a: early experience,” *Radiology*, vol. 210, no. 2, pp. 409–416, Feb. 1999.
- [76] T. Albrecht, M. J. K. Blomley *et al.*, “Improved Detection of Hepatic Metastases with Pulse-Inversion US during the Liver-specific Phase of SHU 508a: Multicenter Study,” *Radiology*, vol. 227, no. 2, pp. 361–370, May 2003.
- [77] T. K. Kim, B. I. Choi *et al.*, “Hepatic Tumors: Contrast Agent-Enhancement Patterns with Pulse-Inversion Harmonic US,” *Radiology*, vol. 216, no. 2, pp. 411–417, Aug. 2000.
- [78] M. J. Blomley, P. S. Sidhu *et al.*, “Do different types of liver lesions differ in their uptake of the microbubble contrast agent SH U 508a in the late liver phase? Early experience,” *Radiology*, vol. 220, no. 3, pp. 661–667, Sep. 2001.

- [79] T. Albrecht, M. J. Blomley *et al.*, “Non-invasive diagnosis of hepatic cirrhosis by transit-time analysis of an ultrasound contrast agent,” *Lancet*, vol. 353, no. 9164, pp. 1579–1583, May 1999.
- [80] M. J. Blomley, T. Albrecht *et al.*, “Liver vascular transit time analyzed with dynamic hepatic venography with bolus injections of an US contrast agent: early experience in seven patients with metastases,” *Radiology*, vol. 209, no. 3, pp. 862–866, Dec. 1998.
- [81] W. G. Pitt, G. A. Hussein, and B. J. Staples, “Ultrasonic Drug Delivery A General Review,” *Expert Opin. Drug Deliv.*, vol. 1, no. 1, pp. 37–56, Nov. 2004.
- [82] S. R. Wilson, P. N. Burns *et al.*, “Harmonic hepatic US with microbubble contrast agent: initial experience showing improved characterization of hemangioma, hepatocellular carcinoma, and metastasis,” *Radiology*, vol. 215, no. 1, pp. 153–161, Apr. 2000.
- [83] S. R. Wilson, H.-J. Jang *et al.*, “Diagnosis of focal liver masses on ultrasonography: comparison of unenhanced and contrast-enhanced scans,” *J. Ultrasound Med.*, vol. 26, no. 6, pp. 775–787; quiz 788–790, Jun. 2007.
- [84] H.-J. Jang, H. Yu, and T. K. Kim, “Contrast-enhanced ultrasound in the detection and characterization of liver tumors,” *Cancer Imaging*, vol. 9, pp. 96–103, 2009.
- [85] J. Furuse, M. Nagase *et al.*, “Contrast enhancement patterns of hepatic tumours during the vascular phase using coded harmonic imaging and Levovist to differentiate hepatocellular carcinoma from other focal lesions,” *Br. J. Radiol.*, vol. 76, no. 906, pp. 385–392, Jun. 2003.
- [86] S. Thakur, A. Jhobta *et al.*, “Role of contrast enhanced ultrasound in characterization of focal liver lesions,” *Egypt. J. Radiol. Nucl. Med.*, vol. 45, no. 1, pp. 7–17, Mar. 2014.
- [87] J.-M. Correas, M. Claudon *et al.*, “The kidney: imaging with microbubble contrast agents,” *Ultrasound Q.*, vol. 22, no. 1, pp. 53–66, Mar. 2006.
- [88] E. J. Halpern, “Contrast-Enhanced Ultrasound Imaging of Prostate Cancer,” *Rev. Urol.*, vol. 8, no. Suppl 1, pp. S29–S37, 2006.
- [89] C. Nicolau, L. Bunesch *et al.*, “Accuracy of contrast-enhanced ultrasound in the detection of bladder cancer,” *Br. J. Radiol.*, vol. 84, no. 1008, pp. 1091–1099, Dec. 2011.
- [90] F. Piscaglia, C. Nolsoe *et al.*, “The EFSUMB Guidelines and Recommendations on the Clinical Practice of Contrast Enhanced Ultrasound (CEUS): update 2011 on non-hepatic applications,” *Ultraschall Med.*, vol. 33, no. 1, pp. 33–59, Feb. 2012.
- [91] “Lumason - FDA prescribing information, side effects and uses.” [Online]. Available: <https://www.drugs.com/pro/lumason.html>
- [92] A. Ignee, B. Straub *et al.*, “Contrast enhanced ultrasound of renal masses,” *World J. Radiol.*, vol. 2, no. 1, pp. 15–31, Jan. 2010.

- [93] R. Williams, J. M. Hudson *et al.*, “Dynamic microbubble contrast-enhanced US to measure tumor response to targeted therapy: a proposed clinical protocol with results from renal cell carcinoma patients receiving antiangiogenic therapy,” *Radiology*, vol. 260, no. 2, pp. 581–590, Aug. 2011.
- [94] N. Lassau, S. Koscielny *et al.*, “Metastatic renal cell carcinoma treated with sunitinib: early evaluation of treatment response using dynamic contrast-enhanced ultrasonography,” *Clin. Cancer Res.*, vol. 16, no. 4, pp. 1216–1225, Feb. 2010.
- [95] N. de Jong, L. Hoff *et al.*, “Absorption and scatter of encapsulated gas filled microspheres: theoretical considerations and some measurements,” *Ultrasonics*, vol. 30, no. 2, pp. 95–103, Mar. 1992.
- [96] R. E. Apfel and C. K. Holland, “Gauging the likelihood of cavitation from short-pulse, low-duty cycle diagnostic ultrasound,” *Ultrasound Med. Biol.*, vol. 17, no. 2, pp. 179–185, 1991.
- [97] L. Hoff, P. C. Sontum, and J. M. Hovem, “Oscillations of polymeric microbubbles: effect of the encapsulating shell,” *J. Acoust. Soc. Am.*, vol. 107, no. 4, pp. 2272–2280, Apr. 2000.
- [98] P. Marmottant, S. van der Meer *et al.*, “A model for large amplitude oscillations of coated bubbles accounting for buckling and rupture,” *J. Acoust. Soc. Am.*, vol. 118, no. 6, pp. 3499–3505, 2005.
- [99] P. J. Frinking, A. Bouakaz *et al.*, “Ultrasound contrast imaging: current and new potential methods,” *Ultrasound Med. Biol.*, vol. 26, no. 6, pp. 965–975, Jul. 2000.
- [100] J.-B. Liu, G. Wansaicheong *et al.*, “Contrast-enhanced Ultrasound Imaging: State of the Art,” *J. Med. Ultrasound*, vol. 13, no. 3, pp. 109–126, Jan. 2005.
- [101] D. H. Simpson, C. T. Chin, and P. N. Burns, “Pulse inversion Doppler: a new method for detecting nonlinear echoes from microbubble contrast agents,” *IEEE Trans. Ultrason. Ferroelectr. Freq. Control*, vol. 46, no. 2, pp. 372–382, 1999.
- [102] B. Haider and R. Chiao, “Higher order nonlinear ultrasonic imaging,” in *1999 IEEE Ultrasonics Symposium, 1999. Proceedings*, vol. 2, 1999, pp. 1527–1531 vol.2.
- [103] V. Mor-Avi, E. G. Caiani *et al.*, “Combined assessment of myocardial perfusion and regional left ventricular function by analysis of contrast-enhanced power modulation images,” *Circulation*, vol. 104, no. 3, pp. 352–357, Jul. 2001.
- [104] R. J. Eckersley, C. T. Chin, and P. N. Burns, “Optimising phase and amplitude modulation schemes for imaging microbubble contrast agents at low acoustic power,” *Ultrasound Med. Biol.*, vol. 31, no. 2, pp. 213–219, Feb. 2005.
- [105] A. Needles, M. Arditi *et al.*, “Nonlinear contrast imaging with an array-based micro-ultrasound system,” *Ultrasound Med. Biol.*, vol. 36, no. 12, pp. 2097–2106, 2010.



- [106] M. Lampaskis and M. Averkiou, "Investigation of the relationship of nonlinear backscattered ultrasound intensity with microbubble concentration at low MI," *Ultrasound Med. Biol.*, vol. 36, no. 2, pp. 306–312, Feb. 2010.
- [107] P. Meier and K. L. Zierler, "On the theory of the indicator-dilution method for measurement of blood flow and volume," *J. Appl. Physiol.*, vol. 6, no. 12, pp. 731–744, Jun. 1954.
- [108] C. Strouthos, M. Lampaskis *et al.*, "Indicator dilution models for the quantification of microvascular blood flow with bolus administration of ultrasound contrast agents," *IEEE Trans. Ultrason. Ferroelectr. Freq. Contr.*, vol. 57, no. 6, pp. 1296–1310, 2010.
- [109] A. L. Koch, "The logarithm in biology. 1. Mechanisms generating the log-normal distribution exactly," *J. Theor. Biol.*, vol. 12, no. 2, pp. 276–290, Nov. 1966.
- [110] A. L. Koch, "The logarithm in biology. II. Distributions simulating the log-normal," *J. Theor. Biol.*, vol. 23, no. 2, pp. 251–268, May 1969.
- [111] R. Karshafian, P. N. Burns, and M. R. Henkelman, "Transit time kinetics in ordered and disordered vascular trees," *Phys. Med. Biol.*, vol. 48, no. 19, p. 3225, 2003.
- [112] K. Tiemann, T. Schlosser *et al.*, "Are microbubbles free flowing tracers through the Myocardium? Comparison of indicator-dilution curves obtained from dye dilution and echo contrast using harmonic power Doppler imaging," *Echocardiography*, vol. 17, no. 1, pp. 17–27, Jan. 2000.
- [113] E. J. Schlossmacher, H. Weinstein *et al.*, "Perfect mixers in series model for fitting venoarterial indicator-dilution curves," *J. Appl. Physiol.*, vol. 22, no. 2, pp. 327–332, Feb. 1967.
- [114] H. K. Thompson, C. F. Starmer *et al.*, "Indicator transit time considered as a gamma variate," *Circ. Res.*, vol. 14, pp. 502–515, Jun. 1964.
- [115] M. T. Madsen, "A simplified formulation of the gamma variate function," *Phys. Med. Biol.*, vol. 37, no. 7, p. 1597, 1992.
- [116] K. H. Norwich and S. Zelin, "The dispersion of indicator in the cardio-pulmonary system," *Bull. Math Biophys.*, vol. 32, no. 1, pp. 25–43, Mar. 1970.
- [117] J. B. Bassingrwhaighre, F. H. Ackerman, and E. H. Wood, "Applications of the Lagged Normal Density Curve as a Model for Arterial Dilution Curves," *Circ. Res.*, vol. 18, no. 4, pp. 398–415, Apr. 1966.
- [118] N. L. Eigler, J. M. Pfaff *et al.*, "Digital angiographic impulse response analysis of regional myocardial perfusion: linearity, reproducibility, accuracy, and comparison with conventional indicator dilution curve parameters in phantom and canine models," *Circ. Res.*, vol. 64, no. 5, pp. 853–866, May 1989.

- [119] M. Krix, F. Kiessling *et al.*, “A multivessel model describing replenishment kinetics of ultrasound contrast agent for quantification of tissue perfusion,” *Ultrasound Med. Biol.*, vol. 29, no. 10, pp. 1421–1430, Oct. 2003.
- [120] M. Arditi, P. J. A. Frinking *et al.*, “A new formalism for the quantification of tissue perfusion by the destruction-replenishment method in contrast ultrasound imaging,” *IEEE Trans. Ultrason. Ferroelectr. Freq. Control*, vol. 53, no. 6, pp. 1118–1129, Jun. 2006.
- [121] J. M. Hudson, R. Karshafian, and P. N. Burns, “Quantification of flow using ultrasound and microbubbles: a disruption replenishment model based on physical principles,” *Ultrasound Med. Biol.*, vol. 35, no. 12, pp. 2007–2020, Dec. 2009.
- [122] J. W. Goodman, *Statistical Optics*. Wiley, Feb. 1985.
- [123] R. F. Wagner, M. F. Insana, and D. G. Brown, “Statistical properties of radio-frequency and envelope-detected signals with applications to medical ultrasound,” *J. Opt. Soc. Am. A Opt. Image. Sci.*, vol. 4, no. 5, pp. 910–922, May 1987.
- [124] R. F. Wagner, S. W. Smith *et al.*, “Statistics of Speckle in Ultrasound B-Scans,” *IEEE Trans. Sonics Ultrason.*, vol. 30, no. 3, pp. 156–163, May 1983.
- [125] E. Jakeman and P. Pusey, “A model for non-Rayleigh sea echo,” *IEEE Trans. Antennas. Propag.*, vol. 24, no. 6, pp. 806–814, Nov. 1976.
- [126] E. Jakeman and R. J. A. Tough, “Generalized K distribution: a statistical model for weak scattering,” *J. Opt. Soc. Am. A*, vol. 4, no. 9, p. 1764, Sep. 1987.
- [127] P. M. Shankar, J. M. Reid *et al.*, “Use of non-Rayleigh statistics for the identification of tumors in ultrasonic B-scans of the breast,” *IEEE Trans Med. Imaging*, vol. 12, no. 4, pp. 687–692, Dec. 1993.
- [128] V. Dutt and J. F. Greenleaf, “Ultrasound echo envelope analysis using a homodyned K distribution signal model,” *Ultrason. Imaging*, vol. 16, no. 4, pp. 265–287, Oct. 1994.
- [129] P. M. Shankar, “A general statistical model for ultrasonic backscattering from tissues,” *IEEE Trans. Ultrason. Ferroelectr. Freq. Contr.*, vol. 47, no. 3, pp. 727–736, 2000.
- [130] M. Nakagami, “The m-Distribution A General Formula of Intensity Distribution of Rapid Fading,” in *Statistical Methods in Radio Wave Propagation*. Elsevier, 1960, pp. 3–36.
- [131] F. Destrepes and G. Cloutier, “Review of envelope statistics models for quantitative ultrasound imaging and tissue characterization,” in *Quantitative Ultrasound in Soft Tissues*, J. Mamou and M. L. Oelze, Eds. Springer Science & Business Media, 2013, ch. 10, pp. 219–274.
- [132] M. Averkiou, M. Lampaskis *et al.*, “Quantification of tumor microvascularity with respiratory gated contrast enhanced ultrasound for monitoring therapy,” *Ultrasound Med. Biol.*, vol. 36, no. 1, pp. 68–77, Jan. 2010.

- [133] J. Zhang, M. Ding *et al.*, “Respiratory motion correction in free-breathing ultrasound image sequence for quantification of hepatic perfusion,” *Med. Phys.*, vol. 38, no. 8, pp. 4737–4748, Aug. 2011.
- [134] M.-X. Tang, H. Mulvana *et al.*, “Quantitative contrast-enhanced ultrasound imaging: a review of sources of variability,” *Interface Focus*, vol. 1, no. 4, pp. 520–539, 2011.
- [135] D. E. Goertz, E. Cherin *et al.*, “High frequency nonlinear b-scan imaging of microbubble contrast agents,” *IEEE Trans. Ultrason. Ferroelectr. Freq. Contr.*, vol. 52, no. 1, pp. 65–79, 2005.
- [136] S. Feingold, R. Gessner *et al.*, “Quantitative volumetric perfusion mapping of the microvasculature using contrast ultrasound,” *Invest. Radiol.*, vol. 45, no. 10, Oct. 2010.
- [137] K. Hoyt, A. Sorace, and R. Saini, “Quantitative Mapping of Tumor Vascularity Using Volumetric Contrast Enhanced Ultrasound,” *Invest. Radiol.*, vol. 47, no. 3, pp. 167–174, Mar. 2012.
- [138] E. Stride, M.-X. Tang, and R. J. Eckersley, “Physical phenomena affecting quantitative imaging of ultrasound contrast agents,” *Appl. Acoust.*, vol. 70, no. 10, pp. 1352–1362, Oct. 2009.
- [139] N. G. Rognin, P. Frinking *et al.*, “In-vivo perfusion quantification by contrast ultrasound: Validation of the use of linearized video data vs. raw RF data,” in *2008 IEEE Ultrasonics Symposium*, Nov. 2008, pp. 1690–1693.

## Chapter 2

# Improved Linear Contrast-Enhanced Ultrasound Imaging via Analysis of First-Order Speckle Statistics

*The contents of this chapter has been adapted from “Improved Linear Contrast-Enhanced Ultrasound Imaging via Analysis of First-Order Speckle Statistics”, published in IEEE Trans. Ultrason., Ferroelect., Freq. Control. vol. 63, pp. 1409-1421, 2016, by M. R. Lowerison, M. N. Hague, A. F. Chambers, and J. C. Lacefield. \**

---

\*© 2016 IEEE. Reprinted, with permission, from M. R. Lowerison, M. N. Hague, A. F. Chambers, and J. C. Lacefield, “Improved Linear Contrast-Enhanced Ultrasound Imaging via Analysis of First-Order Speckle Statistics”, IEEE Trans. Ultrason., Ferroelect., Freq. Control. vol. 63, pp. 1409-1421, 2016.

## 2.1 Introduction

Preventing angiogenesis, the growth of new blood vessels, is a desirable therapeutic goal in the fight against cancer [1]. However, it is difficult to evaluate treatment response with conventional methods of tumor monitoring, which are typically insensitive to vascular changes [2]. Perfusion imaging provides quantifiable metrics of vascularity, blood flow organization, and oxygen delivery within living tissue [3]. Contrast-enhanced ultrasound (CEUS) is an attractive modality for clinical perfusion imaging due to its noninvasiveness, high accessibility, and lack of ionizing radiation. Microbubbles are limited to only the intravascular volume and mimic blood rheology [4]. These properties prevent enhancement of nonfunctioning vessels and the perivascular region, which is an advantage when imaging the functional volume of the characteristically leaky [5] and chaotic [6] vascular networks generated via tumor-induced angiogenesis.

In a preclinical setting, the advantages of CEUS for microvascular imaging include its low relative cost and high spatial and temporal resolution. Unfortunately, the conventional baseline image subtraction methods frequently used for small-animal imaging are susceptible to registration errors and motion artifacts [7], which lead to reduced contrast-to-tissue ratios [8]. These problems were addressed in clinical CEUS by the introduction of nonlinear contrast imaging methods, but the optimal imaging strategy for preclinical nonlinear processing is still being explored [9]. A linear array-based micro-ultrasound imaging system has been commercialized [10], but the large established base [11] of small-animal scanners using single-element, mechanically scanned transducers indicates that many users of preclinical CEUS would still benefit from improvements to linear processing.

This paper proposes a new linear processing approach that quantifies the change in first-order speckle statistics due to the incursion of microbubbles without requiring an image subtraction step. The proposed approach circumvents the artifacts associated with conventional linear CEUS subtraction methods. In the proposed method, the echo signal from circulating microbubbles is modeled as a temporally varying random process that is superimposed onto a Rayleigh distributed signal from tissue backscatter. The microbubble signal component can be viewed as a second population of diffuse scatterers in the active vasculature within the tis-

sue volume. Addition of the microbubble signal component is equivalent to adding additional random walk steps to the speckle signal from a subset of the image data corresponding to perfused pixels, meaning the received backscatter can be modeled as a mixture distribution of signal components from unperfused and perfused pixels. The relative contribution of the microbubble-enhanced subpopulation to the image speckle depends on the contrast signal and therefore can act as a surrogate measure for the active vascular volume fraction of the tumor. The hypothesis is that a speckle statistic-based method of image analysis will provide a more robust metric than conventional frame subtraction to quantify tumor vasculature using linear CEUS.

Analysis of first-order statistical characteristics of speckle in CEUS images has been shown to be useful by other investigators. Tsui et al. [12] developed a method for microvascular flow estimation, called time-Nakagami curves (TNC), in which Nakagami parameter images representing local scatterer concentration are constructed from contrast-enhanced signals. The method was initially tested in flow phantoms and healthy rabbit eyes. Further work [13] demonstrated that Nakagami parameter images are robust to shadowing from microbubbles, so their method improves flow quantification accuracy at deeper regions in flow phantoms.

Mixtures of distributions from multiple signal components have been proposed previously for ultrasonic tissue characterization. Semi-automated segmentation of the intima and media of the carotid artery has been performed in B-mode images by modeling the signal backscattered from the endothelial wall as a mixture of three Nakagami distributions [14]. Recently, mixtures of distributions were also applied to CEUS images by Akkus et al. [15], who employed a Gaussian mixture model to segment neovascularization within carotid plaques. Similar to the motivation for our proposed method, first-order statistical analysis of CEUS images was used in [15] to circumvent artifacts associated with conventional CEUS imaging.

This paper introduces our proposed method for analyzing first-order speckle statistics in a sequence of CEUS images and applies the method to images acquired from a murine xenograft breast cancer model. The method fits a Nakagami distribution to the histogram of the magnitude signal within the tumor and estimates the EDoF of the Nakagami distribution in each frame of the image sequence; the technique is therefore named the *EDoF method*. The time course of the EDoF yields a wash-in curve that can be interpreted using time-intensity analysis

in a manner comparable to conventional CEUS imaging. We show that wash-in curve parameters estimated using the EDoF method demonstrate higher correlation to nonlinear CEUS than the conventional linear method. The hypothesized relationship between the EDoF of first-order CEUS speckle statistics and the complexity of the active tumor vascular network is also discussed.

This paper builds upon the preliminary results reported in [16] in that the EDoF method is applied to linearized speckle signals here, whereas [16] was limited to analysis of log-compressed data. The relationship between the EDoF and TNC methods is also clarified; that comparison was neglected in [16]. The mixture model used in our method was initially developed independently of TNC image analysis and, at first glance, appears to be a different method of contrast image quantification. The analysis in Sect. 2.2 demonstrates that our method is mathematically equivalent to the TNC technique when identical parameter estimation windows are used. This equivalence increases confidence that the EDoF model is appropriate for describing CEUS speckle. However, in our method each component of the mixture distribution is interpreted as originating from a different population of ultrasound scatterers. Therefore, the physical interpretation of the EDoF statistical parameter is different for our method than TNC analysis. We propose that this new parameter is a metric of tumor heterogeneity and may be useful for analysis of vascular tortuosity if used for contrast analysis.

## 2.2 Statistical Model

### 2.2.1 Contrast-Enhanced Speckle Statistics

Consider first the case of a baseline (pre-injection) image of a tumor. The EDoF method assumes that the tumor consists of several subregions whose backscatter characteristics are statistically homogeneous and potentially different from the backscatter characteristics of the remaining subregions. The probability density function (PDF) of the speckle signal analyzed over the entire tumor volume can therefore be viewed as a weighted mixture of distributions, where each component of the mixture corresponds to the speckle in one of the subregions and the weighting depends on the relative volume of each subregion. We assume for simplicity

that the backscatter in each subregion satisfies the conditions for producing fully developed speckle.<sup>1</sup> The PDF of the demodulated analytic signal,  $s$ , over the entire tumor volume is therefore modeled by:

$$f_k[s] = \sum_{i=1}^k \omega_i N(0, \sigma_i^2), \quad (2.1a)$$

$$\sum_{i=1}^k \omega_i = 1, \quad \omega_i \geq 0, \quad (2.1b)$$

where  $N(0, \sigma_i^2)$  is a zero-mean, circularly symmetric complex Gaussian distribution with variance  $\sigma_i^2$ ,  $\omega_i$  denotes the relative weighting of each signal component, and  $k$  is the number of subregions within the tumor. At baseline, the weights,  $\omega_i$ , are in principle constant for fixed imaging conditions.

The PDF of the normalized squared norm (*i.e.*, the backscatter signal intensity, where  $I = |s|^2$ ) of a mixture of an arbitrary number of zero-mean Gaussian distributions, where each component differs in variance, can be expressed as a single chi-squared distribution with reduced effective degrees of freedom [17] (expressed as  $n^* \leq n$ , where  $n$  is degrees of freedom). There are two such mixture distributions in the analytic signal to account for the real and imaginary components of (2.1a); hence, the normalized squared norm of a mixture of  $k$  zero-mean circularly symmetric complex Gaussian distributions follows a chi-squared distribution with  $n^* \leq 2k$  effective degrees of freedom. If the signal intensity,  $I$ , is normalized by  $\sum_{i=1}^k \omega_i \sigma_i^2$ , then, by the substitution of variables in [17] (specifically, Eq. 16), the squared norm of the normalized analytic signal (2.1a) can be expressed as:

$$f_k[I] \approx (n^* - 1) \frac{((n^* - 1)I)^{(n^*/2)-1} e^{-(n^*-1)I/2}}{2^{n^*/2} \Gamma(\frac{n^*}{2})}. \quad (2.2)$$

In Equation (2.2),  $(n^* - 1)I$  possesses a chi-squared distribution with  $n^*$  degrees of freedom. By introducing a scaling parameter  $\rho$  to normalize the area under  $f_k[I]$  to unity, where  $\rho =$

---

<sup>1</sup>The nominal resolution of 75  $\mu\text{m}$  axial by 165  $\mu\text{m}$  lateral by 165  $\mu\text{m}$  elevational in our experimental images would correspond to approximately sixty 40  $\mu\text{m}$  diameter cancer cells per resolution volume, exceeding the scatterer number for Rayleigh speckle statistics. At the time of inoculation, the tumors had a volume of 5  $\text{mm}^3$  which, assuming roughly spherical geometry, would correspond to about 2450 independent samples of the backscatter signal at the nominal resolution.



$\frac{2}{(n^*-1)}(\sum_{i=1}^k \omega_i \sigma_i^2)$ , the PDF of signal intensity without normalization becomes:

$$f_k[I] \approx \frac{1}{\rho^{n^*/2} \Gamma(\frac{n^*}{2})} I^{(n^*/2)-1} e^{-I/\rho}. \quad (2.3)$$

In this context,  $f_k[I]$  represents the square magnitude of the uncompressed echo envelope and follows a gamma distribution. This approximation is more accurate if the variances of the individual components are similar. The upper limit of  $2k$  degrees of freedom corresponds to an analytic signal with independent real and imaginary components. The reduced degrees of freedom in the general case is a consequence of overlap in signal space of the  $k$  Gaussian components of  $s$ , *i.e.*, cases where a sample value could plausibly come from either the distribution it was actually drawn from or one of the higher-variance components. The lower limit of (2.3) is a single complex Gaussian component with  $n^* = 2$  degrees of freedom, in which case the right-hand side of (2.3) simplifies to an exponential PDF.

The norm of a mixture of  $k$  zero-mean Gaussians follows a distribution described by the square root of the random variable  $I = |s|^2$  in (2.3). Applying a transformation of random variables from  $I$  to  $|s|$  in (2.3) yields the PDF of signal magnitude:

$$f_k[|s|] \approx \frac{2}{\rho^{n^*/2} \Gamma(\frac{n^*}{2})} |s|^{n^*-1} e^{-|s|^2/\rho}. \quad (2.4)$$

For the limiting case of a homogeneous tissue region,  $n^* = 2$  again and (2.4) simplifies to a Rayleigh PDF. It can be shown that (2.4) possesses a Nakagami distribution by inducing the variables  $\Omega = m\rho$  and  $m = n^*/2$ , such that:

$$f(|s|; m, \Omega) = \frac{2m^m}{\Gamma(m)\Omega^m} |s|^{2m-1} e^{-\frac{m}{\Omega}|s|^2}, \quad (2.5)$$

where  $m$  is the Nakagami shape parameter and  $\Omega$  is the Nakagami scaling parameter. Therefore, use of the gamma distribution of (2.3) for the PDF of signal intensity is mathematically equivalent to use of the Nakagami distribution of (2.5) for the PDF of the signal magnitude [18] [19]. Shankar demonstrated that the Nakagami distribution can model tissue backscatter [19] and that the Nakagami shape parameter,  $m$ , can be interpreted as the square of the signal-to-noise ratio of the signal intensity.

Consider now the addition of contrast enhancement to the above model. A portion of

the speckles in a subregion of the tumor now include contributions from microbubble echoes. The microbubbles add additional steps to the random walk for the contrast-enhanced speckles, which increases the variance of the PDF for those speckles. The extent to which the variance increases depends on the concentration and scattering strength of the microbubbles in each enhanced speckle. The subregion, which at baseline was statistically homogeneous, now consists of one nonenhanced speckle population and a mixture of contrast-enhanced speckle populations with differing levels of enhancement. The influx of microbubbles has therefore increased the effective degrees of freedom of the speckle pattern for that subregion specifically and for the tumor generally. The EDoF method characterizes the kinematics of this change in the degrees of freedom of the tumor speckle during microbubble wash-in.

Mathematically, contrast enhancement alters (2.1a) by introducing a time dependence to the relative weighting of the analytic signal:

$$f_k[s(t)] = \sum_{i=1}^k \omega_i(t) N(0, \sigma_i^2). \quad (2.6)$$

The weighting function,  $\omega_i(t)$ , is in general a continuous function of time to enable this formulation to fully describe the kinematics of microbubble wash-in to a vascular network. During contrast-enhanced imaging,  $k$  is expected to be greater than the number of tissue subregions in the tumor due to the fact that the image now consists of a mixture of unenhanced and enhanced speckles. The first-order statistics of the magnitude signal over the entire tumor remains a Nakagami PDF with  $n^* \leq 2k$  effective degrees of freedom as in (2.4). Many other mixture models require weighting estimates of each individual component, which introduces an extra step of complexity in analysis with no closed-form solution and generally requires an assumption about the number of components. The advantage of using either the gamma distribution (for intensity) or the Nakagami distribution (for magnitude) is that the first-order speckle statistics of a region of interest (ROI) consisting of a mixture of scatterer populations, such as a contrast-enhanced tumor, can be represented by a single-component distribution if the reduced degrees of freedom are accounted for as in (2.3) and (2.4).

## 2.2.2 Parameter Estimation

During the wash-in phase of a CEUS imaging study, the time-dependent weighting variable  $\omega_i(t)$  changes to reflect an increased relative weighting of the contrast-enhanced Gaussian signal components. This change in weighting increases the effective degrees of freedom of the speckle PDF. The EDoF method models the histogram of the speckle within the ROI using (2.3) for the intensity signal or (2.4) for the magnitude signal and detects the change in the effective degrees of freedom,  $n^*$ , of the distribution during wash-in of a microbubble bolus.

In the current implementation of the EDoF method, a maximum likelihood estimate of the effective degrees of freedom (equivalently, the Nakagami shape parameter) of the speckle in the frame acquired at time  $t$ ,  $\hat{n}(t)$ , is computed from the magnitude image by solving for  $\hat{n}(t)$  using [20, p.156]:

$$\ln\left(\frac{\hat{n}(t)}{2}\right) - \psi\left(\frac{\hat{n}(t)}{2}\right) = \ln\left(\frac{1}{N} \sum_{i=1}^N I_i\right) - \frac{1}{N} \sum_{i=1}^N \ln(I_i), \quad (2.7)$$

where  $\psi(A)$  is the digamma function:

$$\psi(A) = \frac{d}{dA} \ln \Gamma(A) = \frac{\Gamma'(A)}{\Gamma(A)}, \quad (2.8)$$

$N$  is the number of pixels within the ROI, and  $I_i$  is the intensity of the  $i$ th pixel. Equation (2.7) can be solved using the Newton-Raphson method described in [21], or by a binary search algorithm [14]. Alternatively, a less computationally expensive but less accurate estimate of  $\hat{n}(t)$  can be obtained using the method of moments [22]. Since (2.7) does not depend on the scaling of  $I$ , the normalization step in (2.3) does not affect the estimation of  $n^*$ .

## 2.3 Materials and Methods

### 2.3.1 Animal Model

The Western University Council on Animal Care approved all experiments used in this study. Human breast cancer xenografts were induced in 8 female nude mice (nu/nu, 8-10 weeks of age) by injection of  $2 \times 10^6$  MDA-MB-231-luc-D3H2LN cells into the abdominal mammary fat

pad. Cells were suspended in a mixture of 50% phosphate-buffered saline and 50% Matrigel (BD Biosciences, Mississauga, Canada), as per the tumor inoculation procedure described by Goulet et al. [23]. Animals were imaged once weekly starting at three days after tumor inoculation until they were sacrificed at the end of week six.

### 2.3.2 Image Acquisition

The Vevo MicroMarker<sup>TM</sup> (Fujifilm VisualSonics Inc., Toronto, Canada) microbubble solution was reconstituted following the instructions given by the supplier. In brief, a phospholipid and gas (nitrogen and perfluorobutane) vial was mixed with 0.7 mL of sterile saline and agitated manually. This process yielded a solution with approximately  $2 \times 10^9$  microbubbles/mL with median diameter of 2.3 – 2.9  $\mu\text{m}$ .

All ultrasound measurements were performed using a Vevo<sup>®</sup> 2100 high-frequency imaging system (VisualSonics Inc.) equipped with a 256 element linear array transducer (MS-250, 20 MHz center frequency, 70% –6 dB two-way bandwidth; 75  $\mu\text{m}$  nominal axial resolution, 165  $\mu\text{m}$  nominal lateral resolution) transmitting at 18 MHz in nonlinear contrast mode. Animals were gas anesthetized using 3% isoflurane in oxygen for induction and 2% isoflurane in oxygen for maintenance. Following induction of anesthesia, the mouse was secured to a heated physiological monitoring platform (THM-150, VisualSonics Inc.) with transpore surgical tape and electrolytic contact gel. A disposable, autoclaved brace pad was placed between the animal and the platform to support the tail. The surface temperature of the platform was maintained at  $40 \pm 0.1$  °C to heat the pad to approximately 37 °C. The experimental environment is similar to the one illustrated in Fig. 2 of [11].

All visible hair was removed from the site of the primary tumor using depilation cream (Nair<sup>®</sup>, Church & Dwight Co., Inc., Princeton, NJ) and then warmed ultrasound coupling gel was applied. Microbubbles were administered through a bolus tail vein injection (50  $\mu\text{L}$ , about  $1.0 \times 10^8$  microbubbles). The transducer was fixed above the center of the tumor and oriented to produce an anatomical transverse imaging plane. Nonlinear (subharmonic) imaging was performed using an amplitude modulation method [9] over a field of view sized to completely enclose the tumor. Cine loops consisting of 1,500-2,000 frames were acquired at frame rates between 9 and 28 Hz. The frame rate varied because a larger subharmonic field of view was

necessary at later time points. Contrast wash-in cine loops were exported as log-compressed, magnitude signal data files. Linear (B-mode) data were quantized to 8 bits at a 336 MHz sampling frequency; nonlinear contrast images were quantized to 16 bits at a 288 MHz sampling frequency. Linear and nonlinear image data were acquired simultaneously during the same bolus injection, with one B-mode frame acquired for every non-linear frame.

### 2.3.3 Image Analysis

Contrast enhancement was analyzed separately in the linear and nonlinear images using matched ROIs. Tumor boundaries were manually segmented on the first frame of the B-mode cine loops and the tumor was assumed to not move or deform during wash-in. Segmentation coordinates in linear images were rigidly registered to the corresponding nonlinear coordinates via translation and scaling. The dependence of wash-in curve parameter estimation on segmentation accuracy was assessed by scaling the area of manual ROIs by 90% and 110%. All analysis was performed using MATLAB (version R2013a, The MathWorks Inc., Natick, MA).

Linearly scaled envelope data were recovered by reversing the log compression of the exported B-mode images (dynamic range 40 dB, linear gain 30 dB, fixed TGC of 0.54 dB/cm MHz [24]). Nakagami PDFs as in (2.4) were fit to the linearized magnitude data within the ROI in each frame of each cine loop. The effective degrees of freedom of the speckle were obtained by applying the Newton-Raphson method to the maximum likelihood estimator (2.7) with a convergence limit of  $1 \times 10^{-6}$  and a maximum of 200 iterations. The goodness of fit of the Nakagami PDF to the image histogram was visually compared to the goodness of fit of the Rayleigh distribution.

### 2.3.4 Wash-In Curve Analysis

Wash-in time series were constructed to characterize the kinematics of contrast enhancement as measured using conventional linear CEUS, nonlinear CEUS, and the EDoF method. For linear CEUS, a baseline B-mode image was constructed by averaging 150 frames acquired immediately prior to injecting the contrast bolus. Contrast enhancement in each frame during wash-in was estimated on the linearized data by performing pixel-by-pixel subtraction of the

baseline image from each image in the post-injection cine loop and then computing the average signal magnitude within the ROI for each frame of the difference image. For nonlinear CEUS, contrast enhancement was estimated by averaging the nonlinear signal magnitude within the ROI for each frame of the post-injection cine loop. In the EDoF method, contrast enhancement was estimated from the linearized images by determining the time history of the estimated effective degrees of freedom,  $\hat{n}(t)$ , of the Nakagami distribution fit to the B-mode histogram within the ROI for each frame of the post-injection cine loop.

A simplified gamma variate function [25] was fitted to each set of time series data as a wash-in curve model:

$$Y(t) = Y_{max} t'^{\alpha_v} e^{\alpha_v(1-t')}, \quad (2.9)$$

where  $t'$  is  $t/T_{max}$ ,  $T_{max}$  is the time of the wash-in curve peak,  $Y_{max}$  is the amplitude of the curve peak, and  $\alpha_v$  controls the curve shape. There is no coupling between the parameters defining this function, which makes longitudinal comparisons straightforward because the evolution of each parameter can be analyzed independently from the other parameters. Curve parameters were calculated using an unconstrained nonlinear minimization (Nelder-Mead method) of the sum of squared residuals with maximum 800 iterations and a convergence criterion of  $1 \times 10^{-4}$ . Initial estimates for the parameters were  $Y_{max}$  equal to the observed maximum contrast enhancement,  $T_{max}$  equal to the time at which  $Y(t) = Y_{max}$ , and  $\alpha_v = 1$ , where the latter choice yields the wash-in curve for two homogeneous mixing compartments in series [26], which is the simplest model of a hierarchical vessel network. The frame-to-frame variability of each method was assessed by computing the signal-to-noise ratio, SNR, in decibels, of the raw time series signal relative to the fitted curve. This was calculated as the ratio of the summed squared signal magnitude ( $Y(t)$ ) over the summed squared of the curve fitting residual. The area under the curve (AUC) was calculated from the fitted gamma variate parameters as:

$$AUC = Y_{max} T_{max} e^{\alpha_v} \alpha_v^{-\alpha_v} \Gamma(\alpha_v). \quad (2.10)$$

PDFs were constructed as in [12] on the same manual ROIs as above with a sliding window of  $240 \times 240 \mu\text{m}$ . Processing was performed on both the log-compressed images and the linearized images. The estimate of Nakagami shape parameter,  $m$ , was averaged across all

sliding windows for each frame of the cine loop and plotted as a function of time,  $\bar{m}(t)$ . The resulting averaged TNC curves were compared visually to the corresponding EDoF wash-in curves.

The AUC and each of the three wash-in curve parameters derived from analysis of conventional linear and EDoF CEUS wash-in curves were compared to the corresponding nonlinear CEUS estimate using linear regression and the Pearson correlation coefficient such that the nonlinear CEUS parameters were interpreted as the gold-standard measurements. The significance of the difference between each pair of correlation coefficients was assessed using a two-tailed Fisher  $r$ -to- $z$  transform [27].

## 2.4 Results

### 2.4.1 Contrast-Enhanced Speckle Histograms

Figure 2.1 shows a representative segmented tumor image and fits of Nakagami and Rayleigh PDFs to speckle magnitude within the ROI taken prior to injection of contrast agent (Fig. 2.1c) and immediately following the bolus injection of microbubbles (Fig. 2.1d). As predicted by the speckle model, the number of effective degrees of freedom of the fitted Nakagami distribution increased as the tumor became perfused with microbubbles. Visually, the histogram peak shifted to the right and the distribution became more symmetric. There is close visual agreement of the fitted Nakagami functions to the image histograms. The relatively poor agreement between the histograms and the Rayleigh fit illustrates the appropriateness of the mixture model for these images.

### 2.4.2 Wash-In Curves

Figure 2.2 shows time-intensity curves obtained from another representative tumor using the three CEUS imaging techniques. A movie comparing this cine loop with the corresponding dynamic EDoF curve can be found in the online supplement. Note in this cine loop that the gradual increase in EDoF corresponds to the heterogeneity of enhancement in the outlined tumor. In this example, the EDoF method produced less frame-to-frame variability than con-

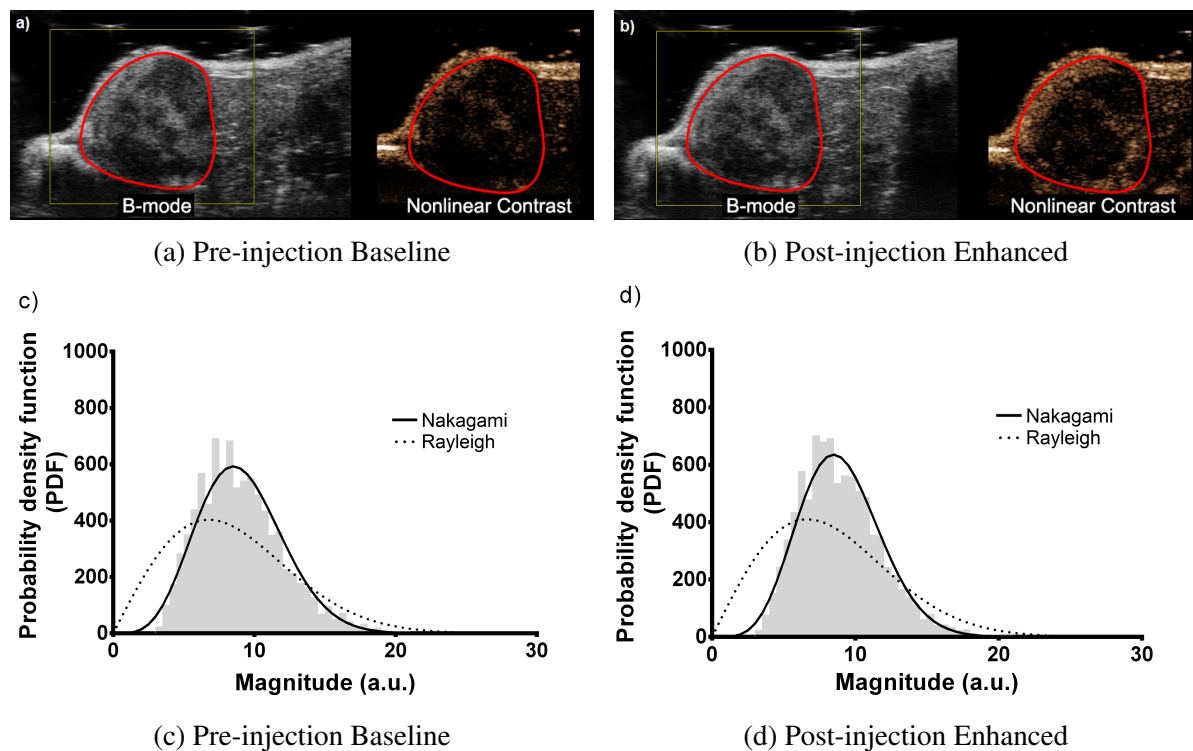


Figure 2.1: Representative tumor images with manual ROIs taken (a) prior to contrast enhancement and (b) immediately following a microbubble bolus and the probability density function fit to image histogram data taken (c) at baseline and (d) after enhancement. The histograms show signal magnitude in arbitrary units (a.u.). A Nakagami distribution with effective degrees of freedom (c)  $n^* = 2.96$  and (d)  $n^* = 4.15$  was the closest fit to the data.



ventional linear image subtraction, as evidenced by a higher signal-to-noise ratio, SNR, with respect to the analytic wash-in function, (2.9). Some frame-to-frame variability in intensity is expected as individual microbubbles move through the image plane. The improved robustness to motion of the EDoF technique in comparison to linear image subtraction is apparent in the example in Fig. 2.3, which shows an example of an especially large subject motion during the manual tail vein injection. Averaging over 47 wash-in curves (8 animals times 6 imaging sessions, one animal was sacrificed a week early), the mean  $\pm$  standard deviation of the SNR between the raw signal and the curve fit from (2.9) was  $23.8 \pm 2.7$  dB for nonlinear CEUS wash-in curves,  $18.3 \pm 3.2$  dB for conventional linear CEUS, and  $33.1 \pm 6.2$  dB for the EDoF method. The higher signal-to-noise ratio for EDoF processing implies reduced frame-to-frame variability compared to image subtraction. The difference in performance between the two linear processing methods was statistically significant (two-tailed Fisher  $r$ -to- $z$  transform,  $p < 0.0001$ ).

Regions of interest were generally consistent on repeated segmentations due to well-defined tumor boundaries in B-mode images, which is an indication of tumor encapsulation. Scaling the segmentation by 110% of the original area led to a consistent overestimation of peak signal enhancement, which was likely caused by the inclusion of highly vascularized adipose and dermal tissues. Furthermore, the sensitivity of all methods was reduced if the ROI was too close to the skin surface, as it would then include pixels within the coupling gel in some frames. Smaller segmentations (area scaled by 90%) generally produced the same results as the original contour; however, the frame-to-frame variability of the signal magnitude was often greater.

### 2.4.3 Comparison of EDoF and TNC Wash-In Curves

Time-Nakagami curves were constructed for the same manual ROIs used in EDoF processing. Figure 2.4 shows an example of an EDoF wash-in curve in comparison to the corresponding TNC wash-in curve on both linearized (left column) and log-compressed (right column) image data. For recovered linearized data the EDoF method performed well, but TNC processing produced wash-in curves that were difficult to interpret and the expected relationship of  $n^* = 2\bar{n}$  did not hold over the entire time course of the wash-in curves. This difference in performance was most apparent for end-point tumors that exhibited heterogeneous contrast enhancement.

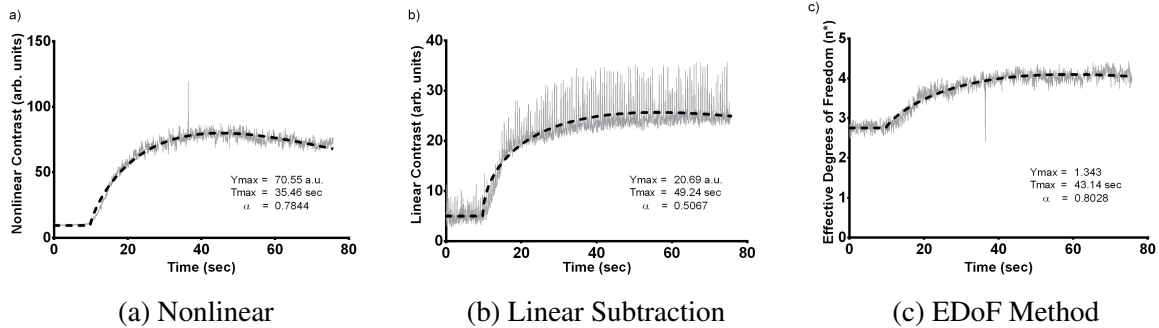


Figure 2.2: Wash-in curves for the three methods of contrast analysis applied to a representative tumor. The dotted line is a nonlinear regression fit to a simplified gamma variate function, (2.9). The curves have signal-to-noise ratios of (a) 25.5 dB for nonlinear CEUS, (b) 18.1 dB for conventional linear CEUS, and (c) 28.7 dB for the EDoF method, respectively. Nonlinear and conventional linear CEUS data are reported in arbitrary unit (a.u.).

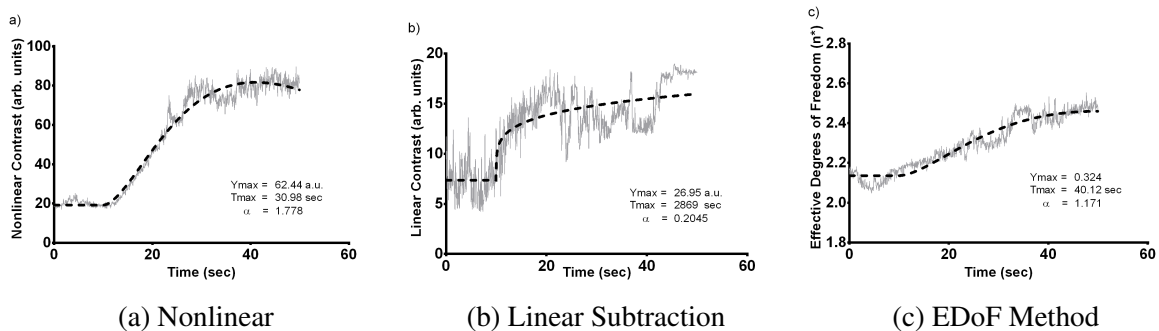


Figure 2.3: Wash-in curves for the three methods of contrast analysis applied to a tumor with high subject movement. The statistical EDoF method demonstrates improved robustness to motion artifacts. Signal-to-noise ratios for the fitted wash-in curves are (a) 23.2 dB for nonlinear CEUS, (b) 16.1 dB for conventional linear CEUS, and (c) 35.7 dB for the EDoF method. Nonlinear and conventional linear CEUS data are reported in arbitrary unit (a.u.).

Although not theoretically justified, both methods performed well on log-compressed data, with the main difference being estimated peak signal amplitude.

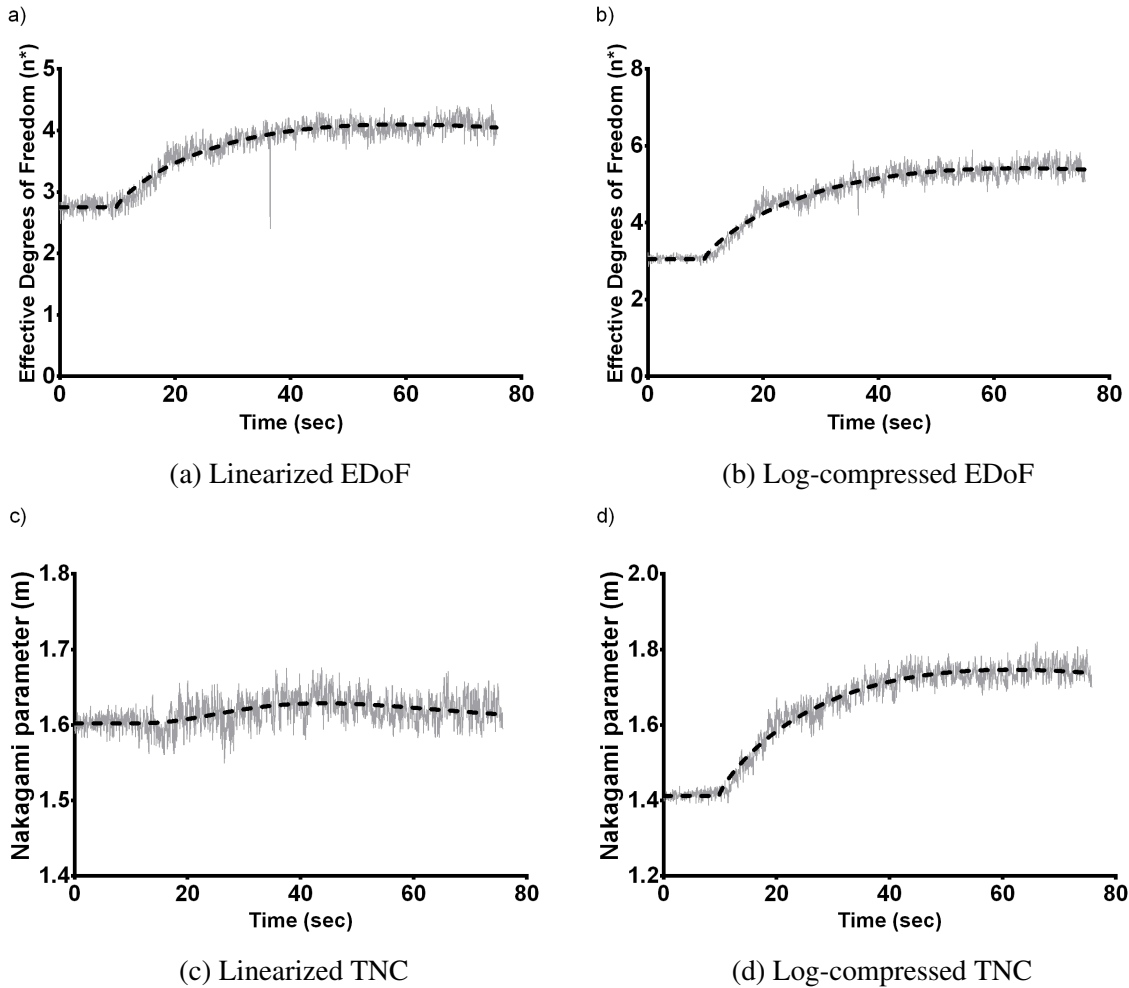


Figure 2.4: An example comparison of the EDoF method to a sliding-window based TNC. On linearized envelope data, the (a) EDoF method produced interpretable wash-in curves, but the (c) results of TNC processing were difficult to analyze. The curve shape of the two methods was very similar on log-compressed image data (b) and (d), with the main difference being the peak signal amplitude.

#### 2.4.4 Wash-In Curve Parameter Estimation

Linear regression analysis of wash-in curve AUC and estimated curve fit parameters for both linear techniques, in comparison to the nonlinear gold standard, can be found in Figs. 2.5 – 2.8. For the AUC (Fig. 2.5), the EDoF method exhibited a higher Pearson correlation to the nonlinear CEUS AUC ( $r = 0.6776$ ) than did conventional linear processing ( $r = 0.4919$ ). The

difference between the EDoF and conventional linear correlation coefficients was not statistically significant ( $p = 0.1738$ ). The correlation of AUC between conventional linear subtraction and EDoF was weak ( $r = 0.5872$ ).

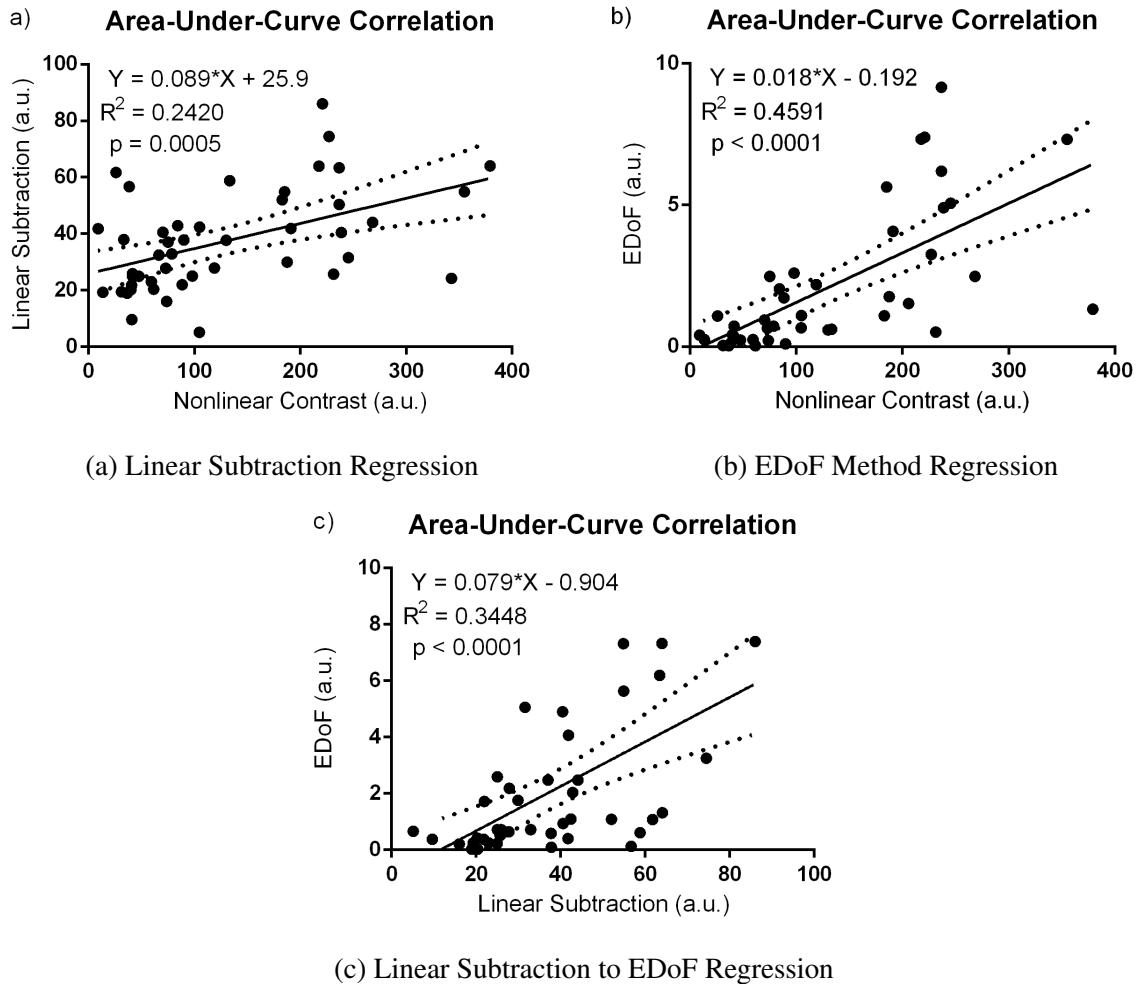


Figure 2.5: Linear regression for area under curve (AUC) for the two linear contrast methods in comparison to gold-standard nonlinear CEUS. The (a) linear subtraction method did not demonstrate a strong correlation to the AUC for nonlinear CEUS ( $R^2 = 0.2420$ ,  $p = 0.0005$ ) and was outperformed by the (b) EDoF method ( $R^2 = 0.4591$ ,  $p < 0.0001$ ). The correlation of AUC between the linear techniques was weak ( $R^2 = 0.3448$ ,  $p < 0.0001$ ). All areas are reported in arbitrary units (a.u.).

The conventional linear and EDoF estimates of maximum amplitude,  $Y_{max}$ , (Fig. 2.6) had similar statistically significant, moderate Pearson correlation to the nonlinear CEUS estimate ( $r = 0.6912$  and  $r = 0.7692$ , respectively). There was no significant difference between the correlation coefficients for  $Y_{max}$  ( $p = 0.4237$ ). The correlation between linear subtraction and

EDoF was also moderately strong ( $r = 0.7171$ ).

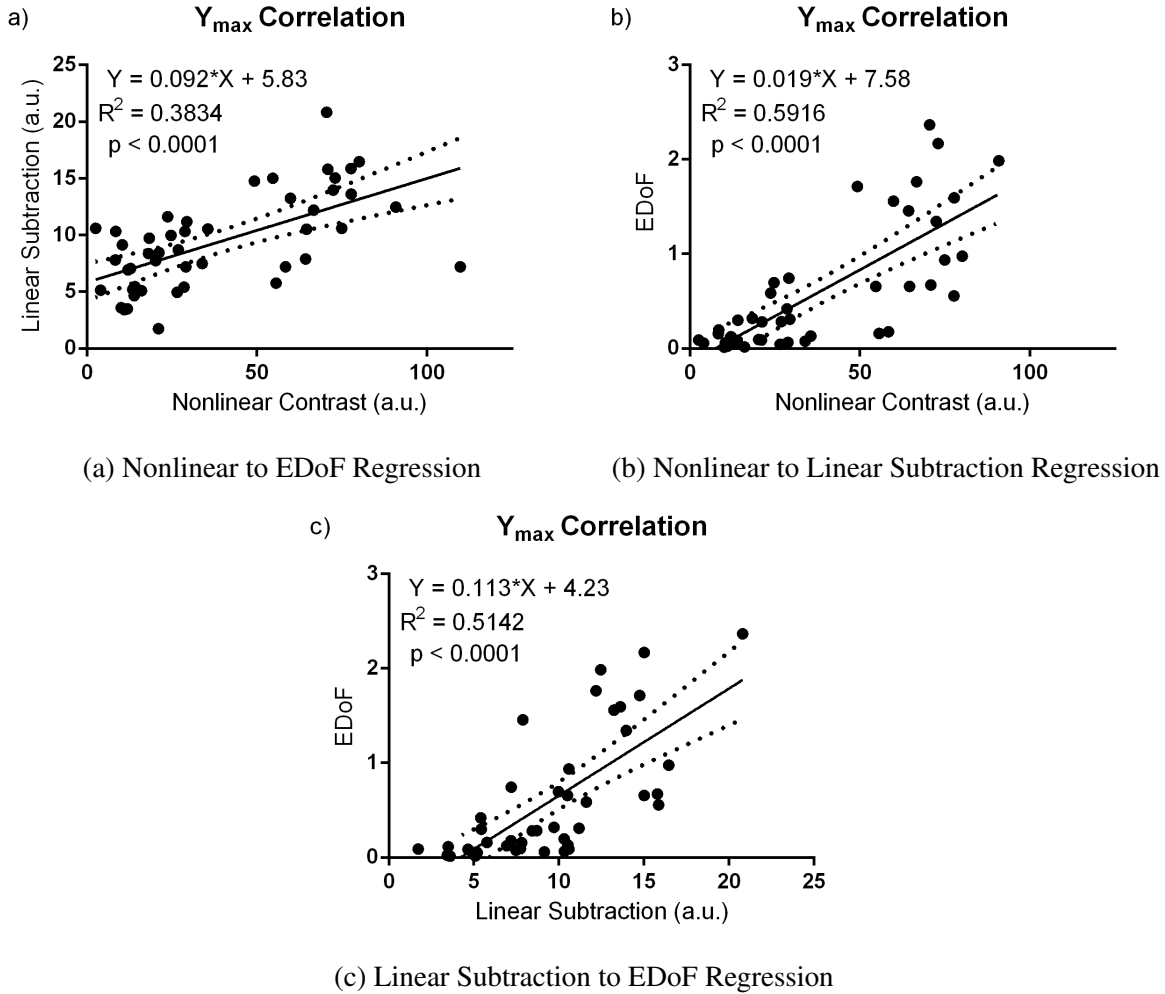


Figure 2.6: Linear regression of the maximum amplitude of the wash-in curve,  $Y_{max}$ , for the two linear contrast methods in comparison to gold-standard nonlinear CEUS. (a) The linear subtraction estimate was statistically significantly correlated with the gold-standard  $Y_{max}$  from nonlinear CEUS ( $R^2 = 0.3834$ ,  $p < 0.0001$ ). (b) The EDoF estimate exhibited marginally higher correlation ( $R^2 = 0.5916$ ,  $p < 0.0001$ ). (c) Comparing the linear methods yielded a coefficient of determination of  $R^2 = 0.5142$ ,  $p < 0.0001$ . Nonlinear and conventional linear CEUS data are reported in arbitrary units (a.u.).

The time to peak enhancement estimated using the conventional linear method was moderately correlated to the nonlinear CEUS estimate ( $r = 0.5553$ , Fig. 2.7). The EDoF correlation coefficient was higher than that of conventional linear subtraction ( $r = 0.6889$ ); the difference in correlation coefficients was not statistically significant ( $p = 0.2983$ ). The correlation for estimated  $T_{max}$  between the two linear techniques was weaker ( $r = 0.4334$ ) than their correlations

to the nonlinear estimate.

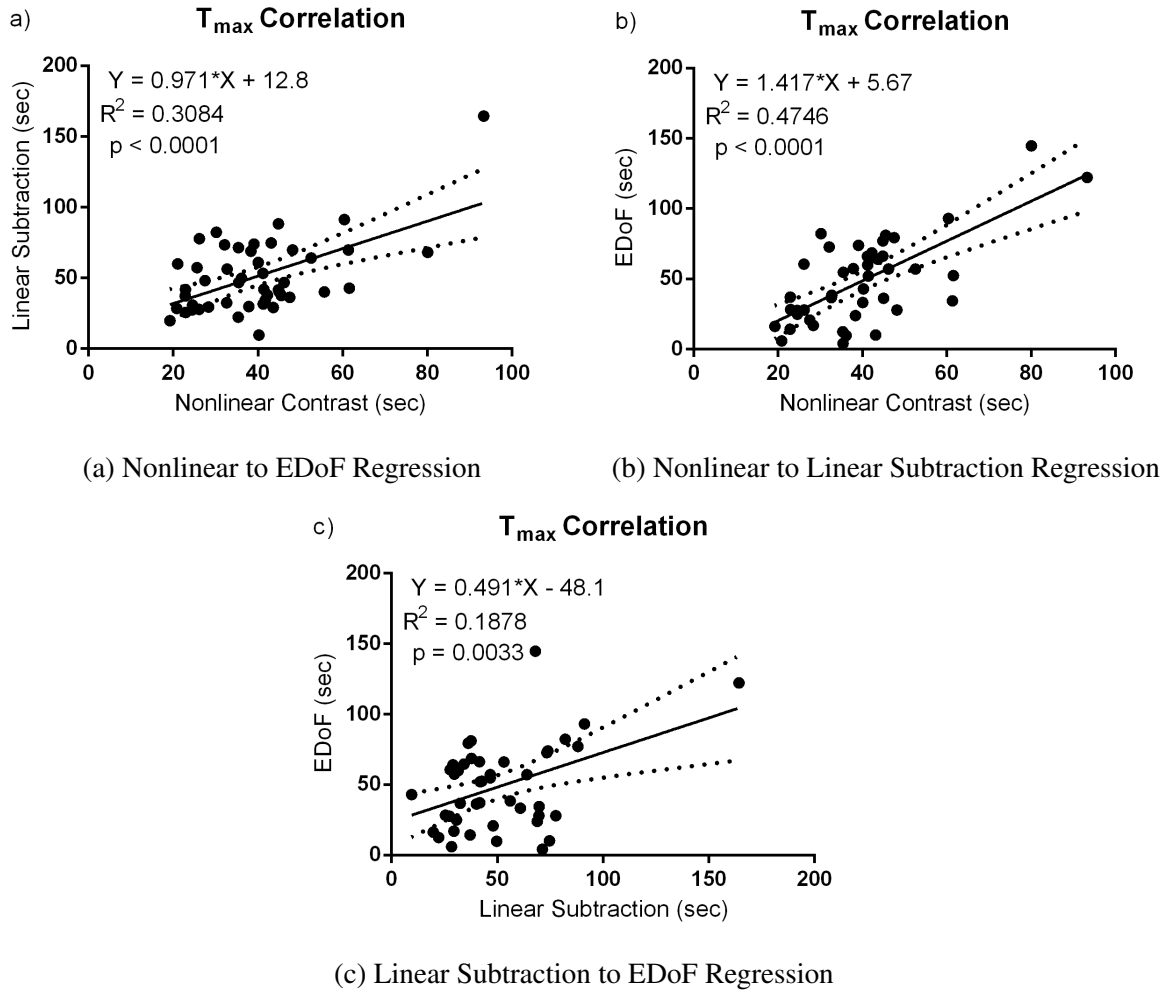


Figure 2.7: Linear regression for time of maximum enhancement  $T_{max}$  estimated using the two linear contrast methods in comparison to gold-standard nonlinear CEUS. The (a) linear subtraction method ( $R^2 = 0.3084$ ,  $p < 0.0001$ ) was similar in performance to the (b) EDoF method ( $R^2 = 0.4746$ ,  $p < 0.0001$ ). (c) The two linear methods were weakly correlated ( $R^2 = 0.1878$ ,  $p = 0.0033$ ).

For the final fitting variable, the shape parameter  $\alpha_v$  (Fig. 2.8), the estimate obtained with conventional linear CEUS was not significantly correlated to the nonlinear CEUS estimate ( $r = 0.2054$ ,  $p = 0.1710$ ). The EDoF estimate was moderately correlated with the nonlinear estimate ( $r = 0.5618$ ,  $p < 0.0001$ ). The difference in correlation coefficients was not statistically significant ( $p = 0.0854$ ). The correlation in  $\alpha_v$  parameter estimates between EDoF and linear subtraction was again weaker than their correlations to the nonlinear estimate ( $r = 0.3636$ ).

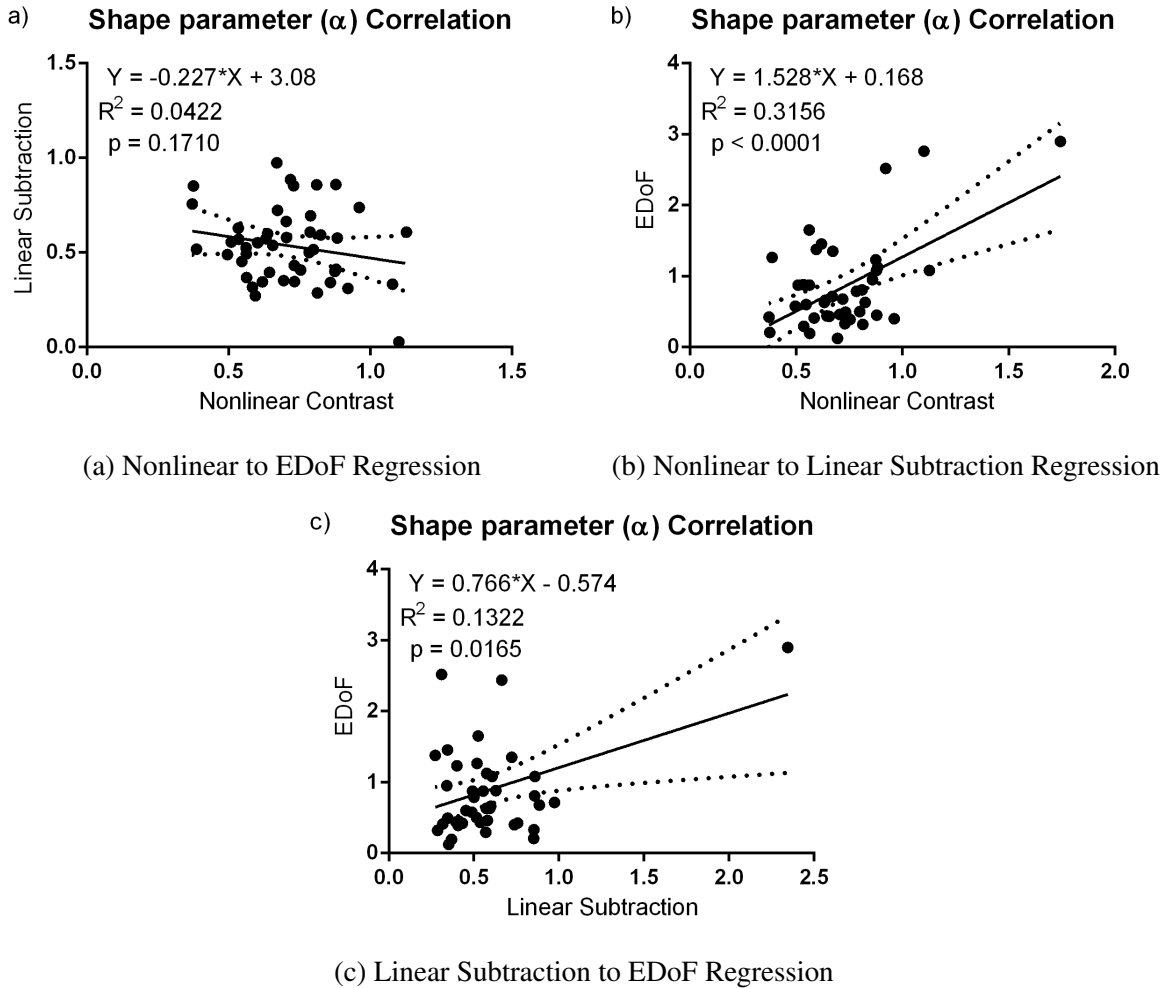


Figure 2.8: Linear regression for the wash-in curve shape parameter,  $\alpha_v$ , estimated using the two linear contrast methods in comparison to gold-standard nonlinear CEUS. The (a) linear subtraction method ( $R^2 = 0.0422$ ,  $p = 0.1710$ ) was outperformed by the (b) EDoF method ( $R^2 = 0.3156$ ,  $p < 0.0001$ ). The correlation in  $\alpha_v$  parameter estimates between the linear techniques was weak ( $R^2 = 0.1322$ ,  $p = 0.0165$ ). All reported units are dimensionless.

## 2.5 Discussion

This study introduces an alternative approach to linear CEUS processing that relies on the non-Rayleigh speckle statistics of contrast-enhanced tumor images. In this approach, the PDFs of the backscattered echoes are described using either a Nakagami or gamma distribution for the first-order statistics of the magnitude and intensity signals, respectively. The number of effective degrees of freedom of the fitted Nakagami distribution increases over baseline during contrast enhancement to produce well-behaved wash-in curves. The measurement of effective degrees of freedom, EDoF, is therefore a promising alternative to baseline subtraction for linear quantification of contrast enhancement.

Effective degrees of freedom is an index of the complexity of the mixture weighting function,  $\omega_i(t)$ , as opposed to microbubble concentration as in conventional time-intensity methods. Therefore, the EDoF wash-in curve should indicate the time dependence of the spatial heterogeneity of the microbubble concentration. The fact that the EDoF method generally underestimated the wash-in rate of the tumor as compared to nonlinear CEUS is consistent with this interpretation. For bolus imaging, the magnitude signal peak is mostly due to the first pass of the initial injection concentration through fast-flowing vessels. While the total microbubble concentration begins to drop after the first pass of the bolus, the mixture weighting function complexity continues to increase as the slow-flow vascular components perfuse with contrast agent. The time of highest contrast enhancement, when the nonlinear wash-in curve peaks, should precede the most heterogeneous spatial distribution of microbubbles, which is expected to coincide with the peak of the EDoF wash-in curve. As a consequence, the interpretation of the EDoF metrics should reflect this difference in the physical basis of the wash-in curves. The microbubble concentration heterogeneity implicitly depends on the vascular organization, so it is hypothesized that the EDoF method would be more sensitive to vascular tortuosity than conventional time-intensity techniques. Specifically, the magnitude of the EDoF wash-in curve peak should correlate with vascular organizational complexity. This prediction could be tested using post-mortem contrast-enhanced micro-CT (*e.g.*, [28, 29]).

The wash-in curves obtained using the two linear processing methods were compared to the nonlinear CEUS gold standard via their area under curve and via estimation of three curve fit-



ting parameters. All techniques are intended to quantify tumor vasculature, so some degree of correlation is expected between all forms of processing. Weak-to-moderate correlations were found for curve-fit parameters estimated using both linear subtraction and the EDoF method in comparison to those estimated using nonlinear CEUS. For all four parameters, the EDoF-to-nonlinear CEUS correlation was slightly higher than the linear-to-nonlinear CEUS correlation, but not significantly so. Intriguingly, despite being drawn from the same set of B-mode cine loops, the EDoF-to-linear CEUS correlation was weaker than the EDoF-to-nonlinear correlation. This again implies that the two linear processing techniques are measuring different aspects of tumor perfusion. The marginal improvement in correlation to nonlinear CEUS gained from EDoF processing could stem from the technique more reliably generating well behaved wash-in curves.

The EDoF approach was able to generate indicator wash-in curves without the need for subtraction of a baseline image. This feature of the EDoF method eliminates errors associated with registering the pre-injection baseline image with a post-injection dataset. There is a risk, particularly with manual tail vein injections, of out-of-plane motion due to subject manipulation. Furthermore, the EDoF method demonstrates reduced frame-to-frame variability compared to linear subtraction, thereby indicating improved robustness to physiological or transducer motion artifacts. The ease of implementation of the EDoF method, requiring only a B-mode cine loop of the contrast wash-in, enables it to be applied retrospectively. Although not theoretically justified, the method appears to produce viable wash-in curves on log-compressed data [16], so the method could potentially be used to salvage preclinical datasets that did not perform adequately in conventional linear subtraction analysis. Users needing to salvage their datasets will more typically have video data rather than raw data. The issue of applicability of this type of analysis to log-compressed data has been previously debated in the context of Nakagami tissue characterization [30] [31] [32]. The ability to perform linear contrast analysis without an image subtraction step would also benefit three-dimensional imaging where registration of pre- and post-enhancement images is particularly problematic.

In view of the mathematical equivalence of the EDoF parameter,  $n^*$ , and the Nakagami shape parameter,  $m$ , computed using the TNC method, it is surprising that the resulting wash-in curves do not match when the techniques are applied to linearized images (*e.g.*, Figs. 2.4(a)

and 2.4(c)). This observation implies that a value of  $m = n^*/2$  computed over a large ROI containing Nakagami-distributed speckle is not necessarily equal to the average value of  $m$  computed within multiple overlapping subregions covering the ROI. This interpretation was confirmed numerically using vectors of Nakagami-distributed random samples drawn from distributions with known values of  $m$ . At window lengths comparable to the TNC windows used in Fig. 2.4, the average sliding-window estimate of  $m$  differed from the whole-population estimate of  $m$  by approximately 20%. This result can be understood by recalling that  $m$  is equal to the squared SNR of the intensity signal, *i.e.*,  $m = E(I)^2/\text{var}(I)$  [19]. The average of many estimates of an SNR is not necessarily equal to the average value of the signal divided by the average value of the noise, where the latter calculation corresponds to estimating a single value of  $m$  over the entire tumor cross-section. Therefore, the EDoF and TNC methods are related but not interchangeable approaches to CEUS image analysis.

The EDoF method failed to produce sigmoidal wash-in curves for very small tumors (approximate volume  $\leq 5 \text{ mm}^3$ ). This limitation may be due to a violation of the assumption of a sufficiently large number of independent samples of the backscattered signal. If the number of samples contributing to one scatterer population (degree of freedom) is small, then the parameter estimate for that population will have high uncertainty. The total number of independent speckle samples is necessarily small for small tumors. The performance of the EDoF method was also degraded by shadowing artifacts. Our mouse model tended to develop skin surface ulcerations above large tumors that acoustically shadowed the center of the tumor. In these images, the shadowing artifact prevented detection of microbubbles in a substantial proportion of the tumor volume, so little to no change was measured in the effective degrees of freedom of the backscattered signal.

In this paper, the performance of the EDoF method for characterizing vessel networks in healthy tissue was not assessed. Vessel networks in organs such as the kidney are known to exhibit approximately fractal architecture [33]. This observation raises the possibility that the contrast-enhanced signal from such structures may possess a coherent component that is not accounted for in (2.6). The effect of a coherent scattering component on the resulting EDoF wash-in curve requires further investigation.

The main focus of this research was to improve preclinical CEUS image analysis, specif-

ically for those researchers who do not have access to nonlinear-contrast capable transducers and systems. In principle, an analysis method similar to the EDoF technique could be applied to nonlinear CEUS images, thereby creating a pathway for clinical translation of the EDoF method. Clinical application of this method would be particularly valuable if further studies support the interpretation that the EDoF method measures vascular complexity. Currently, vascular tortuosity is inferred from indicator-dilution kinematics and analysis of wash-in curve shape [34]. Wash-in time and, especially, time-to-peak metrics suffer from operator dependence [26]. The fact that an EDoF wash-in curve yields multiple parameters that should each depend on vascular tortuosity represents a distinct advantage of this technique because the consistency of the estimated parameters can be evaluated as a test of their reliability.

## 2.6 Conclusions

The statistical EDoF method of wash-in curve analysis shows promise in improving the robustness of linear CEUS, with the important caveat that curve interpretation may differ from conventional time-intensity analysis. The EDoF method appears to outperform conventional linear CEUS with respect to both the SNR of the wash-in curve and the correlation of the wash-in curve with gold standard nonlinear CEUS. The removal of baseline image subtraction streamlines imaging workflow, eliminates the problems associated with registration of pre- and post-injection images, and enables real-time linear CEUS perfusion imaging. The conceptual basis of the EDoF method presented in this paper implies that EDoF wash-in curves should carry information about vascular complexity, although that hypothesis requires testing in future studies. Vascular tortuosity is characteristic of malignant cancers [35], so EDoF analysis may provide valuable new imaging biomarkers for diagnosis and monitoring of treatment response in cancer patients.

# References

- [1] P. Carmeliet, “Angiogenesis in life, disease and medicine,” *Nature*, vol. 438, no. 7070, pp. 932–936, 2005.
- [2] C. Regg, J.-Y. Meuwly *et al.*, “The quest for surrogate markers of angiogenesis: a paradigm for translational research in tumor angiogenesis and anti-angiogenesis trials,” *Curr. Mol. Med.*, vol. 3, no. 8, pp. 673–691, 2003.
- [3] D. Cosgrove and N. Lassau, “Imaging of perfusion using ultrasound,” *Eur. J. Nucl. Med. Mol. Imaging*, vol. 37, Suppl. 1, pp. S65–S85, 2010.
- [4] M. W. Keller, S. S. Segal *et al.*, “The behavior of sonicated albumin microbubbles within the microcirculation: a basis for their use during myocardial contrast echocardiography,” *Circ. Res.*, vol. 65, no. 2, pp. 458–467, 1989.
- [5] H. Hashizume, P. Baluk *et al.*, “Openings between defective endothelial cells explain tumor vessel leakiness,” *Am. J. Pathol.*, vol. 156, no. 4, pp. 1363–1380, 2000.
- [6] B. Warren, “The vascular morphology of tumors,,” in *Tumor Blood Circulation: Angiogenesis, Vascular Morphology, and Blood Flow of Experimental and Human Tumors*, H.-I. Peterson, Ed. Boca Raton, FL: CRC Press, 1979, pp. 1–48.
- [7] M.-X. Tang, H. Mulvana *et al.*, “Quantitative contrast-enhanced ultrasound imaging: a review of sources of variability,” *Interface Focus*, vol. 1, no. 4, pp. 520–539, 2011.
- [8] D. E. Goertz, E. Cherin *et al.*, “High frequency nonlinear b-scan imaging of microbubble contrast agents,” *IEEE Trans. Ultrason. Ferroelectr. Freq. Contr.*, vol. 52, no. 1, pp. 65–79, 2005.
- [9] A. Needles, M. Arditi *et al.*, “Nonlinear contrast imaging with an array-based micro-ultrasound system,” *Ultrasound Med. Biol.*, vol. 36, no. 12, pp. 2097–2106, 2010.
- [10] F. S. Foster, J. Mehi *et al.*, “A new 15-50 MHz array-based micro-ultrasound scanner for preclinical imaging,” *Ultrasound Med. Biol.*, vol. 35, no. 10, pp. 1700–1708, 2009.
- [11] F. S. Foster, J. Hossack, and S. L. Adamson, “Micro-ultrasound for preclinical imaging,” *Interface Focus*, vol. 1, no. 4, pp. 576–601, 2011.
- [12] P.-H. Tsui, C.-K. Yeh, and C.-C. Chang, “Microvascular flow estimation by microbubble-assisted Nakagami imaging,” *Ultrasound Med. Biol.*, vol. 35, no. 4, pp. 653–671, 2009.

- [13] X. Gu, M. Wei *et al.*, “Flow quantification with Nakagami parametric imaging for suppressing contrast microbubbles attenuation,” *Ultrasound Med. Biol.*, vol. 39, no. 4, pp. 660–669, 2013.
- [14] F. Destrempes, J. Meunier *et al.*, “Segmentation in ultrasonic b-mode images of healthy carotid arteries using mixtures of Nakagami distributions and stochastic optimization,” *IEEE Trans. Med. Imaging*, vol. 28, no. 2, pp. 215–229, 2009.
- [15] Z. Akkus, J. G. Bosch *et al.*, “Statistical segmentation of carotid plaque neovascularization,” *Proc. SPIE*, vol. 8675, article 867506, 2013.
- [16] M. R. Lowerison, M. N. Hague *et al.*, “A two-component speckle model for detection of microbubble signals in linear contrast-enhanced ultrasonography,” *Proceedings of Meetings on Acoustics*, vol. 19, article 075026, 2013.
- [17] L. Trailovic and L. Pao, “Variance estimation and ranking of Gaussian mixture distributions in target tracking applications,” *Proc. 41st IEEE Conf. Decision and Control*, vol. 2, pp. 2195–2201, 2002.
- [18] P. M. Shankar, “Concepts of probability and statistics,” in *Fading and Shadowing in Wireless Systems*. Philadelphia: Springer, 2012, ch. 2, pp. 7–102.
- [19] P. M. Shankar, “A general statistical model for ultrasonic backscattering from tissues,” *IEEE Trans. Ultrason. Ferroelectr. Freq. Contr.*, vol. 47, no. 3, pp. 727–736, 2000.
- [20] R. B. D’Agostino and M. A. Stephens, “Tests based on EDF statistics,” in *Goodness of Fit Techniques*. New York: Dekker, 1986, pp. 97–193.
- [21] S. C. Choi and R. Wette, “Maximum likelihood estimation of the parameters of the gamma distribution and their bias,” *Technometrics*, vol. 11, no. 4, pp. 683–690, 1969.
- [22] M. Evans, N. A. J. Hastings, and J. B. Peacock, “Gamma distribution,” in *Statistical Distributions*. New York: Wiley, 2000, pp. 75–81.
- [23] B. Goulet, W. Kennette *et al.*, “Nuclear localization of maspin is essential for its inhibition of tumor growth and metastasis,” *Lab. Invest.*, vol. 91, no. 8, pp. 1181–1187, 2011.
- [24] “RF data export instructions for Vevo 2100,” White Paper, VisualSonics, Feb. 2011.
- [25] M. T. Madsen, “A simplified formulation of the gamma variate function,” *Phys. Med. Biol.*, vol. 37, no. 7, p. 1597, 1992.
- [26] C. Strouthos, M. Lampaskis *et al.*, “Indicator dilution models for the quantification of microvascular blood flow with bolus administration of ultrasound contrast agents,” *IEEE Trans. Ultrason. Ferroelectr. Freq. Contr.*, vol. 57, no. 6, pp. 1296–1310, 2010.
- [27] G. W. Snedecor and W. G. Cochran, “Correlation,” in *Statistical Methods*. Ames, IA: Iowa State University Press, 1989, ch. 10, pp. 177–193.

- [28] M. D. Bentley and M. C. Ortiz, "The use of microcomputed tomography to study microvasculature in small rodents." *Am. J. Physiol. Regul. Integr. Comp. Physiol.*, vol. 282, no. 5, pp. R1267–79, 2002.
- [29] C. M. Downey, A. K. Singla *et al.*, "Quantitative ex-vivo micro-computed tomographic imaging of blood vessels and necrotic regions within tumors," *PLOS One*, vol. 7, no. 7, p. e41685, Jul. 2012.
- [30] P. M. Shankar, "Estimation of the Nakagami parameter from log-compressed ultrasonic backscattered envelopes," *J. Acous. Soc. Am.*, vol. 114, no. 1, pp. 70–72, 2003.
- [31] P.-H. Tsui, S.-H. Wang, and C.-C. Huang, "The effect of logarithmic compression on estimation of the Nakagami parameter for ultrasonic tissue characterization: a simulation study," *Phys. Med. Biol.*, vol. 50, no. 14, pp. 32–35, 2005.
- [32] P. M. Shankar, "Comments on 'The effect of logarithmic compression on the estimation of the Nakagami parameter for ultrasonic tissue characterization'," *Phys. Med. Biol.*, vol. 51, no. 8, pp. L23–26; author reply L27–29, 2006.
- [33] R. Karshafian, P. N. Burns, and M. R. Henkelman, "Transit time kinetics in ordered and disordered vascular trees," *Phys. Med. Biol.*, vol. 48, no. 19, p. 3225, 2003.
- [34] J. M. Hudson, R. Williams *et al.*, "Quantifying vascular heterogeneity using microbubble disruption-replenishment kinetics in patients with renal cell cancer," *Invest. Radiol.*, vol. 49, no. 2, pp. 116–123, Feb. 2014.
- [35] J. W. Baish and R. K. Jain, "Fractals and cancer," *Cancer Res.*, vol. 60, no. 14, pp. 3683–3688, 2000.

## Chapter 3

# Compound Speckle Model Detects Anti-Angiogenic Tumor Response in Preclinical Nonlinear Contrast-Enhanced Ultrasonography

*The contents of this chapter has been adapted from “Compound Speckle Model Detects Anti-Angiogenic Tumor Response in Preclinical Nonlinear Contrast-Enhanced Ultrasonography”, published in Medical Physics, vol. 44, no. 1, p. 99-111, 2017, by M. R. Lowerison, J. J. Tse, M. N. Hague, A. F. Chambers, D. W. Holdsworth, and J. C. Lacefield. \**

---

\*This is the peer reviewed version of the following article: “Compound Speckle Model Detects Anti-Angiogenic Tumor Response in Preclinical Nonlinear Contrast-Enhanced Ultrasonography”, published in Med. Phys., by M. R. Lowerison, J. J. Tse, M. N. Hague, A. F. Chambers, D. W. Holdsworth, and J. C. Lacefield, 2017, which has been published in final form at doi:10.1002/mp.12030. This article may be used for non-commercial purposes in accordance with Wiley Terms and Conditions for Self-Archiving.

## 3.1 Introduction

Tumor angiogenesis leads to the growth of structurally chaotic and tortuous vessel networks in comparison to the organized micro-circulation of healthy tissues [1]. It has been proposed that successful anti-VEGF therapies function in part through a process of vascular normalization [2], where the vascular network is modified toward a more organized structure that improves local blood flow and relieves regional hypoxia. Vascular perfusion imaging, such as contrast-enhanced ultrasound (CEUS), is valuable in evaluating the vascular normalization effects of anti-angiogenic therapies. However, conventional CEUS image analysis involves modeling the wash-in kinetics of a microbubble contrast agent bolus using a point estimate of contrast signal intensity as a surrogate for its concentration. This overlooks additional information that may be available from the first-order speckle statistics in a CEUS image. In particular, structural differences in tumor micro-circulation should lead to heterogeneous contrast enhancement within a region of interest (ROI). A method to quantify those heterogeneities would provide a useful tool for tumor vascular characterization.

This paper proposes a method for analyzing the first-order speckle statistics of sub-harmonic CEUS images from tumors. This statistical model assumes that the signal intensity can be expressed as a compound distribution of exponential probability density functions (PDFs). The relative contribution of each exponential speckle distribution to the image is expressed using a weighting function. The weighting function characterizes the heterogeneity of the contrast speckle pattern which should correspond to microbubble spacing among vessel lumina in the tumor. The proposed method is an extension of our previous work on analysis of B-mode speckle in contrast-enhanced images [3]. The model was first proposed in [4], where the ability to distinguish between different vascular environments in and around the tumor was demonstrated. Further work was required to a) compare the estimates of fractal dimension acquired from this technique to contrast-enhanced casting CT and b) validate the vascular quantification generated through this method using gold-standard estimates of micro-vascular density (MVD) from histology.

Other groups have used CEUS to assess tumor perfusion heterogeneity. To account for flow heterogeneity, a log-normal perfusion model was applied to CEUS data collected from



an anti-angiogenic clinical drug trial on metastatic renal cell carcinomas [5]. They found that velocity filtering reduced measurement variability and improved treatment effect sensitivity. Work has also been done on the diagnostic usefulness of spatial heterogeneity. Microvascular morphology and architecture in breast lesions, assessed using micro flow image processing on clinical CEUS data, were found to reliably distinguish between benign and malignant tumors [6]. However, their classification was a qualitative, subjective analysis by radiologists. A follow-up study [7] performed quantitative perfusion analysis showing that perfusion features, such as regional enhancement and morphologic heterogeneity, provided valuable indices for differentiating between malignant and benign breast tumors. Similar studies have applied a clustering algorithm to CEUS images from murine kidneys [8], where it was found that the number of clusters (related to enhancement heterogeneity) could discriminate between control kidneys and those exposed to anti-angiogenic drugs. Contrast ultrasound dispersion imaging, a spatiotemporal similarity analysis, has demonstrated closer agreement in the localization of prostate cancer on histology sections than conventional CEUS in a preliminary clinical evaluation [9]. Finally, the fractal dimension of tumors has been estimated using the relative dispersion of two CEUS ROIs [10]. It was found that CEUS fractal dimension showed good agreement to, and discrimination of, MVD for two different cell lines of prostate cancer in mice. Our technique, in contrast, quantifies spatial heterogeneity and estimates fractal dimension using a single ROI encompassing the entire tumor cross section analyzed at two time points during wash-in.

This paper introduces our method for analyzing the first-order speckle statistics on a time-series of nonlinear CEUS images acquired from a mouse xenograft model. Animals were inoculated with a human breast cancer cell line (MDA-MB-231-D3H2-LNluc) and treated with a monoclonal anti-VEGF antibody (murine version bevacizumab B20-4.1.1) as an anti-angiogenic therapy. The method is applied to contrast-specific, amplitude-modulated, CEUS cine loops acquired after a bolus injection of microbubbles. For validation, animals were perfused with a quick-fixing erbium-based silicone vascular perfusion agent at end point. Whole animals and selected organs were imaged in a micro-CT scanner to generate three-dimensional volumes of perfused vasculature. Tissue samples were collected for histological analysis. We demonstrate the ability of the weighting function analysis to detect a significant reduction in

MVD, due to the anti-angiogenic therapy, as measured by area under curve during contrast wash-in. We also evaluate the ability of the compound statistical method to detect changes in tumor vascular complexity in response to bevacizumab, using vascular fractal dimension estimated with post-mortem micro-CT as a gold-standard.

## 3.2 Statistical Model

### 3.2.1 Nonlinear Contrast Speckle Statistics

An assumption used in this study is that the statistics of CEUS images, which depend on the concentration of microbubble subpopulations, can be considered using the same models as speckle formation in B-mode images. We only consider the statistics of uncompressed, intensity signal data (*i.e.*, the squared magnitude of the echo envelope measured prior to logarithmic compression). The model assumes that the demodulated analytic signal,  $s$ , of a well dispersed, randomly scattering microbubble solution of homogeneous concentration will follow a complex zero-mean Gaussian PDF. Local changes in microbubble spacing, such as a high concentration microbubble bolus surrounded by a low-intensity tissue background in a contrast-specific image, can be approximated by a mixture of these probability density functions. It follows that the backscatter intensity,  $I$ , of an arbitrary microbubble population can be expressed using a weighted mixture distribution of  $k$  speckle sub-regions:

$$f_k[I] = \sum_{i=1}^k w_i p_i(I), \quad (3.1a)$$

$$\sum_{i=1}^k w_i = 1, \quad w_i \geq 0, \quad (3.1b)$$

where every  $p_i(I)$  is an exponential distribution [11], assuming fully developed speckle. We are only considering the case where every subpopulation is modeled as randomly distributed scatterers (microbubbles) at relatively high concentrations.

A closer approximation to the bolus diffusion example above would account for a diffusion gradient of indicator, which necessitates a continuous weighting function. To relax the constraint on discrete sub-populations of fully developed speckle, we generalize Eq. 3.1a by

parameterizing the weighting function,  $w(\theta)$ , and expressing the exponential distribution as conditional on this new parameter,  $\theta$ :

$$p(I|\theta) = \theta e^{-\theta I}. \quad (3.2)$$

Therefore, the new speckle distribution can be expressed as the compound distribution:

$$f[I] = \int_{\Theta} w(\theta) p(I|\theta) d\theta. \quad (3.3)$$

It has been shown by [12] that an arbitrary vascular network can be simplified by assuming a fractal branching geometry that yields a distribution of vessel diameters and flow velocities governed by a log-normal distribution. Earlier work demonstrated that intercapillary distance can also be modeled as a log-normal distribution [13]. Therefore, a random cross section (*i.e.*, image plane) through a heterogeneous multiple-vessel network, modeled here as random sampling from the distribution of vessel sizes and locations, would be expected to display a log-normal distribution of flow velocities and capillary spacing. As the contrast signal intensity is determined by the microbubble concentration, and assuming good tissue suppression, it is reasonable to state that a log-normal weighting function is most appropriate for the compound model. However, this form of compound model has no known analytic solution [14], which limits its practicality as a model for image analysis. As an alternative, the gamma family of PDFs can serve as an approximation to the log-normal distribution [15], with the distinct advantage that its compound distribution is well characterized. This approximation is further justified by [16], which showed that the spatial distribution of terminal endpoints (*i.e.* capillaries) of an arterial tree model, grown by the method of constrained constructive optimization, was well characterized by a two-parameter gamma distribution. Therefore, the weighting function of the compound distribution is assumed to belong to the gamma family of distributions:

$$w(\theta|\alpha, \beta) = \frac{\alpha^\beta}{\Gamma(\beta)} \theta^{\beta-1} e^{-\alpha\theta}, \quad (3.4)$$

where  $\alpha$  and  $\beta$  are hyper-parameters. Substitution of Eq. 3.2 and Eq. 3.4 into Eq. 3.3 yields the model's approximation to the backscatter intensity distribution, a Type-II Pareto (Lomax) probability function [17]:

$$f(I|\alpha, \beta) = \frac{\beta \alpha^\beta}{(I + \alpha)^{\beta+1}}. \quad (3.5)$$

The hyper-parameters,  $\alpha$  and  $\beta$ , of this compound model can be determined by applying established maximum likelihood estimators (MLE) to intensity samples from the image [18]. The shape of the weighting function can then be reconstructed from the MLE values for further analysis. To draw from the established literature [19, 20] examining the relationship between the log-normal distribution's shape parameter and the fractal dimension of the vascular network, it is useful to demonstrate that the log-normal shape parameter ( $\sigma_{LN}$ ) can be estimated from the gamma parameter,  $\beta$ . By assuming that the coefficient of variation for the two distributions are equal [21], we can state that:

$$\sigma_{LN} = \sqrt{\ln(\beta^{-1} + 1)}. \quad (3.6)$$

It is worth noting that, in this definition of the gamma probability function, the relative dispersion of the distribution is inversely proportional to the square-root of the  $\beta$  parameter. Relative dispersion has been shown to be useful in characterizing the fractal dimension of CEUS images [10].

Each frame in a CEUS cine loop yields a separate estimate of  $\alpha$  and  $\beta$ , so the final step in this model is to make explicit the time-dependence of the hyper-parameters,  $\alpha(t)$  and  $\beta(t)$ , and likewise the time-dependence of the weighting function,  $w(\theta|\alpha(t), \beta(t))$ . Tissue perfusion can then be analyzed from the kinematics of  $w(\theta|\alpha(t), \beta(t))$ , as detailed in section 3.3.4. The log-normal shape parameter ( $\sigma_{LN}$ ) is expected to depend only on microvascular architecture in a fully perfused tumor. Therefore, fractal dimension is estimated as  $\Delta\sigma_{LN} = \sigma_{LN}(t)_{max} - \sigma_{LN}(t)_{min}$  for peak and baseline enhancement, respectively.

### 3.2.2 Parameter Estimation

The maximum likelihood estimates of the Pareto shape and scale parameters of the speckle in the contrast-specific frame acquired at time  $t$ ,  $\hat{\alpha}(t)$  and  $\hat{\beta}(t)$ , are computed from the intensity samples in the ROI as follows [18]:

$$l = n \log(\beta) - n \log(\alpha) - (1 + \alpha) \sum_{i=1}^n \log\left(1 + \frac{I_i}{\alpha}\right), \quad (3.7)$$

and

$$\frac{\partial l}{\partial \alpha} = -\left(\frac{n}{\alpha}\right) + \left[\frac{(1 + \beta)}{\alpha}\right] \sum_{i=1}^n \left[\frac{I_i}{\alpha + I_i}\right], \quad (3.8)$$

$$\frac{\partial l}{\partial \beta} = \left(\frac{n}{\beta}\right) - \sum_{i=1}^n \log\left(1 + \frac{I_i}{\alpha}\right), \quad (3.9)$$

where  $n$  is the number of independent intensity samples within the ROI and  $I_i$  is the intensity of the  $i$ th sample. In principle, this method can be applied to either the intensity samples in the B-mode frame, the intensity samples from the contrast-specific frame, or both. Analysis of contrast-specific frames is preferred due to superior tissue suppression because the gamma weighting function is justified based upon modeling of vascular networks. Based on Eq. 3.8 and Eq. 3.9, there is no closed form solution to Eq. 3.7, but the log-likelihood is strictly concave, permitting numerical methods to solve for the parameters [18]. As such, Eq. 3.7 can be solved using an unconstrained nonlinear optimization with initial guesses from the method of moments as the starting values:

$$\alpha_0 = -0.5 \left( \frac{\bar{I}^2}{\sigma_I - 1} \right), \quad (3.10)$$

$$\beta_0 = 0.5 \bar{I} \left( \frac{\bar{I}^2}{\sigma_I} + 1 \right), \quad (3.11)$$

where  $\bar{I}$  and  $\sigma_I$  are the sample mean and standard deviation of the intensity, respectively. Parameter estimation using the above MLE is generally stable for even relatively small datasets (*i.e.* a low number of intensity samples within a small ROI). In a Monte Carlo simulation, we found that the  $\alpha$  estimator converged to an asymptote at around  $n = 50$ , with a coefficient of variation of approximately 0.02, and the  $\beta$  estimator converged at a sample size of  $n = 120$ , with a coefficient of variation around 0.1. The smallest ROI used in this study had  $n > 2000$  samples.

## 3.3 Materials and Methods

### 3.3.1 Cell Line and Animal Model

The Western University Council on Animal Care approved all experiments used in this study. The human breast carcinoma MDA-MB-231-D3H2-LNluc cell line (D3H2-LN, Caliper Life-Sciences, Alameda, CA) [22] was suspended in a mixture of 50% phosphate-buffered saline and 50% Matrigel (BD Biosciences, Mississauga, ON, Canada). For xenograft inoculation, 36 eight-week old female nude mice (nu/nu, Charles River, MA) were sedated and 50  $\mu$ L ( $2 \times 10^6$  cells) of the cell solution was injected into the right abdominal mammary fat pad without an incision, as per the tumor inoculation procedure described by Goulet *et al.* [23].

A stock solution (17.26 mg/mL) of Murine version bevacizumab (B20-4.1.1, Genentech, South San Francisco, CA) was diluted with PBS to a concentration of 1.1 mg/mL. On day 2 of the experiment (48 hours after tumor cell inoculation), half of the mice (n = 18) were injected intravenously with a dose of 5 mg/kg dilute B20-4.1.1 (approximately 0.1 mL for the average 22 g mouse). The control group (n = 18) received 0.1 mL of PBS vehicle. The antibody or vehicle control were administered twice weekly. Mice were divided into three cohorts with endpoints at the end of T = 1, 2, and 3 weeks.

### 3.3.2 CEUS Image Acquisition

All contrast-enhanced ultrasound imaging was performed using Vevo MicroMarker™ (Fuji-Film VisualSonics Inc., Toronto, ON, Canada) microbubble solution, reconstituted following the instructions given by the supplier (concentration of  $2 \times 10^9$  microbubbles/mL). Animal anesthesia was initiated using a gas induction chamber containing an atmosphere of 3% isoflurane mixed with O<sub>2</sub> and maintained with an anesthesia maintenance mask supplying 2% isoflurane mixed with O<sub>2</sub>. All visible hair was removed from the site of the primary tumor using depilation cream (Nair®, Church & Dwight Co., Inc., Princeton, NJ) and then warmed ultrasound coupling gel (Aquasonic® 100, Parker Laboratories, Inc., Fairfield, NJ) was applied over the entire palpable region.

Sonography was performed at the study endpoint, just prior to animal sacrifice, CT per-

fusion, and formalin fixation. All ultrasound measurements were performed using a Vevo 2100 high-frequency imaging system (VisualSonics Inc.) equipped with a 20 MHz linear array (MS-250, 75  $\mu\text{m}$  nominal axial resolution, 165  $\mu\text{m}$  nominal lateral resolution) transmitting at 18 MHz in nonlinear contrast mode. The transducer was fixed above the center of the tumor and oriented to produce an anatomical transverse imaging plane. Microbubbles were then administered via a tail-vein injection as a manual bolus (50  $\mu\text{L}$ ,  $\sim 1.0 \times 10^8$  microbubbles). Nonlinear (sub-harmonic) imaging was performed over a field of view sized to completely enclose the tumor and cine loops consisting of 1000 two-dimensional images were acquired at a frame rate of 20 Hz.

### 3.3.3 CEUS Image Analysis

Contrast wash-in cine loops were exported as uncompressed, intensity signal data files. Nonlinear contrast images were quantized to 16 bits at a 288 MHz sampling frequency. Regions of interest surrounding the tumor were manually segmented on the first frame of the cine loop with the assumption that the tumor would not move or deform substantially during wash-in. This assumption was qualitatively validated by reviewing all of the cine loops, and can be attributed to the placement of the tumor in a location that does not experience much respiratory motion. All image analysis was performed using MATLAB (version R2013a, The MathWorks Inc., Natick, MA).

Generalized Pareto PDFs (Eq. 3.5) were fit to the contrast intensity samples within the ROI in each frame of each cine loop. Maximum likelihood estimates of the Pareto shape ( $\alpha$ ) and scale ( $\beta$ ) parameters of the nonlinear speckle (Eq. 3.7) were solved for using an unconstrained nonlinear optimization (MATLAB function *fminsearch*, Nelder-Mead simplex direct search) with initial guesses from the method of moments. The maximum number of function evaluations and iterations allowed was set to 200 times the number of sample points. The termination tolerances on the function value and on the input value were set to  $1 \times 10^{-4}$ .

Estimates of the log-normal distribution's shape parameter ( $\sigma_{LN}(t)$ ) were generated at every time-point in the cine loop from the fitted gamma parameter ( $\beta(t)$ ), as in Eq. 3.6. The increase in  $\sigma_{LN}(t)$  from unenhanced tumor to peak enhancement level was taken as a surrogate measure of vascular complexity.

### 3.3.4 Wash-In Curve Analysis

Wash-in time series were constructed to characterize the kinematics of contrast enhancement as measured using conventional nonlinear CEUS processing and a method based upon the weighting function (Eq. 3.4). For conventional nonlinear CEUS, contrast enhancement was estimated by taking the mean nonlinear signal intensity within the ROI for each frame of the cine loop. For the compound method, the weighting function was reconstructed at every time-point  $t$  from the estimates of the Pareto parameters ( $\alpha(t)$  and  $\beta(t)$ ). These were used to estimate the enhanced volume percentage of the tumor over time by determining the area of overlap between the weighting function at timepoint  $t$  and the weighting function of the unenhanced tissue, when  $t = t_0$ . The weighting function is a PDF describing the expected value of the exponential speckle distribution, and so any area of overlap with the baseline weighting function should represent unenhanced populations of speckle. One minus this area of overlap, termed the weighting function discrepancy, was plotted as a function of time and serves as an estimate for total tracer mass in our kinematic analysis.

The local density random walk model (LDRW) [24] was selected for fitting to the bolus wash-in curves due to its superior fitting performance [25]:

$$Y(t) = AUC \left( \frac{e^\lambda}{\mu} \right) \sqrt{\frac{\mu}{t-t_0} \frac{\lambda}{2\pi}} \exp \left[ -\frac{\lambda}{2} \left( \frac{\mu}{t-t_0} + \frac{t-t_0}{\mu} \right) \right] + Y_0 \quad (3.12)$$

where  $AUC$  is the area under the curve,  $\mu$  is the mean transit time of microbubbles,  $\lambda$  controls the curve skewness,  $t_0$  is the time delay, and  $Y_0$  is a signal offset. Curve parameters were calculated using an unconstrained nonlinear minimization (Nelder-Mead method) of the sum of squared residuals. Maximum iterations was set to 800 with a tolerance of  $1 \times 10^{-4}$ . Initial estimates for the parameters were  $AUC$  equal to the integral of unfitted data points,  $\mu$  equal to the time at which  $Y(t) = Y_{max}$ ,  $\lambda = 1$ , and  $t_0$  was set to the first cine loop frame when enhancement reached 10% of the maximum observed intensity,  $Y_{max}$ . Data fitting was truncated in the wash-out tail to where the intensity value decreased to 50% of  $Y_{max}$  in an effort to isolate the first pass of indicator and thus avoid a recirculation artifact.

Quantitative perfusion metrics were calculated from the fitting parameters of the LDRW model to the wash-in curves. In this study, we considered commonly used perfusion parameters



that reflect MVD (from the area under curve, given by the integral of the fitted LDRW model), blood velocity (from the mean transit time, and time to peak, given by  $MTT = \mu$  and  $t_p = \left(\frac{\mu}{2\lambda}\right) \left(\sqrt{1 + 4\lambda^2} - 1\right)$ , respectively), and blood flow (from the wash-in rate, given by  $Y_{max}/t_p$ ).

The area under curve (*AUC*) of CEUS time-intensity data has been previously correlated with micro-vascular density (MVD) [26, 27], which is a key measure of angiogenesis. This perfusion parameter is of particular interest for this study design as successful anti-angiogenic therapy would manifest predictably as a decrease in MVD in the mouse tumor model [28]. Furthermore, *AUC* has been shown to be useful in discriminating responsive from non-responsive patients who are undergoing bevacizumab therapy for hepatocellular carcinoma [29]. Treatment-induced changes in the other parameters, which depend on blood flow rate and velocity, are less easily predicted due to the potential confounding effect of improved blood perfusion from vascular normalization.

### 3.3.5 Whole Mouse CT Contrast Agent Perfusion

The contrast agent used for CT imaging was a quick-fixing erbium-based silicone vascular casting agent. For contrast-enhanced CT analysis, animals were prepared in accordance with [30]. The procedure is briefly outlined below.

Animals were anesthetized, via a mask, with a mixture of 5% isoflurane mixed with O<sub>2</sub>, at a flow rate of 2 mL/min. In preparation for vascular perfusion, animals received an intra-peritoneal injection of 150  $\mu$ L heparin (1000 USP/mL, Sandoz, Boucherville, QC, Canada) contra-lateral to the tumor mass. Heparin was allowed to circulate for 5 minutes before an incision was made laterally, just below the sternum, through the peritoneum to expose the abdominal cavity. The diaphragm was pierced and the incision was then continued along both sides of the ribcage. A hemostat was secured to the sternum and the ribcage was pulled up to reveal the heart.

A 500 mL saline bag was heparinized with 1 mL of the heparin stock solution. The bag was secured to an IV-drip stand and attached to a blunted 21G butterfly catheter (BD Systems, Franklin Lakes, NJ). The blunted catheter was pushed into the left ventricle parallel to the apex of the heart. The right atrium was cut open to allow the saline full passage through the vasculature, displacing blood. Animals were perfused with saline for 20 minutes (250 mL of

heparinized saline), followed by perfusion of the erbium-based contrast agent. The contrast agent was allowed to circulate for 30 minutes before flow was stopped and the silicone was allowed to cure for an additional 20 minutes. Whole animals were then placed in 4% buffered formaldehyde solution for fixation and storage. CT imaging took place at least one month after fixation.

### 3.3.6 CT Imaging

Whole animal CT scans were performed on a GE Vision 120 (speCZT, GE HealthCare, London, ON, Canada). Data were acquired at 90 kVp, 40 mA, over 900 projections at 0.4° increments, with a scan time of 5 minutes. Images were collected and reconstructed with 50  $\mu\text{m}$  isotropic voxels. All samples were imaged with a water filled calibrator to allow for image rescaling into Hounsfield units (HU).

Tumor-containing mammary fat pads, as well as contra-lateral kidneys, were then excised for high resolution CT scanning. Each organ was embedded in paraffin to minimize sample movement and scanned using a GE Locus (GE HealthCare, London, ON, Canada) at 80 kVp, 450 mA, over 900 projections at 0.4° increments, 5 frames averaged per view, with a scan time of 6.5 hours. Images were collected and reconstructed with 20  $\mu\text{m}$  isotropic voxels. A vial of water and bone mimicking calibrator (SB3, Gamex RMI, Middleton, WI) were concurrently run with each sample to allow for image rescaling into HU.

### 3.3.7 CT Analysis

Tumor volume segmentation from the surrounding fat pad in the excised samples was performed in MicroView (v.2.1.2.; GE Healthcare, London, ON, Canada) through manual boundary contouring in parallel planes with 60  $\mu\text{m}$  spacing. Contours were then combined serially to produce three-dimensional ROIs. Kidney samples also underwent the same manual segmentation procedure. Segmented image volumes were exported as Sun TAAC (.vff) uncompressed raster image files and then imported into MATLAB (version R2013a, The MathWorks Inc., Natick, MA) for quantification.

Surrogate estimates of vascular volume fraction were generated by taking the mean HU

value for the segmented tumor mass, under the assumption that the volume contains only soft tissue and contrast agent. Both tumor and kidney texture volumes were then processed using power spectrum analysis to estimate the fractal dimension of the image. The erbium-based contrast medium had an average radiodensity of 3500-4000 HU compared to about 50 HU for soft tissue, so the power spectrum of the image was dominated by the contributions from the enhanced voxels. Fractal dimension was calculated from the slope,  $m_{FD}$ , of a straight line fitted to a log-log plot of power vs. frequency considering the following equation:

$$P(\omega) \propto \omega^{-(9-2F_D)}, \quad (3.13)$$

based on the power spectrum dependence of fractional Brownian motion [31]. The fractal dimension  $F_D$  is calculated as  $F_D = (m_{FD} + 9)/2$ . The slope of the curve is a measure of the spatial correlation in the image volume. Volumes that express some degree of self-similarity (or, more precisely, self-affinity) will have steeper slopes than those that do not, where the upper limit of  $F_D = 4$  represents a volume composed entirely of white noise. An advantage of this technique over direct measures of tortuosity, such as the distance metric, is that it is applied directly to the images, thus avoiding need to preprocess the image data (*e.g.*, by applying a threshold for skeletonization).

### 3.3.8 Histology and Staining

A MVD assessment protocol adapted from [32] was followed. Briefly, 5  $\mu\text{m}$  thick sections were acquired at six evenly spaced locations throughout the paraffin embedded tumors. Hematoxylin and eosin (H&E) staining was applied to all tissues. Each tumor section was examined first at a low magnification (25x) to identify 5 regions of high vascularization, *i.e.*, so-called “hot spots” [33]. Vessels were identified by the presence of CT contrast agent on the histological section (see Fig. 3.4). Slides were digitized with a TISSUEScope™ 4000 (Huron Technologies, Waterloo, ON, Canada) and then exported to ImageJ [34] for processing. Vessel segmentation was performed in a semi-automated fashion by applying Huang’s fuzzy threshold [35] to each RGB channel separately, using a sample of in-frame contrast agent to select threshold limits. Microvessel counts were then performed manually at a higher magnification

(200x; 10x magnification, 20x ocular). MVD is reported as the mean number of microvessels per  $mm^2$  of tumor cross-section.

### 3.3.9 Statistical Analysis

All statistical analysis was performed using GraphPad Prism version 6.04 (GraphPad Software, La Jolla, CA) with a  $p$  value of 0.05 to determine significance. An ordinary two-way ANOVA was conducted on each dataset to compare the main effects of treatment status and tumor age on the dependent measure of vascularity. Treatment status included two levels (control or bevacizumab) and tumor age consisted of three levels (T = 1, 2, and 3 weeks). A linear discriminant analysis (LDA) was performed using the *classify* function in MATLAB, which applies Fisher's LDA algorithm, on each dataset to estimate the classification error of the measured parameter. The performance of each vascularity measure's LDA was assessed by taking the average test error of 10 cycles of 10-fold cross validation, yielding a 95% confidence interval for each measure. Significance of correlation between metrics was calculated via a Pearson's correlation coefficient test.

## 3.4 Results

### 3.4.1 Weighting Function Analysis

The CEUS intensity within the tumor ROI demonstrated a close agreement to the generalized Pareto probability density function (Eq. 3.5) at every frame in each cine loop. The Nelder-Mead simplex direct search, described in section 3.3.3, converged within the supplied termination tolerances for all analyzed frames. An example of a Pareto fitting to two selected cine loop frames, along with their corresponding weighting functions, is shown in Fig. 3.1. The area of overlap in Fig. 3.1d, shaded in green, represents the unenhanced fraction of tumor cross-section at that time point, which can be used as a time-kinetic measure for perfusion analysis. Fig. 3.1e shows a plot of a wash-in curve generated using the technique.

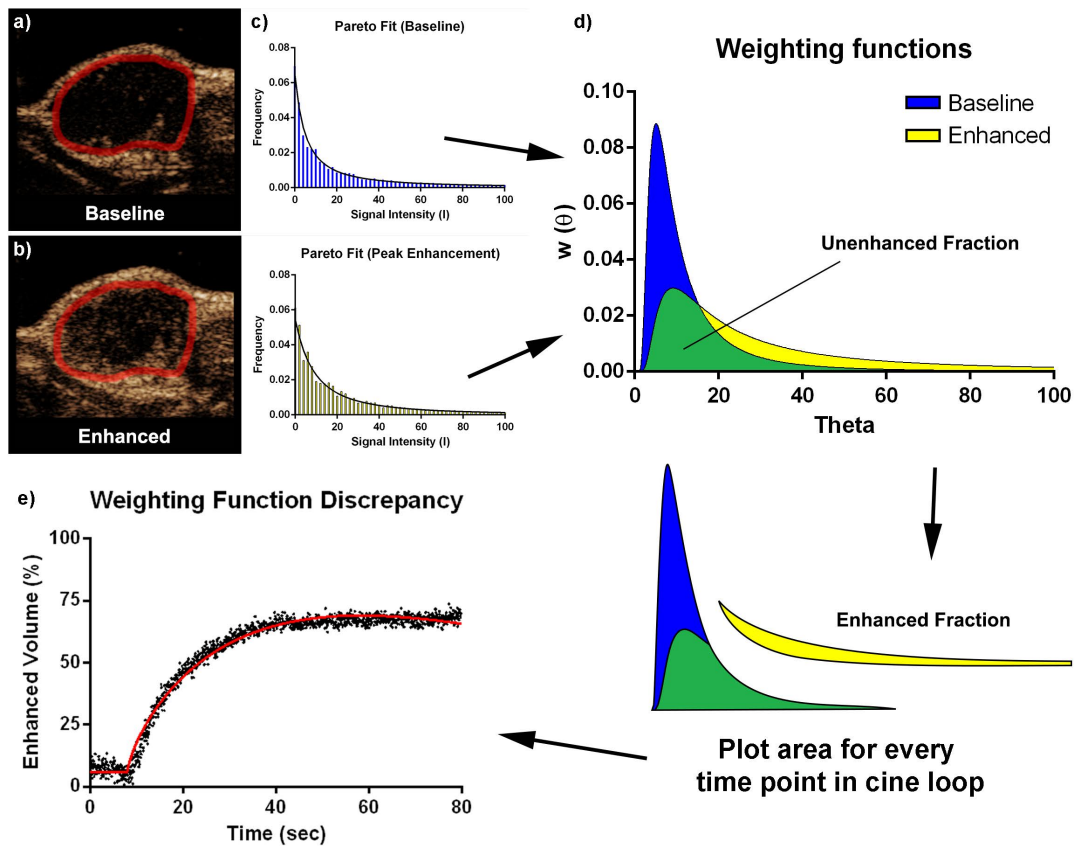


Figure 3.1: Representative CEUS tumor images (anatomical transverse plane, 14 days post inoculation) taken at (a) baseline (unenhanced) and at (b) peak bolus enhancement, with (c) corresponding Pareto fits to intensity ROI histograms, and (d) weighting functions. The change in area of overlap (yellow region) over time in (d) was used to construct wash-in curves as demonstrated in (e).

### 3.4.2 Contrast-Enhanced MicroCT

Fig. 3.2 shows CT images of a mouse acquired after vascular perfusion with an erbium-based silicone contrast agent. A maximum-intensity projection (MIP) image of the (a) whole mouse body reveals well-enhanced vasculature with evidence of complete venous return and no contrast pooling, implying contrast perfusion at the capillary level. Selected organs were extracted and re-scanned at a higher resolution. The following representative images (Fig. 3.2) were generated by applying an isosurface with a threshold of 800 HU: (b) a control kidney (week 1), (c) a control tumor (week 2), and (d) a bevacizumab treated tumor (week 2). Visual inspection supports a decrease in active tumor vasculature in response to bevacizumab therapy, which is supported by (e) the box-plot of the mean HU of the segmented tumor volumes and (f) the corresponding linear discriminant (LDA) analysis used to distinguish treated from untreated (control) tumors.

A two-way ANOVA was conducted on the influence of the two independent variables (drug group, time) on the mean HU of the tumor sample. The only statistically significant effect ( $p < 0.05$ ) was the drug group ( $p = 0.0176$ , Sidak's multiple comparison correction). The 95% confidence interval of the classification accuracy of linear discriminant analysis was  $66\% \pm 2.4\%$ , where tumors lying below the decision boundary were classified as "treated".

### 3.4.3 Surrogate Measures of Vascular Complexity

Fig. 3.3a demonstrates an analysis of the estimated log-normal shape parameter (Eq. 3.6) of the contrast weighting function. The span of this value  $\Delta\sigma_{LN} = \sigma_{LN2} - \sigma_{LN1}$ , where  $\sigma_{LN2}$  is measured at peak enhancement and  $\sigma_{LN1}$  at baseline, is summarized as a box-plot in (b), with the corresponding LDA in (c). The estimated fractal dimension ( $F_D$ ) of the contrast-enhanced CT volumes serves as a validation for these results. Fig. 3.3d is a diagrammatic example of power spectrum analysis on one representative tumor, where the fitted slope was used to estimate  $F_D$ . Fig. 3.3e is a box-plot of tumor fractal dimension data, with kidney data for comparison. A linear discriminant analysis was performed in panel (f).

A two-way ANOVA reported that both techniques had a statistically significant effect for the drug group factor ( $p = 0.0416$  for CEUS log-normal shape parameter,  $p = 0.0275$  for

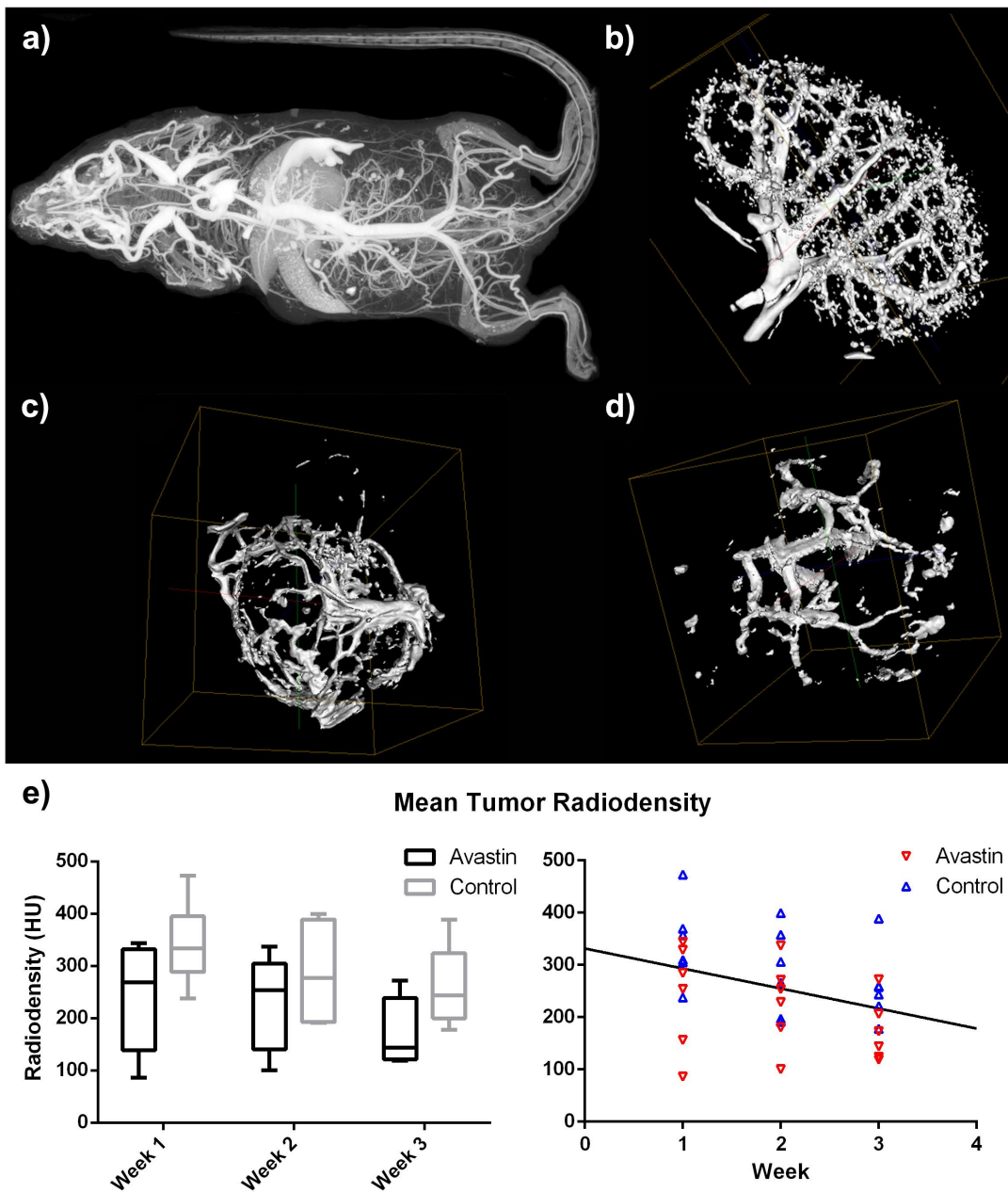


Figure 3.2: Contrast-enhanced CT images of (a) a MIP projection through the whole mouse body, (b) a binarized kidney, (c) a control tumor, and (d) bevacizumab treated tumor. The box-plot in (e) demonstrates the mean HU of the segmented tumor volumes (whiskers are min to max, box extends from the 25th to 75th percentiles), along with the corresponding LDA analysis to the right.

CT  $F_D$ ). A Pearson's correlation test did not report a significant correlation between these two measures of vascular complexity ( $r = 0.322$ ,  $p = 0.06$ ). Linear discriminant analysis of contrast CT data had a 95% confidence interval for classification accuracy of  $61.7\% \pm 1.9\%$ , where tumors lying below the decision boundary were classified as "treated". For the compound CEUS data,  $56.8\% \pm 1.2\%$  of tumors were correctly classified as "treated" when below the boundary.

### 3.4.4 Histological Validation

Representative H&E stained histology sections, taken from both PBS vehicle and bevacizumab treated tumors, are shown in Fig. 3.4. The arrows in panels (c) and (d) highlight the presence of the CT contrast agent perfusing blood vessels at the capillary level. Measures of MVD, shown as a box-plot in panel (e), yielded a clear difference between treated and control groups. A two-way ANOVA on this dataset detected significance for both drug group and time ( $p < 0.001$  for both). Linear discriminant analysis on MVD, panel (f), had a 95% confidence interval for classification accuracy of  $92.8\% \pm 0.19\%$ , where tumors lying below the decision boundary were classified as "treated".

### 3.4.5 Bolus Time-Intensity Kinematics

#### Area Under Curve (AUC):

The AUC for both methods of image analysis are shown in Fig 3.5. Only the compound model detected a significant reduction of AUC in bevacizumab treated tumors ( $p < 0.001$ ). Linear discriminant analysis, panels (c) and (d), accurately classified  $59.7\% \pm 3.7\%$  of tumors using conventional CEUS processing and  $77.5\% \pm 1.7\%$  of tumors with the compound method. For both techniques, tumors lying below the decision boundary were classified as "treated". This is a significant improvement in classification performance ( $p < 0.001$ ). The measures from the two techniques had a significant correlation to each other ( $r = 0.40$ ,  $p = 0.016$ ). Longitudinal trends imply rapid vascularization of untreated tumors, and gradual vessel growth in bevacizumab treated tumors.



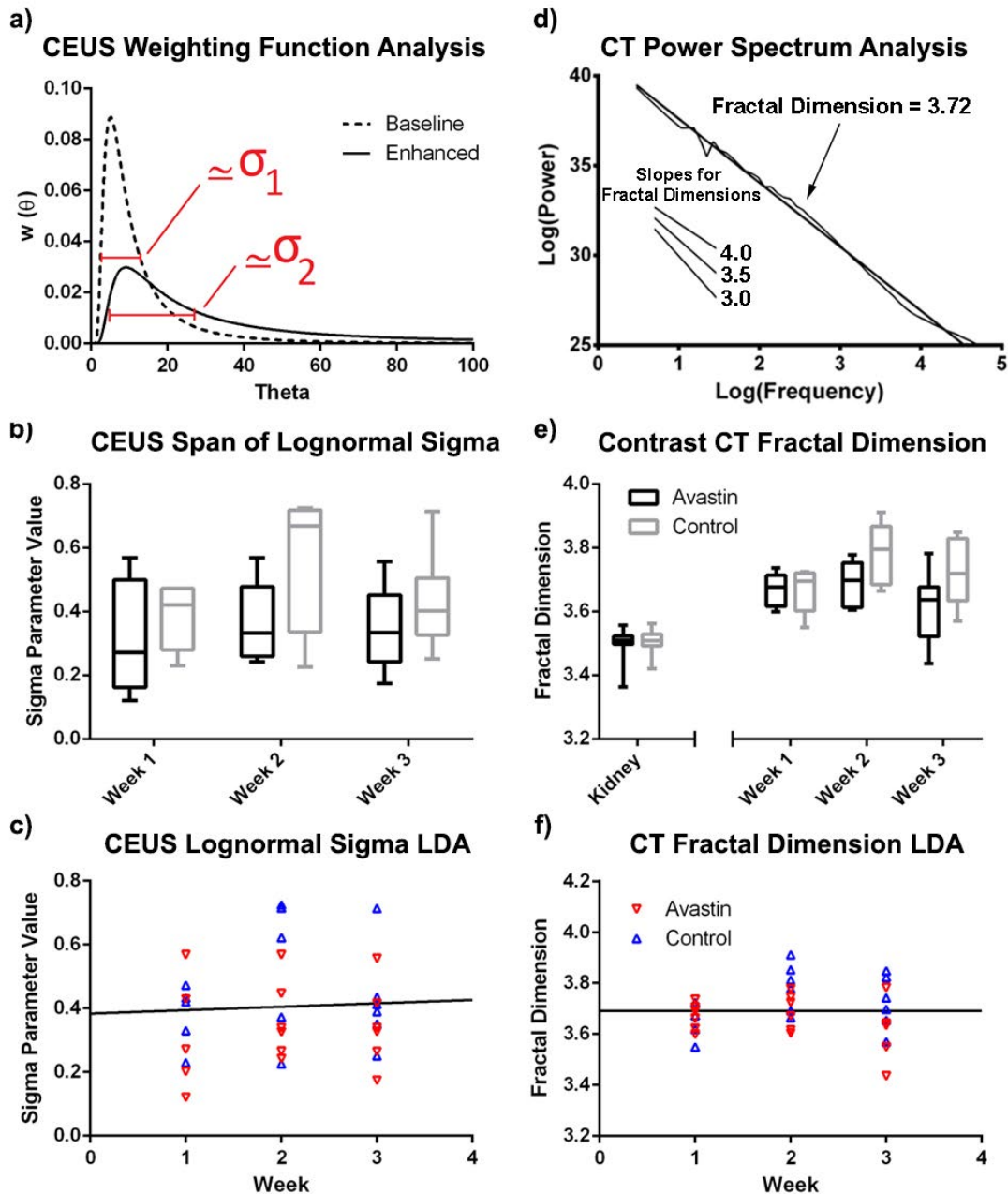


Figure 3.3: The (a) compound model weighting functions for a representative tumor at both baseline and peak enhancement levels. (b) Box-plot of span of the estimated sigma value with corresponding (c) linear discriminant analysis. (d) Diagrammatic example of power spectrum analysis on a contrast-enhanced CT tumor volume. (e) Box-plot of fractal dimension of contrast-CT tumors and kidneys, along with (f) linear discriminant analysis.

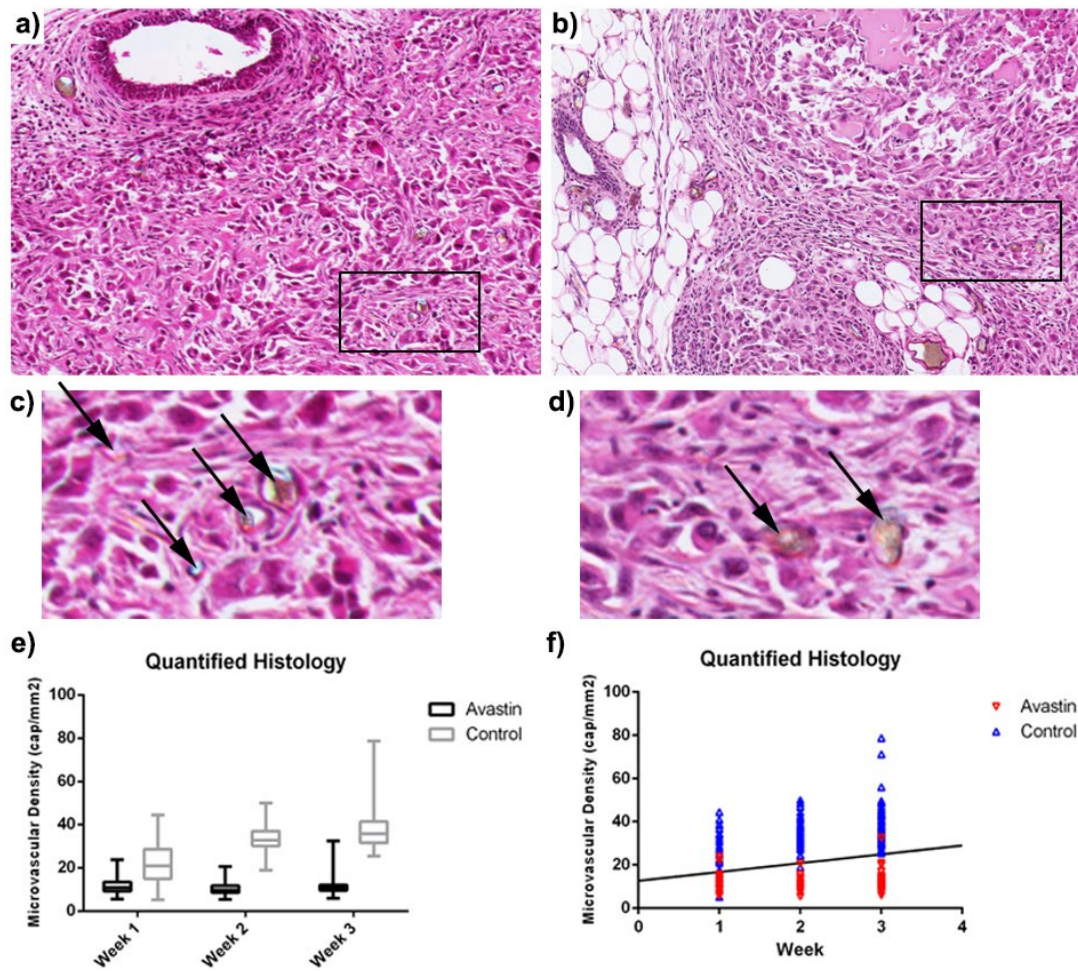


Figure 3.4: Low magnification images of H&E stained histology sections taken from (a) vehicle treated tumor and (b) bevacizumab treated tumor. Higher magnification reveals evidence of vascular perfusion of silicone-based contrast agent (arrows), with the relatively higher microvascular density of (c) control tumors compared to (d) bevacizumab treated tumors. Quantified MVD is plotted in (e) with an LDA performed in (f).

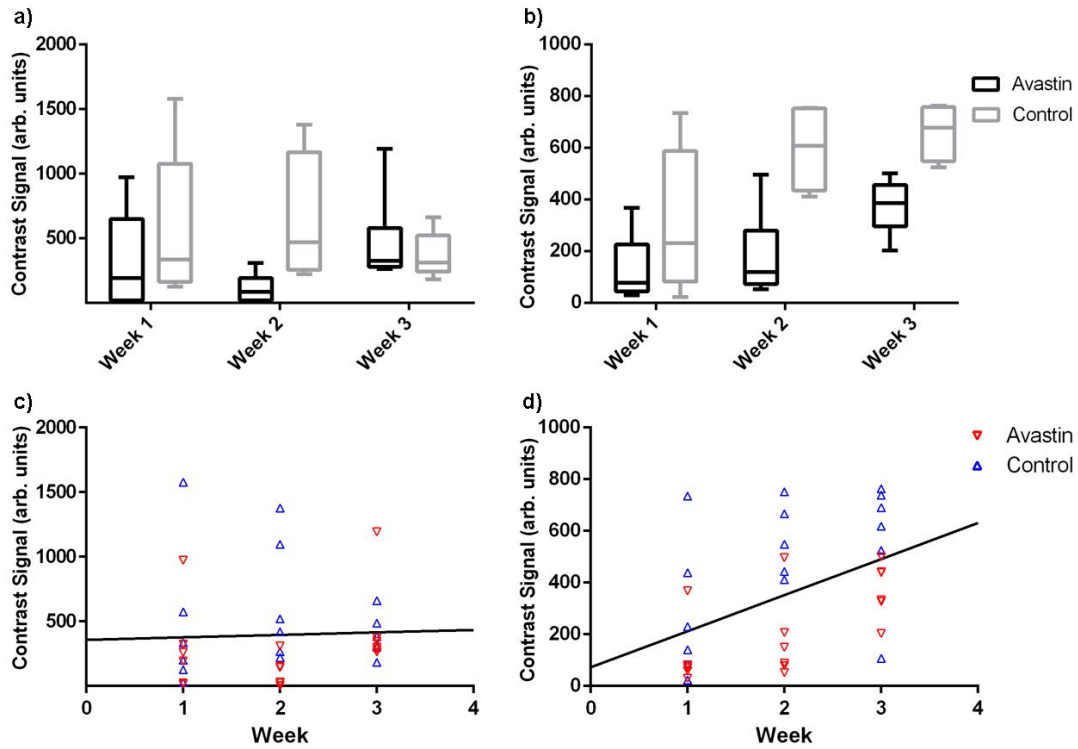


Figure 3.5: The compound model detected a significant reduction of  $AUC$  in bevacizumab treated tumors compared to control. Conventional processing did not demonstrate a significant effect. (a) Box-plot of conventional CEUS analysis  $AUC$  with corresponding (c) linear discriminant analysis. (b) Box-plot of compound model's  $AUC$ , along with (d) linear discriminant analysis.

**Blood Velocity Metrics ( $MTT$  and  $t_p$ ):**

A two-way ANOVA analysis on the measures of blood flow velocity, as measured by both image analysis techniques, yielded significant increases in the metrics over the course of the study. For conventional CEUS analysis the significance level was  $p = 0.0023$  for an increase in  $MTT$ , and  $p = 0.0239$  for  $t_p$ . This reflects a progressively slower rate of contrast wash-in as the tumors developed. Compound CEUS analysis detected an increase in  $MTT$  ( $p = 0.0215$ ), but not  $t_p$ . Neither image processing technique showed a significant difference between drug treated and control tumors, and neither had its LDA classification perform better than random chance.

**Wash-in Rate ( $WiR$ ):**

Conventional CEUS analysis detected a time dependent decrease in  $WiR$ , implying that the blood flow in the tumors became more sluggish as they grew ( $p = 0.0243$ ). However, it did not detect a significant difference in  $WiR$  between the drug groups. The compound model detected a significant difference in the  $WiR$  of bevacizumab treated and control tumors ( $p = 0.0237$ ), and opposing non-significant trends in  $WiR$  for either group. The control tumors showed a trend of lower  $WiR$  over time, and the bevacizumab treated tumors had a trend of progressively increasing  $WiR$ . Linear discriminant analysis of conventional CEUS  $WiR$  accurately classified  $50\% \pm 3.7\%$  of tumors, where tumors lying below the decision boundary were classified as “treated”. For the compound CEUS data,  $69\% \pm 1.8\%$  of tumors were correctly classified as “treated” when below the boundary.

## 3.5 Discussion

This study proposes a compound model for analyzing the first-order speckle statistics on a time-series of nonlinear CEUS images. The compound PDF of the statistical model exhibits close agreement to the CEUS intensity histogram over the entire duration of the wash-in dataset, implying that the model is an accurate description of nonlinear CEUS speckle from tumors. The model produced well-behaved wash-in curves, and the introduction of a weighting function

that relates first-order statistics of CEUS speckle to fractal vessel geometry is potentially useful for quantifying microvascular morphology. This was tested in an mouse model of breast cancer, treated with a monoclonal anti-VEGF antibody (murine version bevacizumab B20-4.1.1), to produce a dramatic change in tumor vasculature.

It has previously been reported that the  $AUC$  of a CEUS time-intensity series will correlate positively with the microvascular density of an imaged tumor [26, 27, 36]. It is expected that anti-VEGF treatment would result in reduced neovascularization, lowered MVD, and a corresponding reduction in  $AUC$ . A significant decrease in tumor MVD, due to bevacizumab therapy, was validated with gold-standard histological techniques. Only the compound CEUS model detected a significant reduction of  $AUC$  in bevacizumab treated tumors; the conventional method showed no detectable treatment effect. Although this apparent increase in treatment effect sensitivity is promising, it is not clear if this is a general result.

Several other indices of vascular perfusion were explored in this study. For contrast-enhanced CT, a measure of the mean HU of the segmented tumor volumes served as an estimate for vascular volume fraction. A reduction in relative vascular volume, represented by a decrease in mean HU, was the expected result of anti-angiogenic therapy. The decreased HU correlated well with the decrease in MVD as measured by histology. For CEUS imaging, the  $MTT$ ,  $t_p$ , and wash-in rate of the tumor were quantified through both conventional CEUS processing and the compound method. Neither image analysis technique found a main effect for treatment group on  $MTT$  or  $t_p$ . For wash-in rate, conventional CEUS detected a time dependent decrease in wash-in rate, but no treatment effect, and the compound method found a significant treatment effect, but no longitudinal effect. Overall, the performance of these two CEUS techniques in quantifying additional perfusion indices seems similar. However, these results must be considered within the context of the curve-fitting performed in this study. A number of groups [37–39] have shown that the multiplicative nature of speckle noise in CEUS cine loops necessitates the use of MLE fitting of indicator-dilution curve models instead of a nonlinear least squares method. There is a possibility that switching to MLE for LDRW fitting would result in improved discrimination of treatment groups. We opted to use nonlinear least squares to provide a direct head-to-head comparison between the techniques as nature of the variability, and hence the optimal curve fitting method, for the statistical technique requires

further study.

This study also assessed whether the metrics derived from the weighting function were related to microvascular morphology. Specifically, it assessed if the metrics could be used to infer fractal vessel geometry as a surrogate for vascular tortuosity. This was tested with power spectrum analysis on tumors that underwent micro-CT perfusion casting, with contra-lateral kidneys as a second control group. It is expected that vascular normalization would produce vessel networks with a more regular branching structure and thus the measured fractal dimension of bevacizumab-treated tumors would be lower than untreated (control) tumors. Kidneys had the lowest fractal dimension, followed by treated tumors, then untreated tumors; however, the difference between the treatment groups was modest. Direct measures of tortuosity, such as the distance metric, were consistent with measures of  $F_D$  in exhibiting at most a modest difference between the treatment groups. The motivation for the use of power spectrum analysis over other metrics of tortuosity in this study was to avoid a threshold and skeletonization step. The trend in  $F_D$  aligns with the expected increase in vascular complexity going from highly organized organs (kidneys) to chaotic vessel beds (untreated tumors). Both the compound CEUS model and micro-CT analysis detected a significant treatment effect for their respective measure of vascular complexity, but the measures themselves had a weak correlation, and neither performed particularly well as a classifier. An important consideration for these results is that the degree of vascular normalization caused by bevacizumab therapy was not known in advance for this study. It is not clear what experimental design would produce a predictable and major change in the fractal dimension of tumor vasculature.

A limitation of the proposed statistical model is a bias toward overestimating the weighting function width in small tumor volumes. More robust estimators of the Pareto parameters [40] are being explored to address this overestimation of the weighting function variance. A further limitation is the assumption of a gamma-family weighting function. In principle, if an arbitrary vascular network may be approximated by a fractal branching tree, then the weighting function should be log-normal to be consistent with the results of Qian *et al.* [12]. The gamma function used in this analysis served as an approximation to the log-normal distribution to facilitate parameter estimation. This was justified by literature indicating that these two distributions are often interchangeable [15]; however, this statement may not hold for strongly enhanced tumors

that would be more accurately described with the heavier tailed log-normal distribution. Furthermore, the assumption of fully developed speckle in all microbubble sub-populations does not hold for low concentrations of indicator. This is particularly important in the early wash-in phases of contrast-enhancement. Addressing this would require a change in the parameterized distribution from an exponential to a K distribution [39], but the gain in model accuracy may be outweighed by decrease in parameter estimation stability.

### 3.6 Conclusions

The proposed compound statistical model describing nonlinear CEUS speckle shows promise in providing additional information for CEUS analysis. The *AUC* of wash-in curves produced using the compound statistical model could more accurately discriminate anti-VEGF treated tumors from control tumors than could conventional CEUS; these results were confirmed with gold-standard histological measures of tumor MVD. The model's weighting function can characterize tumor fractal vessel geometry, which is theoretically a good measure of vascular normalization; however, gold-standard micro-CT perfusion casting demonstrated that the design of this study only had a modest effect on vascular fractal dimension. It is also possible to extract estimates of blood velocity and wash-in rate using the statistical model, with a classification performance that is similar to conventional CEUS analysis. The proposed technique quantifies the perfusion within a tumor and simultaneously provides an index of vascular complexity, making it a potentially useful addition to the clinical detection of vascular normalization in anti-angiogenic combination therapies.

# References

- [1] B. Warren, “The vascular morphology of tumors,,” in *Tumor Blood Circulation: Angiogenesis, Vascular Morphology, and Blood Flow of Experimental and Human Tumors*, H.-I. Peterson, Ed. Boca Raton, FL: CRC Press, 1979, pp. 1–48.
- [2] S. Goel, D. G. Duda *et al.*, “Normalization of the vasculature for treatment of cancer and other diseases,” *Physiol. Rev.*, vol. 91, no. 3, pp. 1071–1121, Jul. 2011.
- [3] M. R. Lowerison, M. N. Hague *et al.*, “Improved Linear Contrast-Enhanced Ultrasound Imaging via Analysis of First-Order Speckle Statistics,” *IEEE Trans. Ultrason., Ferroelectr., Freq. Control.*, vol. 63, no. 9, pp. 1409–1421, 2016.
- [4] M. Lowerison, M. Hague *et al.*, “A compound speckle model for vascular complexity quantification in nonlinear contrast-enhanced ultrasonography,” in *Ultrasonics Symposium (IUS), 2014 IEEE International*, Sep. 2014, pp. 2249–2252.
- [5] J. M. Hudson, R. Williams *et al.*, “Improved Flow Measurement Using Microbubble Contrast Agents and Disruption-Replenishment: Clinical Application to Tumour Monitoring,” *Ultrasound Med. Biol.*, vol. 37, no. 8, pp. 1210–1221, 2011.
- [6] J. Du, F.-H. Li *et al.*, “Microvascular architecture of breast lesions: evaluation with contrast-enhanced ultrasonographic micro flow imaging,” *J. Ultrasound Med.*, vol. 27, no. 6, pp. 833–842, 2008.
- [7] Y.-J. Li, G. Wen *et al.*, “Perfusion heterogeneity in breast tumors for assessment of angiogenesis,” *J. Ultrasound Med.*, vol. 32, no. 7, pp. 1145–1155, Jul. 2013.
- [8] G. Barrois, A. Coron, and S. Lori Bridal, “Detection of early therapeutic response with dynamic contrast enhanced ultrasound using a perfusion clustering algorithm,” in *Ultrasonics Symposium (IUS), 2014 IEEE International*, 2014, pp. 1754–1757.
- [9] M. P. J. Kuenen, T. A. Saidov *et al.*, “Contrast-Ultrasound Dispersion Imaging for Prostate Cancer Localization by Improved Spatiotemporal Similarity Analysis,” *Ultrasound Med. Biol.*, vol. 39, no. 9, pp. 1631–1641, 2013.
- [10] M. Mischi, C. Heneweer *et al.*, “Fractal dimension of tumor microvasculature by dynamic contrast-enhanced ultrasound,” in *Ultrasonics Symposium (IUS), 2015 IEEE International*, 2015, pp. 1–4.



- [11] R. F. Wagner, S. W. Smith *et al.*, “Statistics of Speckle in Ultrasound B-Scans,” *IEEE Trans. Sonics Ultrason.*, vol. 30, no. 3, pp. 156–163, May 1983.
- [12] H. Qian and J. B. Bassingthwaite, “A class of flow bifurcation models with lognormal distribution and fractal dispersion,” *J. Theor. Biol.*, vol. 205, no. 2, pp. 261–268, 2000.
- [13] Z. Turek and K. RakuÅan, “Lognormal distribution of intercapillary distance in normal and hypertrophic rat heart as estimated by the method of concentric circles: its effect on tissue oxygenation,” *Pflugers Arch., EJP*, vol. 391, no. 1, pp. 17–21, 1981.
- [14] D. Kelly and C. Smith, *Bayesian Inference for Probabilistic Risk Assessment: A Practitioner’s Guidebook*. Springer Science & Business Media, 2011.
- [15] B. L. Wiens, “When log-normal and gamma models give different results: A case study,” *Am. Stat.*, vol. 53, no. 2, pp. 89–93, 1999.
- [16] R. Karch, F. Neumann *et al.*, “Voronoi Polyhedra Analysis of Optimized Arterial Tree Models,” *Ann. Biomed. Eng.*, vol. 31, no. 5, pp. 548–563, 2003.
- [17] S. D. Dubey, “Compound gamma, beta and f distributions,” *Metrika*, vol. 16, no. 1, pp. 27–31, 1970.
- [18] B. C. Arnold, “Pareto and Generalized Pareto Distributions,” in *Modeling Income Distributions and Lorenz Curves*, ser. Economic Studies in Equality, Social Exclusion and Well-Being, D. Chotikapanich, Ed. Springer New York, 2008, no. 5, pp. 119–145.
- [19] R. Karshafian, P. N. Burns, and M. R. Henkelman, “Transit time kinetics in ordered and disordered vascular trees,” *Phys. Med. Biol.*, vol. 48, no. 19, p. 3225, 2003.
- [20] R. Karch, F. Neumann *et al.*, “Fractal Properties of Perfusion Heterogeneity in Optimized Arterial Trees,” *J. Gen. Physiol.*, vol. 122, no. 3, pp. 307–322, 2003.
- [21] P. McCullagh and J. A. Nelder, *Generalized Linear Models, Second Edition*. CRC Press, Aug. 1989.
- [22] D. E. Jenkins, Y. S. Hornig *et al.*, “Bioluminescent human breast cancer cell lines that permit rapid and sensitive in vivo detection of mammary tumors and multiple metastases in immune deficient mice,” *Breast cancer res.*, vol. 7, no. 4, pp. R444–454, 2005.
- [23] B. Goulet, W. Kennette *et al.*, “Nuclear localization of maspin is essential for its inhibition of tumor growth and metastasis,” *Lab. Invest.*, vol. 91, no. 8, pp. 1181–1187, 2011.
- [24] K. H. Norwich and S. Zelin, “The dispersion of indicator in the cardio-pulmonary system,” *Bull. Math Biophys.*, vol. 32, no. 1, pp. 25–43, Mar. 1970.
- [25] C. Strouthos, M. Lampaskis *et al.*, “Indicator dilution models for the quantification of microvascular blood flow with bolus administration of ultrasound contrast agents,” *IEEE Trans. Ultrason. Ferroelectr. Freq. Contr.*, vol. 57, no. 6, pp. 1296–1310, 2010.

- [26] H. Zhuang, Z.-G. Yang *et al.*, “Time-intensity curve parameters in colorectal tumours measured using double contrast-enhanced ultrasound: correlations with tumour angiogenesis,” *Colorectal Dis.*, vol. 14, no. 2, pp. 181–187, 2012.
- [27] J. Du, F.-H. Li *et al.*, “Correlation of real-time gray scale contrast-enhanced ultrasonography with microvessel density and vascular endothelial growth factor expression for assessment of angiogenesis in breast lesions,” *J. Ultrasound Med.*, vol. 27, no. 6, pp. 821–831, 2008.
- [28] C. L. Roland, S. P. Dineen *et al.*, “Inhibition of vascular endothelial growth factor reduces angiogenesis and modulates immune cell infiltration of orthotopic breast cancer xenografts,” *Mol. Cancer Ther.*, vol. 8, no. 7, pp. 1761–1771, Jul. 2009.
- [29] N. Lassau, S. Koscielny *et al.*, “Advanced hepatocellular carcinoma: early evaluation of response to bevacizumab therapy at dynamic contrast-enhanced US with quantification—preliminary results,” *Radiology*, vol. 258, no. 1, pp. 291–300, 2011.
- [30] P. V. Granton, S. I. Pollmann *et al.*, “Implementation of dual- and triple-energy cone-beam micro-CT for postreconstruction material decomposition,” *Med. Phys.*, vol. 35, no. 11, pp. 5030–5042, 2008.
- [31] H. E. Schepers, J. H. van Beek, and J. B. Bassingthwaighe, “Four Methods to Estimate the Fractal Dimension from Self-Affine Signals,” *IEEE Eng. Med. Biol. Mag.*, vol. 11, no. 2, pp. 57–64, Aug. 2002.
- [32] J. Ahlgren, B. Risberg *et al.*, “Angiogenesis in invasive breast carcinoma—a prospective study of tumour heterogeneity,” *Eur. J. Cancer*, vol. 38, no. 1, pp. 64–69, Jan. 2002.
- [33] N. Weidner, J. P. Semple *et al.*, “Tumor angiogenesis and metastasis—correlation in invasive breast carcinoma,” *N. Engl. J. Med.*, vol. 324, no. 1, pp. 1–8, 1991.
- [34] C. A. Schneider, W. S. Rasband, and K. W. Eliceiri, “NIH Image to ImageJ: 25 years of image analysis,” *Nature Methods*, vol. 9, no. 7, pp. 671–675, 2012.
- [35] L.-K. Huang and M.-J. J. Wang, “Image thresholding by minimizing the measures of fuzziness,” *Pattern Recogn.*, vol. 28, no. 1, pp. 41–51, 1995.
- [36] J. Wang, F. Lv *et al.*, “Study on the characteristics of contrast-enhanced ultrasound and its utility in assessing the microvessel density in ovarian tumors or tumor-like lesions,” *Int. J. Biol. Sci.*, vol. 7, no. 5, pp. 600–606, 2011.
- [37] G. Barrois, A. Coron *et al.*, “A multiplicative model for improving microvascular flow estimation in dynamic contrast-enhanced ultrasound (DCE-US): theory and experimental validation,” *IEEE Trans. Ultrason. Ferroelectr. Freq. Contr.*, vol. 60, no. 11, pp. 2284–2294, 2013.
- [38] M. P. J. Kuenen, I. H. F. Herold *et al.*, “Maximum-likelihood estimation for indicator dilution analysis,” *IEEE Trans. Biomed. Eng.*, vol. 61, no. 3, pp. 821–831, 2014.

- [39] A. D. Bar-Zion, C. Tremblay-Darveau *et al.*, “Denoising of Contrast-Enhanced Ultrasound Cine Sequences Based on a Multiplicative Model,” *IEEE Trans. Biomed. Eng.*, vol. 62, no. 8, pp. 1969–1980, 2015.
- [40] D. E. Giles, H. Feng, and R. T. Godwin, “On the bias of the maximum likelihood estimator for the two-parameter Lomax distribution,” *Commun. Stat. Part A Theor.*, vol. 42, no. 11, pp. 1934–1950, 2013.

## **Chapter 4**

# **PDXovo: Ultrafast Prediction of Drug Sensitivities via Intratumoral Multiregional Analysis**

*The contents of this chapter are in preparation to be submitted to: Nature as: “PDXovo: Ultrafast Prediction of Drug Sensitivities via Intratumoral Multiregional Analysis”, by Matthew R. Lowerison, Hon S. Leong, Yaroslav Fedyshyn, Stephenie Prokopec, Karla C. Williams, Carson T. Gavin, Chantalle Willie, Clarisse Mazzola, Qi Zhang, Jose Gomez-Lemus, James Brugarolas, Ann F. Chambers, Paul C. Boutros, James C. Laceyfield, and Nicholas E. Power.*

## 4.1 Introduction

Renal Cell Carcinoma (RCC) is resistant to chemotherapy and high-dose radiation therapy, with partial/full nephrectomy offered when the primary tumor is >4 cm. Following tumor resection, metastatic RCC patients (mRCC) receive targeted therapy drugs such as sunitinib (a VEGF receptor tyrosine kinase inhibitor), which antagonizes tumor angiogenic and metabolic pathways. Targeted therapy is initially effective in most cases, as RCC is highly dependent on tumor-driven angiogenesis [1], but a minority of RCC patients will exhibit *de novo* resistance to their selected therapy. This renders such first-line treatments ineffective at the outset for these patients [2]. The molecular mechanisms responsible for drug resistance are unclear, with no biochemical or genetic signature assays available to identify this patient population [3–5]. Furthermore, for patients with mRCC, sensitivity to sunitinib at the outset is temporary, with drug resistance eventually occurring in all patients within 2-3 years [6]. This resistant phenotype is collectively driven by intrinsic and extrinsic factors (e.g. tumor, microenvironment) that parry the targeted therapy regardless of dose [7, 8].

We have developed an ultra-fast RCC patient derived xenograft (PDX) model for high-throughput phenotype-based evaluation of intratumoral specimen responses to various targeted therapies within 10 days using the *ex ovo* chick embryo (hence PDX<sub>OVO</sub>). The effectiveness of this tumor avatar model is leveraged by high-frequency ultrasound imaging to quantify tumor vasculature, blood flow, and growth after continual drug treatment. This imaging modality is non-invasive and is an excellent readout for anti-angiogenic interventions. The PDX<sub>OVO</sub> tumor avatar model is superior to immunocompromised mouse PDX models with respect to engraftment efficiency. Mouse PDX models are currently beset by low tumor take rates (~10-12% will have a palpable tumor after implantation) in comparison to the tumor take rates observed in the chorioallantoic membrane (CAM) of the chick embryo [9, 10]. The *ex ovo* CAM of the chick embryo is essentially an exposed two-dimensional ‘lung’ with a dense capillary bed that can accommodate various xenografts. CAM xenografts can then be topically treated with drug(s) and visualized longitudinally with light microscopy and/or ultrasound imaging. Xenograft growth is rapid in the CAM, and drug treatment of xenografts is straightforward, wherein drugs are topically administered to the tumor surface. Although previous studies have demonstrated the

CAM's ability to accommodate PDXs from RCC biopsies [11, 12], its utility as a preclinical drug evaluation model for PDXs has not been described. More importantly, its usefulness as a preclinical model for optimizing targeted therapy within the context of personalized medicine has also not been explored.

The notion of a genetic biomarker to guide personalized medicine for RCC is questionable, given recent reports describing tumor heterogeneity in RCC [13, 14], and the relative abundance of intratumoral clones that harbor mutations which may render the tumor unresponsive to current pharmacological offerings. This intratumoral heterogeneity is further complicated by temporal heterogeneity, wherein changes in distinct clonal populations are observed over time within the same tumor, notably during and after treatment with targeted therapy [14]. Evaluating the impact of, or resistance to, targeted therapy due to tumor heterogeneity using mouse based PDX models is challenging, since the majority of biopsies fail to grow in mice. Engraftment into the CAM of the chick embryo overcomes this logistical challenge, provided that each biopsy is equally capable of "taking" in each embryo host. Another requirement for evaluating PDX response to anti-angiogenic therapies, such as sunitinib, is a non-invasive means to quantify functional vasculature within the tumor.

We describe the preclinical utility of the CAM as a "tumor avatar" PDX model for the evaluation of tumor and microvasculature response when treated with anti-angiogenic drugs, hence the *PDXovo* model. This economical and high-throughput preclinical model offers simultaneous evaluation of several drugs within two weeks from freshly collected tumor specimens. This model offers high engraftment rates of patient tumor samples, either directly implanted or cultured in vitro and expanded prior to engraftment. This model is ideal for identifying genetic signatures for drug resistance due to prospective analysis of treated and untreated PDXs from the same patient, taking into account intratumoral heterogeneity and temporal heterogeneity. This is in contrast to the majority of resistance gene signature studies which are, by their nature, case control studies that do not control for patient tumor variability and temporal heterogeneity over the course of drug treatment. We show that a vascular phenotype based prediction scheme, where tumors are implanted and evaluated by ultrasound imaging for tumor perfusion rates, offers a more convenient and effective means of predicting drug resistance than genotype based readouts.

## **4.2 Material and Methods**

### **4.2.1 Regulatory Ethics Board Approvals**

Tumor samples were obtained from patients that provided oral and written consent to a University of Western Ontario Research Ethics Board approved protocol (REB #104278), allowing for the use of surgical specimens for research at the London Health Sciences Centre.

### **4.2.2 Preparation of Reagents**

Stock solutions of the following small-molecule, multi-targeted receptor tyrosine kinase inhibitors sunitinib, sorafenib, axitinib, pazopanib, dovitinib, sirolimus, and everlimous were obtained from LC Laboratories (Woburn, MA). TAK-441 was obtained from Takeda Pharmaceuticals, JA. Samples were dissolved with dimethyl sulfoxide (DMSO) to a concentration of 10  $\mu$ M (Sigma, ON). Vehicle control was DMSO diluted with PBS at a 1:5 dilution ratio.

### **4.2.3 Cell Culture Techniques**

The 786-O cell line was obtained from American Type Culture Collection Inc. (Bethesda, MD). The primary RCC cell lines, XP127, XP158, XP185, XP206, and T258, were provided by Dr. James Brugarolas (UT Southwestern Medical Center, Austin, TX). 786-O cells were maintained in RPMI 1640 (Wisent, QC) supplemented with 20 mM HEPES pH 7.4 and 5 g/L glucose. Primary RCC cells were maintained in MEM with Earles salts and 2 mM glutamine, 10 ng/ml EGF (Sigma), 1% MEM non-essential amino acid (Wisent), and 0.4  $\mu$ g/ml hydrocortisone (Sigma). All media were supplemented with 10% FBS (Hyclone, UT) and 1% Penicillin/Streptomycin (Wisent) unless otherwise specified. All cells were grown in a 37°C, 5% CO<sub>2</sub> humidified incubator.

### **4.2.4 Primary RCC cell line generation and culture**

Tumor core samples (8 mm diameter) were taken from patient tumors at the time of partial/full nephrectomy. Cores were kept in transport medium (MEM with Earles salts and

2 mM glutamine supplemented with 50  $\mu\text{g}/\text{mL}$  of gentamycin (Life Technologies), 1% Penicillin/Streptomycin and 1% Fungizone (Wisent)) and processed immediately upon return to the lab. Tissues were transferred to 33 mm Petri-dish (Cellstar) and minced to  $<0.5$  mm. Subsequently, 1 mL of tissue digestion medium (consisting of transport medium supplemented with 0.1 mg/mL collagenase (Sigma), 0.1 mg/mL hyaluronidase (Sigma) and 20  $\mu\text{g}/\text{mL}$  deoxyribonuclease I (Sigma)) was added. Processed tissues were incubated in a 37°C humidified incubator with 5%  $\text{CO}_2$  for 1-2 hrs. Samples were transferred to 1 mL Eppendorf tubes and centrifuged for 2 minutes at  $600 \times g$ . Pellets were washed with 1 mL of transport medium and centrifuged again for 2 minutes at  $600 \times g$ . Pellets were resuspended with primary RCC cell medium (described for RCC cell maintenance, above) and plated in 12-well plates. Medium was changed every 3 days and cells were split 1:2 as necessary. Primary RCC cells were transduced with a lentivirus encoding cytoplasmic zsGreen (pLVX-ZsGreen1-C1, Clontech) and selected with puromycin (2 mg/mL, Sigma) to generate fluorescently green versions of each cell line prior to CAM implantation.

#### **4.2.5 Cancer Cell Preparation for chick embryo CAM engraftment**

Cells were grown to full confluency for the day of engraftment. Cell culture flasks were washed twice with PBS, trypsinized (0.05% Trypsin-EDTA, Wisent) until completely detached, and then transferred to 50 mL tubes. Cells were centrifuged for 5 minutes at  $200 \times g$ . Supernatant was removed and the pellet resuspended in 10 mL of PBS. 10  $\mu\text{L}$  samples of the cell suspension were analyzed using the Countess cell counter (Life Technologies). Basement Membrane Matrix LDEV-Free, BD Matrigel (BD Bioscience) was used to dilute cells to obtain a final mixture of  $1 \times 10^6$  cells/10  $\mu\text{L}$  inoculation dose. The cell-Matrigel mix was kept on ice until implantation into the CAM.

#### **4.2.6 Engraftment of Cell lines and/or Patient derived xenografts into the CAM**

Fertilized chicken eggs were obtained from McKinley Hatchery (St Marys, ON). We refer the reader to a protocol describing each step of the chick embryo cultivation process, as described



in [15, 16]. On day 9 of embryonic development (EDD-9), a 5 mm disk of autoclaved Whatman No.1 filter paper was briefly placed over some of the smaller allantoic vessels near the center of the CAM. The disk is allowed to adhere to the CAM, and when detached, scores the chorionic epithelium, exposing the capillary bed of the CAM. Immediately after, 10  $\mu$ L of the cell-Matrigel mixture is pipetted into the abrasion. The embryo is then immediately placed back into the incubator. At EDD-12, EDD-14, and EDD-16 tumors were topically treated with 5  $\mu$ L of the indicated drug at varying concentrations. At EDD-18 when the tumors have spent  $T > 7$  days in the CAM, xenografts are submitted to a variety of endpoint analyses.

#### **4.2.7 Engraftment of Patient Tumor Fragments into the CAM**

Tumor engraftment procedures were performed on EDD-9 embryos ( $N > 300$ /patient tumor). At the time of partial/full nephrectomy, 5-9 tumor cores (8 mm diameter) were extracted per patient to obtain ample coverage of the entire tumor. Each tumor core was stored in transport medium until engraftment. Using a scalpel blade, tumor cores were cut into  $\sim 2 \times 2 \times 2$  mm tumor fragments. Immediately after removal of the chorionic epithelium with Whatman filter paper, a single tumor fragment was placed into the scored area, followed by the addition of 10  $\mu$ L of diluted Matrigel (1:10 in RPMI media). Embryos were immediately returned to the incubator after tumor implantation. At 24 hours post implantation, 10  $\mu$ L of BLES lung surfactant (BLES Biochemicals Inc. ON) was applied topically over the tumor.

#### **4.2.8 Volumetric Ultrasound Imaging Protocol**

All ultrasound measurements were performed using a Vevo<sup>®</sup> 2100 high-frequency imaging system (VisualSonics Inc., Toronto, Canada). The transducer was attached to the supplied linear stepper motor (VisualSonics Inc.) and fixed above the center of the tumor. Ultrasound coupling gel (Aquasonic<sup>®</sup> 100, Parker Laboratories, Inc., Fairfield, NJ) was applied over the interface surface of the transducer to provide an acoustic standoff between the piezoelectric elements and the CAM surface. To prevent the acoustic gel from adhering to the CAM, a small amount of saline was deposited on the tumor surface prior to coupling. The saline allowed the transducer to glide over the CAM surface.

B-mode images were acquired using a 40 MHz linear array (MS-550D, 40  $\mu\text{m}$  nominal axial resolution, 80  $\mu\text{m}$  nominal lateral resolution). The imaging field of view was set to 10.00 mm in the axial direction and 14.08 mm in the lateral direction. Three-dimensional volumetric images were acquired, before any injection of contrast agent, using the stepper motor with a step size 0.076 mm and a total step distance 15.01 mm. This provided an imaging volume large enough to cover the entire tumor in all of the imaged embryos. Doppler images were acquired using the same 40 MHz linear array transmitting in power Doppler mode. Three-dimensional Doppler acquisition was performed using a color box sized to completely enclose the largest cross-section of tumor. Operator settings were fixed to 100% transmit power, a 2RF-cycle pulse length, 22 dB receiver gain, 3 kHz PRF, a low wall filter, a high priority (92%), and frame rate of 32 Hz.

#### **4.2.9 Contrast-Enhanced Ultrasound Protocol**

All contrast-enhanced ultrasound imaging was performed using an intravenous injection of the commercially available Vevo MicroMarker<sup>TM</sup> (VisualSonics Inc.) microbubble solution. For this study, the microbubbles were reconstituted with 0.7 mL of sterile saline yielding a solution with approximately  $2 \times 10^9$  microbubbles/mL, with a nominal median microbubble diameter in the range of 2.3 – 2.9  $\mu\text{m}$ . This size range allows the microbubbles to pass through capillaries, allowing complete pulmonary transit and venous recirculation. The contrast agent has a biological half-life of approximately 20 minutes in active vasculature, well within the imaging time window of this study.

For CAM injection, an 18G x 1 1/2 in. beveled needle tip was attached to 8 cm of Tygon<sup>®</sup> R-3603 laboratory tubing. The open end of tubing was fitted with a glass capillary needle. With the aid of a confocal microscope, the glass capillary needle tip was manually cannulated into a high-order vein on the CAM surface for contrast injection. A total volume of 50  $\mu\text{L}$  of the microbubble solution was injected into each embryo.

For microbubble specific imaging the system was equipped with a 20 MHz linear array (MS-250, 75  $\mu\text{m}$  nominal axial resolution, 165  $\mu\text{m}$  nominal lateral resolution) transmitting at 18 MHz in nonlinear contrast mode. Nonlinear imaging was performed over a field of view sized to completely enclose the tumor. Destruction reperfusion cine loops consisting of 700

frames were acquired at a frame rate of 20 Hz, with a 1-second bursting pulse ( $MI = 0.9$ ) at frame 100. The bursting pulse destroys all microbubbles within the imaging volume, creating what is effectively a negative bolus for indicator-dilution analysis. Destruction reperfusion imaging was repeated for five anatomical planes throughout the tumor volume to acquire independent perfusion sampling.

#### **4.2.10 Volumetric Ultrasound Quantification**

Volumetric image reconstruction and analysis was performed using the supplied software (Vevo 2100 workstation, VisualSonics Inc.). Estimates of tumor volume were computed from the B-mode dataset via manual planimetry on reconstructed three-dimensional images. The blood volume in the tumor was calculated by summing the number of Doppler color pixels in the segmented volume and dividing by the total number of voxels in the volume. This Doppler metric is termed the vascularization index (VI) of the tumor.

#### **4.2.11 Contrast-Enhanced Ultrasound Perfusion Analysis**

Cine loops of the contrast-enhanced ultrasound data were exported as uncompressed, intensity signal data files. One B-mode frame was acquired for every non-linear frame, with the linear and nonlinear image data being acquired simultaneously during the destruction reperfusion sequence. The encapsulated tumor tissue boundary layer was easier to delineate on the anatomical images. Manual regions of interest segmenting the tumor were placed on the first frame of the B-mode cine loop, and reused for every subsequent frame in that cine loop, as the amount of subject motion was low during acquisition. These segmentations were then rigidly registered to the nonlinear images via translation and scaling. All analysis was performed using MATLAB (version R2013a, The MathWorks Inc., Natick, MA). The mean intensity of the nonlinear signal within the ROI was calculated at each frame of the cine loop to serve as an estimate of the total indicator mass. The kinematic model used in this study was the conventional mono-exponential fit first proposed by Wei et al [17]. The fitted mono-exponential parameters, and the Stewart-Hamilton relations, were used to quantify three blood perfusion parameters: relative blood flow, relative blood velocity, and relative blood volume.

### **4.2.12 Biopsy Classification Matrix**

Tumor biopsies were classified as sunitinib sensitive/resistant based on an F-statistic calculated from power Doppler (VI) and CEUS (relative blood volume) data in a two-way ANOVA to determine if the population means between the sunitinib group and DMSO control were significantly different. The factors in this analysis were drug group (sunitinib or DMSO) and imaging modality (power Doppler or CEUS). A biopsy was classified as sunitinib sensitive if the F-statistic was greater than 3.17, sunitinib resistant if the F-statistic was below 1.46, and partial response otherwise. The threshold values were set based on a pilot study testing the sunitinib sensitive 786-O cell line, and the sunitinib resistance XP121 cell line, each with 4 embryos per treatment group. The threshold value of  $F = 3.17$  corresponds to an alpha level of 0.10, and the  $F = 1.46$  value corresponds to an alpha level of 0.25.

## **4.3 Results**

### **4.3.1 Engrafted Renal Cell Carcinoma Tumors on the Chorioallantoic Membrane of Chick Embryos**

The CAM is a vascular membrane, spread above the embryo, yolk, and surrounding albumin, acting as the main site of gas exchange for the embryo. Resected RCC tumor specimens were  $>5$  cm in diameter, yielding 5-6 cores per primary tumor (Figure 4.1A). Tumor cores were sectioned into  $2 \times 2 \times 2$  mm fragments ( $>36$  fragments per patient tumor core), and then directly implanted onto CAMs on EDD-9 (Figure 4.1A). Within 2 days, individual tumor fragments were viable and revealed marginal growth over an 8 day incubation period (Figure 4.1B). A characteristic spoke-wheel patterning of CAM vasculature surrounding the xenografts was observed, with the network radiating toward the center of the tumor fragments (Figure 4.1B, middle and right panels). All patients enrolled during the course of the prospective PDX studies were evaluable (12-14 days of drug testing and analysis), highlighting the high engraftment rate efficiency of RCC PDXs into the chick embryo CAM. Every core from every patient tumor in this study produced viable xenografts on the CAM, with our engraftment technique

yielding a ~90% tumor take rate for patient tumor fragments and 100% take rate of all tumor regions. During growth, engrafted tumors extend below the CAM, leaving only a portion of tumor volume visible from the surface (Figure 4.1C). Histological examination of tumor fragments revealed viable tumor cells juxtaposing CAM stromal tissue (Figure 4.1D, middle and right panels). High magnification pathology revealed a clear cell RCC subtype, corroborating reports from the nephrectomy samples which represented the entire tumor pathology (Supplementary Figure 4.1). Engrafted RCC tumors induce a strong angiogenic response, resulting in co-option of surrounding CAM vessels and the establishment of a microvascular capillary network in the tumor interior. The recruitment of pre-existing vessels by the tumor (vascular co-option) is a potential mechanism of resistance to anti-angiogenic therapy [18, 19]. The high degree of tumor vascularization was confirmed using high-frequency ultrasound (Figure 4.1E); microbubble enhancement permits rapid quantification of contrast agent perfusion, a surrogate measure of the relative amount of active vasculature in a cross-section of the engrafted tumor.

### **4.3.2 Ultrasound Evaluation of Intratumoral Hemodynamics in RCC PDXs in the CAM**

Although the majority of the tumor is generally hidden below the CAM surface (Figure 4.1C, left panel), tumor volume can be superficially estimated when tumor cells are fluorescently labeled (Figure 4.2A). This technique is used to qualitatively verify that sunitinib sensitive cell lines in the CAM model exhibit reduced tumor burden and vascularization in response to targeted therapy. Topical application of sunitinib on XP185 tumors resulted in a reduction of tumor growth and vessel formation (Figure 4.2A, left panels). The sunitinib resistant cell line T258 [9] did not demonstrate a treatment effect (Figure 4.2A, right panels). These results suggest that the CAM supports RCC PDX growth while preserving their drug resistant/sensitive phenotype.

High-frequency ultrasound permitted rapid generation of reconstructed 3-D xenograft image volumes at a high spatial resolution (Figure 4.2B). Segmentation of tumor boundaries via manual planimetry generated precise and reproducible estimates of tumor volume (Figure 4.2B, left panel). Power Doppler acquisition allowed visualization and quantification of

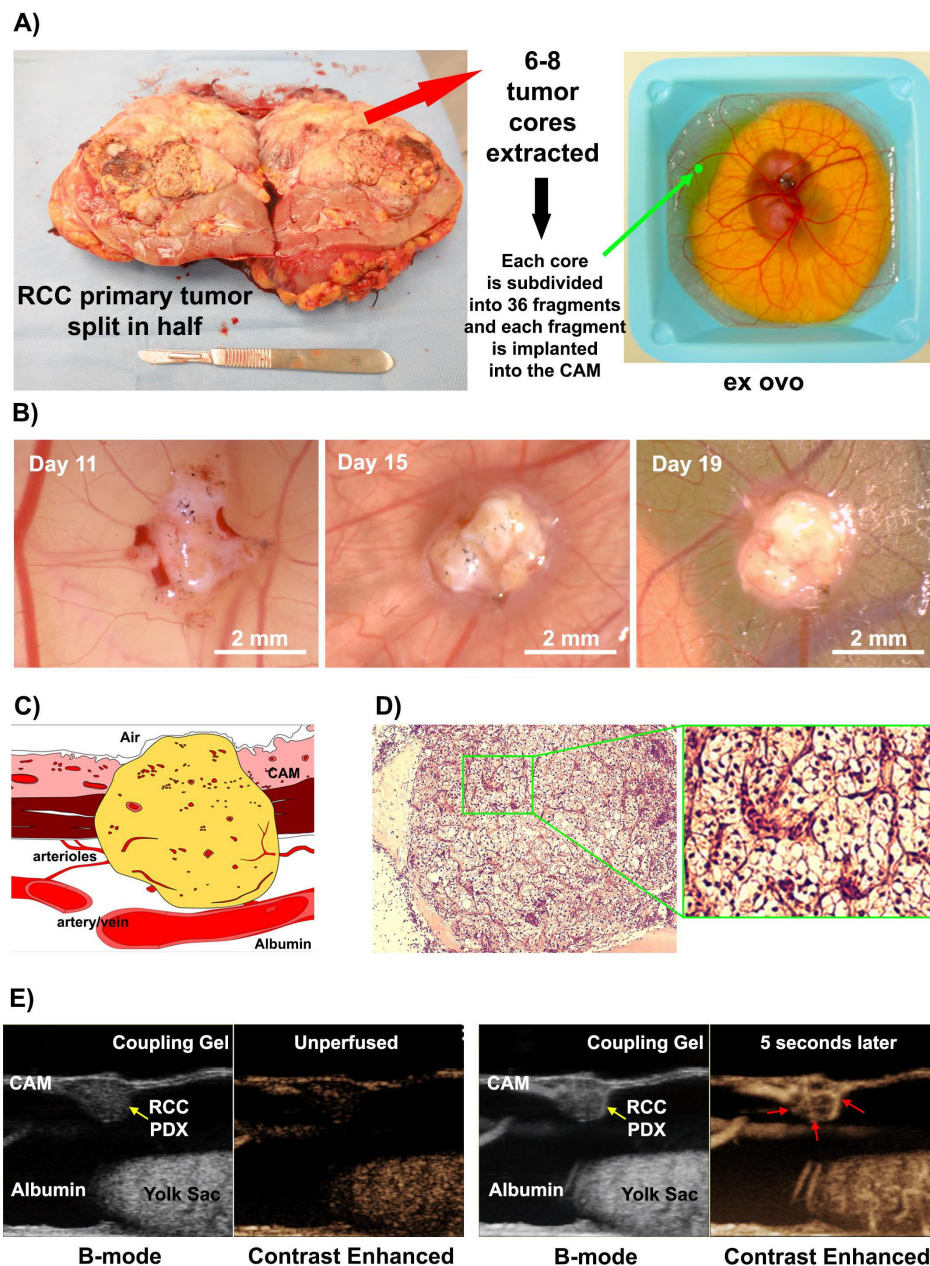


Figure 4.1: Patient derived xenograft (PDX) models for renal cell carcinoma (RCC) tumors using chick embryos. A) Primary RCC tumor resected for intratumor core extraction. Each core is divided into fragments and then implanted into the chorioallantoic membrane (CAM) of a chick embryo ex ovo. B) RCC tumor fragments are implanted on EDD-9 embryos and are viable on the CAM for another 10 days. C) Diagram demonstrating that tumor tissue extends below the surface of the CAM. D) Histological examination of tumor sections revealed viable xenograft tissue and a clear cell RCC subtype. E) At endpoint, contrast agent (microbubbles) is intravenously injected and then high-frequency ultrasound imaging performed to quantify tumor volume and the rate of tumor perfusion using a destruction-reperfusion protocol. This permits the investigator to definitively reveal functional tumor vasculature with various biophysical parameters (relative blood flow, relative blood volume).

feeding arterioles surrounding the tumor (Figure 4.2B, right panel) with B-mode acquisition providing anatomical context (Figure 4.2B, middle panel). Perfusion imaging of tumors was performed using a ‘destruction-reperfusion’ sequence following an intravenous injection of microbubble contrast agent (Figure 4.2C). Maximum intensity projections over time demonstrate a reduction in contrast signal intensity, a measure of microvascular density, in sunitinib treated XP185 tumors in comparison to vehicle control (Figure 4.2C, left panel). It should also be noted that sunitinib treated XP185 tumors exhibited a pattern of peripheral contrast enhancement (Figure 4.2C, bottom left panel), implying a lack of capillary support in the tumor core. Contrast enhanced images of resistant tumors did not show a trend between signal intensity and treatment group (Figure 4.2C, right panel). Quantified metrics of tumor perfusion (blood flow, velocity, and volume) are derived from a time-series analysis of the contrast-enhanced ultrasound image sequences [17].

### 4.3.3 Functional Heterogeneity of Intratumoral Biopsies on RCC PDXs Ex Ovo

Anti-angiogenic drugs, such as sunitinib, are first-line treatments for patients with RCC as they commonly produce strong anti-tumor effects by impeding tumor vasculature formation and causing tumor vessel collapse [20]. A subset of patients will exhibit *de novo* resistance to targeted therapy upfront, prompting the need to identify these patients prior to administration of targeted therapy. Furthermore, the diverse tumor microenvironment poses a number of regionalized stresses to cancer cells, which, in combination with Darwinian selection, lead to intratumoral heterogeneity on both a genetic and phenotypic level [14]. In Patient #2, the ccRCC and Fuhrman Grade scores were consistent between the renal biopsy, CAM PDX on-plant, and nephrectomy sample, but in Patient #1 the nephrectomy whole mount specimen revealed regions of ccRCC tumor with a Fuhrman Grade of 4 compared to a Fuhrman Grade of 3 in the renal biopsy and CAM PDX onplant (Supplementary Figure 4.1). As such, a single core biopsy for PDX engraftment may underestimate tumor heterogeneity and be insufficient for fully informed intervention by the PDX model.

RCC tumor core samples readily form viable xenografts with high engraftment percentage

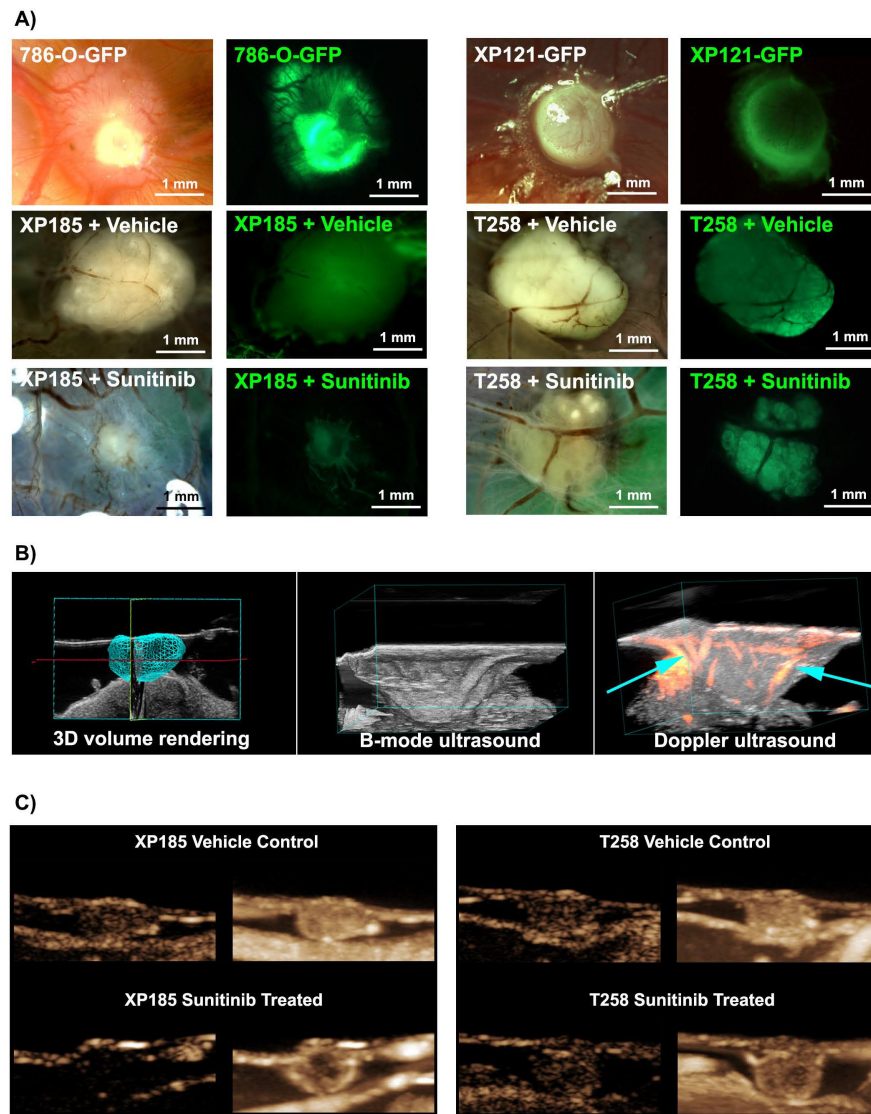


Figure 4.2: Ultrasound evaluation of intratumoral hemodynamics in RCC PDXs in the CAM. A) Tumor volume and vasculature superficially estimated when tumor cells are fluorescently labeled. Tumors generated using sunitinib sensitive cell lines (786-O and XP185) demonstrated a reduction in tumor growth and vessel formation in response to topical application of the targeted therapy. In comparison, tumors grown from resistant cell lines (XP121 and T258) did not demonstrate a treatment effect. B) When ultrasound imaging is performed, the tumor volume can be delineated (left panel), and fine structures of the tumor can be imaged when using B-mode ultrasound imaging (middle panel). When power Doppler mode ultrasound imaging is performed, areas of red blood cell movement are identified throughout the tumor and overlaid onto the B-mode image (orange-red signal, right panel). Feeding arterioles have been labeled with cyan arrows. C) Contrast enhanced ultrasound imaging confirms the presence of internal tumor vasculature. Sunitinib treated XP185 tumors demonstrated a reduction in vessel specific enhancement in comparison to vehicle control (left panel). Peripheral enhancement pattern implies lack of capillary bed in tumor core. Therapy on resistant T258 tumors did not show a trend between signal intensity and treatment group.



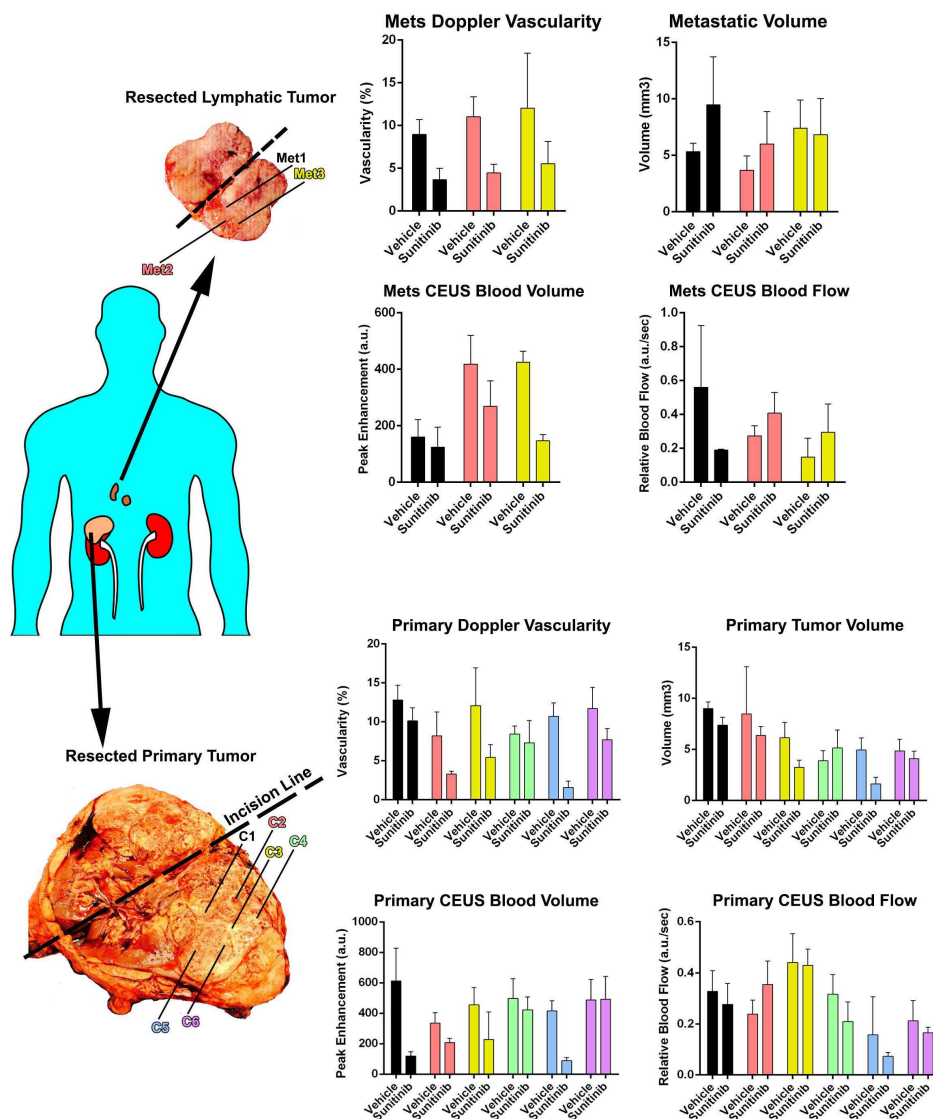


Figure 4.3: Functional heterogeneity of intratumoral cores on RCC PDXs *ex ovo*. A representative patient had 6 tumor cores taken from their primary tumor (labeled C1-C6), and 3 tumor cores taken from a nearby metastatic site (labeled Met1-Met3), for CAM engraftment ( $n > 36$  embryos/core). One half of each tumor core cohort received topical application of sunitinib and the other half received vehicle control. Patient tumor fragments underwent both volumetric and perfusion ultrasound analysis (middle graphs, shown here only from this representative patient). This patient exhibited intratumoral functional heterogeneity both within untreated tumor cores, and in response to sunitinib therapy. The metastatic cores also exhibited heterogeneity within untreated samples, but was more consistently sensitive to sunitinib.

rates in the CAM, making this an ideal model to assess functional intratumoral heterogeneity in a highly powered manner. Selected patients have 5-9 tumor cores taken from distinct sites in their primary tumor for engraftment. Each tumor core is implanted into  $n > 36$  embryos/core, with one half receiving topical application of sunitinib and the other half receiving vehicle control over the next 7 days (Figure 4.3). This set of “tumor avatars” is submitted to high-frequency ultrasound imaging to determine any difference in tumor characteristics such as tumor volume, tumor vascularity, and tumor blood flow in the context of sunitinib treatment. RCC cells were also cultured in media containing either DMSO (vehicle) or sunitinib, and no difference in cell viability was noted for either therapy (Supplementary Figure 4.2B). In all patients, we observed intratumoral functional heterogeneity regardless of treatment with vehicle or sunitinib (Figure 4.4A). Using this technique, patient cores were classified as responder (green), partial responder (yellow), and non-responder (red).

#### **4.3.4 Targeted Therapy Drug Panel Evaluation on RCC PDXs with the PDXovo Platform**

There are several different targeted therapies that are indicated for metastatic RCC patients that antagonize tumor angiogenesis (sunitinib, sorafenib, axitinib, pazopanib) or growth factor driven proliferation (dovitinib). For these large drug matrix studies, patient derived cell lines that recapitulate drug resistance phenotypes were used. Three commercially available RCC cell lines were evaluated with this drug panel (Figure 4.5A, 1  $\mu$ M final concentration each drug treatment) and all three cell lines exhibited decreased tumor take rates compared to vehicle control (DMSO  $< 1\%$ ). When three RCC PDX cell lines from sunitinib sensitive patients (XP158, XP185, and XP206) were evaluated with this drug panel, significant decreases in tumor take rates were observed (Figure 4.5B). However, XP206 exhibited minor resistance to pazopanib (1/6 compared to 3/6 for vehicle treatment) and XP158 exhibited strong resistance to sorafenib (7/13 compared to 11/14 for vehicle treatment). When three RCC PDX cell lines from sunitinib resistant patients were evaluated with the same drug panel (Figure 4.5C), major resistance to several other targeted therapies was observed with no single drug outperforming any other drug in these experiments. For XP121, sunitinib and sorafenib exhibited no impact on tumor

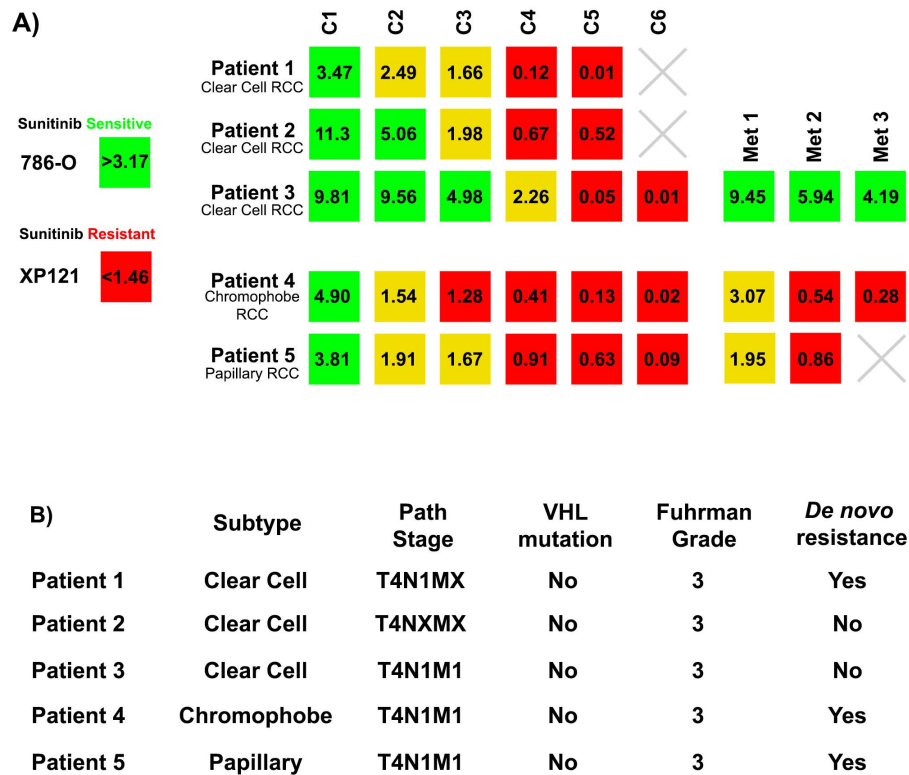


Figure 4.4: Core classification and genomic analysis of RCC PDXs *ex ovo*. A) Sunitinib sensitivity matrix for each core biopsies taken from all patients. Patient tumor cores were classified as being a responder (green), partial responder (yellow), or non-responder (red) on the basis of both the power Doppler vascularity metric and contrast-enhanced ultrasound blood volume. The number in each box represents the F-statistic for that particular core. B) Exome and copy number variation (CNV) analysis was performed on all biopsy samples, and representative PDX samples from each tumor core that was implanted into the PDX<sub>ovo</sub> model.

take rates (7/12 and 6/9 respectively compared to 4/8 for vehicle control) whereas pazopanib, dovitinib, and axitinib (1/8, 1/7, 0/6) treatments resulted in significantly decreased tumor take rates. For XP127, minor resistance was observed in all drug treatments with no single drug outperforming the entire drug panel. However, for T258, major resistance was observed with sunitinib treatment, but this PDX was highly sensitive to sorafenib (0/10), with minor resistance observed for pazopanib, dovitinib, and axitinib (2/10, 2/8, and 3/8 respectively). These drug paneling results indicate that sensitivity to sunitinib in our RCC PDX model results in similar drug responses with other targeted therapies, with some exceptions between RCC PDX cell lines. This technique offers a straightforward means to corroborate sensitivity to sunitinib and other indicated targeted therapies for RCC treatment, whilst identifying *de novo* resistance to drugs ahead of administration of targeted therapy. This technique can also provide the opportunity to identify targeted therapies for sunitinib-resistant RCC patients for improved sequencing of targeted therapy treatments.

A similar drug panel was performed on a patient derived cell line that exhibited potential sunitinib resistance, harvested from a “partial responder” metastatic tumor core. Tumor volume and vascularization index (VI) was quantified for each treatment group using reconstructed 3-D power Doppler ultrasound. A trend toward reduced tumor volume was noted for all tested antiangiogenic therapies (sunitinib, pazopanib, sorafenib), but this did not reach statistical significance (Figure 4.5D). No consistent trend for tumor volume was noted for the anti-proliferative drugs (everolimus and sirolimus). A statistically significant reduction in tumor vascularity was observed only for sorafenib therapy ( $22.5 \pm 5.6\%$  vs.  $6.8 \pm 1.3\%$ ,  $p < 0.05$ ), with no trend observed in tumor vascularity for any of the other treatments (Figure 4.5E). A scatter plot of tumor vascularity versus tumor volume demonstrated no clear correlation between the two measures (Figure 4.5F).

### **4.3.5 Engrafted Patient Tumors Maintain Viability in the CAM through Co-Option of Pre-Existing Tumor Vasculature**

Histology of patient xenografts grown in the CAM reveal viable and well-vascularized tumor tissue with an absence of large regions of necrosis (Figure 4.6A). Our method appears to ac-

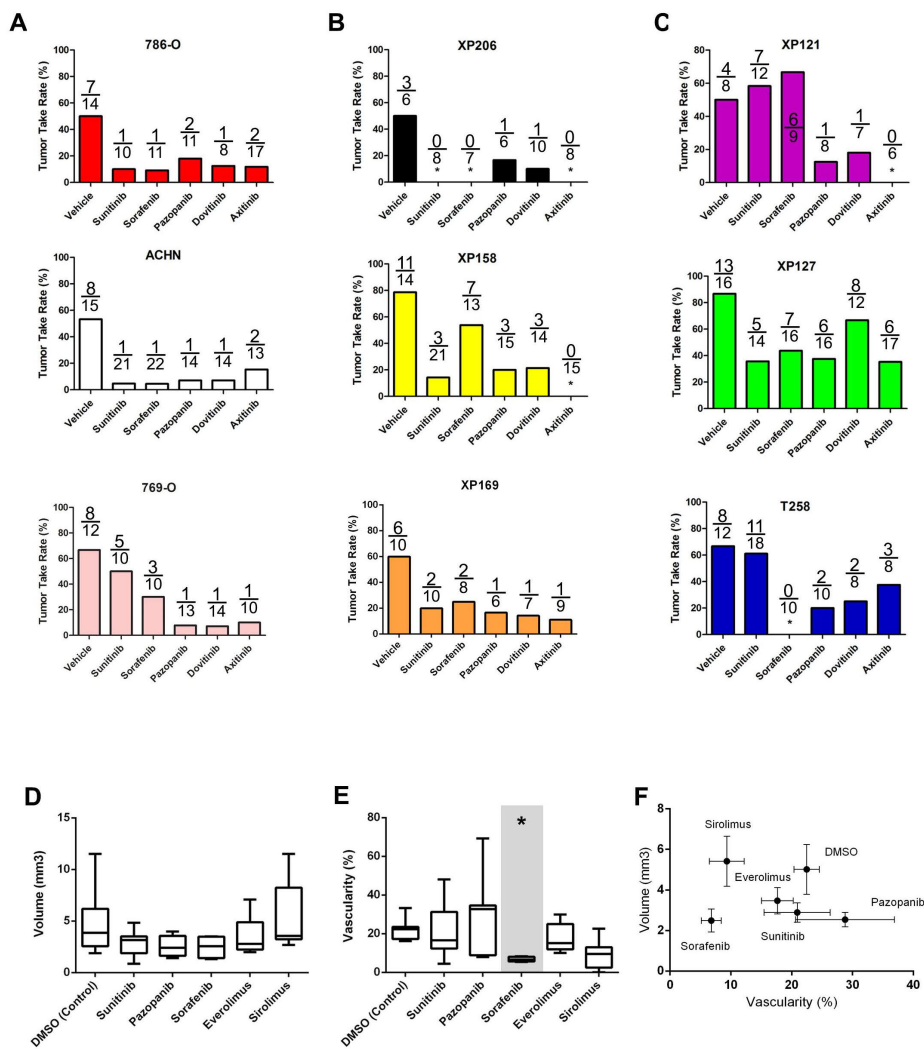


Figure 4.5: Targeted therapy drug panel evaluation on RCC PDXs. Five different targeted therapies used for the treatment of metastasis were evaluated on A) three commercially available RCC cell lines, B) three RCC PDX cell lines from patients sensitive to sunitinib and, C) three RCC PDX cell lines from patients resistant to sunitinib. The asterisk denotes lack of tumor take in that drug treatment group. The fraction of tumor take rates is presented above each bar for each drug treatment group. D-F) A patient derived cell line, harvested from a “partial responder” metastatic core, subjected to a drug panel of antiangiogenic and anti-proliferative drugs. Tumor volume and VI was quantified for each treatment group using reconstructed 3-D power Doppler ultrasound. D) A trend toward reduced tumor volume was noted for all tested antiangiogenic therapies (sunitinib, pazopanib, sorafenib), but this did not reach statistical significance. No consistent trend for tumor volume was noted for the anti-proliferative drugs (everlimus and sirolimus). E) A statistically significant reduction in tumor vascularity was observed only for sorafenib therapy ( $22.5 \pm 5.6\%$  vs.  $6.8 \pm 1.3\%$ ,  $p < 0.05$ ), with no trend observed in tumor vascularity for any of the other treatments. F) A scatter plot of tumor vascularity versus tumor volume demonstrated no clear correlation between the two measures.

commodate the majority of RCC xenografts, with relatively high rates of engraftment (>90%) across different patient tumors. The CAM microenvironment is highly angiogenic, resulting in well perfused RCC PDX specimens as determined by contrast-enhanced high-frequency ultrasound imaging (Figure 4.6B). When selected embryos with RCC PDXs were injected with a chick and human endothelial cell specific lectin (lens culinaris agglutinin, [21, 22]), the majority of human CD31+ve microvessels (green) were also positive for lectin (red) (Figure 4.6C-D), revealing a co-option of both host (chick) and tumor (human) vessels. To our knowledge this has not been previously described in literature. Confocal imaging at a low magnification (10x) demonstrates extensive tumor vasculature throughout the PDX, (Figure 4.6C) and upon higher magnification (20x), shows the CAM reperfusing pre-existing tumor vasculature to maintain PDX tissue viability (Figure 4.6D). This pattern of vascular co-option was consistent among all examined patient tumors regardless of subtype (Figure 4.6E, chromophobe RCC). Although the rate of *de novo* angiogenesis from the CAM could support a tumor, our model reveals the ability of the CAM to “re-cannulate” pre-existing tumor vasculature, thus foregoing the typical time lag needed for vascular perfusion throughout a tumor xenograft. This results in viable RCC PDXs within two days, preempting studies for immediate drug testing/matrices. In some areas of the tumor, red blood cells can be seen present in the microvasculature (Figure 4.6A, lower half), consistent with the contrast-enhanced ultrasound imaging data (Figure 4.6B) and lectin labeling results (Figure 4.6C-E).

### 4.3.6 Multi-region Exome and Gene Copy Number Variation Analysis of PDX Samples

Total exome and single nucleotide variation (SNV) analyses was performed on tumor material in Figure 4.4A that had already been submitted to multi-regional analysis for drug resistance to sunitinib. For each biopsy region (primary or metastatic) a total of three fragments were selected for genomic sequencing analysis: one CAM engrafted tumor fragment that was submitted to vehicle treatment ( $T_{veh}$ ), one CAM engrafted tumor fragment that was submitted to sunitinib treatment ( $T_{sun}$ ), and one tumor fragment ( $T_0$ ) that was not xenografted. Comparison of the  $T_0$  vs.  $T_{veh}$  tumor fragments revealed minimal differences in terms of SNV and copy

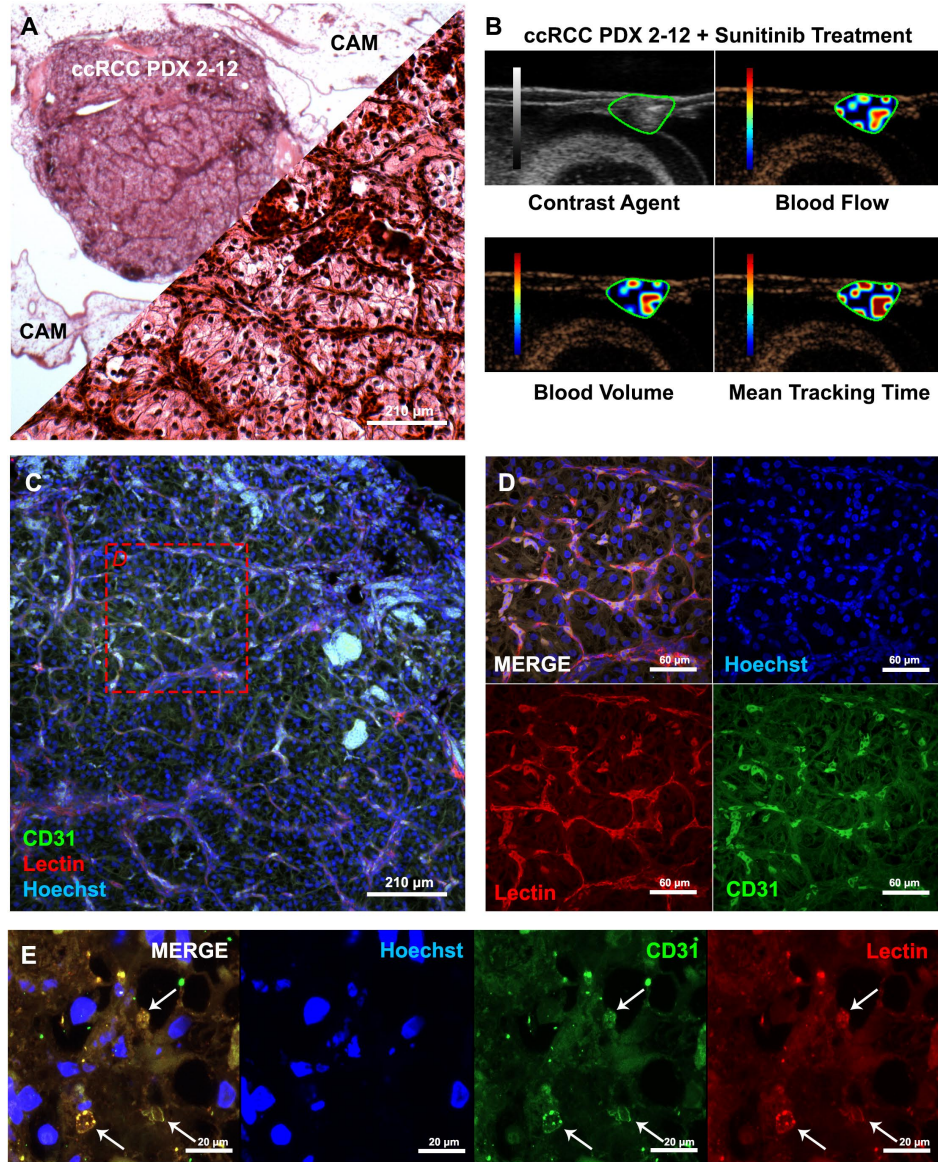


Figure 4.6: Pre-existing vessel co-option leads to rapid vascularization of patient tissues. A) Histology of engrafted PDX show densely vascularized tumor tissue evident from a large amount of red blood cells present in the section. B) Parametric contrast-enhanced ultrasound imaging corroborates dense vascularization and highlights functional heterogeneity in this PDX tumor. Structural and temporal vessel heterogeneity are also apparent in the time kinetics of the contrast enhancement. C) Sections from RCC PDX bearing embryos that were injected with an endothelial cell specific lectin (lens culinaris agglutinin) and stained with anti-CD31-FITC antibody and Hoechst. Low magnification (10x) confocal imaging demonstrates extensive tumor vasculature throughout the PDX. D) High magnification (20x) reveals that the majority of human CD31+ve microvessels (green) were also positive for lectin (red), revealing a co-option of both host (chick) and tumor (human) vessels. This implies that the CAM reperfuses pre-existing tumor vasculature to maintain PDX tissue viability. E) This pattern of vascular co-option was consistent among all examined patient tumors regardless of subtype (chromophobe RCC).

number variation (CNV) analysis, confirming that the implantation procedure does select parts of the tumor for phenotypic analysis. In terms of tumor heterogeneity prior to sunitinib treatment, multi-regional analysis also revealed substantial heterogeneity in terms of SNVs and the identities of genes mostly commonly held with SNVs, thus corroborating earlier reports by Gerlinger and colleagues [22]. Treatment with sunitinib did not yield differences in SNVs and CNVs between  $T_{veh}$  and  $T_{sun}$ , indicating that drug treatment does not alter the tumor fragments genetic blueprint over a drug treatment time course of 7-9 days.

Based on the SNV profile of the mostly commonly mutated genes present *de novo* in each tumor fragment, the RCC fragments that exhibited resistance to sunitinib clustered on the basis of SNVs in the ZNF569 gene locus (Figure 4.7A). This included tumor regions C1, C4, and C3, which all exhibited resistance to sunitinib treatment according to the PDX*ovo* platform (Figure 4.4A). Moreover, the ZNF569 SNVs within the ZNF569 gene loci were the most abundant SNV type throughout the tumor regardless of region (Figure 4.7D). Regions of the tumor sampled that were shown to be sensitive to sunitinib, including the metastases (Met1-Met3), did not have nonsynonymous SNV mutations in the ZNF569 gene locus and fewer SNVs relative to those regions resistant to sunitinib (C1, C4, C3). In terms of branched evolution, none of the metastases (Met1-Met3) were related to any regions of the primary tumor (C1-C6), likely due to lack of multi-region representation of the primary tumor in our analysis. Of greater interest was the lack of the ZNF569 mutation in the metastases which were shown to be sensitive to sunitinib in the PDX*ovo* platform and the presence of ZNF569 mutations in regions C1, C4, and C3 that were resistant to sunitinib according to PDX*ovo* testing.

## 4.4 Discussion

This study is the first to describe a functional consequence of tumor genetic heterogeneity [22] and the pre-existence of drug resistant clones or regions within primary and metastatic tumors prior to therapy. Our PDX platform revealed stark variations in targeted therapy response throughout a patient's tumor. These variations also correlate to patient clinical outcome, particularly for the clear cell RCC subtype where a significant portion of patients will be sensitive to sunitinib or pazopanib, whereas chromophobe and papillary RCC subtypes seldom respond



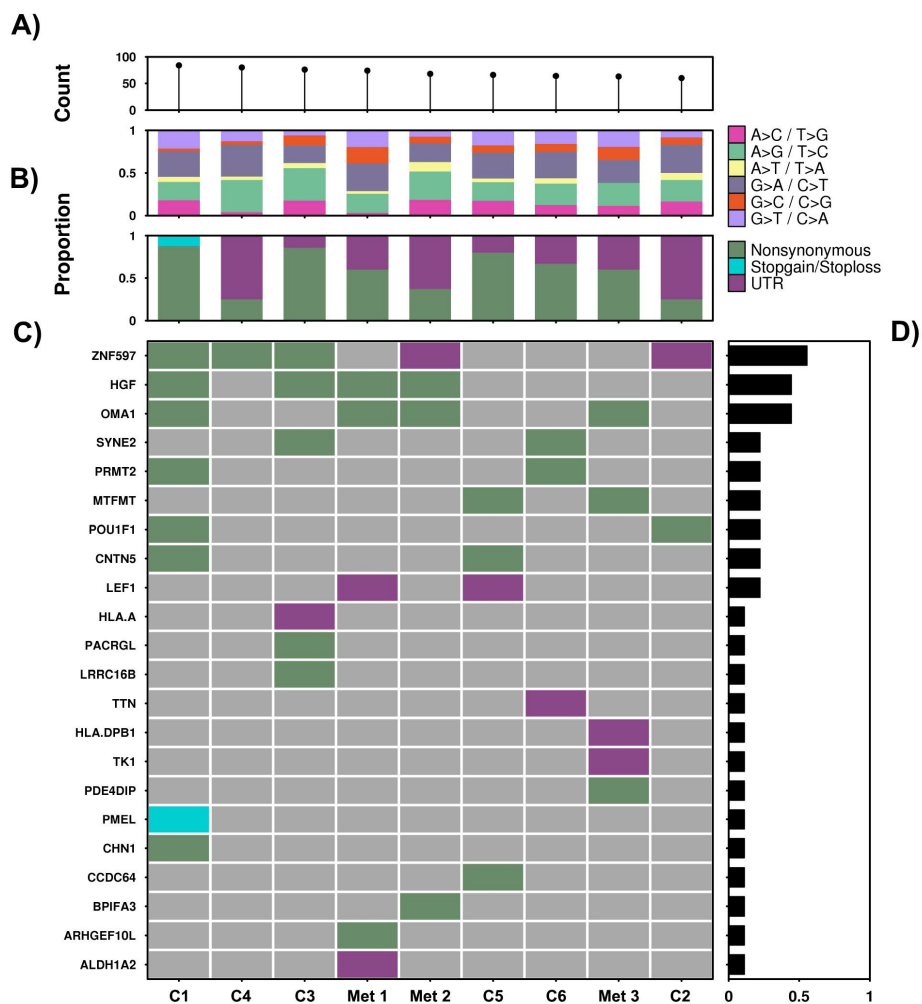


Figure 4.7: A) The total SNV count per fragment sample. B) The proportion of variants of the given base change and the functional consequence per fragment sample. C) The profile of the mutated genes for each sample demonstrating the functional consequence on that gene. RCC fragments that exhibited resistance to sunitinib (C1, C4, and C3) clustered on the basis of SNVs in the ZNF569 gene locus. D) The proportion of samples demonstrating a variant within each gene, the ZNF569 SNVs within the ZNF569 gene loci were the most abundant SNV type throughout the tumor regardless of region.

to these drugs. Exome and gene copy number variation analysis did not reveal a genetic signature specific for a drug resistant phenotype, even when the same tumor biopsy samples were used for both baseline and drug resistance modeling. For one such patient, half of the biopsies responded well to sunitinib, whereas the other half exhibited a drug resistant phenotype, with 12-18 PDXs for each treated biopsy. Biopsies of the metastases were also evaluated, revealing potential branched evolution from the sunitinib-responsive portions of the tumor, as per functional analysis but not via total exome sequencing. Most importantly, we discovered the prevalence of pre-existing drug resistant phenotypes throughout the primary tumor prior to administration of sunitinib or pazopanib; however, the intrinsic qualities that produce the drug resistant phenotype *de novo* remain unclear.

The PDX<sub>ovo</sub> model presents many advantages over conventional mouse PDX models due to one key strength: efficient tumor take rates. Regardless of subtype, the PDX<sub>ovo</sub> model is capable of ~90% tumor take rates which occurs within the first 48 hours of implantation onto the CAM of the chick embryo. Consequently, the utility and potential of this PDX model directly depends on the amount of tumor tissue obtained for evaluation. In this study, we were able to prepare >300 PDX models for each tumor, permitting multi-regional analysis of both the primary tumor (6 sites) and any nearby metastases (3 metastases) in a well-powered manner (n>36 per tumor core). Due to the nature of implantation, the tumor is readily accessible for manipulation or drug treatment, eliminating the need for intravenous injection of drug. Pairing this PDX model with high-frequency ultrasound imaging allows for a high-throughput means of quantifying tumor blood flow rates and vascularity (5–10 minutes/tumor). This is an ideal readout for evaluating the efficacy of anti-angiogenic targeted therapies on the xenograft. Tumor xenografts from the same biopsy core generate consistently similar results in terms of tumor blood flow rates and vascularity, even in response to targeted therapy, underscoring the reliability and utility of the model in accommodating xenografts. However, the relationship between topical sunitinib dosing on the CAM xenograft model and clinical dosages remains unclear. The concentrations set in this study were based on patient-derived cell lines that exhibited sensitive/resistant phenotypes in mouse PDX studies. Determining the clinical equivalence of a PDX<sub>ovo</sub> therapy is ongoing work.

Contrary to previous findings [23], the xenografts were re-vascularized via the pre-existing

tumor vasculature by the CAM, which was confirmed by immunohistochemistry and vessel mapping. This mechanism is more plausible than the CAM exclusively vascularizing the tumor through the production of new chick blood vessels, because xenograft blood flow is very active within 48 hours post-implantation of the RCC tumor implants. Furthermore, the tumor microvasculature of RCC xenografts is dense, indicating that a portion of the tumor vasculature would be eventually re-cannulated over the 7-9 day implantation period. The implantation rates of these tumor fragments is similar to results found by Folkman et al. [23], in which various normal tissue types were re-vascularized by the CAM within 1-3 days post-implantation. The novelty in this report is that we observe high tumor take-rates within 24-48 hours after implantation, regardless of the biopsy site, and these xenografts can be treated with drug or vehicle over the course of 7-9 days.

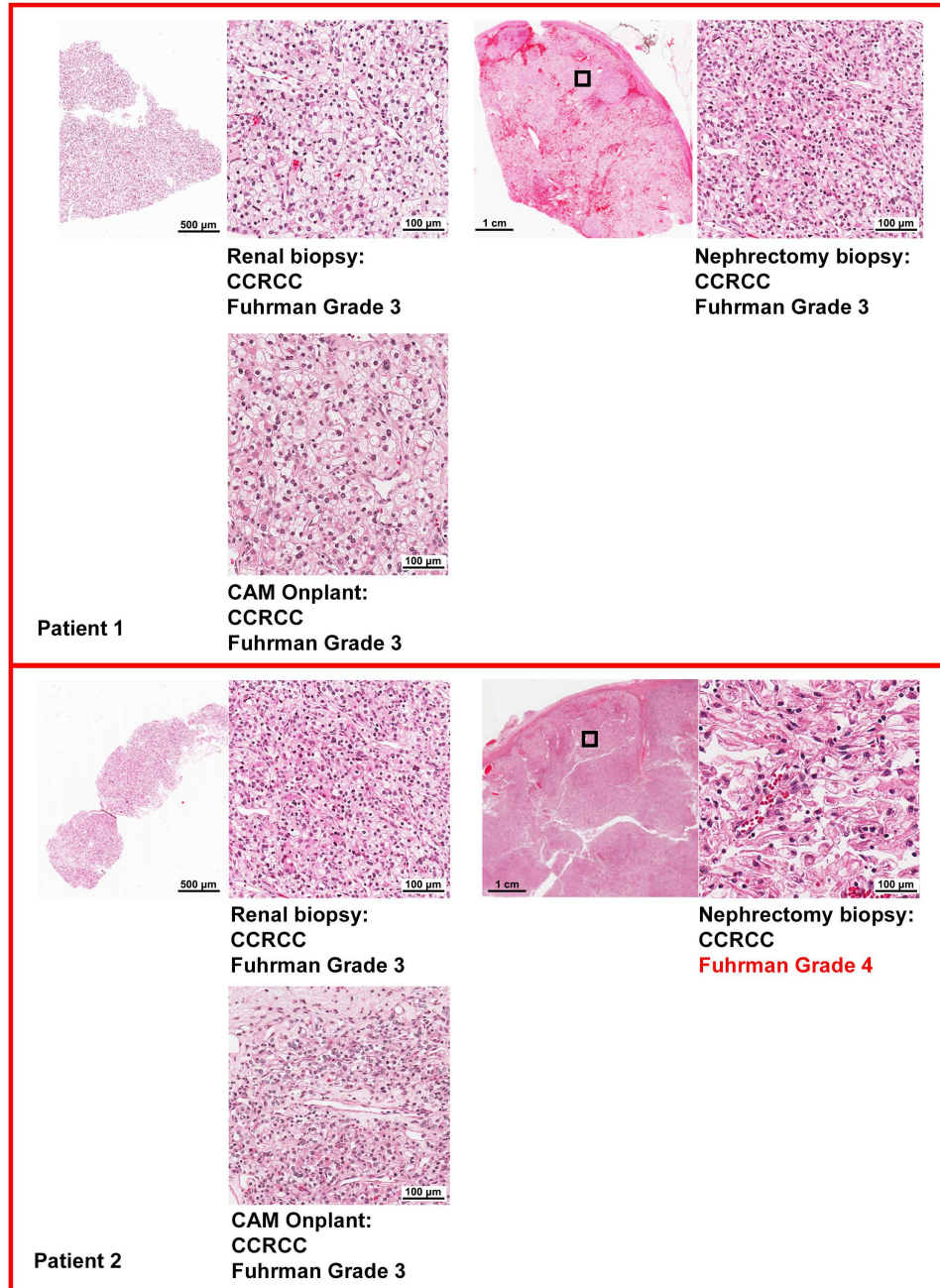
Based on our data, multi-region analysis of the tumor is critical and requires phenotype-based evaluation that can directly inform clinical management. In this case, we rely on high-frequency ultrasound to quantify tumor perfusion rates and vascularity to monitor functional changes, or a lack thereof, caused by targeted therapy. Although genomics-based approaches are more scalable, we have opted for a phenotype-based understanding of drug resistance, as opposed to a biomarker-driven approach which would eventually necessitate the studies described here. Understanding the genetic “blueprint” responsible for drug resistance is clearly needed; however, the use of a phenotype-based readout, as presented here, can at least provide clinically actionable information for RCC patients who are at risk of *de novo* drug resistance. In essence, this platform allows us to predict the location of drug resistant clones at the time of nephrectomy and before they are manifest in the patient, outmaneuvering the tumor before it can become refractory to any targeted therapy. A genetic signature for drug resistance will eventually arise, and the PDX<sub>OVO</sub> model can be used to confirm those results in a prospective fashion, as opposed to case-control genomics studies.

Our genotype analysis of these biopsies is unique, despite various other next-generation sequencing (NGS) efforts focused on RCC, because of the prospective nature of our analysis on *de novo* resistant clones. By definition, all previous NGS efforts have been highly-powered case-control studies consisting of extracted tumors from patients at baseline; these are then compared to clinical outcomes. While these efforts are valid in the a priori sense of genotype-

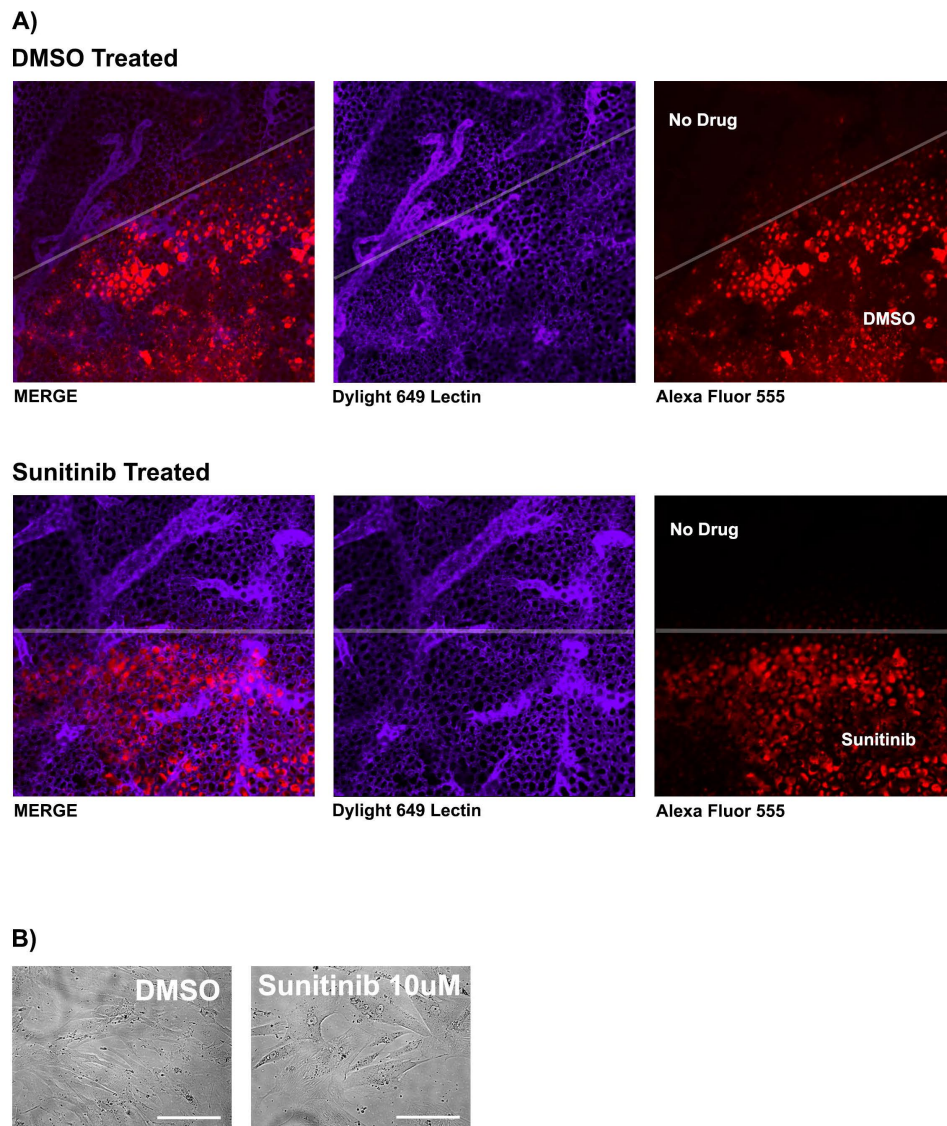
based causality, the extent of intratumoral diversity between patients within the same cohort may obscure several genotypes that initiate the drug-resistant phenotype. Therefore, in this prospective PDX study, there does not appear to be a bonafide drug-resistant genotype (or gene signature) when comparing intratumor clones that successfully respond to sunitinib. This conclusion was made possible through the use of an equal number of untreated clones for comparison.

## **4.5 Conclusions**

Functional tumor heterogeneity exists at the time of nephrectomy, which gives rise to significant future considerations for clinicians who will select the targeted therapy for the first-line treatment. This functional tumor heterogeneity may also warrant further studies in combination with PD-1 based immunotherapy regimens, which have already suggested that functional tumor heterogeneity can influence clinical outcomes. It may also explain, to an extent, why some patients exhibit partial response to PD-1 based immunotherapies [24] and reinvigorate the discussion of optimal dosages of currently used targeted therapies, prior to introduction of immunotherapies.



Supplementary Figure 4.1: Intratumoral heterogeneity is evident from multiple core biopsies. Tissues taken during renal biopsy and the nephrectomy whole mount specimen reveal intratumoral heterogeneity. Patient #1 demonstrated a consistent clear cell renal cell carcinoma pathology and Fuhrman Grade scores between the renal biopsy, nephrectomy sample, and CAM PDX onplant. In contrast, Patient #2 had regions of ccRCC tumor with a Fuhrman Grade of 4, whereas renal biopsy was classified as Fuhrman Grade 3. Tumor pathology and Fuhrman Grade of the renal biopsy is maintained after CAM engraftment of tissue specimens. This indicates that a single core biopsy for PDX onplanting may underestimate tumor heterogeneity is likely insufficient to inform patient therapy.



Supplementary Figure 4.2: Clinically relevant sunitinib dosages do not negatively impact the structure and function of developing CAM vasculature. A) Mock onplanted embryos were treated with either sunitinib, or DMSO control, with the same dose and schedule used in main section of this study. Topical drugs were mixed with dilute (100x) Alexa Fluor 555 dye to visualize surface concentration. At the end of the nine day therapy, animals were intravascularly injected with Dylight 649 agglutinin (1:10 dilution with PBS). Confocal imaging reveals that sunitinib treatment did not impact on the CAMs vascular development when compared to control. The gray line highlights the border between drug treated and drug free regions of CAM. B) Digital microscope images of RCC cells cultured with DMSO (vehicle) or sunitinib. No difference in cell viability was noted for either therapy.

# References

- [1] R. J. Motzer, M. D. Michaelson *et al.*, “Activity of SU11248, a multitargeted inhibitor of vascular endothelial growth factor receptor and platelet-derived growth factor receptor, in patients with metastatic renal cell carcinoma,” *J. Clin. Oncol.*, vol. 24, no. 1, pp. 16–24, Jan. 2006.
- [2] R. S. Bhatt, X. Wang *et al.*, “Renal cancer resistance to antiangiogenic therapy is delayed by restoration of angiostatic signaling,” *Mol. Cancer Ther.*, vol. 9, no. 10, pp. 2793–2802, Oct. 2010.
- [3] M. Gerlinger and C. Swanton, “How Darwinian models inform therapeutic failure initiated by clonal heterogeneity in cancer medicine,” *Br. J. Cancer*, vol. 103, no. 8, pp. 1139–1143, Oct. 2010.
- [4] T. A. Yap, M. Gerlinger *et al.*, “Intratumor heterogeneity: seeing the wood for the trees,” *Sci. Transl. Med.*, vol. 4, no. 127, p. 127ps10, Mar. 2012.
- [5] M. Gerlinger, S. Horswell *et al.*, “Genomic architecture and evolution of clear cell renal cell carcinomas defined by multiregion sequencing,” *Nature Genet.*, vol. 46, no. 3, pp. 225–233, Mar. 2014.
- [6] B. I. Rini and M. B. Atkins, “Resistance to targeted therapy in renal-cell carcinoma,” *The Lancet. Oncology*, vol. 10, no. 10, pp. 992–1000, Oct. 2009.
- [7] D. Huang, Y. Ding *et al.*, “Interleukin-8 mediates resistance to antiangiogenic agent sunitinib in renal cell carcinoma,” *Cancer Res.*, vol. 70, no. 3, pp. 1063–1071, Feb. 2010.
- [8] H. J. Hammers, H. M. Verheul *et al.*, “Reversible epithelial to mesenchymal transition and acquired resistance to sunitinib in patients with renal cell carcinoma: evidence from a xenograft study,” *Mol. Cancer Ther.*, vol. 9, no. 6, pp. 1525–1535, Jun. 2010.
- [9] S. Sivanand, S. Pea-Llopis *et al.*, “A validated tumorgraft model reveals activity of dovitinib against renal cell carcinoma,” *Sci. Transl. Med.*, vol. 4, no. 137, p. 137ra75, Jun. 2012.
- [10] A. Pava-Jimnez, V. T. Tcheuyap, and J. Brugarolas, “Establishing a human renal cell carcinoma tumorgraft platform for preclinical drug testing,” *Nat. Protoc.*, vol. 9, no. 8, pp. 1848–1859, Aug. 2014.

- [11] K. Okamura, Y. Tsuji *et al.*, “Growth of human tumor xenografts on chorioallantoic membrane of chick embryo,” *Acta Urol. Jap.*, vol. 41, no. 3, pp. 163–170, Mar. 1995.
- [12] P. Fergelot, J.-C. Bernhard *et al.*, “The experimental renal cell carcinoma model in the chick embryo,” *Angiogenesis*, vol. 16, no. 1, pp. 181–194, Jan. 2013.
- [13] C. J. Ricketts and W. M. Linehan, “Intratumoral heterogeneity in kidney cancer,” *Nature Genet.*, vol. 46, no. 3, pp. 214–215, Mar. 2014.
- [14] I. F. Tannock, “Re: Intratumor Heterogeneity and Branched Evolution Revealed by Multiregion Sequencing,” *Eur. Urol.*, vol. 65, no. 4, pp. 846–847, Apr. 2014.
- [15] C.-F. Cho, A. Ablack *et al.*, “Evaluation of nanoparticle uptake in tumors in real time using intravital imaging,” *J. Vis. Exp: JoVE*, no. 52, Jun. 2011.
- [16] H. S. Leong, N. F. Steinmetz *et al.*, “Intravital imaging of embryonic and tumor neovasculature using viral nanoparticles,” *Nat. Protoc.*, vol. 5, no. 8, pp. 1406–1417, Aug. 2010.
- [17] K. Wei, A. R. Jayaweera *et al.*, “Quantification of Myocardial Blood Flow With Ultrasound-Induced Destruction of Microbubbles Administered as a Constant Venous Infusion,” *Circulation*, vol. 97, no. 5, pp. 473–483, Feb. 1998.
- [18] T. Donnem, J. Hu *et al.*, “Vessel co-option in primary human tumors and metastases: an obstacle to effective anti-angiogenic treatment?” *Cancer Med.*, vol. 2, no. 4, pp. 427–436, Aug. 2013.
- [19] E. A. Kuczynski, M. Yin *et al.*, “Co-option of Liver Vessels and Not Sprouting Angiogenesis Drives Acquired Sorafenib Resistance in Hepatocellular Carcinoma,” *J. Natl. Cancer Inst.*, vol. 108, no. 8, Apr. 2016.
- [20] S. Goel, D. G. Duda *et al.*, “Normalization of the vasculature for treatment of cancer and other diseases,” *Physiol. Rev.*, vol. 91, no. 3, pp. 1071–1121, Jul. 2011.
- [21] S. M. Jilani, T. J. Murphy *et al.*, “Selective binding of lectins to embryonic chicken vasculature,” *J. Histochem. Cytochem.*, vol. 51, no. 5, pp. 597–604, May 2003.
- [22] M. Gerlinger, A. J. Rowan *et al.*, “Intratumor Heterogeneity and Branched Evolution Revealed by Multiregion Sequencing,” *N. Engl. J. Med.*, vol. 366, no. 10, pp. 883–892, Mar. 2012.
- [23] D. H. Ausprunk, D. R. Knighton, and J. Folkman, “Vascularization of normal and neoplastic tissues grafted to the chick chorioallantois. Role of host and preexisting graft blood vessels,” *Am. J. Pathol.*, vol. 79, no. 3, pp. 597–618, Jun. 1975.
- [24] M. Sznol and L. Chen, “Antagonist Antibodies to PD-1 and B7-H1 (PD-L1) in the Treatment of Advanced Human Cancer,” *Clin. Cancer Res.*, vol. 19, no. 5, pp. 1021–1034, Mar. 2013.



## **Chapter 5**

# **Compound Speckle Model Reduces Contrast Ultrasound Variability in a Patient-Derived Xenograft Model of Renal Cell Carcinoma**

*The contents of this chapter are in preparation to be submitted to: *Ultrasound in Medicine & Biology* as: “Compound Speckle Model Reduces Contrast Ultrasound Variability in a Patient-Derived Xenograft Model of Renal Cell Carcinoma”, by Matthew R. Lowerison, Ann F. Chambers, Hon S. Leong, Nicholas E. Power, and James C. Laceyfield.*

## 5.1 Introduction

Contrast-enhanced ultrasound (CEUS) permits rapid, longitudinal, and non-destructive quantification of blood perfusion in normal and pathological tissues. This capability is particularly important for detection of neoplastic lesions and characterization of tumor-associated angiogenesis. CEUS has seen application in the clinical setting for liver specific contrast imaging, where the administration of microbubbles improves the visibility of focal liver lesions (such as metastatic tumors and hepatocellular carcinoma), and is increasingly being used for the assessment of tissue vascularity [1–3]. In a preliminary study on patients diagnosed with metastatic renal cell carcinoma (RCC), CEUS was found to be sensitive to the vascular changes induced by sunitinib therapy [4]. In the preclinical setting, CEUS has been used on animal models of tumor-induced angiogenesis to evaluate anti-angiogenic therapy efficacy [5–7]. To quantify tumor perfusion, investigators will typically fit time-series CEUS data to an indicator-dilution model to extract surrogate indices of blood volume, velocity, and flow [8–10]. However, conventional CEUS image analysis relies on the mean backscatter signal intensity from microbubbles to estimate indicator concentration for indicator-dilution modeling. This discounts additional information that may be available from heterogeneous contrast enhancement in the imaged tumor cross-section. Furthermore, the widespread application of CEUS analysis in anti-angiogenic trials has been limited due to the high variability and low reproducibility of flow parameters [11].

A compound statistical model for the analysis of the first-order speckle statistics of CEUS images was introduced by Lowerison *et al.* [12] as a method for improving the perfusion quantification of tumor vasculature during anti-angiogenic therapy. In the model, contrast signal intensity,  $I$ , is considered as a compound distribution of exponential probability density functions,  $p(I)$ , weighted by a gamma probability function,  $w(\theta|\alpha, \beta)$ , as shown in Eqs. 5.1a- 5.1b. This formulation yields a Type-II Pareto (Lomax) probability density function (Eq. 5.1c) [13] for the signal intensity in a region of interest:

$$f(I|\alpha, \beta) = \int_{\Theta} w(\theta|\alpha, \beta) p(I) d\theta, \quad (5.1a)$$

$$f(I|\alpha, \beta) = \int_{\Theta} \left[ \frac{\alpha^\beta}{\Gamma(\beta)} \theta^{\beta-1} e^{-\alpha\theta} \right] \theta e^{-\theta I} d\theta, \quad (5.1b)$$

$$f(I|\alpha, \beta) = \frac{\beta \alpha^\beta}{(I + \alpha)^{\beta+1}}. \quad (5.1c)$$

The gamma probability weighting function serves as an approximation for log-normally distributed flow velocities in tumor vasculature. The technique yields two metrics for the evaluation of tumor perfusion: an estimate of the time-dependent change in enhanced tumor fraction, and an estimate of the fractal dimension of the tumor vasculature. Enhanced tumor fraction is calculated by reconstructing the weighting function at every time point during enhancement and comparing it to the unenhanced weighting function (Figure 5.1B). The time-dependent discrepancy between these two distributions serves as an estimate of enhanced volume percentage and can be analyzed using the same tools as conventional indicator-dilution curves. The fractal dimension of the tumor vasculature is related to the log-normal shape parameter  $\sigma_{LN}$ , which can be estimated from the gamma parameter,  $\beta$ , by assuming that the coefficient of variation for the two distributions are equal [14]:

$$\sigma_{LN} = \sqrt{\ln(\beta^{-1} + 1)}. \quad (5.2)$$

When applied to a mouse xenograft model of breast cancer [12], the compound speckle model significantly improved the classification accuracy between control and bevacizumab-treated tumors over conventional CEUS analysis, demonstrated reduced frame-to-frame variability, and showed promise in providing quantified metrics of vascular heterogeneity as verified by contrast-enhanced micro-CT. These studies provided a framework for evaluating the performance of the statistical method for detecting anti-angiogenic treatment responses that were validated with gold-standard histological and imaging techniques in a well-established murine breast cancer model. However, that study was limited in its clinical translatability due to a focus on antiangiogenic therapy for breast cancer. There is growing evidence that VEGF targeting therapies do not improve overall survival of patients with this disease, a finding that

led to the FDA withdrawing its approval of bevacizumab for treatment of metastatic breast cancer [15–17].

In this article, we apply the compound statistical technique to CEUS images acquired from a patient-derived xenograft (PDX) model of renal cell carcinoma (RCC) in the chorioallantoic membrane (CAM) of chick embryos (Chapter 4). RCC accounts for the majority of diagnosed kidney cancers in North American adults and is the most lethal of all genitourinary cancers [18]. Targeted therapies, such as sunitinib, are initially effective in most cases as RCC is highly dependent on tumor-driven angiogenesis. Four FDA-approved tyrosine kinase inhibitors (TKI) that target VEGF-A (sunitinib, pazopanib, sorafenib, and axitinib) have been shown to improve progression free and overall survival of patients with metastatic RCC [19–22]. However, an estimated 25-30% of patients exhibit *de novo* resistance to their prescribed front-line therapy [23–25]. There is currently no established means to identify resistant patients before cancer progression, which is observed months after the beginning of therapy. We have developed an ultra-fast RCC PDX assay for high-throughput phenotype-based evaluation of intratumoral specimen responses to targeted therapy within 10 days. Response to therapy in tumor fragments, a predictor of patient response, is evaluated using a combination of both power Doppler and CEUS estimates of vascular perfusion. Additionally, this PDX assay uses RCC tumor fragments taken from multiple biopsy sites in the primary tumor and metastatic lesions to further improve its potential utility as a predictor of treatment efficacy. This is possible due to the superior engraftment efficiency that chick CAM PDXs demonstrate over immunocompromised mouse PDX models.

The rationale for applying the compound statistical technique to CEUS images from the CAM RCC PDX model is two-fold. Firstly, RCC tumors have been reported to exhibit a high degree of intratumoral genetic heterogeneity that may promote resistance to antiangiogenic strategies [26, 27]. It is reasonable to assume that some of this genetic heterogeneity would manifest as intratumoral functional heterogeneity both within untreated core biopsies and in the response to antiangiogenic therapy. Thus, applying the compound statistical model, which was developed as a technique to quantify enhancement heterogeneity independently of indicator dilution modelling, may add new information to this PDX platform. Secondly, the original analysis of the CEUS images from the CAM PDX model demonstrated a high amount of

variability in the quantification of flow parameters. Reducing the variability of tumor perfusion quantification would improve the confidence of classification of tumor biopsies as being either sensitive or resistant to therapy.

Thus, this is a hypothesis-generating pilot study to determine whether statistical processing of CEUS images might add new information to the chick CAM PDX assay. In the study presented here, two sets of sunitinib drug sensitivity matrices, one generated using conventional CEUS analysis and the other with the statistical model, are produced for four patients with metastatic RCC. Drug sensitivity matrices (Chapter 4) classify individual tumor biopsies from a patient as being either sensitive or resistant to sunitinib in an effort to capture treatment response consequences of intratumoral heterogeneity. We demonstrate that analysis of the first-order speckle statistics of nonlinear (subharmonic) CEUS images reduces the variability in tumor perfusion quantification, particularly for estimates of blood volume, and reduces the sensitive/resistant classification ambiguity caused by heterogeneous tumor samples.

## **5.2 Materials and Methods**

### **5.2.1 Patient Characteristics**

Tumor samples were obtained from patients that provided oral and written consent to a University of Western Ontario Research Ethics Board approved protocol (REB #104278), allowing for the use of surgical specimens for research at the London Health Sciences Centre. CAM PDX engraftment was performed for specimens obtained from four patients diagnosed with large kidney lesions (>5 cm), two of which also had chest-wall metastases. Pathological analysis confirmed that three patients had clear cell RCC (1 with metastases) and the remaining patient had chromophobe RCC with metastases. All patients underwent complete nephrectomy.

### **5.2.2 Preparation of Reagents**

A stock solution of sunitinib, which is a small-molecule, multi-targeted receptor tyrosine kinase inhibitor, was obtained from LC Laboratories (Woburn, MA). Sunitinib was diluted with dimethyl sulfoxide (DMSO) to a concentration of 10  $\mu$ M (Sigma, ON). Vehicle control was

produced by diluting DMSO with PBS at a 1:5 dilution ratio.

### 5.2.3 Engraftment of Patient Tumor Fragments into the CAM

Fertilized chicken eggs were obtained from McKinley Hatchery (St Mary's, ON) and stored in a humidified incubator at 38 °C. We refer the reader to [28, 29] for a protocol describing each step of the chicken embryo cultivation process. Tumor engraftment procedures were performed on the ninth day of embryonic development (EDD-9) with at least 300 embryos per patient tumor. At the time of partial or full nephrectomy, 5-9 tumor core biopsies (8 mm diameter) were extracted from multiple independent sites in the primary tumor, and any nearby metastases, to sample for tumor heterogeneity. Biopsies were sectioned into  $\sim 2 \times 2 \times 2$  mm fragments and implanted into the CAM immediately after the abrasion of a small area of chorionic epithelium. At 24 hours post implantation, 10  $\mu$ L of BLES lung surfactant (BLES Biochemicals Inc., London, ON) was topically applied to the tumor fragment. Tumor fragments were treated every two days, starting on EDD-11, with either 3  $\mu$ L (10  $\mu$ M) of sunitinib or DMSO control, until imaging on EDD-18.

### 5.2.4 Volumetric Ultrasound Imaging Acquisition Protocol

All ultrasound imaging was performed using a Vevo<sup>®</sup> 2100 high-frequency imaging system (VisualSonics Inc., Toronto, Canada). B-mode and power Doppler images were acquired using a 40 MHz linear array transducer (MS-550D, 40  $\mu$ m nominal axial resolution, 80  $\mu$ m nominal lateral resolution). Ultrasound coupling gel (Aquasonic<sup>®</sup> 100, Parker Laboratories, Inc., Fairfield, NJ) was liberally applied over the surface of the transducer to provide an acoustic standoff between the transducer and the CAM. Saline was topically applied to the tumor surface immediately prior to coupling to prevent the acoustic gel from adhering to the CAM. The imaging field of view was set to 10.00 mm in the axial direction and 14.08 mm in the lateral direction, with a Doppler color box sized to completely enclose the largest cross-section of tumor. Three-dimensional volumetric images were acquired with a linear stepper motor (P/N 11484, VisualSonics Inc.) with a step size of 0.076 mm and a total travel distance of 15.01 mm. This imaging volume was large enough to enclose the entire tumor in all of the imaged embryos.

### 5.2.5 Contrast-Enhanced Ultrasound Image Acquisition Protocol

All contrast-enhanced ultrasound imaging was performed with the Vevo MicroMarker™ (VisualSonics Inc.) microbubble agent reconstituted with 0.7 mL of sterile saline to yield a solution with approximately  $2 \times 10^9$  microbubbles/mL. CAM vasculature was manually cannulated with a glass capillary needle to inject a total volume of 50  $\mu\text{L}$  of the microbubble solution into each embryo. The Vevo 2100 system was equipped with a 20 MHz linear array transducer (MS-250, 75  $\mu\text{m}$  nominal axial resolution, 165  $\mu\text{m}$  nominal lateral resolution), transmitting at 18 MHz in nonlinear contrast mode for all CEUS acquisition. The nonlinear contrast mode performs subharmonic imaging using a two-pulse amplitude modulation method [30]. Destruction-reperfusion imaging was performed over a field of view sized to completely enclose the cross-section of the tumor. Cine loops consisting of 700 frames were acquired at a frame rate of 20 Hz with a 1-second bursting pulse ( $MI = 0.9$ ) at frame 100. This acquisition protocol was repeated for five anatomical planes throughout the tumor volume.

### 5.2.6 Volumetric Ultrasound Image Analysis

Volumetric image reconstruction and analysis was performed using the manufacturer's software (Vevo 2100 Workstation, VisualSonics Inc.). Estimates of tumor volume and vascularity were computed via manual planimetry on the reconstructed three-dimensional images. The vascularization index (VI) of the tumor was estimated by calculating the percentage of voxels in the segmented volume that contained detected blood flow (*i.e.* Doppler color pixels).

### 5.2.7 Contrast-Enhanced Ultrasound Image Analysis

All CEUS image analysis was performed using MATLAB (version R2013a, The MathWorks Inc., Natick, MA). Cine loops of the nonlinear contrast image data were acquired using the Vevo 2100's digital RF mode and exported as uncompressed, intensity signal data files (quantized to 16 bits at a 288 MHz sampling frequency). The first frame of each cine loop was manually segmented to produce the tumor region of interest (ROI) used in the analysis of all subsequent frames.

Generalized Pareto PDFs (Eq. 5.1c) were fit to the contrast intensity samples taken from the ROI in each frame of each cine loop. Maximum likelihood estimates of the Pareto parameters  $(\alpha, \beta)$  were solved for using an unconstrained nonlinear optimization (Nelder-Mead simplex direct search) with initial guesses from the method of moments. The maximum number of function evaluations and iterations allowed was set to 200 times the number of sample points in the ROI. The termination tolerances on the function value and on the input value were set to  $10^{-4}$ . Estimates of the log-normal distribution's shape parameter ( $\sigma_{LN}$ ) were generated at every time-point in the cine loop from the fitted gamma parameter ( $\beta$ ), as in Eq. 5.1c. The image analysis procedure is described in more detail in [12].

### 5.2.8 Wash-in Curve Analysis

The kinematics of contrast enhancement were characterized for both the conventional method of CEUS analysis, as well as the method based on the statistical model, using a mono-exponential fit [31]. For conventional CEUS, wash-in curves were constructed by plotting the mean signal intensity within the ROI for every frame in the cine loop. Relative blood volume was estimated from the scaling parameter of the fitted mono-exponential function. For the statistical model technique, the gamma probability density weighting function in Eq. 5.1b was reconstructed using the extracted Pareto parameters  $(\alpha, \beta)$  for every frame in the cine loop. The time-dependent gamma PDF was then used to estimate the enhanced tumor fraction (Figure 5.1B) by determining the overlapping area between the weighting function at time point  $t$  and the gamma weighting function of unenhanced tissue (*i.e.*, just after the destruction pulse). One minus this area of overlap, which represents enhanced populations of speckle, was plotted as a function of time and is considered comparable to the conventional CEUS blood volume estimate.

### 5.2.9 Biopsy Classification as Drug Resistant or Sensitive

Sunitinib sensitivity matrices were constructed (as in Chapter 4) to classify every tumor biopsy taken from all patients in this study as being either a responder (green), partial responder (yellow), or non-responder (red). Classification of tumor biopsies was performed via the calculation of an F-statistic in a two-way ANOVA to determine if the population means between the



sunitinib group and DMSO control were significantly different using both the power Doppler VI and CEUS data measures. Two such biopsy classification matrices were completed to compare the performance between both CEUS techniques, with factors being drug group and imaging modality (power Doppler with conventional CEUS, or with compound CEUS). In either case, a biopsy was classified as sunitinib-sensitive if it was found to have an F-statistic of greater than 3.17, and sunitinib-resistant if the F-statistic was below 1.46. Biopsies between these values were classified as an intermediate, or partial, response. The threshold values for the F-statistic were determined from a pilot study testing CAMs engrafted with a known sunitinib-sensitive cell line (786-O) and a known sunitinib-resistant cell line (XP121). Each pilot study had 4 embryos per treatment group, where the  $F = 3.17$  value corresponds to an alpha level of 0.10, and the  $F = 1.46$  to an alpha level of 0.25.

## 5.3 Results

### 5.3.1 Engraftment Efficiency of Renal Cell Carcinoma Tumors

All of the patients in this study had primary RCC tumors that were at least 5 cm in diameter at the time of nephrectomy. This permitted multiregional analysis of sunitinib response via the extraction of multiple biopsies from the primary tumor (5-6 biopsies) and any nearby metastases (3 biopsies in both patients with metastases). The total number of biopsies per patient in this study was 5-9. Each biopsy was subdivided into at least 36 fragments, and fragments were engrafted directly into the CAM on EDD-09, yielding 200-320 engrafted embryos per patient in this study. Engrafted fragments rapidly vascularized and maintained a high viability in the CAM over the duration of the study ( $N > 5$  fragments in each treatment group survived until imaging on EDD-18, per core biopsy). Ultrasound imaging confirmed a high degree of vascularization as depicted by power Doppler and CEUS acquisitions (Figure 5.2).

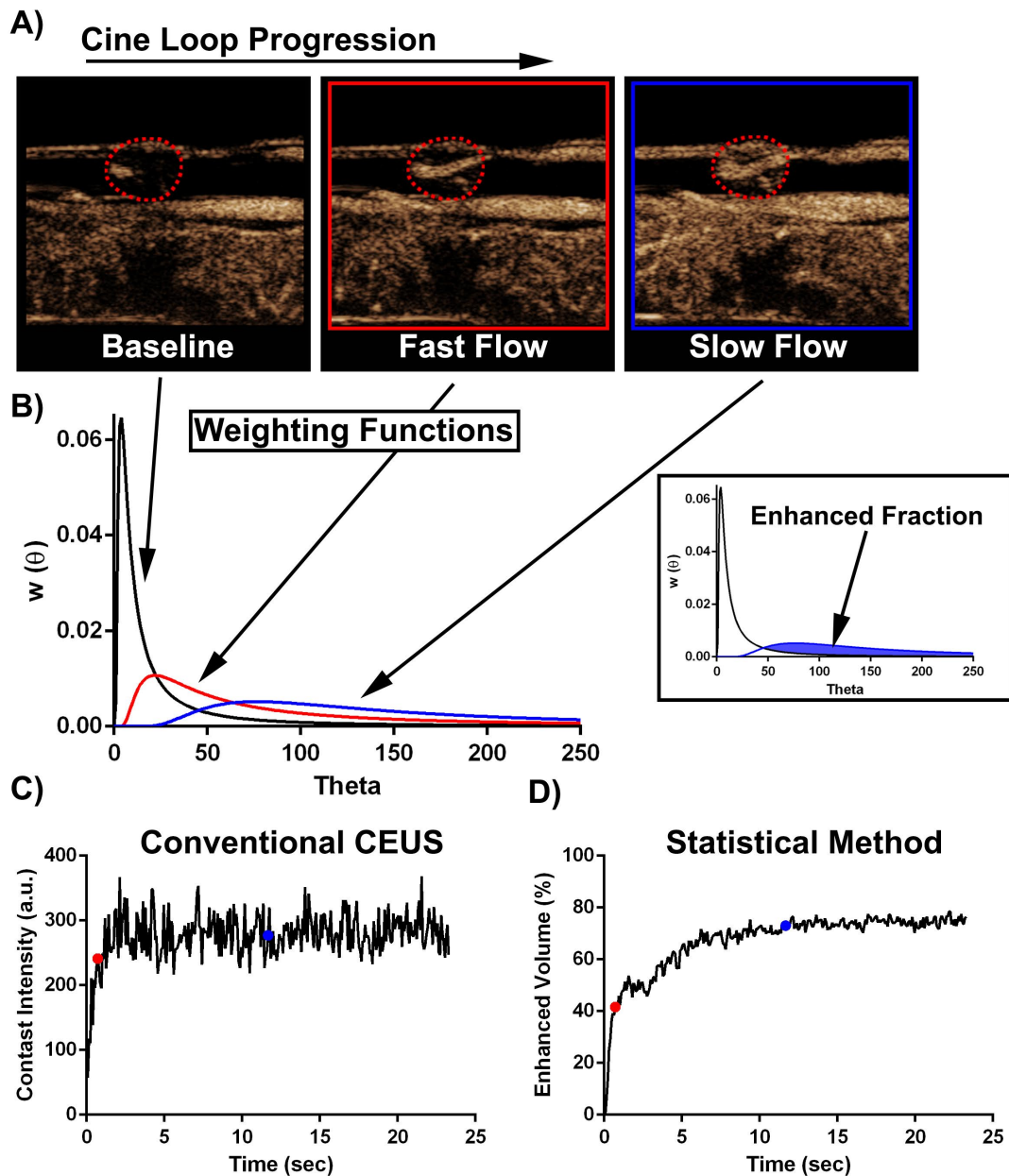


Figure 5.1: CEUS analysis of a sample tumor. A) Selected frames from a CEUS cine loop that represent different phases of contrast wash in. From left to right these frames represent baseline signal, arteriole enhancement, and complete perfusion. B) Weighting functions constructed using intensity samples taken from the CEUS frames shown in (A). The inset to the right demonstrates how the enhanced fraction at the third time point was calculated. C) The conventional CEUS wash-in curve of contrast signal intensity for this tumor. D) A wash-in curve constructed using the enhanced fraction estimated from the statistical method's weighting functions. The wash-in curve samples highlighted by the red and blue dots in (c) and (d) correspond to the "fast flow" and "slow flow" frames, respectively, in (a).

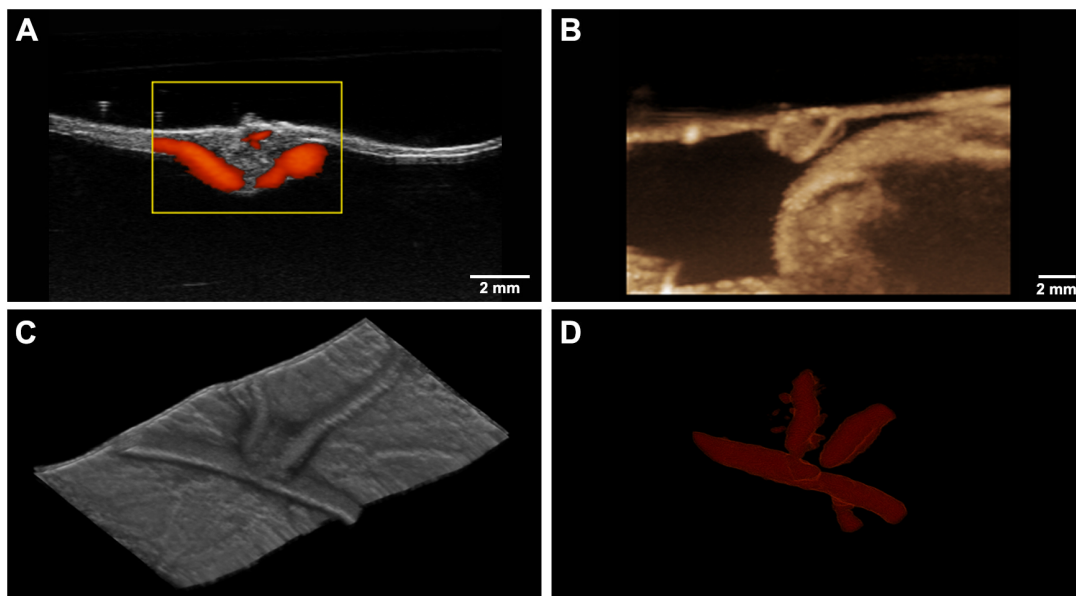


Figure 5.2: Example ultrasound images taken from a tumor-bearing embryo, showing evidence of A) feeding arterioles (2-D power Doppler image, yellow lines denote placement of Doppler color box) and B) dense capillary networks (nonlinear CEUS image). Bottom panels show 3-D reconstruction of C) tumor anatomy (B-mode) and D) arteriole network (power Doppler).

### 5.3.2 Application of the Compound Speckle Model to RCC PDX CEUS

#### Data

The contrast intensity data from tumor ROIs demonstrated a close agreement to the Type-II Pareto probability density function (Eq. 5.1c) in every frame of each CEUS cine loop, and in all cases the model fitting converged within the specified termination tolerances. Figure 5.1A shows an example of selected frames from a CEUS tumor reperfusion cine loop with distinct phases of wash-in. The left frame shows the tumor just following the destruction pulse sequence, where very little enhancement is present. The middle panel is taken just after the complete filling of an arteriole within the middle of the tumor ( $t = 1.58$  seconds). The last panel is a later time point when all of the slower flowing vasculature has perfused ( $t = 12.07$  seconds). These three time points have the example weighting functions constructed in Figure 5.1B. The inset demonstrates how the enhanced fraction of the tumor is calculated at every time point in the cine loop. A comparison of the two wash-in curves constructed from this example cine loop are shown in Figure 5.1C-D. The conventional CEUS processing shows a very rapid wash-in to an asymptote at or around the time that the arteriole is perfused, whereas

the curve constructed with the statistical method shows distinct fast and slow flow phases of wash in.

### 5.3.3 Compound Model Reduces Coefficient of Variation of CEUS Blood Volume Estimates

One of the advantages of the compound statistical model that was demonstrated in our previous work [12] was reduced frame-to-frame variability in indicator dilution curves. An example wash in curve demonstrating this advantage can be found in the comparison in Figure 5.1C-D. Furthermore, the analysis of first-order speckle statistics reduced the coefficient of variation (CoV) of CEUS estimates of blood volume when compared to conventional CEUS methods (CoV of 0.554 vs. 0.828, Brown-Forsythe test,  $p$ -value  $<0.05$ ). The CoV was significantly higher in the sunitinib-treated cohort (CoV of 0.677 and 0.901 for compound and conventional CEUS, respectively) than in the DMSO cohort (CoV of 0.388 and 0.756 for compound and conventional CEUS, respectively).

### 5.3.4 Correlations Among Ultrasound Vascular Metrics

Linear regression analysis of power Doppler vascularization index in comparison to both CEUS analysis techniques can be found in Figure 5.3. Conventional CEUS blood volume demonstrated a weak correlation to power Doppler VI (Figure 5.3A,  $R^2 = 0.1955$ ,  $p = 0.0013$ ), and compound statistical analysis of CEUS data marginally improved this correlation (Figure 5.3B,  $R^2 = 0.4331$ ,  $p < 0.0001$ ). There was only a slight correlation between the two CEUS analysis techniques (Figure 5.3C,  $R^2 = 0.2707$ ,  $p = 0.0001$ ). Generally, the  $\sigma_{LN}$  value exhibited the same trends as the compound-model enhanced volume fraction, implying that it does not add new information to CEUS analysis. The correlation between the compound-model enhanced volume fraction and the  $\sigma_{LN}$  parameter was weak, but statistically significant (Figure 5.3D,  $R^2 = 0.2302$ ,  $p = 0.0004$ ).

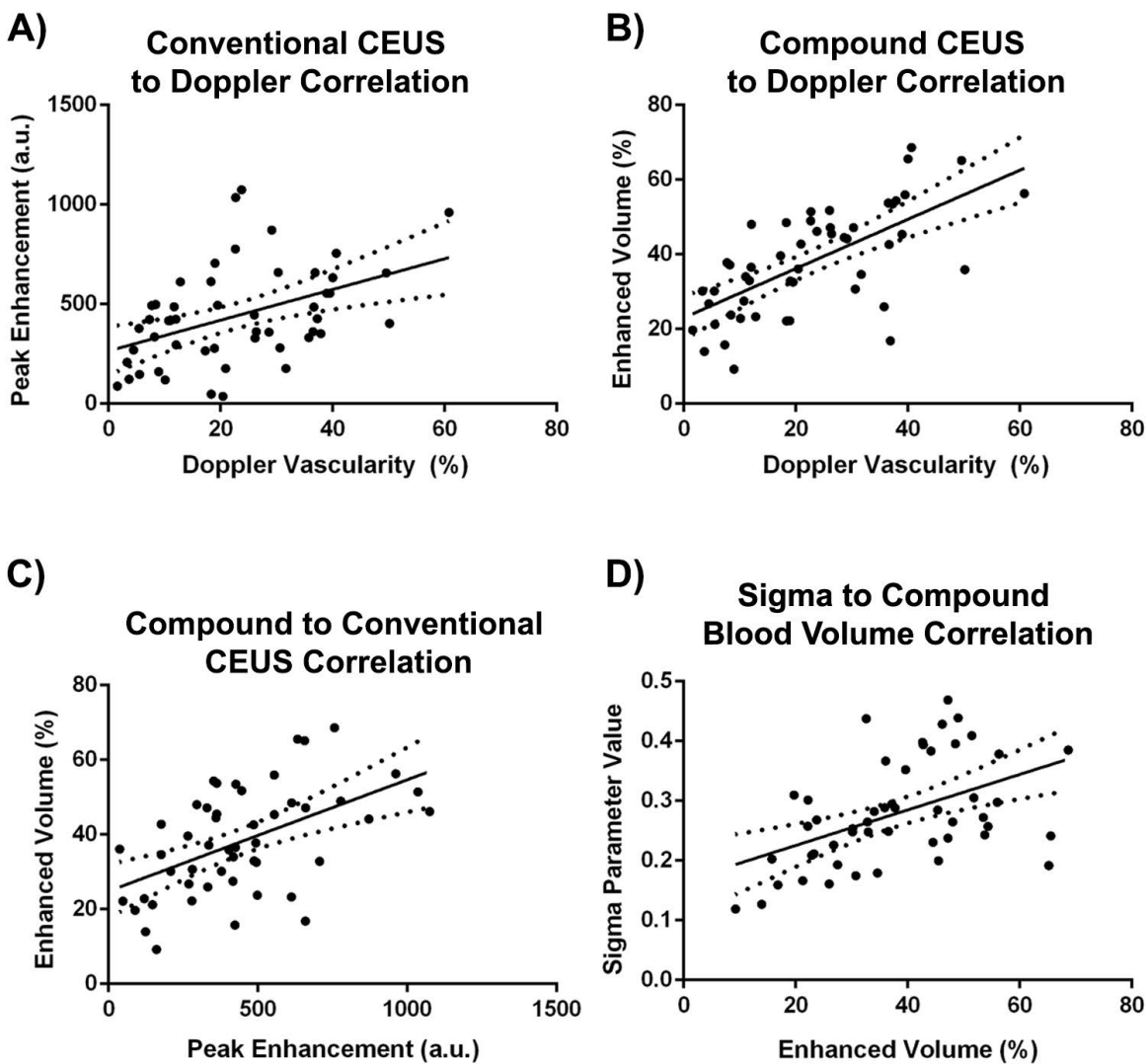


Figure 5.3: Comparisons of perfusion and vascularity parameters produced in this study. A-C) Linear regressions between the three modalities were significant in all cases. A) Conventional CEUS blood volume to Doppler vascularization index correlation ( $R^2 = 0.1955$ ,  $p = 0.0013$ ). B) Compound CEUS enhanced volume fraction to Doppler vascularization index correlation ( $R^2 = 0.4331$ ,  $p < 0.0001$ ). C) Correlation between the two CEUS analysis blood volume estimates ( $R^2 = 0.2707$ ,  $p = 0.0001$ ). D) The correlation between the log-normal  $\sigma_{LN}$  and compound model's blood volume estimate ( $R^2 = 0.2302$ ,  $p = 0.0004$ ).

### 5.3.5 Quantification of Ultrasound Images to Classify Tumor Biopsies

All of the tumor biopsy fragments from every patient in this study were imaged using both power Doppler and CEUS acquisition (Figure 5.2). Every group of sunitinib-treated tumor fragments was compared to the DMSO control group from that same biopsy to detect a significant decrease in vascularization index (as measured by 3-D power Doppler), relative blood volume (conventional CEUS), or enhanced volume fraction (compound model CEUS). Figure 5.4A shows the combined Doppler and CEUS metrics for the primary tumor biopsies of a patient diagnosed with clear cell RCC. This patient demonstrates sunitinib-dependent decreases in VI and blood volume or enhanced volume fraction in the majority of the biopsies, implying that this patient would exhibit sensitivity to sunitinib therapy. In comparison, for the patient represented by the plots in Figure 5.4B, fewer biopsies showed a treatment response to sunitinib. This patient, diagnosed with chromophobe RCC, is not expected to respond well to sunitinib therapy in the clinical setting. Classification matrices for treatment sensitivity were produced for each of the three ultrasound modalities (Figure 5.4C, sensitive biopsies in green and resistant in red). A significant difference (*i.e.*, reduction in an ultrasound vascular metric) between sunitinib and DMSO treated tumor fragments would classify that biopsy as being sensitive to therapy. The clear cell RCC patients are Patients 1, 2, and 3 in Figure 5.4C; the chromophobe RCC patient is Patient 4. There was a high degree of heterogeneity in treatment sensitivity within each patient as well as frequent differences in classification results for individual biopsies using different ultrasound modalities (only 18 out of 28 examined cores had the same classification with all 3 methods).

### 5.3.6 Dual Modality Patient Classification

Evaluating treatment sensitivity by considering both power Doppler and CEUS measurements has the advantage of providing two independently acquired measures of tumor vascularization. Scatter plots of Doppler VI versus either of the CEUS perfusion metrics demonstrate that a linear decision boundary can distinguish treated from control specimens for most of the tumor fragments from a biopsy that is suspected to be sunitinib-sensitive, taken from a patient with clear cell RCC (Figure 5.5A). An equivalent scatter plot from the chromophobe RCC

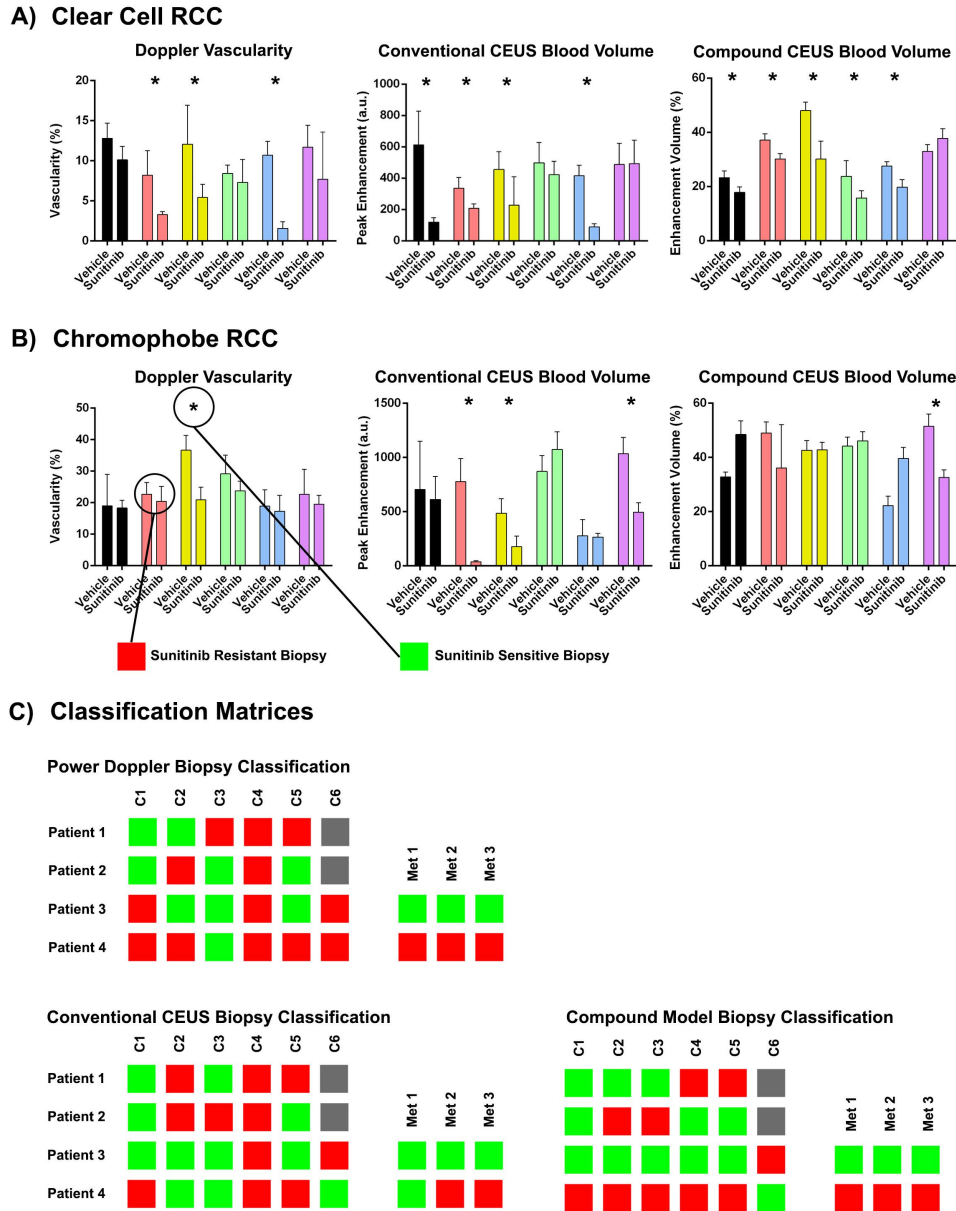


Figure 5.4: Sensitivity or resistance classification of tumor biopsies based on ultrasound image quantification. A) Doppler and CEUS vascular metrics from a representative patient diagnosed with clear cell RCC, taken from Patient 3. Note that most biopsies demonstrate a sunitinib-dependent decrease in vascularization index and/or blood volume or enhanced volume fraction. B) Doppler and CEUS vascular metrics from the patient diagnosed with chromophobe RCC (Patient 4). In each case a statistically significant decrease in a vascular metric would classify that biopsy as sunitinib sensitive (in green); otherwise, the biopsy was considered resistant (in red). C) Matrices demonstrating the sensitive/resistant classification using each ultrasound modality for every biopsy from all patients in this study.

patient, who is expected to be sunitinib resistant, shows substantial overlap in the ultrasound data from the treated and control tumor fragments (Figure 5.5B).

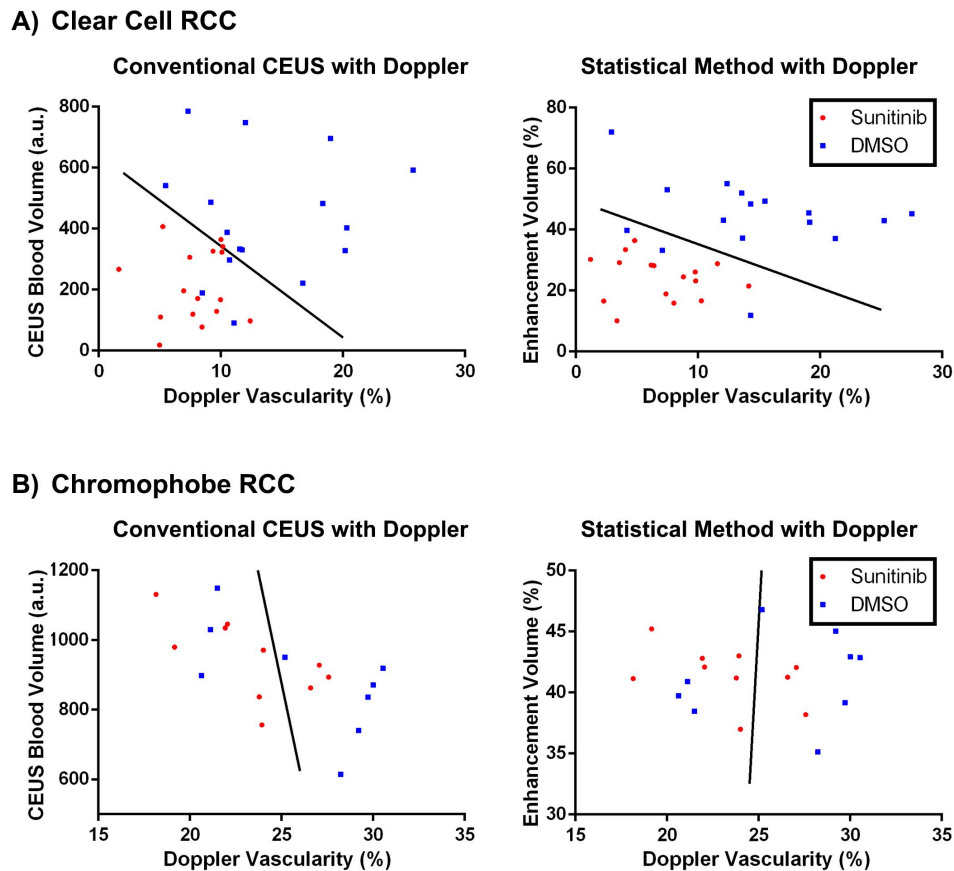
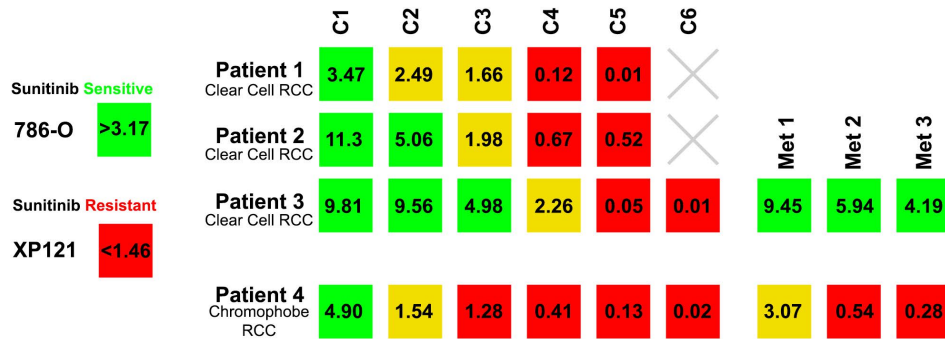


Figure 5.5: A) Scatter plots of Doppler VI and CEUS blood volume or enhanced volume fraction from a suspected sunitinib-sensitive biopsy. A linear discriminant analysis demonstrates that a simple decision boundary is able to correctly classify the majority of treated and untreated tumor fragments in a drug sensitive biopsy. B) An equivalent scatter plot from a sunitinib-resistant biopsy taken from the patient with chromophobe RCC. The choice of decision boundary is less obvious, and does not perform well as a classifier.

Two sets of drug sensitivity matrices were produced using power Doppler along with either CEUS analysis technique for all patients in this study (Figure 5.6). Each biopsy core was classified as sunitinib sensitive (green), partial responder (yellow), or resistant (red) based on the F-statistic calculated to assess the differences in Doppler VI and one of the CEUS parameters between the treated and control fragments for that core (number in each box in Figure 5.6). Clear cell RCC cores were more consistently classified as sunitinib sensitive, and cores from the chromophobe patient as sunitinib resistant, with the compound CEUS model.



**A) Conventional CEUS**



**B) Compound CEUS**

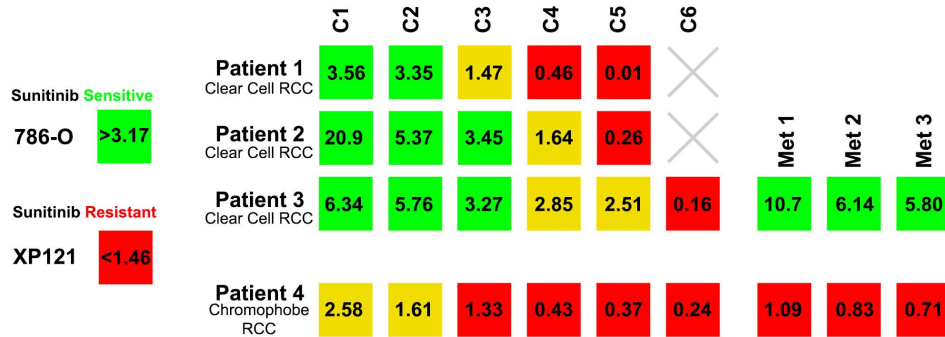


Figure 5.6: Treatment sensitivity of tumor biopsies was classified using a combination of power Doppler VI with one of the CEUS techniques. A) Drug sensitivity matrix constructed using Doppler VI and conventional CEUS blood volume for all patient cores in this study. B) An equivalent sensitivity matrix generated using Doppler VI and the compound statistical CEUS enhanced volume fraction. The number in each box is the F-statistic comparing ultrasound vascular metrics for treated and control fragments from that particular core.

## 5.4 Discussion

This study applied a compound probability density function model to analyze the speckle statistics of CEUS images acquired from a CAM PDX model of RCC that underwent sunitinib therapy. The contrast intensity samples taken from tumor ROIs demonstrated a close agreement to the compound PDF at every frame of each CEUS cine loop. The model produced well behaved wash-in curves with a reduced coefficient of variation in blood volume estimates over conventional CEUS analysis, implying that the compound model provides more reproducible quantification of tumor vasculature. The compound model demonstrated distinct wash-in phases, corresponding to fast-flow and slow-flow, in CEUS cine loops taken from tumor fragments with large in-plane arterioles. The application of the compound technique to this RCC PDX model improved the confidence of patient core biopsy classification as being either sensitive or resistant to sunitinib therapy.

For both CEUS techniques, the CoV of blood volume estimates was consistently higher in the treated tumor fragment group in comparison to the vehicle control group. There are several possible explanations for this observation. First, RCC tumors exhibit a high degree of genetic heterogeneity, which implies that the tumor core biopsies themselves could contain distinct sub-clones that may have varied intrinsic resistance to sunitinib. This could be tested through similar drug dosing studies on expanded clones from patient tumors, under the assumption that the timeline of the study is short enough to avoid acquired resistance from random mutation events. Secondly, this study applied sunitinib dosing topically, a technique that adds experimental variability to the total dose of drug absorbed by the tumor fragment versus spill-over into the surrounding tissues. Intravascular injection of sunitinib would allow for tighter control of sunitinib pharmacodynamics at the expense of study power. An intravascular drug dosing scheme would require scaling back the scope of the project as it is more time consuming, and prone to embryo attrition, compared to topical dosing. Finally, the dose of sunitinib has not yet been optimized for maximum vascular impact at safe-to-embryo doses in the tumor fragment CAM xenograft model.

Many of the CEUS cine loops from this PDX platform demonstrated distinct wash-in phases that correspond to fast-flow and slow-flow (*i.e.*, arteriole and capillary) enhancement,

as in Figure 5.1. Arteriole enhancement can often obscure the perfusion kinematics of the surrounding capillary bed in CEUS acquisition, which necessitates manual segmentation of these features to exclude them from the analysis ROI. This additional segmentation step is cumbersome, time consuming, and operator dependent, but is often required for conventional CEUS analysis of tumors/organs with dominant vascular features [11]. However, indicator-dilution curves generated using the compound model demonstrated these phases of wash-in distinctly, using only a single tumor-encompassing ROI, which could permit the study of slow-flow components of wash-in without the need for re-segmentation. Identification of the most appropriate indicator-dilution model to decompose the two (or more) components of wash-in for this type of analysis requires further investigation.

The motivation for this study is ultimately the diagnosis of *de novo* sunitinib resistance in patients with metastatic RCC. We have opted to attempt this using 3-D power Doppler ultrasound in combination with serial 2-D CEUS acquisitions. Even at high frequencies, power Doppler is relatively insensitive to the capillary level effects of sunitinib therapy, being only able to detect feeding arterioles in tumors (*i.e.* no smaller than the nominal scanner resolution of  $40\ \mu\text{m}$  axial by  $80\ \mu\text{m}$  lateral [32]), but the 3-D acquisition provides a global measure of tumor blood volume. CEUS is sensitive to microvascular flow, but the 2-D time-series acquisition means that tumors will be spatially under-sampled for perfusion, even with multiple imaging planes. Therefore, Doppler VI and the CEUS vascular metrics are not expected to be strongly correlated [33, 34]; this assumption was confirmed for this study in Figure 5.3A and 5.3B. Rather, the expectation is that the strength of one technique will compensate for the limitations of the other, and thus the combination will provide the best classification of biopsies as sunitinib sensitive/resistant. This study demonstrates the merit of applying the compound statistical model to RCC biopsy classification as the technique more consistently classified clear cell RCC biopsies as being sunitinib sensitive, and chromophobe RCC biopsies as being sunitinib resistant, over conventional CEUS.

Our previous research demonstrated the compound speckle model's ability to significantly improve the classification accuracy between control and bevacizumab treated tumors in a mouse xenograft model of breast cancer, over conventional CEUS analysis [12]. This improvement in performance was attributed to an increased sensitivity of CEUS area under the

curve to the changes in micro-vascular density caused by the anti-angiogenic agent. This observation may explain the improved classification performance presented in this study from application of the statistical CEUS method. We also previously reported that the lognormal  $\sigma_{LN}$  value (Eq. 5.2) was modestly correlated with the fractal dimension of tumor vasculature, as verified with contrast-enhanced micro-CT [12]. This drove the hypothesis that the compound model could capture differences in fractal vessel geometry in this CAM PDX model, potentially supplying more information for classifiers to discriminate between sunitinib sensitive/resistant cores. However, the estimated  $\sigma_{LN}$  value was found to exhibit the same trends as estimates of blood volume. Sensitivity matrices could have been produced using Doppler VI and  $\sigma_{LN}$  (or Doppler VI, enhanced volume fraction, and  $\sigma_{LN}$  together), but this was not explored because Figure 5.3D suggests that  $\sigma_{LN}$  does not add enough new information to be useful. Further work is required to determine what physiological features affect the compound model's estimate of  $\sigma_{LN}$ .

The treatment sensitivity matrices produced in this study demonstrated an ability to discriminate clear cell from chromophobe RCC tumor fragments based only on functional imaging of their treatment response to sunitinib therapy. This suggests that the assay can detect treatment sensitivity of individual tumor biopsies and may be suitable for screening of *de novo* drug resistance in patients with metastatic RCC. However, these results have yet to be validated on a per core basis (we expect heterogeneous treatment sensitivity within a single patient) or through patient outcome measures. Given the poor track record of microvascular density in evaluating anti-angiogenic treatment response [35], tumor fragment resistance status should be validated through serial histology to quantify endothelial cell proliferation [36]. Next-generation sequencing provides an alternative means of validation, but total exome and single nucleotide variation analyses provided no stand-out biomarker for sunitinib resistance in the CAM RCC PDX model (Chapter 4). Transcriptome profiling (*e.g.* RNA-Seq) may be more sensitive to changes in angiogenic status.

A major limitation of this study is the low number of patients, and low representation of known sunitinib resistant samples, which restricts the interpretation of the presented results. At the time of writing, the three clear cell patients in this study have undergone systemic targeted therapy, but for TKIs other than sunitinib. Patients 1 and 2 have shown signs of pro-

gression and have discontinued systemic therapy due to intolerable side effects (PFS of 5.3 and 7.5 months, respectively). Patient 3 has not shown evidence of progression after 5 months of pazopanib therapy. Patient 4, diagnosed with chromophobe RCC, has not started systemic therapy. It is not clear how resistance/sensitivity to one drug translates to other TKIs. Future studies should include a wider array of patient populations, including clear cell, papillary, and chromophobe RCC tumors, compared against outcome measures from patients undergoing systemic targeted therapy with the TKI used in the screen. The genetic heterogeneity of RCC tumors, which in turn implies heterogeneous treatment sensitivity within a single patient, further complicates study design as variable intra-patient response needs to be accounted for. To assess whether this protocol can be predictive of patient outcome (including *de novo* resistance, acquired resistance, and progression free-survival) would require adequate representation from these patient populations. The compound statistical model provided a more reproducible quantification of tumor vasculature, and both treatment matrices presented in this study could discriminate presumably sunitinib-resistant (chromophobe) tumor fragments from presumably sunitinib-sensitive ones (clear cell). A larger study appears justified, provided the validation techniques and outcome measures discussed above are taken into consideration.

## 5.5 Conclusion

Implantation of RCC tumor specimens into the CAM resulted in high engraftment efficiencies (take rate of 90%) relative to those typically observed in immunocompromised mice [37]. Intratumoral functional heterogeneity was observed, both within untreated core biopsies and in the response to antiangiogenic therapy, with all three of the vascular quantification techniques presented in this study. First-order speckle analysis reduced the coefficient of variation of CEUS estimates of blood volume compared to conventional CEUS methods (CoV of 0.554 vs. 0.828, Brown-Forsythe test  $p$ -value  $<0.05$ ) and thereby improved patient classification confidence. Indicator-dilution curves generated using the compound model demonstrated distinct slow-flow and fast-flow phases of wash-in for tumor fragments with dominant vascular features (*i.e.* in-plane arterioles), permitting the study of slow-flow components of wash-in without the need for manual vessel segmentation. Treatment sensitivity matrices, which classified individ-

ual tumor biopsies as being sunitinib resistant or sensitive, could discriminate clear cell from chromophobe RCC samples, suggesting that the assay may be suitable for screening of *de novo* drug resistance. Further studies, with a larger and more representative patient population, are required to assess whether this protocol can be predictive of patient outcome.

# References

- [1] T. Albrecht, M. J. K. Blomley *et al.*, “Improved Detection of Hepatic Metastases with Pulse-Inversion US during the Liver-specific Phase of SHU 508a: Multicenter Study,” *Radiology*, vol. 227, no. 2, pp. 361–370, May 2003.
- [2] M. J. Blomley, P. S. Sidhu *et al.*, “Do different types of liver lesions differ in their uptake of the microbubble contrast agent SH U 508a in the late liver phase? Early experience,” *Radiology*, vol. 220, no. 3, pp. 661–667, Sep. 2001.
- [3] T. K. Kim, B. I. Choi *et al.*, “Hepatic Tumors: Contrast Agent-Enhancement Patterns with Pulse-Inversion Harmonic US,” *Radiology*, vol. 216, no. 2, pp. 411–417, Aug. 2000.
- [4] R. Williams, J. M. Hudson *et al.*, “Dynamic microbubble contrast-enhanced US to measure tumor response to targeted therapy: a proposed clinical protocol with results from renal cell carcinoma patients receiving antiangiogenic therapy,” *Radiology*, vol. 260, no. 2, pp. 581–590, Aug. 2011.
- [5] H.-P. Zhang, Q.-S. Shi *et al.*, “Regions of interest and parameters for the quantitative analysis of contrast-enhanced ultrasound to evaluate the anti-angiogenic effects of bevacizumab,” *Mol. Med. Rep.*, vol. 8, no. 1, pp. 154–160, Jul. 2013.
- [6] M. Merz, D. Komljenovic *et al.*, “Quantitative contrast-enhanced ultrasound for imaging antiangiogenic treatment response in experimental osteolytic breast cancer bone metastases,” *Invest. Radiol.*, vol. 47, no. 7, pp. 422–429, Jul. 2012.
- [7] K. Yoshida, T. Hirokawa *et al.*, “Arterial-phase contrast-enhanced ultrasonography for evaluating anti-angiogenesis treatment: A pilot study,” *World J. Gastroenterol.*, vol. 17, no. 8, pp. 1045–1050, Feb. 2011.
- [8] C. Strouthos, M. Lampaskis *et al.*, “Indicator dilution models for the quantification of microvascular blood flow with bolus administration of ultrasound contrast agents,” *IEEE Trans. Ultrason. Ferroelectr. Freq. Contr.*, vol. 57, no. 6, pp. 1296–1310, 2010.
- [9] A. R. Broumas, R. E. Pollard *et al.*, “Contrast-enhanced computed tomography and ultrasound for the evaluation of tumor blood flow,” *Invest. Radiol.*, vol. 40, no. 3, pp. 134–147, Mar. 2005.
- [10] J. M. Correias, L. Bridal *et al.*, “Ultrasound contrast agents: properties, principles of action, tolerance, and artifacts,” *Eur. Radiol.*, vol. 11, no. 8, pp. 1316–1328, 2001.

- [11] M.-X. Tang, H. Mulvana *et al.*, “Quantitative contrast-enhanced ultrasound imaging: a review of sources of variability,” *Interface Focus*, vol. 1, no. 4, pp. 520–539, 2011.
- [12] M. R. Lowerison, J. J. Tse *et al.*, “Compound speckle model detects anti-angiogenic tumor response in preclinical nonlinear contrast-enhanced ultrasonography,” *Med. Phys.*, vol. 44, no. 1, pp. 99–111, Jan. 2017.
- [13] S. D. Dubey, “Compound gamma, beta and f distributions,” *Metrika*, vol. 16, no. 1, pp. 27–31, 1970.
- [14] P. McCullagh and J. A. Nelder, *Generalized Linear Models, Second Edition*. CRC Press, Aug. 1989.
- [15] J. P. Crown, V. Diras *et al.*, “Phase III trial of sunitinib in combination with capecitabine versus capecitabine monotherapy for the treatment of patients with pretreated metastatic breast cancer,” *J. Clin. Oncol.*, vol. 31, no. 23, pp. 2870–2878, Aug. 2013.
- [16] J. Lenzer, “FDA committee votes to withdraw bevacizumab for breast cancer,” *BMJ (Clinical research ed.)*, vol. 343, p. d4244, 2011.
- [17] N. S. Vasudev and A. R. Reynolds, “Anti-angiogenic therapy for cancer: current progress, unresolved questions and future directions,” *Angiogenesis*, vol. 17, no. 3, pp. 471–494, 2014.
- [18] P. Cairns, “Renal Cell Carcinoma,” *Cancer Biomarkers*, vol. 9, no. 1-6, pp. 461–473, 2011.
- [19] R. J. Motzer, T. E. Hutson *et al.*, “Sunitinib versus interferon alfa in metastatic renal-cell carcinoma,” *N. Engl. J. Med.*, vol. 356, no. 2, pp. 115–124, Jan. 2007.
- [20] C. N. Sternberg, I. D. Davis *et al.*, “Pazopanib in locally advanced or metastatic renal cell carcinoma: results of a randomized phase III trial,” *J. Clin. Oncol.*, vol. 28, no. 6, pp. 1061–1068, Feb. 2010.
- [21] B. Escudier, T. Eisen *et al.*, “Sorafenib in advanced clear-cell renal-cell carcinoma,” *N. Engl. J. Med.*, vol. 356, no. 2, pp. 125–134, Jan. 2007.
- [22] B. I. Rini, B. Escudier *et al.*, “Comparative effectiveness of axitinib versus sorafenib in advanced renal cell carcinoma (AXIS): a randomised phase 3 trial,” *Lancet*, vol. 378, no. 9807, pp. 1931–1939, Dec. 2011.
- [23] C. Porta, R. Sabbatini *et al.*, “Primary resistance to tyrosine kinase inhibitors in patients with advanced renal cell carcinoma: state-of-the-science,” *Expert Rev. Anticancer Ther.*, vol. 12, no. 12, pp. 1571–1577, Dec. 2012.
- [24] D. Y. Heng, M. J. Mackenzie *et al.*, “Primary anti-vascular endothelial growth factor (VEGF)-refractory metastatic renal cell carcinoma: clinical characteristics, risk factors, and subsequent therapy,” *Ann. Oncol.*, vol. 23, no. 6, pp. 1549–1555, Jun. 2012.



- [25] J. Busch, C. Seidel *et al.*, “Intrinsic resistance to tyrosine kinase inhibitors is associated with poor clinical outcome in metastatic renal cell carcinoma,” *BMC cancer*, vol. 11, p. 295, 2011.
- [26] J. M. Clarke and H. I. Hurwitz, “Understanding and targeting resistance to anti-angiogenic therapies,” *J. Gastrointest. Oncol.*, vol. 4, no. 3, pp. 253–263, Sep. 2013.
- [27] M. Gerlinger, A. J. Rowan *et al.*, “Intratumor Heterogeneity and Branched Evolution Revealed by Multiregion Sequencing,” *N. Engl. J. Med.*, vol. 366, no. 10, pp. 883–892, Mar. 2012.
- [28] C.-F. Cho, A. Ablack *et al.*, “Evaluation of nanoparticle uptake in tumors in real time using intravital imaging,” *J. Vis. Exp: JoVE*, no. 52, Jun. 2011.
- [29] H. S. Leong, N. F. Steinmetz *et al.*, “Intravital imaging of embryonic and tumor neo-vasculature using viral nanoparticles,” *Nat. Protoc.*, vol. 5, no. 8, pp. 1406–1417, Aug. 2010.
- [30] A. Needles, M. Arditi *et al.*, “Nonlinear contrast imaging with an array-based micro-ultrasound system,” *Ultrasound Med. Biol.*, vol. 36, no. 12, pp. 2097–2106, 2010.
- [31] K. Wei, A. R. Jayaweera *et al.*, “Quantification of Myocardial Blood Flow With Ultrasound-Induced Destruction of Microbubbles Administered as a Constant Venous Infusion,” *Circulation*, vol. 97, no. 5, pp. 473–483, Feb. 1998.
- [32] F. S. Foster, J. Mehi *et al.*, “A new 15-50 MHz array-based micro-ultrasound scanner for preclinical imaging,” *Ultrasound Med. Biol.*, vol. 35, no. 10, pp. 1700–1708, 2009.
- [33] M. Palmowski, J. Huppert *et al.*, “Vessel fractions in tumor xenografts depicted by flow- or contrast-sensitive three-dimensional high-frequency Doppler ultrasound respond differently to antiangiogenic treatment,” *Cancer Res.*, vol. 68, no. 17, pp. 7042–7049, Sep. 2008.
- [34] A. Rix, W. Lederle *et al.*, “Evaluation of high frequency ultrasound methods and contrast agents for characterising tumor response to anti-angiogenic treatment,” *Eur. J. Radiol.*, vol. 81, no. 10, pp. 2710–2716, Oct. 2012.
- [35] L. Hlatky, P. Hahnfeldt, and J. Folkman, “Clinical application of antiangiogenic therapy: microvessel density, what it does and doesn’t tell us,” *J. Natl. Cancer Inst.*, vol. 94, no. 12, pp. 883–893, Jun. 2002.
- [36] A. Eberhard, S. Kahlert *et al.*, “Heterogeneity of angiogenesis and blood vessel maturation in human tumors: implications for antiangiogenic tumor therapies,” *Cancer Res.*, vol. 60, no. 5, pp. 1388–1393, Mar. 2000.
- [37] S. Sivanand, S. Pea-Llopis *et al.*, “A validated tumorgraft model reveals activity of dovitinib against renal cell carcinoma,” *Sci. Transl. Med.*, vol. 4, no. 137, p. 137ra75, Jun. 2012.

# Chapter 6

## Summary and Future Work

### 6.1 Summary

#### 6.1.1 Chapter 2: Improved Linear Contrast-Enhanced Ultrasound Imaging via Analysis of First-Order Speckle Statistics

Chapter 2 demonstrated a linear (B-mode) processing approach to quantify the change in the first-order speckle statistics of B-mode cine loops from the incursion of microbubbles. The technique, named the EDoF (effective degrees of freedom) method, showed promise for improving the robustness of linear CEUS based on a reduced frame-to-frame variability compared with conventional linear subtraction time-intensity curves. The reduced frame-to-frame variability manifested as a statistically significantly higher SNR ( $p < 0.0001$ ) of the EDoF method's wash-in curves ( $33.1 \pm 6.2$  dB) compared with the conventional linear technique ( $18.3 \pm 3.2$  dB). Wash-in curve parameters estimated using the EDoF method also demonstrated a higher correlation to nonlinear CEUS than the conventional linear method. In particular, the AUC of the EDoF method exhibited a higher Pearson correlation to the nonlinear CEUS AUC ( $r = 0.6776$ ) than did conventional linear processing ( $r = 0.4919$ ).

### **6.1.2 Chapter 3: Compound Speckle Model Detects Anti-Angiogenic Tumor Response in Preclinical Nonlinear Contrast-Enhanced Ultrasonography**

Chapter 3 expanded the potential clinical applicability of the technique presented in Chapter 2 by presenting a second-generation model for the analysis of the first-order speckle statistics of two-pulse amplitude modulated contrast-enhanced ultrasound images. The area under curve produced using the compound statistical model could more accurately discriminate anti-VEGF treated tumors from untreated tumors than conventional contrast-enhanced ultrasound image processing. A linear discriminant analysis accurately classified  $59.7\% \pm 3.7\%$  of tumors using conventional CEUS processing and  $77.5\% \pm 1.7\%$  of tumors with the compound method. Both the compound CEUS model and micro-CT analysis detected a significant treatment effect for their respective measure of vascular complexity ( $p = 0.0416$  for CEUS  $\sigma_{LN}$  parameter,  $p = 0.0275$  for CT  $F_D$ ), but the measures themselves had a weak correlation ( $r = 0.322$ ,  $p = 0.06$ ), and neither performed particularly well as a classifier (accuracy of  $56.8\% \pm 1.2\%$  and  $61.7\% \pm 1.9\%$ , respectively). An important consideration for these results is that the degree of vascular normalization caused by bevacizumab therapy was not known in advance for this study.

### **6.1.3 Chapter 4: PDX<sub>ovo</sub>: Ultrafast Prediction of Drug Sensitivities via Intratumoral Multiregional Analysis**

Chapter 4 demonstrated an ultrafast PDX model of RCC in *ex ovo* chicken embryos (PDX<sub>ovo</sub>) that permitted quantification of tumor volume, tumor vascularity, and tumor perfusion via ultrasound in a high-throughput manner. This proof of concept study relied on conventional ultrasound indices of vascularity (power Doppler VI) and perfusion (CEUS). The PDX<sub>ovo</sub> model exhibited a high engraftment efficiency ( $\sim 90\%$  tumor take rate), regardless of RCC subtype or biopsy site. We were able to prepare  $>300$  PDX models for each tumor, permitting multi-regional analysis of both the primary tumor (6 sites) and any nearby metastases (3 metastases) in a well-powered manner ( $n > 36$  per tumor core). These large scale “tumor avatar” studies demonstrated intratumoral functional heterogeneity in the context of sunitinib treatment, and

suggest that genetic tumor heterogeneity exists, but evidence for a direct relationship to the drug resistant phenotype did not manifest in DNA mutations. These results support a phenotype based readout to predict drug resistance as opposed to a genotype signature, and provide evidence that drug resistance to targeted therapy is heterogeneous across the patient's tumor.

### **6.1.4 Chapter 5: Compound Speckle Model Reduces Contrast Ultrasound Variability in a Patient-Derived Xenograft Model of Renal Cell Carcinoma**

Chapter 5 applied the compound speckle model presented in Chapter 3 to the CEUS cine loops acquired in Chapter 4. Intratumoral functional heterogeneity was observed, both within untreated core biopsies and in the response to antiangiogenic therapy, with all three of the vascular quantification techniques presented in this study. First-order speckle analysis reduced the coefficient of variation of CEUS estimates of blood volume compared to conventional CEUS methods (CoV of 0.554 vs. 0.828, Brown-Forsythe test  $p$ -value  $<0.05$ ) and thereby improved patient classification confidence. The compound model was hypothesized to capture fractal vessel geometry in this CAM PDX model, but the estimated lognormal sigma value was found to exhibit the same trends as estimates of blood volume. Treatment sensitivity matrices, which classified individual tumor biopsies as being sunitinib resistant or sensitive, could discriminate clear cell from chromophobe RCC samples, suggesting that the assay may be suitable for screening of *de novo* drug resistance. Further studies, with a larger and more representative patient population, are required to assess whether this protocol can be predictive of patient outcome.

## **6.2 Future Work**

### **6.2.1 Technical improvements**

There are a number of potential technical improvements that should be addressed to further develop this model. During this thesis we only considered the statistics of uncompressed,

intensity signal data (*i.e.*, the squared magnitude of the echo envelope measured prior to logarithmic compression). This limits the applicability of the model, particularly for retrospective studies, as CEUS datasets will more typically be acquired as video data rather than raw data. Future work should include a derivation of this model (or similar) for log-compressed CEUS images.

A further limitation concerns the assumptions of the distributions of scatterers (*i.e.* microbubbles). We assumed that the weighting function will be a gamma probability distribution. If an arbitrary vascular network can be approximated by a fractal branching tree, then the weighting function should be log-normal to be consistent with the results of Qian *et al.* [1]. This was justified in this thesis as these two distributions are often interchangeable [2], but this may not hold for strongly enhanced vascular beds that would be more accurately described with the heavier tailed log-normal distribution. Furthermore, we are only considering the case where every microbubble subpopulation was modeled as randomly distributed scatterers at relatively high concentrations. We justified this choice in the model by assuming that the average mouse weighs approximately 20 grams with a density that is close to water ( $1 \text{ g/cm}^3$ ). At a nominal scanner resolution of  $75 \mu\text{m}$  axial by  $165 \mu\text{m}$  lateral by  $165 \mu\text{m}$  elevational, with an injection volume of  $50 \mu\text{L}$  at  $2 \times 10^9$  microbubbles/mL, this yields an average of 10.25 microbubbles per mouse voxel - just over the line for Rayleigh speckle statistics to hold. However, the inherent heterogeneity of tissue vasculature implies that some regions will not have fully developed speckle even when fully perfused with microbubbles. This especially does not hold for the early phases of wash-in where there is necessarily a low concentration of microbubbles. To address this, the parameterized distribution should be changed from an exponential to a K distribution [3].

The optimal choice of wash-in function is unknown for the time-dependent statistical parameters presented in this thesis. We opted to use the same indicator-dilution models for both the conventional CEUS analysis as well as the statistical analysis to provide a direct comparison of the quantified perfusion parameters. This is particularly important for Chapters 4 and 5, which employed a mono-exponential fit to their destruction-reperfusion curves. The mono-exponential model has received a fair amount of criticism as it is not a realistic model of tissue perfusion and the reproducibility of the parameters is low. More sophisticated kinematic mod-

els, such as the Hudson lognormal perfusion model [4], which use physiologically plausible blood perfusion and take into account the ultrasound beam geometry should be used for all future studies of tumor heterogeneity. Additional work should be done to characterize and model the time-dependency of the extracted statistical parameters and more rigorously determine the best curve to fit. Furthermore, it was noted in Chapter 5 that several of CEUS cine loops acquired from the CAM PDX model had distinct ‘slow-flow’ and ‘fast-flow’ components in their wash-in curves when analyzed with the compound statistical model. A preliminary result, shown in Figure 6.1, demonstrates that a superposition of two monoexponential curve fits can extract these components for independent analysis. It is currently unknown what impact this could have on the technique’s ability to discriminate responding from non-responding tumor fragments.

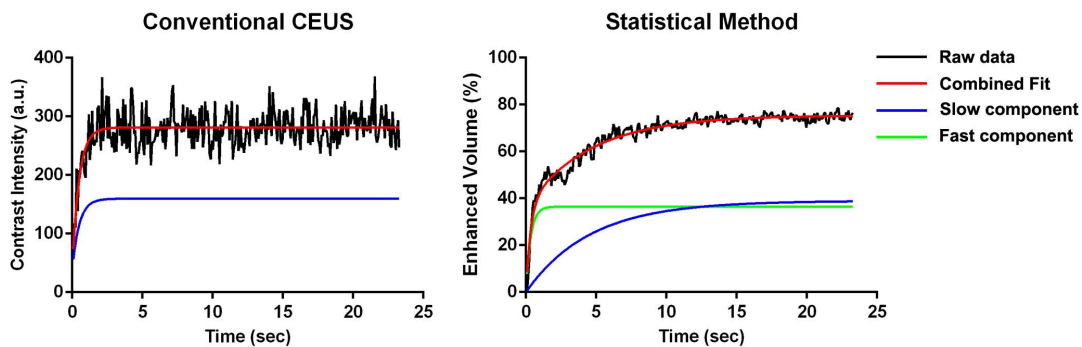


Figure 6.1: Example superposition of two monoexponential curve fits to the wash-in curves from Figure 5.1. This relatively simple analysis could extract the fast and slow-flow components of the compound model’s wash-in curve. On the conventional CEUS data, both of the components are overlapping.

Finally, all of the work presented in this thesis focused on first-order statistical modeling. Heterogeneity in CEUS cine loops may be captured more finely through second-order speckle analysis. For example, there is a large amount of established literature on the utility of gray level co-occurrence matrices for the characterization of medical images [5]. Applying similar analyses to CEUS data may yield fruitful indices of vascular perfusion, provided such methods are properly tuned to the task at hand.

### 6.2.2 Next steps for preclinical validation

The statistical speckle models presented in this thesis produce estimates of heterogeneity that are hypothesized to correspond with vascular tortuosity. In Chapter 3, the compound model's estimated  $\sigma_{LN}$  value was modestly correlated with the fractal dimension of tumor vasculature from a mouse xenograft model of breast cancer, as verified with contrast-enhanced micro-CT. However, in Chapter 5, the estimated  $\sigma_{LN}$  value was found to exhibit the same trends as estimates of blood volume in a CAM PDX model of RCC. Further work is required to determine what physiological features affect the compound model's estimate of  $\sigma_{LN}$  and how this value can be used for therapy monitoring. Ideally, these studies would include several vascular environments (including normal and pathological tissues) and be validated with gold-standard measures of vascular structure (very high-resolution contrast-enhanced micro-CT and/or corrosion casting). Vascular tortuosity is characteristic of malignant cancers [6], and may be indicative of the vascular normalization effects encountered in successful anti-angiogenic therapy.

The studies presented in Chapters 4 and 5 analyzed CEUS cine loops acquired from RCC tumor fragments that underwent sunitinib therapy at a fixed drug dose. Future studies should include all four FDA approved tyrosine kinase inhibitors (TKIs) that target VEGF-A (sunitinib, pazopanib, sorafenib, and axitinib), as these all have improved progression free and overall survival for patients with mRCC [7–10]. The optimal dose of each TKI for maximum tumor vascular impact, that is still safe for the embryo, needs to be determined via dose-response analysis (for example, see Figure 6.2 which shows preliminary results of an RCC CAM model study we have initiated in collaboration with Drs. Leong and Power). The relationship between topical sunitinib dosing on the CAM xenograft model and clinical dosages remains unclear, so further work must be done to determine the clinical dose equivalence. Additionally, an alternative to straight topical dosing for these TKIs should be explored, such as mixing the drug with a gelling agent to maintain consistent dosing. These alterations could increase the magnitude of treatment response in sensitive cores, and reduce the experimental variability with CEUS datasets, and thereby improve confidence of classification accuracy.

The treatment sensitivity matrices produced in Chapters 4 and 5 demonstrated an ability to discriminate clear cell from chromophobe RCC tumor fragments based only on functional

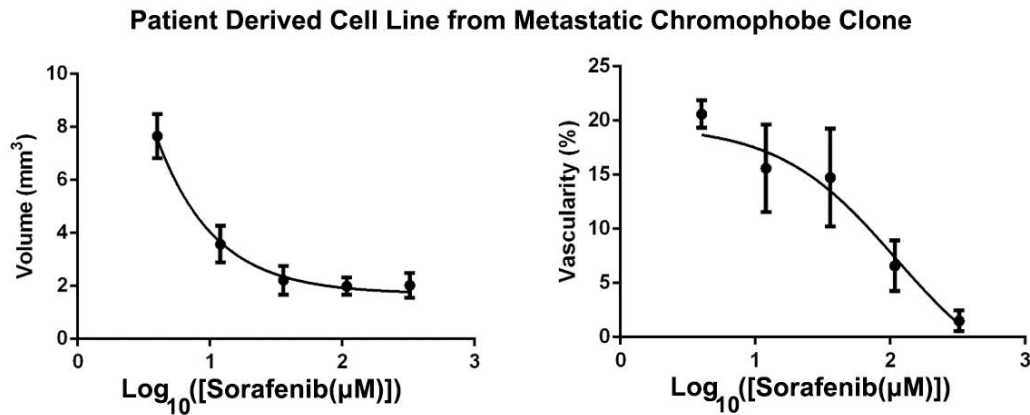


Figure 6.2: Sorafenib dose response curves of tumor volume and power Doppler VI, taken from a patient derived cell line engrafted into the CAM. The cell line originated from one of the metastatic biopsies taken from the patient diagnosed with chromophobe RCC.

imaging of their treatment response to sunitinib therapy. However, given that we expect heterogeneous treatment sensitivity within a single patient, tumor fragment resistance status should be validated through serial histology to quantify endothelial cell proliferation [11]. This would give a gold-standard measure of the impact that the anti-angiogenic therapy has on tumor fragment vasculature.

### 6.2.3 Plans for clinical translation

The above section discussed the need to validate patient treatment sensitivity matrices on a per core basis to confirm anti-angiogenic therapy effect. However, the most important gold-standard for this technique is patient overall, or progression-free, survival. A prospective study, where patients are assigned to a TKI based on the output of the treatment sensitivity matrices, would be ideal from a project design standpoint but is unethical. Instead, the plan for clinical translation is through a retrospective study, where patients are assigned to systemic TKI therapy by their physician, and their outcome measures are compared against the predictions of the treatment sensitivity matrices presented in Chapters 4 and 5.

This study design would also benefit from the additional acquisition and analysis of genetic information from patient samples. The data in Chapters 4 and 5 presented the consequences of tumor heterogeneity through a phenotype-based analysis, highlighting the need for multi-



regional analysis of patient tumors. Genomics-based approaches are more scalable than the CAM PDX, but the genetic “blueprint” responsible for drug resistance is currently unknown. The PDXovo model can potentially confirm the results of a genetic signature for drug resistance in a prospective fashion, as opposed to case-control genomics studies.

A growing area of research for the treatment of RCC is PD1 based immunotherapy regimens (*e.g.* Nivolumab), either as a mono-therapy or in combination with target therapies, where it has been suggested that functional tumor heterogeneity can influence clinical outcomes. This may also explain, to an extent, why some patients exhibit partial response to PD1 based immunotherapies [12]. The PDXovo platform may be able to predict immunotherapy drug responses for patients with metastatic renal cell carcinoma due to its high engraftment efficiency and lack of host immune cell function. The treatment response seen in CAM PDXs following immunotherapy would be due to the activation of human leukocytes and macrophages present in the tumor fragment when biopsied. PDXs would be submitted to high frequency ultrasound to determine if there is a treatment effect in terms of tumor vascularity and blood perfusion, and to estimate the degree of necrosis. After imaging, each PDX could be submitted to cell dissolution and stained with leukocyte markers and activation markers for flow cytometric enumeration of all immune cells and the proportion of activated immune cells within the PDX. Since the tumor volume is quantified by high-frequency ultrasound imaging, calculations can be made based on the percentage and abundance of non-activated and activated immune cells within each PDX.

One of the main motivations for the development of the compound speckle model for non-linear CEUS imaging was the potential for clinical translation of the analysis technique. Although this has not been explicitly tested, there is no reason to believe that the basic principles of the model would not apply to clinical frequencies. However, there is a concern that the dosages of microbubbles used in clinical CEUS scanning would be insufficient to permit the assumption of fully developed speckle in nonlinear images to hold. The parameterized distribution should be changed from an exponential to a K distribution [3] to account for pre-Rayleigh speckle statistics. The proposed technique quantified the perfusion within a tumor and simultaneously provided an index of vascular complexity, making it a potentially useful addition to the clinical detection of vascular normalization in anti-angiogenic combination therapies.

## 6.3 Final Remarks

The analysis of the first-order speckle statistics of contrast-enhanced ultrasound cine loops provides more robust and reproducible estimates of tumor blood perfusion than conventional image analysis. Theoretically this form of analysis could quantify perfusion heterogeneity and provide estimates of vascular fractal dimension, but further work is required to determine what physiological features influence these measures. Treatment sensitivity matrices, which combine vascular measures from CEUS and power Doppler, may be suitable for screening of *de novo* sunitinib resistance in patients diagnosed with renal cell carcinoma. Further studies are required to assess whether this protocol can be predictive of patient outcome.

# References

- [1] H. Qian and J. B. Bassingthwaite, “A class of flow bifurcation models with lognormal distribution and fractal dispersion,” *J. Theor. Biol.*, vol. 205, no. 2, pp. 261–268, 2000.
- [2] B. L. Wiens, “When log-normal and gamma models give different results: A case study,” *Am. Stat.*, vol. 53, no. 2, pp. 89–93, 1999.
- [3] A. D. Bar-Zion, C. Tremblay-Darveau *et al.*, “Denoising of Contrast-Enhanced Ultrasound Cine Sequences Based on a Multiplicative Model,” *IEEE Trans. Biomed. Eng.*, vol. 62, no. 8, pp. 1969–1980, 2015.
- [4] J. M. Hudson, R. Karshafian, and P. N. Burns, “Quantification of flow using ultrasound and microbubbles: a disruption replenishment model based on physical principles,” *Ultrasound Med. Biol.*, vol. 35, no. 12, pp. 2007–2020, Dec. 2009.
- [5] R. M. Haralick, K. Shanmugam, and I. Dinstein, “Textural Features for Image Classification,” *IEEE Trans. Syst. Man Cybern.*, vol. SMC-3, no. 6, pp. 610–621, Nov. 1973.
- [6] J. W. Baish and R. K. Jain, “Fractals and cancer,” *Cancer Res.*, vol. 60, no. 14, pp. 3683–3688, 2000.
- [7] R. J. Motzer, T. E. Hutson *et al.*, “Sunitinib versus interferon alfa in metastatic renal-cell carcinoma,” *N. Engl. J. Med.*, vol. 356, no. 2, pp. 115–124, Jan. 2007.
- [8] C. N. Sternberg, I. D. Davis *et al.*, “Pazopanib in locally advanced or metastatic renal cell carcinoma: results of a randomized phase III trial,” *J. Clin. Oncol.*, vol. 28, no. 6, pp. 1061–1068, Feb. 2010.
- [9] B. Escudier, T. Eisen *et al.*, “Sorafenib in advanced clear-cell renal-cell carcinoma,” *N. Engl. J. Med.*, vol. 356, no. 2, pp. 125–134, Jan. 2007.
- [10] B. I. Rini, B. Escudier *et al.*, “Comparative effectiveness of axitinib versus sorafenib in advanced renal cell carcinoma (AXIS): a randomised phase 3 trial,” *Lancet*, vol. 378, no. 9807, pp. 1931–1939, Dec. 2011.
- [11] A. Eberhard, S. Kahlert *et al.*, “Heterogeneity of angiogenesis and blood vessel maturation in human tumors: implications for antiangiogenic tumor therapies,” *Cancer Res.*, vol. 60, no. 5, pp. 1388–1393, Mar. 2000.

- [12] M. Sznol and L. Chen, "Antagonist Antibodies to PD-1 and B7-H1 (PD-L1) in the Treatment of Advanced Human Cancer," *Clin. Cancer Res.*, vol. 19, no. 5, pp. 1021–1034, Mar. 2013.

## Appendix A: Copyright Agreements

The IEEE does not require individuals working on a thesis to obtain a formal reuse license however, you must follow the requirements listed below:

### Textual Material

Using short quotes or referring to the work within these papers) users must give full credit to the original source (author, paper, publication) followed by the IEEE copyright line © [Year of publication] IEEE.

In the case of illustrations or tabular material, we require that the copyright line © [Year of original publication] IEEE appear prominently with each reprinted figure and/or table. If a substantial portion of the original paper is to be used, and if you are not the senior author, also obtain the senior author's approval.

### Full-Text Article

If you are using the entire IEEE copyright owned article, the following IEEE copyright/ credit notice should be placed prominently in the references: © [year of original publication] IEEE. Reprinted, with permission, from [author names, paper title, IEEE publication title, and month/year of publication]

Only the accepted version of an IEEE copyrighted paper can be used when posting the paper or your thesis on-line. You may not use the final published version

In placing the thesis on the author's university website, please display the following message in a prominent place on the website: In reference to IEEE copyrighted material which is used with permission in this thesis, the IEEE does not endorse any of [university/educational entity's name goes here]'s products or services. Internal or personal use of this material is permitted. If interested in reprinting/republishing IEEE copyrighted material for advertising or promotional purposes or for creating new collective works for resale or redistribution, please go to [http://www.ieee.org/publications\\_standards/publications/rights/rights\\_link.html](http://www.ieee.org/publications_standards/publications/rights/rights_link.html) to learn how to obtain a License from RightsLink.

If applicable, University Microfilms and/or ProQuest Library, or the Archives of Canada may supply single copies of the dissertation.

## Medical Physics

### Wiley's Self-Archiving Policy

Authors of articles published in Wiley journals are permitted to self-archive the submitted (preprint) version of the article at any time, and may self-archive the accepted (peer-reviewed) version after an embargo period.

#### Accepted (peer-reviewed) Version -

The accepted version of an article is the version that incorporates all amendments made during the peer review process, but prior to the final published version (the Version of Record, which includes; copy and stylistic edits, online and print formatting, citation and other linking, deposit in abstracting and indexing services, and the addition of bibliographic and other material).

Self-archiving of the accepted version is subject to an embargo period of 12-24 months. The embargo period is 12 months for scientific, technical, and medical (STM) journals and 24 months for social science and humanities (SSH) journals following publication of the final article.

The accepted version may be placed on:

- the author's personal website
- the author's company/institutional repository or archive
- not for profit subject-based repositories such as PubMed Central

Articles may be deposited into repositories on acceptance, but access to the article is subject to the embargo period.

The version posted must include the following notice on the first page:

“This is the peer reviewed version of the following article: [FULL CITE], which has been published in final form at [Link to final article using the DOI]. This article may be used for non-commercial purposes in accordance with Wiley Terms and Conditions for Self-Archiving.”

The version posted may not be updated or replaced with the final published version (the Version of Record). Authors may transmit, print and share copies of the accepted version with colleagues, provided that there is no systematic distribution, e.g. a posting on a listserv, network or automated delivery.

There is no obligation upon authors to remove preprints posted to not for profit preprint servers prior to submission.

## Appendix B: Ethics Approval for Animal Subjects



**AUP Number:** 2009-072

**AUP Title:** Steps of Breast Cancer Metastasis: Experimental Models and Identification of Targets for Intervention

**Yearly Renewal Date:** 01/01/2016

**The YEARLY RENEWAL to Animal Use Protocol (AUP) 2009-072 has been approved, and will be approved for one year following the above review date.**

1. This AUP number must be indicated when ordering animals for this project.
2. Animals for other projects may not be ordered under this AUP number.
3. Purchases of animals other than through this system must be cleared through the ACVS office. Health certificates will be required.

### **REQUIREMENTS/COMMENTS**

Please ensure that individual(s) performing procedures on live animals, as described in this protocol, are familiar with the contents of this document.

The holder of this Animal Use Protocol is responsible to ensure that all associated safety components (biosafety, radiation safety, general laboratory safety) comply with institutional safety standards and have received all necessary approvals. Please consult directly with your institutional safety officers.

Submitted by: Kinchlea, Will D  
on behalf of the Animal Use Subcommittee

*The University of Western Ontario*  
Animal Use Subcommittee / University Council on Animal Care  
Health Sciences Centre, • London, Ontario • CANADA – N6A 5C1  
PH: 519-661-2111 ext. 86768 • FL 519-661-2028  
Email: [auspc@uwo.ca](mailto:auspc@uwo.ca) • <http://www.uwo.ca/animal/website/>

## Appendix C: Ethics Approval for Surgical Specimens from Human Patients



**Western  
Research**

Research Ethics

### Western University Health Science Research Ethics Board HSREB Annual Continuing Ethics Approval Notice

**Date:** October 07, 2016

**Principal Investigator:** Dr. Nicholas Power

**Department & Institution:** Schulich School of Medicine and Dentistry\Surgery,London Health Sciences Centre

**Review Type:** Expedited

**HSREB File Number:** 104278

**Study Title:** Predicting drug resistance in metastatic renal cell carcinoma: Individualizing targeted therapy for xenografting patient tumors into chick embryos

**HSREB Renewal Due Date & HSREB Expiry Date:**

Renewal Due -2017/10/31

Expiry Date -2017/11/05

The Western University Health Science Research Ethics Board (HSREB) has reviewed the Continuing Ethics Review (CER) Form and is re-issuing approval for the above noted study.

The Western University HSREB operates in compliance with the Tri-Council Policy Statement Ethical Conduct for Research Involving Humans (TCPS2), the International Conference on Harmonization of Technical Requirements for Registration of Pharmaceuticals for Human Use Guideline for Good Clinical Practice (ICH E6 R1), the Ontario Freedom of Information and Protection of Privacy Act (FIPPA, 1990), the Ontario Personal Health Information Protection Act (PHIPA, 2004), Part 4 of the Natural Health Product Regulations, Health Canada Medical Device Regulations and Part C, Division 5, of the Food and Drug Regulations of Health Canada.

Members of the HSREB who are named as Investigators in research studies do not participate in discussions related to, nor vote on such studies when they are presented to the REB.

The HSREB is registered with the U.S. Department of Health & Human Services under the IRB registration number IRB 00000940.

\_\_\_\_\_  
Ethics Officer, on behalf of Dr. Joseph Gilbert, HSREB Chair

Ethics Officer: Erika Basile  Katelyn Harris \_\_\_ Nicole Kaniki \_\_\_ Grace Kelly \_\_\_ Vikki Tran \_\_\_ Karen Gopaul \_\_\_



# Curriculum Vitae

**Name:** Matthew Lowerison

**Post-Secondary Education and Degrees:** University of Western Ontario  
London, ON  
2011-2017, Ph.D., Medical Biophysics  
Thesis: First-order statistical speckle models improve robustness and reproducibility of contrast-enhanced ultrasound perfusion estimates  
Supervisors: Dr. James C. Lacefield and Dr. Ann F. Chambers

University of Western Ontario  
London, ON  
2008 - 2011, B.M.Sc., Medical Biophysics

Vanier College  
Montreal, QC  
2006 - 2008, International Baccalaureate Diploma (Sciences)

Vanier College  
Montreal, QC  
2006 - 2008, Diplôme d'études collégiales, Natural Science

**Honours and Awards:** Kidney Cancer Research Network of Canada Studentship  
2016 - 2017

Best Poster, Basic Science - Robert Zhong Department of Surgery Research Day  
2016

Second Place Podium Prize - London Health Research Day  
2016

Vevo Young Investigator Award  
2015

First Place Podium Prize - London Health Research Day  
2015

Ontario Graduate Scholarship  
2015-2016

Translational Breast Cancer Studentship - London Regional Cancer Program  
2012-2015

Ontario Graduate Scholarship  
2012-2013

Western Graduate Research Scholarship  
2011-2016

Gold Medal for Highest Academic Average  
2011

Alan C. Burton Course Prize in Medical Biophysics  
2011

In-course Scholarship (Yr. III - UWO)  
2010

#### **Peer-Reviewed Journals:**

**M. R. Lowerison**, J. J. Tse, M. N. Hague, A. F. Chambers, D. W. Holdsworth, and J. C. Lacefield, "Compound Speckle Model Detects Anti-Angiogenic Tumor Response in Preclinical Nonlinear Contrast-Enhanced Ultrasonography," *Med. Phys.*, vol. 44, no. 1, p. 99-111, 2017.

**M. R. Lowerison**, M. N. Hague, A. F. Chambers, and J. C. Lacefield, "Improved Linear Contrast-Enhanced Ultrasound Imaging via Analysis of First-Order Speckle Statistics," *IEEE Trans. Ultrason., Ferroelect., Freq. Control.*, vol. 63, no. 9 p. 1409-1421, 2016.

#### **Conference Proceedings:**

**M.R. Lowerison**, M.N. Hague, A.F. Chambers, and J.C. Lacefield, "A Compound Speckle Model for Vascular Complexity Quantification in Nonlinear Contrast-Enhanced Ultrasonography," Ultrasonics Symposium (IUS), 2014 IEEE International, pp. 2249-2252, 2014.

M. Elfarnawany, **M.R. Lowerison**, M.N. Hague, A.F. Chambers, and J.C. Lacefield, "In Vivo Evaluation of An Objective Method to Select Power Doppler Wall Filter Cut-Off Frequency for Microvascular Quantification," Ultrasonics Symposium (IUS), 2014 IEEE International, pp. 436-439, 2014.

**M.R. Lowerison**, M.N. Hague, A.F. Chambers, and J.C. Lacefield, “A two-component speckle model for detection of microbubble signals in linear contrast-enhanced ultrasonography,” 21st International Congress on Acoustics, *Proc. Meetings Acoust.*, vol. 19, article 75026, 2013.

## Conference Presentations and Abstracts:

### Webinars

FUJIFILM VisualSonics Webinar Series:

**Matthew R. Lowerison**, Hon S. Leong, Yaroslav Fedyshyn, Ann F. Chambers, James C. Lacefield, and Nicholas E. Power, “Ultrasound evaluation of patient-derived renal cell carcinoma xenografts in the chicken embryo models,” May 25, 2016. (Invited)

Available: <http://www.visualsonics.com/resources/education/past-webinar>

### Selected Presentations

**Matthew R. Lowerison**, Yaroslav Fedyshyn, James C. Lacefield, Nicholas E. Power, and Hon S. Leong, “Patient Derived Xenografts of Metastatic Renal Cell Carcinoma to Guide Dose Escalation Regimens and Drug Matching,” 8th Canadian Kidney Cancer Forum, Toronto, ON, Canada, February 2-4, 2017. (Oral)

**Matthew R. Lowerison**, Ann F. Chambers, Hon S. Leong, Nicholas E. Power, and James C. Lacefield, “Compound Speckle Model Reduces Contrast Ultrasound Variability in a Patient-Derived Xenograft Model of Renal Cell Carcinoma,” Innovations Toronto 2016, Toronto, ON, Canada, November 16-17, 2016. (Poster)

**Matthew R. Lowerison**, Hon S. Leong, Yaroslav Fedyshyn, Ann F. Chambers, James C. Lacefield, and Nicholas E. Power, “Use of High Frequency Ultrasound Imaging to Quantify Drug Responses in Patient Derived Xenografts of Renal Cell Carcinoma,” Tumor Models Boston, Boston, MA, USA, July 21, 2016. (Oral)

**Matthew R. Lowerison**, Hon S. Leong, Yaroslav Fedyshyn, Ann F. Chambers, James C. Lacefield, and Nicholas E. Power, “PDXovo: Ultra-Fast In Vivo Drug Sensitivity Matrices for Renal Cell Carcinoma Patients Prior to Administration of Targeted Therapy,” AACR: Patient-Derived Cancer Models, New Orleans, LA, USA. *Clin. Cancer Res.*, vol. 22, no. 16 (suppl.), abstract A09, February 11-14, 2016. (Poster)

J. Li, C. Willie, **M. Lowerison**, S.E. Pautler, J. Izawa, J. Lacefield, H. Leong, and N.E. Power, “Establishing a new animal model for pre-clinical drug testing in testicular germ cell tumors,” 70th Canadian Urological Association Meeting, *Can. Urol. Assoc. J.*, vol. 9, suppl. 2, p. S117, 2015.

**Matthew R. Lowerison**, Chantalle J. Willie, Siddika Pardhan, Nicholas E. Power, Ann F. Chambers, Hon S. Leong, and James C. Lacefield, “Ultrasonic evaluation of antiangiogenic

therapy on patient-derived renal cell carcinoma xenograft tumors in the chicken embryo model,” Canadian Student Health Research Forum, Winnipeg, MB, Canada, June 3-4, 2015. (Poster)

**Matthew R. Lowerison**, Chantalle J. Willie, Siddika Pardhan, Nicholas E. Power, Ann F. Chambers, Hon S. Leong, and James C. Lacefield, “Ultrasonic evaluation of antiangiogenic therapy on patient-derived renal cell carcinoma xenograft tumors in the chicken embryo model,” AACR: Tumor Angiogenesis and Vascular Normalization, Orlando, FL, USA. *Mol. Cancer Ther.*, vol. 14, no. 12 (suppl. 1), abstract B02, March 5-8, 2015. (Poster)

**Matthew R. Lowerison**, M. Nicole Hague, Ann F. Chambers, and James C. Lacefield, “A compound speckle model for vascular complexity quantification in nonlinear contrast-enhanced ultrasonography,” 2014 IEEE International Ultrasonics Symposium (IUS), Chicago, IL, USA, September 3-6, 2014. (Poster)

**Matthew R. Lowerison**, M. Nicole Hague, Ann F. Chambers, and James C. Lacefield, “A Two-Component Speckle Model for Detection of Microbubble Signals in Linear Contrast-Enhanced Ultrasonography,” 2013 Artimino Ultrasound Conference, Lake Rosseau, ON, Canada, June 16, 2013. (Oral)

**Matthew R. Lowerison**, M. Nicole Hague, Ann F. Chambers, and James C. Lacefield, “A Two-Component Speckle Model for Detection of Microbubble Signals in Linear Contrast-Enhanced Ultrasonography,” 21st International Congress on Acoustics, Montreal, QC, Canada, June 3, 2013. (Oral)

**Matthew R. Lowerison**, M. Nicole Hague, Ann F. Chambers, and James C. Lacefield, “A Two-Component Speckle Model for Detection of Microbubble Signals in Linear Contrast-Enhanced Ultrasonography,” 11th Imaging Network Ontario Symposium, Toronto, ON, Canada, February 4, 2013. (Oral)